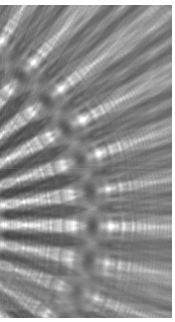

Göttingen Series in
X-ray Physics

Jakob Soltau

Hard X-ray Microscopy Enhanced by Coherent Image Reconstruction

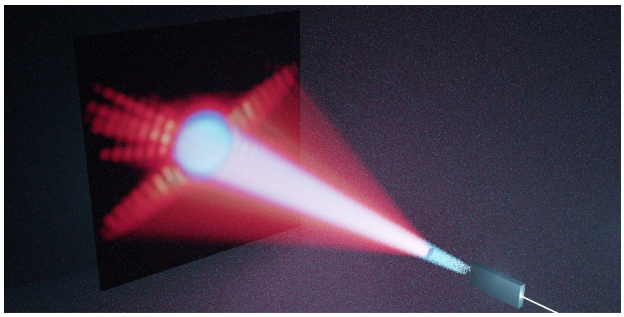

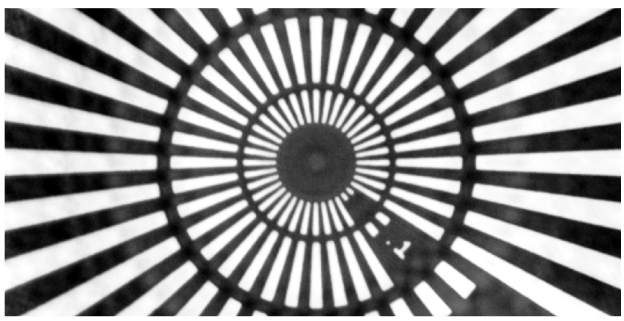

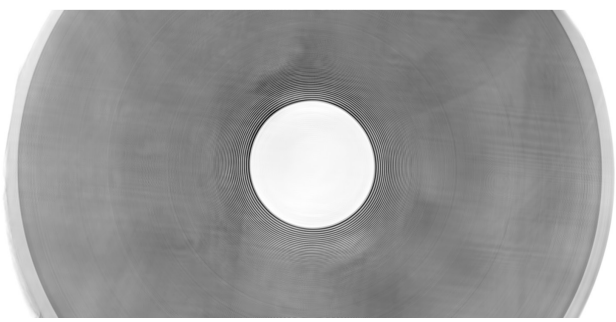

Universitätsverlag Göttingen

Jakob Alexander Soltau

Hard X-ray Microscopy Enhanced by Coherent Image Reconstruction

Published in 2022 by Universitätsverlag Göttingen
as volume 29 in the series “Göttingen series in X-ray physics”

Jakob Alexander Soltau

Hard X-ray Microscopy Enhanced by Coherent Image Reconstruction

Göttingen series in X-ray physics
Volume 29

Universitätsverlag Göttingen
2022

Bibliographic information

The Deutsche Nationalbibliothek lists this publication in the Deutsche Nationalbibliografie; detailed bibliographic data are available on the Internet at http://dnb.dnb.de.

Funded by the Deutsche Forschungsgemeinschaft (DFG) Grant No. SFB 755 "Nanoscale Photonic Imaging" and the German Federal Ministry of Education and Research (BMBF) through Grant No. 05K19MG2.

Address of the author
Jakob Alexander Soltau
Email: jakob.soltau@uni-goettingen.de

Dissertation
for the award of the degree "Doctor rerum naturalium"
of Georg-August-Universität Göttingen
within the doctoral program in Physics
of the Georg-August University School of Science (GAUSS)

Thesis Committee
Prof. Dr. Tim Salditt, Institute for X-Ray Physics, University of Göttingen
Prof. Dr. Christian Jooß, Institut für Materialphysik, University of Göttingen
Dr. Markus Osterhoff, Institute for X-Ray Physics, University of Göttingen

Date of the oral examination: 30.08.2021

Setting and layout: Jakob Alexander Soltau
Cover image: Jakob Alexander Soltau

GEORG-AUGUST-UNIVERSITÄT GÖTTINGEN IN PUBLICA COMMODA SEIT 1737

© 2022 Universitätsverlag Göttingen
https://univerlag.uni-goettingen.de
ISBN: 978-3-86395-553-3
DOI: https://doi.org/10.17875/gup2022-2037
ISSN: 2191-9860
eISSN: 2512-6326

Preface of the series editors

The Göttingen series in x-ray physics is intended as a collection of research monographs in x-ray science, carried out at the Institute for X-ray Physics at the Georg-August-Universität in Göttingen, and in the framework of its related research networks and collaborations.

It covers topics ranging from x-ray microscopy, nano-focusing, wave propagation, image reconstruction, tomography, short x-ray pulses to applications of nanoscale x-ray imaging and biomolecular structure analysis.

In most but not all cases, the contributions are based on Ph.D. dissertations. The individual monographs should be enhanced by putting them in the context of related work, often based on a common long term research strategy, and funded by the same research networks. We hope that the series will also help to enhance the visibility of the research carried out here and help others in the field to advance similar projects.

Prof. Dr. Tim Salditt
Prof. Dr. Sarah Köster
Editors
Göttingen June 2014

Preface to the present volume

X-ray microscopes can be realized based on several different approaches, which have been developed almost independently as quite quite distinct techniques. From classical X-ray microscopy based on Fresnel zone plates to lensless coherent diffractive imaging (CDI) and finally to propagation imaging and holography, the different methods each have their merits and limitations.

This work now offers a new perspective, and a way to overcome some of the long standing limits. It first shows how Fresnel zone plate optics can be designed for higher photon energies and higher resolution, taking volume diffraction fully into account. Next, it demonstrates that X-ray holography is no longer limited by the numerical aperture of the probing beam, if holographic and diffractive signals are jointly recorded and exploited. Finally, the work achieves phasing of extended objects from single shot recordings, based on a combination of objective lenses with a cleverly implemented phase retrieval scheme. After all, we may ask whether different X-ray microscopy approaches can be finally reconciled ? United they may stand stronger than ever before!

Prof. Dr. Tim Salditt
Göttingen, June 2022

Contents

Introduction

1

X-ray microscopy has evolved into a powerful tool to study the structure and dynamics of matter with unprecedented resolution in different scientific disciplines ranging from physics and chemistry to material and life sciences. In the past two decades, progress in x-ray microscopy was driven either by improvements in x-ray optics or by improvements in the image reconstruction by using algorithms as computational lenses. In this work we combine both approaches to exploit the advantages of x-ray imaging with a large numerical aperture and the advantages of coherent image reconstruction. We show that a combined x-ray microscope using both, advanced optics and algorithms, is neither limited by flawed optics nor by constraints imposed by reconstruction algorithms, which enables to go beyond current limits in resolution and applications.

The advent of microscopy can be dated back to the introduction of the first lens-based optical microscopes built in the 17$^{\text{th}}$ century [Dar12]. These enabled a completely new perspective in almost all scientific fields. Nevertheless, it took two centuries until Abbe derived a formula describing the best resolution that can be achieved by an imaging system. He derived the formula as he was annoyed by the lack of theory in the design of optical microscopes and their improvements, or as he stated "fast ausschliesslich Sache der Empirie, geschickten und ausdauernden Probierens von Seiten erfahrener Praktiker" [Abb73]. This today well known resolution limit for an optical system, which is valid for visible light as for x-rays, is written as

$$d_{\text{min}} = \frac{\lambda}{2n_\lambda \sin\theta} \,. \tag{1.1}$$

The resolution d_{min} describes the smallest distance at which two points are still distinguishable[1]. It is defined as a function of the wavelength λ divided by the product of the refractive index ${n_\lambda}$[2] and the sine of the half diffraction opening angle θ. The product is known as the numerical aperture (NA $= n_\lambda \sin\theta$). Over the last centuries, improve-

[1] A conventional definition of the resolution is the full width at half maximum (FWHM) of the point spread function: $d_{\text{min}} = 0.51 \cdot \lambda/\text{NA}$ [BW13]

[2] For the calculation of d_{min} only the real part of the refractive index n_λ is used.

ments in the fabrication of lenses and immersion media for microscopes operating in the visible range enabled resolutions better than $\lambda/2$.

In the case of hard x-rays[3], where the wavelength is shorter by a factor of about 5000 compared to the optical regime, a microscope with a NA similar to optical microscopes would promise resolutions in the sub-Angstrom range. This would even allow imaging of atoms. In contrast to electron microscopes, which use an even shorter wavelength, the high penetration depth of hard x-rays into matter enables the investigation of thick samples and bulk properties in two and three dimensions, without any vacuum constraints.

Since the discovery of x-rays by Röntgen in 1895 [Rön95], x-ray imaging has developed from plain shadowgraphy [Ard39] to x-ray microscopes which can resolve nanoscale structures [Cha19]. Today x-ray microscopes are used for example for medical imaging to gain understanding of diseases such as Alzheimer [Töp+18] or Covid-19 [Eck+20], for material science improving life-time and capacity of batteries [Lim+16] or nanowires which are promising materials for next-generation photovoltaics [Cha+19a], time-resolved imaging of three-dimensional nanoscale magnetization dynamics [Don+20] or for cultural heritage to study artwork and to restore famous fifteenth-century paintings [Van+17].

Although the short wavelength of x-rays favours high resolution microscopy, the NA of optical components for x-rays is rather low. This is due to the low interaction cross-section of x-rays with matter, which can be described by the complex refractive index $n_\lambda = 1 - \delta_\lambda + i\beta_\lambda$. The variable δ_λ describes the refraction and β_λ describes the absorption of a wavefield. Typical values[4] in the case of soft x-rays are in the order of $\delta_\lambda \approx 10^{-3}$ and $\beta_\lambda \approx 10^{-4}$ for 0.5 keV [HGD93]. With $\delta_\lambda \approx 10^{-6}$ and $\beta_\lambda \approx 10^{-9}$ for 10 keV, the interaction of hard x-rays with matter is over three orders of magnitude lower. The increased photon energy also leads to a larger difference between refracting (δ_λ) and absorbing part (β_λ) of the complex refractive index. The latter is not only relevant for the development of x-ray optics but also for the investigation of samples. This is the reason why in the case of hard x-rays the refraction (δ_λ) or phase sensitivity of microscopes becomes more relevant than the absorption (β_λ) sensitivity.

Early x-ray microscopes used a lens system with the sample positioned between a condenser and an imaging lens, as known from optical microscopes. But the low interaction cross-section of x-rays with matter inhibited the fabrication of efficient large numerical aperture optics and limited first x-ray microscopes to the energy range

[3] We define hard x-rays to be roughly in the range of $E_{\mathrm{ph}} = 5$ keV to 300 keV

[4] Here for amorphous carbon (C).

of soft x-rays. This restricted the variety of samples to objects which are optically thin and robust against high radiation doses [Att00]. Moreover, imperfections in the optics and related aberrations impeded x-ray microscopes from reaching the theoretical resolution limit. Over the last decades image formation in x-ray microscopes has fundamentally changed. The change was driven by the advent of synchrotrons as bright monochromatic and coherent x-ray sources, new techniques in the development and fabrication of optics, and the possibility for the quantitative analysis of the recorded data. The latter was enabled by pixelated x-ray detectors and powerful computers [SA10; CN10]. The concepts today exploit the advantages of bright radiation sources and the high penetration power of hard x-rays, overcoming challenges such as missing highly efficient point-to-point imaging optics or the lack of detectors with sub-micrometer pixel sizes.

In this work, experiments were performed with two different approaches of x-ray microscopy. The first is based on optics with a large NA and thus a small focus to scan the sample, namely scanning transmission x-ray microscopy. The second approach uses the full-field illumination of the sample and the subsequent image reconstruction, namely coherent full-field imaging. Both methods can be used for imaging with absorption and phase contrast.

In scanning transmission x-ray microscopy (STXM) the sample is scanned with a focused x-ray beam [Att00]. Behind the sample the transmitted beam is recorded and the detected signal is plotted as a function of the position, to generate a map of the sample structure. The signal can be either the measured transmission of the x-ray beam for absorption contrast or the deflection of the x-ray beam by the sample which results in an image of the differential phase contrast. The resolution in a scanning transmission x-ray microscope is given by the focus size of the probing x-ray beam. Newly developed diffractive x-ray optics such as multilayer zone plates (MZP) or multilayer Laue lenses (MLL) can focus an x-ray beam down to 5 nm [Dör+13], and can be utilized for hard x-rays up to 100 keV [Ost+17b]. These optics fabricated by thin film multilayer deposition promise to extent the possible image resolutions of hard x-ray scanning experiments to sub-10 nm. Additionally, the rather simple approach of scanning the sample and recording the transmitted signal has the advantage that the method can be easily combined with other techniques such as measuring the fluorescence photons to get an element specific map of the sample [Van+17], determining the conductivity of the sample by measuring the x-ray beam induced current (see chapter 4) or new concepts such as Compton x-ray microscopy which has the potential to enable low dose imaging [Vil+21]. Furthermore the approach does not depend on complex reconstruction

algorithms in contrast to full-field methods introduced next. The drawback is the necessity to scan samples, which makes imaging of quasi-instantaneous acquisitions of pulsed sources such as XFELs as well as the acquisition of large data sets, needed for three dimensional imaging, challenging or even impossible.

The second approach which is used and further developed in this thesis is coherent full-field imaging. In general, the method is based on recording the interference pattern of the wavefield diffracted by the sample and performing a subsequent reconstruction. A distinction can be made whether the interference pattern is formed by (i) the interference of the diffracted with the non-diffracted wavefield or (ii) the interference of the diffracted wavefields between each other. The case (i) is called holography. In the ideal case of holography a cone beam emanating from an x-ray point source illuminates the sample. Behind the sample an interference pattern is formed of the diffracted and non-diffracted wavefield. The interference pattern encodes the information of the absorption and the phase shift of the sample. A geometrical magnification of the interference pattern can be achieved, if a divergent beam is used to illuminate the sample. In in-line holography the highest possible resolution is limited by the opening angle of the cone beam illumination ($\theta = \theta_{\mathrm{CB}}$). The case (ii) is called coherent diffractive imaging (CDI). In the simplest case a confined parallel beam illuminates the sample. In contrast to in-line holography the non-diffracted (primary) beam is in most cases not resolved, and often even blocked by a beam stop. For CDI the resolution is defined by the maximum detected scattering angle which is limited by the opening angle of the detector ($\theta = \theta_{\mathrm{De}}$). Both imaging approaches, in-line holography and CDI, seem quite similar at first, but differ in robustness, resolution, and constraints on the experimental setup. Nevertheless all techniques - CDI, in-line holography and especially scanning microscopy - depend on the illumination properties, such as confinement, spatial coherence, divergence, and focal spot size.

The goal of this thesis was the development of new methods for hard x-ray microscopy, to push the resolution limit and to overcome current constraints regarding working distance, field-of-view and photon efficiency.

This thesis is structured as follows: In chapter 3 we simulate a new type of hard x-ray lenses, MZPs, to investigate volume diffraction effects within the multilayer structure, and to improve future MZPs with smaller focus sizes (sub-5 nm) and higher efficiencies (up to 100 %). In chapter 4 we characterize the MZPs experimentally and apply the MZPs in first applications. In chapter 5 we present a new imaging scheme, which combines aspects of in-line holography and CDI in a joint approach. We show that this

method overcomes the current resolution limit of in-line holography and can achieve super-resolution with respect to the NA of the illuminating beam. Chapter 6 provides an outlook to use the MZP similar to an objective lens in a coherent full-field imaging experiment with iterative phase retrieval.

Detailed outline

In chapter 2 we present a conceptual and historical overview of different x-ray microscopy methods: From plain shadowgraphy to nanoscale coherent imaging based on the reconstruction of interference patterns.

In chapter 3 we present a new type of hard x-ray multilayer optics currently in development for sub-5 nm focus sizes and high diffraction efficiencies up to 100 %. We address the question of diffraction inside these new multilayer structures. As pointed out by [Mas+04; Kan+05], the description of multilayer optics by the classical kinematic diffraction theory is insufficient when the layer width is reduced to few nanometers and the optical depth is increased to several micrometers. Therefore we perform finite difference simulations, for the propagation of the x-ray wavefields, which offer high accuracy at reasonable numerical complexity. Further we extend the simulations from single optical elements to full experimental setups. The goal is the development of a forward (propagation) model using the MZP similar to an objective lens in a scenario where it is coherently illuminated. This scenario is demonstrated experimentally in chapter 6.

In chapter 4 we demonstrate the application of the newly developed MZPs with outer zone widths of 5 nm, and fabricated by pulsed laser deposition in a scanning experiment. We show by ptychographic reconstruction that with a fully illuminated MZP focus sizes below 10 nm can be achieved. Additionally, we demonstrate a new configuration of an off-axis illuminated MZP for an improved contrast and relaxed working-distances. The small focus is used for real-space mapping of local charge carrier recombination in a single InP nanowire using the method of x-ray beam induced currents (XBIC). This marks the transition from the MZPs fabricated by pulsed laser deposition as optics in development to optics for the investigation of samples in real experiments.

In chapter 5 we demonstrate a new approach of full-field holographic x-ray imaging based on cone-beam illumination, beyond the resolution limit given by the cone-beam numerical aperture. We therefore refer to this approach as *super-resolution in-line holography*. We exploit the image information encoded in the far-field diffraction and in holographic self-interference in a combined reconstruction scheme, without the

usual empty beam correction step of in-line holography. We show that an illumination profile tailored by waveguide optics and known by prior probe retrieval is sufficient for solving the phase problem. The approach paves the way towards high resolution and dose-efficient x-ray imaging in two and three dimensions.

In chapter 6 we present an outlook by demonstrating an additional new imaging scheme, to which we refer as *reporter based imaging*. In this imaging scheme the MZP is not used as a focusing lens but as a 'reporting' structure positioned in the near-field of the diffracted beam behind the sample. At first, this configuration seems identical to a conventional transmission x-ray microscope or optical microscope, but instead of recording a sharp image of the sample directly, we exploit the advantage of the coherent illumination and of the propagation based phase contrast. By developing a new iterative phase retrieval process based on the knowledge of the MZP's complex transmission function, we can reconstruct the structure of the sample without aberrations induced by the optics. Furthermore, the resolution of the image is not limited by the NA of the MZP but is extended by the diffraction signal of the sample. This results in a better image quality concerning both resolution and contrast compared to conventional transmission x-ray microscopy. We obtain sub-10 nm spatial resolution in an experimental demonstration.

Chapter 7 gives a conclusion and outlook of the thesis.

From plain shadowgraphy to nanoscale imaging

2

2.1 Introduction to the interference of wavefields

The first attempts of x-ray microscopes were based on the approach to copy the concept of an optical imaging system with at least two imaging lenses and the sample positioned in between the lenses. Despite first successes in the energy range of soft x-rays (0.3-5 keV), the idea faced obstacles especially for the implementation with hard x-rays (5-300 keV). The application of hard x-rays for microscopy is beneficial as it is not limited to vacuum propagation and has a significantly higher penetration depth. This allows the analysis of bulk properties of higher Z materials. But the low interaction makes it also challenging to build a lens and detector system. Nowadays, the common approach for high resolution and high contrast x-ray microscopy is to illuminate the sample with an x-ray beam and record the interference pattern at a sufficient distance. Though optics are used to guide and focus the x-ray beam, no lens is positioned between the sample and the detector. The task of the lens to resolve a sharp image or in other words to decode the sample structure from the interference pattern is performed by phase retrieval algorithms. This is called lensless imaging and provides a solution for the lack of aberration- and distortion-free optics.

One of the first who postulated this approach was Gabor in 1948 [Gab48]. He was motivated to build an electron microscope but was limited by the quality of electron lenses at that time. He suggested that by detecting the full wavefield behind the sample, especially the interference of the non-diffracted and the diffracted wavefields, the structure of a sample can be reconstructed by optical means (today numerical means). He concluded that this is only possible under the constraint of a coherent illumination[1].

Coherent x-ray sources as described by Gabor, are used in in-line holography for the

[1] A coherent illumination is spatially coherent and temporally coherent. The latter can also be referred to as monochromatic.

interference of the diffracted and the non-diffracted wavefield and in CDI in a modified version for the interference of the diffracted wavefields with one another. In both cases the forward problem, the interaction of the sample with the incident x-ray beam and the propagation to the detector plane, can be described by classical wave optics and can be solved by numerical calculations. Contrarily, the inverse problem, which represents the reconstruction of the sample structure from the measured interference pattern, is challenging to solve, as only the intensity and not the phase of the wavefield can be measured [2]. This is often referred to as the phase problem. The inverse problem can be solved by the retrieval of the phase of the wavefield. For this purpose, the calculation of the forward problem is often an indispensable tool, as it gives access to the process of image formation. This tool is used throughout this thesis for the design and improvement of x-ray optics and the development of new imaging schemes.

In free space the time evolution of an electromagnetic field at any point in real space can be defined based on the Maxwell equations [Pag06]. Assuming constant material conditions we can derive the Helmholtz equation

$$\left[\Delta + k^2 n_\lambda^2 (x,y,z)\right] \psi_\lambda (x,y,z) = 0 \,, \tag{2.1}$$

here Δ defines the Laplace operator, $k = 2\pi/\lambda$ the wavenumber in free space for wavelength λ, n_λ the refractive index describing wavefield matter interaction and $\psi_\lambda (x,y,z)$ the time-independent monochromatic wavefield in three dimensions [3]. Two coherent wavefields, ψ_1 and ψ_2, are shown in Fig. 2.1 propagating in the same direction and with the same initial conditions. In the region of free space both have a constant amplitude and an equal phase. In the region where ψ_2 propagates through matter the amplitude decreases and a phase shift ($\Delta\varphi$) relative to the unperturbed wavefield ψ_1 occurs. Suppose both wavefields were overlapping and a detector positioned at the right side would record interference of both wavefields. The impact of matter on the wavefield can be described by solving the Helmholtz equation (2.1). This can be done by e.g. using a finite differences solver as shown in chapter 3. For most biological samples, it is possible to neglect volume diffraction effects in the propagation direction. This allows to assume the refractive index along the optical axis as one projection for the calculation of the outgoing wavefield. This is known as projection approximation. The approximation fails with increasing optical thickness and decreasing

[2] The electromagnetic field oscillates at rates of $\approx$ 10 PHz. This can not be resolved by electronic devices.

[3] The description is valid for the absence of matter $n_\lambda = 1$ as well as for the case of matter if we assume that the materials are non-magnetic and only slowly varying compared to the wavelength λ. These conditions can be satisfied for all cases described in the following.

size or increasing density of sub-features. The important parameter for the wavefield matter interaction is the index of refraction which is defined as $n_\lambda = 1 - \delta_\lambda + i\beta_\lambda$ with a real-valued part δ_λ which describes the resulting phase shift $\Delta\varphi$ of the wavefield behind the matter compared with a wavefield in free space and an imaginary part $i\beta_\lambda$ which describes the change in the amplitude ($|\psi_2| > |\psi_2'|$), namely the absorption. For x-rays, δ_λ relates to the electron density and decreases with increasing x-ray energy[4]. In contrast the absorption can be described in the particle description as the sum of the effects: photo-absorption, elastic- (Rayleigh), and inelastic- (Compton) scattering as well as pair-production [AM11].

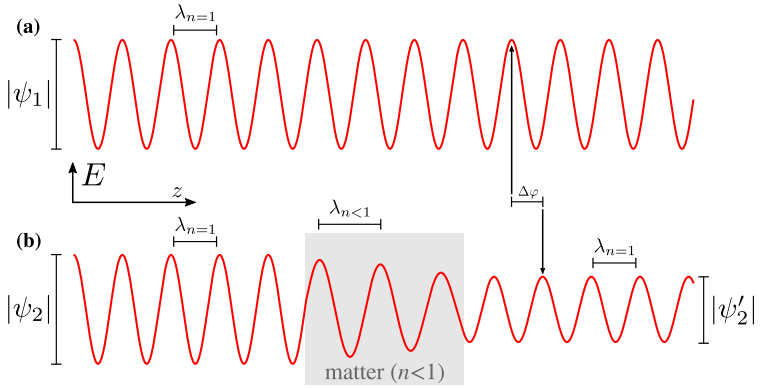

Fig. 2.1: (a) Illustration of an x-ray wavefield ψ_1, with wavelength $\lambda_{n=1}$ and an amplitude $|\psi_1|$ propagating through vacuum ($n = 1$) in direction z. (b) A second wavefield ψ_2 with the same initial parameters but with a material slab ($n < 1$) in propagation direction. The wavelength in the material is $\lambda_{n<1} > \lambda_{n=1}$. Behind the material block the amplitude of the wavefield is lower due to absorption ($|\psi_2'| < |\psi_2|$) and the phase is shifted by $\Delta\varphi$ relative to the unperturbed wavefield ψ_1.

The reconstruction of a sample from an interference pattern recorded in a distant plane is based on the assumption that the interfering wavefields in the detection plane can be propagated back to the plane of the sample. This is given if (i) both wavefields are monochromatic (temporal coherence) and (ii) all points of the wavefields are correlated with each other (spatial coherence). The latter can be defined by the spatial coherence length L_C describing the length for which the source spot of size σ_S can not be distinguished from a point source. L_C is defined at a distance z as

$$L_C = \frac{z\lambda}{\pi\sigma_S}.$$

[4] Exceptions are x-ray energies near the absorption edges.

The equation can be derived from wave optics [Goo17]. A source can be considered as diffraction limited if it fulfills the above equation.

2.2 Conceptual and historical overview of x-ray microscopy

To our knowledge, the first x-ray microscope was the *Röntgenstrahlen-Schattenmikroskop* proposed but not experimentally realized in 1939 by von Ardenne [Ard39]. A magnified image of the sample was obtained by using a small x-ray point source, the sample positioned at close distance to the source and recording the shadow image of the divergent beam at a far distance. The recorded shadow image showed the magnified absorption pattern of the sample. The concept was adapted among others by Cosslett and colleagues around 1960 [Cos59; Cos65].

For the generation of a small x-ray source spot an electron beam was focused on an anode and x-ray photons were emitted by bremsstrahlung and characteristic radiation in 4π sr and shaped by optical elements. This is the same concept Röntgen used when he discovered x-rays in 1895 [Rön95]. Since most of the electron energy is converted into heat while impinging on the anode, the dissipated power leads to an increase of the anode temperature. The efficient transfer of the dissipated power to a heat sink is limited by geometrical and thermo-mechanical constraints. Nevertheless, the basic concept of conventional x-ray sources in the laboratory has not changed. Some improvements for a better heat transfer allowing a higher electron current have been achieved using rotating anodes [Beh21] or liquid jet anodes [HOH03; Ote+08].

The development of synchrotrons as a new x-ray source is closely linked to the development and improvements of x-ray microscopy. Early synchrotrons were outstanding in their brightness as well as temporal and spatial coherence compared to laboratory x-ray sources. Developments of synchrotrons over the past two decades have improved nearly all properties of the generated x-ray beams. The improvements of spatial coherence were in particularly decisive for the realization of new imaging experiments with higher resolution and contrast [AM11]. Recently, the first diffraction limited synchrotrons have been constructed [Ebe15].

Transmission x-ray microscopy Transmission x-ray microscopy (TXM) is conceptually similar to the (incoherent) visible light microscopy. The basic setup is shown

in Fig. 2.2 (a). An incoming x-ray beam is focused by a condenser lens onto a sample. Behind the sample a second lens is positioned, the imaging lens. The position of the imaging lens, relative to the sample and the detector is known from the thin lens equation of optical lenses $1/g + 1/b = 1/f$ with g the distance between the object and the imaging lens, b the distance between the imaging lens and the detector and f the focal length of the imaging lens [Att00]. If adjusted properly, the detector records a sharp magnified image of the intensity of the beam in the sample plane. As illustrated, only the absorption contrast of the sample is detected, not the phase contrast. However, for phase contrast imaging, a phase plate can be used similar to visible light microscopy [Sch98; Att00].

The construction of TXM setups was enabled by the development of zone plates as x-ray optics. Zone plates are basically circular diffraction gratings of opaque and transparent zones that can be used for point-to-point imaging or focusing due to their specific, gradually decreasing grating spacings (see Fig. 2.3). The outermost grating spacing respectively zone width is approximately equal to the size of the focal point and defines the resolution of TXM. Since the opaque zones need to absorb the incoming wavefield, zone plates need a sufficient optical depth, making the fabrication of zone plates for hard x-ray energies challenging.

First zone plates for soft x-rays were developed using the method of holographic fabrication in 1969 by the group of Schmahl, Rudolph, Niemann and colleagues from the University of Göttingen [SR69]. Schmahl and coworkers superimposed two coherent UV laser beams to illuminate a photo-resist covering a substrate. Later the method was extended to electron beam lithography[5] [Sha+79; Ker+84].

In principle, imaging can be performed by TXM using incoherent light. The coherence constraint in TXM is only given by the spectral bandwidth of the incoming x-ray beam. The constraint is not imposed due to image formation, but due to the limited spectral bandwidth of zone plates. The maximum spectral bandwidth $\Delta\lambda$ which can be used for zone plates is defined as a function of the number of illuminated zones N as $\Delta\lambda/\lambda \leq 1/N$ [Att00].

Diffractive optics such as zone plates, diffract the wavefield in multiple orders. This results in the formation of multiple focal points, where the $+1^{st}$ and -1^{st} order focal points have the highest intensity. To block unwanted diffraction orders, a central beam stop is positioned in front of the condenser zone plate and a pinhole – the so called order sorting aperture (OSA) – is positioned in the sample plane, as depicted in

[5] Zone plates fabricated with lithography are often referred to as Fresnel zone plates (FZP).

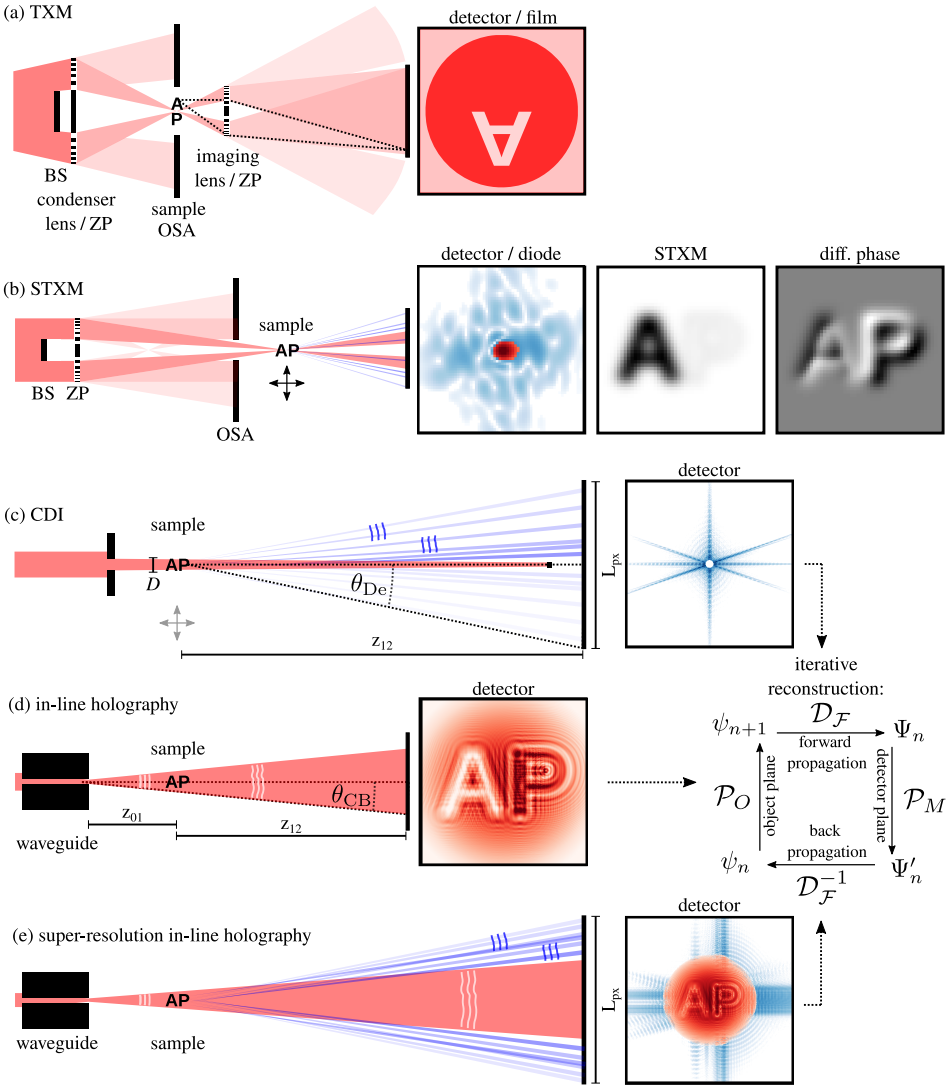

Fig. 2.2: *(caption next page)*

Fig. 2.2 *(previous page)*: Conceptual overview of different x-ray microscopes. In all cases the same sample consisting of a pure absorption object A and a pure phase object P is depicted. (a) Illustrates the transmission x-ray microscope (TXM). A monochromatic spatially incoherent beam illuminates a condenser zone plate (ZP). The sample is positioned in the focal plane. A second zone plate (ZP), the imaging zone plate, forms a sharp image of the sample on a detector. In this case only an image of the pure absorption object becomes visible. The sample, imaging zone plate and the detector needs to be positioned at the positions given by the thin lens formula. Additionally a beam stop (BS) and an order sorting aperture (OSA) can be added to block the unwanted diffraction orders. (b) Illustration of a scanning transmission x-ray microscope (STXM). A monochromatic and spatially coherent beam illuminates a zone plate (ZP). The sample is positioned in the focal plane of the zone plate. The transmitted beam is detected behind the sample. By scanning the sample a map of the absorption is recorded. By detecting the deflection of the transmitted beam, a map of the differential phase contrast can be obtained. (b) Shows a single detector image on the left, the transmission map in the middle and the map of differential phase contrast on the right. Similar to the TXM, a beam stop (BS) and an order sorting aperture (OSA) to block unwanted diffraction orders are positioned. (c) Illustration of a coherent diffractive imaging (CDI) experiment. A fully coherent beam is confined by an aperture. The sample is positioned in the approximately parallel beam and is fully illuminated. The scattered radiation interferes coherently and is detected in the far-field by a large area detector. To protect the detector a beam stop is positioned in front of the detector. The largest detected scattering angle is denoted as θ_{De}. From the detector image the phase and amplitude of the sample structure can be reconstructed. In CDI the sample needs to full-fill the sampling constraint. This limits the sample and the illumination to a maximum size of D (see equation 2.2). (d) Experimental setup for in-line holography. The incident coherent beam is filtered by an x-ray waveguide generating approximately a point source. The self-interference of the diffracted and non-diffracted wavefield is detected by a detector. The opening angle of the cone beam is denoted as θ_{CB}. From the recorded hologram the phase and amplitude of the sample structure can be reconstructed. (e) Illustrates the novel imaging scheme of super-resolution in-line holography presented in this work. The imaging scheme is described in detail in chapter 5. Similarly to in-line holography, the incoming beam is filtered and a quasi point source is generated. In contrast to in-line holography the far-field diffraction and the holographic self-interference is detected. Therefore a resolution beyond the limit imposed by the NA of the cone-beam illumination can be achieved. For the case of (c-e) the sample structure can be reconstructed by iterative algorithms, as sketched on the right side.

Fig. 2.2 (a). The diffraction into multiple orders limits the focusing efficiency of the zone plate to about 20 % [6] [Pag06] but more realistic 10 % or less [Ung89].

Both, the limited spectral bandwidth, and especially the low focusing efficiency of the binary zone plates impose limits for the application of TXM with laboratory sources. The success of TXM came with the advent of synchrotron facilities with x-ray beams of high brightness and high coherence.

In 1974 a first TXM setup was constructed and used in the laboratory with $C\text{-}K_\alpha$ radiation (0.3 keV). By imaging simple test structures a resolution of 2 μm could be achieved [NRS74]. In 1980 Schmahl and colleagues moved their TXM setup to the synchrotron facility L.U.R.E. in France [Sch+80] and in 1984 to the synchrotron BESSY in Berlin [Rud+84]. The resolution was significantly increased, down to 50 nm, and also first biological samples were imaged i.e. chromosomes. Early TXM setups were usually operated with soft x-rays. Firstly because of the decreasing efficiency of zone plates for higher photon energies and secondly due to the good absorption contrast of biological samples in the so-called water window (0.3 keV-0.5 keV). Imaging with phase contrast was therefore not needed. Also today, TXM is primarily performed in the x-ray energy range below 5 keV to study bio materials [Par+08] or to address questions in material science such as the degradation of batteries [Yan+19]. The relaxed coherence requirements and thereby reduced necessity to filter the incident beam enables image acquisition with high photon flux. The high photon flux can be exploited for the fast acquisition of large data sets. This was shown by the acquisition of an one-minute nano-tomogram with sub-50 nm spatial resolution [Ge+18]. Nevertheless, in a recent publication it was shown that TXM can also be performed at a photon energy of 8 keV for imaging a test structure with absorption contrast and an impressive resolution of 10 nm with an image acquisition time of 20 s [De +21].

Scanning transmission x-ray microscopy A different approach to full-field imaging is to scan the sample with a focused beam and to record the transmission signal as a function of the scan position. This approach is called scanning transmission x-ray microscopy (STXM). A STXM setup is depicted in Fig. 2.2 (b). An incoming x-ray beam is confined and focused by x-ray optics. The focused beam is used to scan the sample in the focal plane. Behind the sample, the transmitted beam is detected by a diode or a pixel detector. No objective lens is used. The pixel detector has the advantage that beside the transmitted photon flux used for absorption contrast, the deflection

[6] 40 % for the case of the later introduced phase zone plates, respectively MZPs.

of the transmitted beam can be recorded to access differential phase contrast. For the depicted setup an exemplary detector image is shown. Additionally two scanning images are plotted: The left shows the integrated photon flux as a function of scan position (absorption contrast) and the right shows the beam deflection (differential phase contrast) as a function of scan position, giving access to the detection of pure phase objects. The deflection can be determined by calculating the center-of-mass in each recording. In both cases the best achievable resolution is defined by the focus size of the x-ray beam, which can vary from several micrometers down to sub-10 nm. Beside the detection of the transmitted beam, the measurement can be combined with other detection methods, such as fluorescence detectors for an element specific map, or as shown in chapter 4 with the method of x-ray beam induced current (XBIC) to measure the spatial distribution of the conducting properties of a sample. For the generation of (small) diffraction limited focal spot sizes, the focusing optics need to be illuminated fully spatially coherent. This is in contrast to the incoherent imaging approach of TXM. Therefore most high resolution STXM experiments are performed at synchrotron facilities. On the other hand, STXM has the advantage that no optical element is positioned between the sample and the detector. This overcomes the disadvantage imposed by x-ray optics with a low efficiency and enables imaging of the sample with a low dose. Furthermore, the absence of imaging optics reduces the effect of distortions and aberrations. A first STXM experiment was realised in 1972 using a simple pinhole [HH72] but soon, in 1980, improved by zone plates as focusing optics in combination with piezoelectric translators [Rar+80] for a precise sample movement.

The imaging method of STXM is today still used especially in combination with new high-resolution focusing optics such as the multilayer zone plates (MZP) presented in this thesis or multialyer laue lenses (MLL). These newly developed optics can focus an x-ray beam to a size of sub-10 nm (see chapter 4 and [Dör+13; Baj+18]) and have shown to operate at photon energies of up to even 100 keV [Ost+17b]. The improvements in fabrication of zone plates can be seen in Fig. 2.3. In (a,b) zone plates from 1989 are shown, with an outermost zone width of 50 nm, an optical depth of 150 nm and developed for photon energies in the water window (< 0.5 keV). In (b) the profile of an early phase zone plate from 1996 is shown, with only few zones (80) and an outermost zone width of 40 nm. The phase zone plate was fabricated by depositing different material layers on a glass wire. This is in contrast to classical zone plates, where the structure consists of alternating opaque and transparent zones. In case of phase zone plates and later multilayer zone plates, the materials and the optical depth are chosen such that the phase between neighbouring layers is shifted by π. This

enables constructive interference of the wavefields diffracted in all zones in the focal spot which results in an increased efficiency and enables the use of high x-ray energies. In (c) the currently developed multilayer zone plates (MZP) with outermost zone width of 5 nm, an optical depth of 6 µm and 784 layers for high resolution is shown. This MZP is further analyzed in chapter 3 and applied in experiments in chapter 4.

Not only zone plates, but also other x-ray optics are applied for nanoscale imaging with STXM, each with different advantages. An overview is given at the end of this section. STXM is today used in many different fields, from the analysis of meteorite samples [Lo+19], to studies of the distribution of metallic elements in the human brain [Eve+21], the investigation of particles emitted from the damaged reactor at Fukushima [Oku+20], or in chapter 4 of this thesis for the characterization of the specification of nanowires which are promising materials for next-generation photovoltaics.

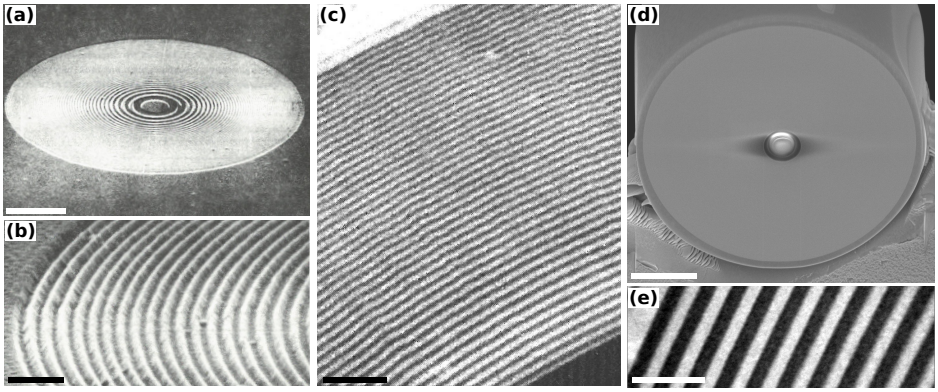

Fig. 2.3: History of zone plates. (a-b) Zone plates fabricated in 1989 using sputter etching with argon ions, with a smallest outer zone width of 50 nm fabricated for the use of imaging experiments in the water window [Ung89]. (c) First fabricated MZP from 1996 with smallest outer zone width of 40 nm and 80 layers in total for experiments in the hard x-ray energy range 5 keV-10 keV [Kau96]. (d-e) Multilayer zone plate from 2014 and used today, with 784 zones, an outer zone width of 5 nm and an optical depth of 6 µm for experiments in the hard x-ray energy range 8 keV-15 keV [Ebe16]. Scalebars: (a) 4 µm, (b) 400 nm, (c) 662 nm, (d) 4 µm, (e) 20 nm.

Coherent diffractive imaging TXM and STXM are based on the direct measurement of the sample structure. This is different for the methods introduced next: Coherent diffractive imaging and holography. These two methods rely purely on phase retrieval. Both methods enable nanoscale x-ray imaging especially in the hard x-ray energy range where phase contrast is often necessary e.g. for three dimensional imaging

of viruses [Sei+11], dynamic processes [RS19; Vas+21], complex biological samples [Töp+18; Den+18] or integrated circuits [Hol+17]. Different review articles with different perspectives on coherent lensless imaging are found in [Gie+10; TE10; CN10; She+15].

In Fig. 2.2 (c) the basic setup of a CDI experiment is illustrated. A temporally and spatially coherent x-ray beam is confined in its spatial extent. The incident beam is in most CDI experiments parallel or has only a low divergence. The beam is diffracted by the sample. The scattered radiation results in a diffraction pattern in the far-field which is recorded by a pixel detector. The shape of the diffraction pattern is the result of the coherent interference of the diffracted wavefields. In most experiments a beam stop is positioned in front of the detector, since the parallel incident beam illuminates only few center pixels and can result in beam damage of the detector. A diffraction pattern is composed of low spatial frequencies and high spatial frequencies. The low spatial frequencies are diffracted close to the center of the diffraction pattern. These frequencies encode the basic shape of the sample. With increasing distance to the center, and therefore increasing scattering angle, the interference of higher spatial frequencies is recorded. These high spatial frequencies encode the fine features of the sample, such as sub-structures. The highest spatial frequencies that can be recorded directly relate to the best achievable spatial resolution. In case of the depicted diffraction pattern in Fig. 2.2 (c) the high spatial frequencies encode the edge steepness of the sample. The highest scattering angle (θ_{De}) resolved is limited either by the size of the detector or by the signal to noise ratio.

The reconstruction of the sample structure is performed by algorithms which iterative seek a solution that is consistent with the measured diffraction pattern (the amplitude of the wavefield in the detector plane) and prior known information about the sample. This can be done by propagating a wavefield between the sample plane and the detector plane, back and forth, while in each plane the wavefield is updated by the application of a constraint.

The resolution limit of the reconstructed sample can be calculated by using equation (1.1) as a function of the sample detector distance z_{12} and the size of the detector respectively the size to which the diffraction signal can be differentiated from noise L_{px}. We can define the smallest feature d_{min} which can be resolved in a CDI experiment using the small angle approximation as

$$d_{\mathrm{min}} = \frac{\lambda z_{12}}{2L_{\mathrm{px}}} \,.$$

The smallest feature d_{min} depends on the size of the detector L_{px}, but is independent of the detector pixel size Δ_{px}. Nevertheless, detectors with small pixels are needed and/or the detector needs to be positioned at a far distance behind the sample to resolve the low spatial frequencies. The lowest spatial frequency which can be resolved defines the extent D of the largest structure which can be reconstructed in the sample plane. This is valid for the sample and as well for the illumination. D can be calculated as a function of the sample detector distance z_{12} and the detector pixel size Δ_{px} resulting in

$$D = \frac{\lambda z_{12}}{\Delta_{\text{px}}}. \tag{2.2}$$

This is referred to as the sampling constraint, since it sets the lower limit of the sampling interval of the recorded wavefield. In other words, the sampling constraint limits CDI to image only isolated samples (sample needs to be smaller than D) and to image only with an isolated illumination (size of illumination needs to be smaller than D). An alternative expression of the sampling constraint is often given by the oversampling ratio σ_{os}. The oversampling ratio needs to fulfill the expression $\sigma_{os} = \lambda z_{12}/(2D\Delta_{\text{px}}) \geq 2$ [MSC98], which can be derived by using equation (2.2).

The phase retrieval algorithms have their origin in an iterative scheme first proposed by Gerchberg and Saxton in 1972, for image reconstruction in electron microscopy [GS72] and still applied, also in this thesis. The iterative reconstruction algorithm is outlined on the lower right side of Fig. 2.2. Input parameters are: the detector image, an initial guess of the wavefield ψ_0 and some prior knowledge of the sample. The latter is most commonly the physical extent of the sample, known as 'support'. The reconstruction can be separated in five subsequent steps: (I) Propagation of the wavefield ψ_n from the sample plane to the detector plane Ψ_n, (II) updating the wavefield using the recorded amplitude, (III) back-propagation to the sample plane and (IV) enforcing the a priori known information of the sample. (V) Subsequently, the updated wavefield ψ_{n+1} is used as an input for the next iteration ($\psi_n = \psi_{n+1}$). This is repeated until convergence is achieved. The propagation step of (I) is indicated by $\mathcal{D}_{\mathcal{F}}$ and commonly performed in CDI using the Fourier transformation. The Fourier transformation can be used if the wavefield can be assumed to be fully coherent and the detector is positioned at a sufficient distance (far-field). (II) Ψ_n is updated in the detector plane by applying a magnitude constraint indicated by the projector $\mathcal{P}_M$. The magnitude constraint replaces the amplitude of the wavefield Ψ_n by the recorded amplitude but the phase is kept as calculated. (III) The updated wavefield Ψ'_n is back-propagated to the sample

plane using the inverse Fourier transformation indicated here with $\mathcal{D}_{\mathcal{F}}^{-1}$. (IV) The enforcement of the prior knowledge about the sample in the sample plane is indicated by the object plane projector $\mathcal{P}_O$. Besides the most commonly used support constraint $\mathcal{P}_S$, other possible constraints are: The pure phase constraint $\mathcal{P}_P$ which is often applied for optically thin objects and biological samples were the absorption can be neglected. The homogeneous object constraint $\mathcal{P}_h$ which can be applied for samples composed of a single material. Here, the absorbing part β and the decrement δ of the index of refraction are coupled (a more detailed description of update constraints can be found in chapter 5.5.2). (V) The updated wavefield ψ_{n+1} is subsequently used for the next iteration ($\psi_n = \psi_{n+1}$). The number of iterations that must be performed varies from experiment to experiment.

Today, many different algorithms for the update process can be used, such as solvent flipping (SF), hybrid input output (HIO), relaxed averaged alternating reflectors (RAAR), or difference map (DM) to name a few. These are designed for faster convergence and to overcome challenges such as a low signal-to-noise images and missing data due to beam stops or detector gaps. Overviews on reconstruction algorithms are given in [Mar07] and [SEL20].

The origin of CDI can be traced back to crystallography which dates back to 1912 when Laue theoretically described an experiment performed by Friedrich and Knipping in Munich [FKL12]. An x-ray beam generated by an anode illuminated a chalcanthite crystal. A diffraction pattern was recorded on a photographic plate. Laue explained and numerically reconstructed the diffraction patterns by the periodicity of the atoms, which can be seen as a natural three dimensional grating illuminated by an electromagnetic wave. This was the first prove that x-rays can be described as an electromagnetic wave with a wavelength much shorter than optical light. Shortly after the publication of Laue, Bragg reasoned respectively simplified [Bra12] that the peaks could be interpreted by reflection of x-rays by planes of atoms in the crystals, and that their position can be calculated using the today well known Bragg equation. These experiments have been possible with laboratory sources since the spatial coherence length L_C only needed to be greater than a few unit cells of the illuminated crystal. For the case of the chalcanthite crystal used by Friedrich and Knipping a unit cell is about 0.6 nm in size. The detected intensity in crystallography is the incoherent superposition of diffracted wavefields of different regions which are only coherent within themselves. The intensity can be written as $I_{\text{inc}} = \sum_i^N I_i = \sum_i^N |\psi_i|^2$, with N the number of diffracted wavefields ψ. The interest in a crystallography measurement are primarily the discrete Bragg peaks. The information which is not resolved between the Bragg

peaks prohibits the reconstruction of a structure other than a crystal.

In CDI the interest is not to measure the discrete Bragg peaks formed by multiple copies of the same (small) unit cell, but to measure a continuous diffraction pattern of one sample which is at least by a factor of 1000 larger. It was first suggested by Sayre in 1952 [Say52] that if the intensity between the peaks is measured in a diffraction pattern, enough information is acquired to uniquely reconstruct a single isolated object. In 1980 he further specified his approach [Say80]. The intensity of the diffracted coherent wavefield in the detection plane is then given by $I_{\text{coh}} = |\sum_i^N \psi_i|^2$, with N defining the number of coherent scattering sources from which wavefields ψ_i are scattered and coherently interfere in the detection plane. This requires that the spatial coherence length L_C expands the size of the sample. It took 80 years after the first crystallographic diffraction experiment that an image of a non crystalline sample could be reconstructed using a single x-ray diffraction pattern [Mia+99]. The experiment performed by Miao and colleagues was only possible with new synchrotron sources that had improved in their spatial coherence.

Fig. 2.4 (a) shows a diffraction pattern by a crystalline sample (Si-crystal) with dedicated Bragg peaks. (b) Shows diffraction pattern of a coherently illuminated non-crystalline sample which contains two nanowires with a diameter of 200 nm and a length of 3 µm resulting in a continuous diffraction pattern.

As already mentioned, CDI is only applicable if the sample is isolated. If not, the recovery of the sample structure fails. This can be overcome by scanning the sample with an isolated illumination and a sufficient overlap of the illuminated regions of neighbouring scan points. This approach is called ptychography and it reconstructs the phase and amplitude of the sample and the illumination simultaneously. Ptychography is a computational imaging technique. It solves the phase problem by folding (Greek: *ptycho*, or more easily speaking combining) the information from more than one diffraction pattern together [HS19]. The idea dates back to 1970 to Hoppe and Hegerl which first introduced the basic concept (and the Greek name) [HH70]. Ptychography today has only little in common with its first proposal. The first description of ptychography as it is used today was published in 2004 by Rodenburg and Faulkner [FR04; RF04]. It was first realized for hard x-rays in 2007 by Rodenburg and colleagues [Rod+07] and is today implemented by many different groups in coherent x-ray and electron microscopy [HS19]. Already in 1996 a first experiment with soft x-rays using a similar approach was performed by Chapman [Cha96], the large amount of data and the high demand on computational resources inhibited an adaption by other groups

and a further development. An introduction of ptychographic algorithms can be found here [MJL17].

Nowadays, CDI and its scanning counterpart ptychography are widely used for high-resolution imaging in biology and material science with resolutions down to a few nanometers. Since CDI is based on the reconstruction of single shot images it is well suited for in-situ imaging of dynamic processes as was shown by [Lo+18]. In contrast, ptychography allows the investigation of non-isolated objects with a resolution limited by the largest detected scattering angle and is used for experiments such as the imaging of integrated circuits [Hol+17]. Also crystallography is still performed given its ability to analyse crystal parameters at length scales of few Angstroms, especially in the field of structural biology with increasingly larger crystal unit cells [SM12].

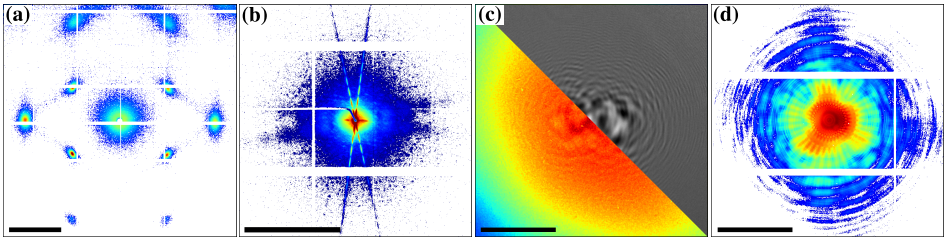

Fig. 2.4: (a) Diffraction pattern of a Si-crystal (photon energy 60 keV). (b) CDI diffraction pattern of two nanowires with a diameter of 200 nm and a length of 3 µm (photon energy 8 keV). (c) In-line hologram. The sample was a world map shaped test pattern. The lower left half shows the detected intensity and is scaled logarithmically. The upper right part shows the empty beam divided image with a linear color scaling. The hologram is especially visible in the upper right part (photon energy 8 keV). (d) Super-resolution in-line holography diffraction pattern of a Siemens star. The center shows the holographic self-interference, in the outer regions the diffraction signal becomes visible (photon energy 8 keV). All four presented images were acquired during the course of this PhD-thesis. The color scaling is logarithmically scaled and encodes in all cases the intensity, the only exception is the empty beam divided image (grayscale) which scales linearly. Scalebars: in pixel (a) 282, (b) 411, (c) 474, (d) 411, corresponding scattering vector q (a) 15 nm^{-1}, (b) 0.25 nm^{-1}, (c) 0.025 nm^{-1}, (d) 0.25 nm^{-1}.

Holography A different method of coherent lensless imaging is in-line-holography also referred to as near-field holography or propagation based phase contrast imaging. In holography the interference of the diffracted wavefield with a reference wavefield is used for phase retrieval. This is different to CDI where the interference of the different diffracted wavefields is used. In in-line holography the reference wavefield is given

by the non-diffracted wavefield. The method was first proposed by Gabor [Gab48] for electron microscopy, who named the interference pattern of reference and diffracted wavefield a hologram.

In Fig. 2.2 (d) the basic setup of in-line holography for nanoscale imaging is depicted. An incoming x-ray beam is coupled into an x-ray waveguide which is used to filter the coherence of the incident beam and generates a small quasi-point source with high divergence at the waveguide output. The divergent beam interacts with the sample which is placed in close distance to the waveguide[7]. The hologram is recorded by a pixel detector. As can be seen in Fig. 2.2 (d) both amplitude and phase shifting impact on the sample result in an interference pattern. With increasing distance between the sample and the detector the interference fringes become larger.

Since in-line holography is based on the interference of the non-diffracted and diffracted wavefields, the resolution is limited by the numerical aperture of the divergent beam as postulated by Abbe (see equation (1.1)). Furthermore, a geometrical magnification of the sample is achieved by using a divergent beam, similar to the *Röntgenstrahlen-Schattenmikroskop* build in 1939 by von Ardenne. The geometric magnification M is given by the ratio of the source-to-detector distance z_{02} and the source-to-sample distance z_{01}, as $M = z_{02}/z_{01}$. In contrast to CDI where the resolution is defined by the scattering extent, is in in-line holography the resolution defined by the detector pixel size and the magnification of the setup within the limits given by the NA of the cone beam illumination. For high magnification a divergent beam can be generated using focusing optics such as Fresnel zone plates, multilayer zone plates or Kirkpatrick and Baez mirror optics. However, the wave-front errors induced by the optics lead to a severe loss of image quality. In contrast waveguide optics filter the spatial coherence of the illuminating wavefield and generate a quasi point source, which significantly reduces wave-front aberrations and increases the spatial coherence. Waveguides used today have channel diameters down to 10 nm (see Fig. 2.5) and an optical depth of about 1 mm, and are used with photon energies between 5 keV to 25 keV, depending on the material.

Already before Gabor, first experiments used near-field diffraction for x-ray imaging. The probably first study using the in-line interference scheme was conducted by Kellström in 1932 [Kel32]. X-ray holography was first performed at a synchrotron by Ato and Kikuta to image red blood cells in 1974 [AK74]. Nevertheless, similar to the case of CDI, the availability of synchrotron x-ray sources with high spatial coherence resulted

[7] In-line holography can also be performed with a parallel beam, but since the resolution is given by the detector pixels ($\approx 1\,\mu$m) in a parallel beam geometry it is not considered in this enumeration.

in a breakthrough of x-ray in-line-holography [FOS06; Bar+15].

As indicated in the Fig. 2.2 (d), the reconstruction of the hologram can be performed by an iterative approach, similar to CDI with the only difference that a near-field propagator is used. Further, Cloetens and colleagues showed the possibility to invert the contrast transfer function in a single step [Clo+99] yielding a fast reconstruction scheme. Since the contrast of the holographic inference fringes can be weak compared to artefacts imposed by the illumination and optical elements, the detector image needs to be corrected for empty beam artefacts. This is especially the case for the reconstruction by single step inversion. The correction is often done by empty beam division, although this approach is strictly speaking mathematically wrong or at best approximate. Nevertheless, today this approach is used in most cases. In Fig. 2.4 (c) the recorded intensity of a holographic imaging experiment is shown, in the lower left half. In the upper right half the same image is shown, but divided by the empty beam. The fringes of the holographic self-inference can more easily be observed and exploited for phase retrieval. Nevertheless, the empty beam division compromises resolution and is one reason why in in-line holography the resolution given by the NA of the divergent beam is not reached [Hom+15; Hag+14].

The constraint of spatial coherence in case of holography yields two restrictions [Vas21]. First, in the sample plane a structure must be illuminated coherently, to enable the interference of the diffracted wavefields in the detector plane. Second, to obtain interference in the detection plane the diffracted wavefield and the non-diffracted reference wavefield need to be coherent as well. In contrast to CDI, holographic imaging is mathematically better posed [Mar15] and a deviation of the coherence does not result in an unsuccessful reconstruction but only in a decreased resolution [HS18]. Nevertheless, for highest resolutions a high spatial coherence is required. An additional difference to CDI is that for highest resolution it is also a requirement that the fringes caused by the interference of the diffracted and the reference beam need to be resolved.

In-line holography has already proven that it is well suited for hard x-ray microscopy of biological specimens, since a non isolated sample can be imaged with a low dose [HS17a] and a large field of view without the necessity of scanning or an isolated illumination. The higher acquisition speed makes in-line holography especially practical for three dimensional tomographic imaging by the simple rotation of the sample [Töp+18] and for imaging of dynamic processes [RS19]. Nevertheless, diffraction signals of high spatial frequencies and with large scattering angles are often beyond the cone beam

illumination and are therefore not exploited. As a result, the resolutions in holographic imaging experiments often do not reach the resolution achieved in CDI experiments. On the other hand CDI experiments are limited in their sampling and therefore by constraints in their field of view.

Super resolution in-line holography In this thesis we present a new full-field imaging scheme, combining the approaches of CDI and in-line holography, or differently speaking, the advantages of recording and resolving low (holography) and high (CDI) spatial frequencies simultaneously. CDI offers high resolution which is defined by the largest detected scattering angle but is limited by constraints to imaging of isolated samples. By directly resolving the low and moderate spatial frequencies, in-line holography is not limited to isolated samples, but is limited in its resolution by the numerical aperture of the cone beam illumination. In Fig. 2.2 (e) the new approach of super-resolution in-line holography is illustrated. Similar to conventional in-line holography, a sample is illuminated by a cone beam e.g. by a waveguide. A large area pixel detector positioned in the far-field records the coherent holographic self-interference and the diffraction pattern beyond the reference beam in a single detector recording. The image information is treated in a common iterative reconstruction scheme, without the usual empty beam correction step of in-line holography. For the reconstruction it is sufficient to use only the constraint of a known probe, which can be retrieved by ptychography or alternatively in single shot approaches. The imaging scheme offers super-resolution with respect to the NA of the cone beam. In fact, the resolution is only limited by the largest scattering angle detected, similar to CDI. However, unlike CDI, non-isolated samples can be imaged. A detailed introduction and description of this new approach can be found in chapter 5.

X-ray optics In the last decades the resolution of hard x-ray imaging has significantly increased, due to improvements of x-ray sources, detectors, advanced image reconstruction algorithms and also strongly due to improvements of x-ray optics. For best imaging results the previously described x-ray microscopes rely on optical elements for point-to-point imaging, probing with a small beam, or on the full-field illumination by a confined or strongly diverging beam. Fig. 2.5 shows the smallest source sizes achieved by different hard x-ray optics during the last two decades. X-ray optics from the 1990s had focus sizes between 1 μm and 100 nm, nowadays focus sizes of down to 5 nm are achieved. The progress was driven by advances in nanofabrication, such as electron beam lithography and thin-film deposition [IBP11]. Six different types of x-ray optics

are listed in Fig. 2.5: compound refractive lenses (CRL), Fresnel zone plates (FZP), multilayer Laue lenses (MLL) and multilayer zone plates (MZP), Kirkpatrick–Baez mirror (KB) and combined optics using KB-mirrors and a waveguide (WG). KB-mirrors could be additionally separated into grazing incidence by a single reflective surface and multilayer mirrors which were developed for very small (sub-10 nm) focus sizes. The various optics use different physical effects. CRLs are based on refraction, FZP, MLL and MZP on diffraction, KB on reflection and WG on mode-filtering by waveguide propagation. The optics have advantages and disadvantages such as high-flux for KB-mirrors, highly-confined beams for CRL-optics, small focus sizes for MLLs and MZPs or a highly coherent point source in case of the WG. Nevertheless the question of the smallest practical limit for x-ray beam sizes is currently unanswered, with only the lower bound given by Abbe (see equation (1.1)). The strongest constraint is given by the perfection of the fabrication. However, smaller and smaller structures also require adapted and new approaches for focusing the wavefield. To reach focus sizes of sub-10 nm hard x-ray optics are based on multiple diffraction, reflection or refraction of an incident x-ray wavefield. This can no longer be described by only analytical solutions, resulting in the need for accurate and high performance wavefield simulations beyond the projection approximation. An example for the necessity of simulations is the development of hard x-ray optics with large NAs such as MZPs and MLLs. By means of simulations it could be shown that proposed limits [BKV03] for focal spot sizes can be overcome [Sch06]. Furthermore, new geometries have been developed that are adapted to multiple scattering within the multilayers [Yan+07], and possible aberrations of future multilayer optics for focal spot sizes of less than 1 nm have already been investigated [CB20].

For a more detailed comparison of different x-ray optics we refer to the following review articles [SA10; IBP11; SEL20].

In the next chapter (3) we present simulations of high NA MZPs and MLLs. We investigate how small focal spot sizes and highest diffraction efficiency can be achieved. Furthermore, we simulate a novel imaging scheme using the MZP similar to an objective lens to study in detail the process of image formation.

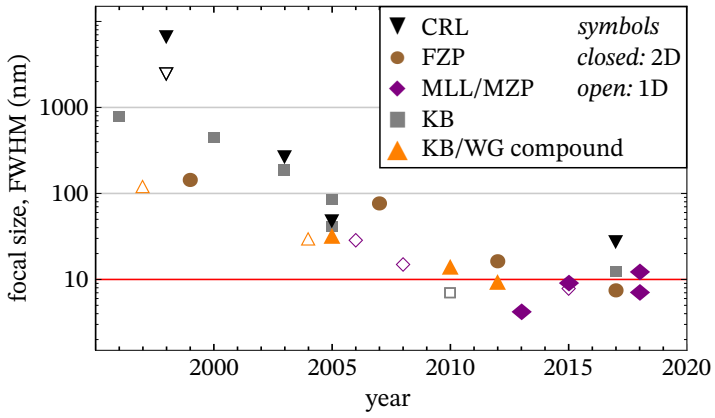

Fig. 2.5: Development of hard x-ray optics for nano-focusing over the last two decades since the advent of 3rd generation synchrotrons. A distinction is made between the different kinds of optics and whether these focus in 1D (empty symbol) or 2D (full symbol). FZP [Che+08; Moh+17; Vil+11; Yun+99], CRL [Len+99; Len+98; Pat+17; Sch+03; Sch+05; Sni+96], KB [EFR95; Hig+03; Hig+05; Ice+00; IH96; Mim+08; Ces+17], MLL/MZP [Dör+13; Baj+18; Kan+06; Kan+08; Mor+15; Ost+15; Yan+18; Sol+21a], and WG [Fuh+04; Jar+05; Krü+10; Krü+12; Lag+97]. Updated version from [SEL20].

Finite-difference propagation for simulation of x-ray multilayer optics

3

JAKOB SOLTAU, LEON LOHSE, MARKUS OSTERHOFF, AND TIM SALDITT

reproduced[1] *from Optics Express 25, 29, 41932-41953 (2021)* [Sol+21c]

Recent progress in nanofabrication, namely of multilayer optics, and the construction of coherent hard x-ray sources has enabled high resolution x-ray microscopy with large numerical aperture optics for small focal spot sizes. Sub-10 nm and even sub-5 nm focal spot sizes have already been achieved using multilayer optics such as multilayer Laue lenses and multilayer zone plates. However these optics can not be described by the kinematic theory given their extreme aspect-ratio between the depth (thickness) and the layer width. Moreover, the numerical simulation of these optics is challenging, and the absence of an accessible numerical framework inhibits further progress in their design and utilization. Here, we simulate the propagation of x-ray wavefields within and behind optical multilayer elements using a finite-difference propagation method. We show that the method offers high accuracy at reasonable computational cost. We investigate how small focal spot sizes and highest diffraction efficiency of multilayer optics can be achieved, considering volume diffraction effects such as waveguiding and Pendellösung. Finally, we show the simulation of a novel imaging scheme, allowing for a detailed study of image formation and the development of customized phase retrieval schemes.

[1] subject to minor corrections

3.1 Introduction

High-resolution hard x-ray imaging relies on optics with depths ranging from several micrometers for diffractive optics up to centimeters for reflective or refractive optics. In all cases, the depths are many orders of magnitude higher than the wavelength λ, resulting from the rather low interaction compared to other spectral ranges, notably visible light. This is the case for compound refractive lenses (CRL), reaching sub-50 nm focal sizes [Sch+05], waveguide (WG) optics, which most recently reached sub-15 nm resolution in holographic full-field imaging (see chapter 5), as well as for multilayer optics, with focus sizes below 10 nm [Dör+13; Baj+18; Sol+21a] and high focusing efficiencies [Mim+10; Ces+17]. The (graded) multilayer architecture can be separated in focusing by diffractive optics such as Fresnel zone plates (FZP), including its two modern sub-types multilayer zone plates (MZP) and multilayer Laue lenses (MLL), as well as in reflective x-ray optics, such as multilayer coated Kirkpatrick–Baez mirrors [Ost+12; Ost+13]. With improved fabrication and experimental capabilities comes the demand for accurate and performant wavefield simulations beyond the projection approximation, where propagation effects and volume diffraction within the optical element are neglected. In particular, the extended design and use of thick x-ray optics can often no longer be described by analytical solutions.

In particular, the simulation of x-ray optics is challenging for two reasons in particular. First, there is a large mismatch between the wavelength, typically around 0.1 nm, and the computational field-of-view, which has to encompass the full numerical aperture (NA) of the optical element in two (2D) or even three dimensions (3D). Second, thick optics are required because the interaction of x-rays with matter is intrinsically weak, resulting in small refraction and diffraction angles. To capture these small angles, a high accuracy in wavefield computation is necessary. Most software packages for numerical calculations of wavefields are designed for optical wavelengths and are therefore not applied for x-ray optics.

Several approaches have been developed to numerically calculate the propagation of hard x-ray wavefields interacting with x-ray optics. Examples are modified multi-slice (MS) propagation [LWJ17], methods of solving the parabolic wave equation eigenfunctions [Sch06; Pfe+06], the description by the coupled wave theory [MS92; Reh+15], an approach based on the Takagi-Taupin equations [Yan+07], and ray-tracing methods [CB20]. Although all these methods are used for the simulation of x-ray optics, the algorithms differ depending on the specific questions addressed. For example MS was used to simulate classical FZPs with zone widths down to 20 nm [LWJ17].

The Takagi-Taupin equations, the approach of parabolic wave eigenfunction, and the coupled wave theory were all used for MLLs, albeit only in 2D simulations [MS92; Sch06; Pfe+06; Yan+07; Reh+15]. Furthermore, ray-tracing was used to study focus shape and lens aberrations of MLLs [CB20]. Finally, finite element method were used to simulate dynamical diffraction problems in crystal and reflective optics [RFM97; Hon+18; Wan+20]. Beyond these selected examples, many more applications of x-ray wavefield simulations can be found in the literature in the context of imaging. The reason is that the wavefield simulation is a prerequisite for many imaging schemes, including in particular iterative phase retrieval algorithms [Fie78; Mia+99], which have revolutionized x-ray imaging since the invention of coherent diffractive imaging (CDI) and ptychography over twenty years ago [FR04; RF04; Thi+08].

In this work, we use finite-difference propagation (FD) to simulate optical elements based on multilayers. FD is well-established for the simulation of optical waveguides (see [Oka06] and the references therein) but has to date been used only for a few x-ray optical studies [SO91; KP02; FS05; FS06a]. We show that FD offers high accuracy at reasonable numerical complexity. We then investigate the volume diffraction inside (graded) multilayer structures in detail, as well as the focusing capabilities of different types of multilayer optics with large NA in 2D and 3D. Finally, we also show that FD can be combined with steps of free-space (FS) propagation in order to compute a complete imaging scheme.

The simulations of a complete imaging scheme demonstrates that the approach is not limited to single optical components but also well-suited for relevant imaging setups. We demonstrate this by simulating an experimental setup based on an MZP used as an objective lens and placed in the near-field of the sample. The experimental setup, at first sight, seems to be very similar to the classic transmission x-ray microscope (TXM) constructed by pioneers of x-ray microscopy over forty years ago in Göttingen [NRS76]. However, diffractive optical elements (FZP, MZP, MLL), have never been exploited as an objective lens in an iterative phase retrieval approach, despite the potential to improve the resolution and contrast sensitivity. Importantly, the ability to simulate the setup promises to emancipate imaging from lens aberrations, as the real lens can be incorporated in the algorithmic processing, rather than an idealized assumption of a lens.

This manuscript is structured as follows. After this introduction, in section 3.2 the basic theory of diffractive focusing multilayer optics is outlined. In section 3.3 the numerical approach is presented. In the subsequent section 3.4 the convergence of the

FD method for different sampling properties is studied, followed by the investigation of the diffraction inside representative multilayer structures and the impact of possible real structure effects in section 3.5. Section 3.6 presents a study of different multilayer focusing optics with an emphasis on the focus shape, intensity and efficiency. Finally in section 3.7 we introduce a new imaging approach based on off-axis MZP objective lenses. The manuscript closes with section 3.8, jointly presenting discussion, summary, and an outlook.

3.2 Diffractive focusing multilayer optics

We briefly introduce multilayer optics as a special case of FZPs. In fact, diffractive multilayer optics, such as MZPs or MLLs, are entire or partial FZPs that are thicker than classical FZPs along the optical axis. Further, the fabrication is based on thin film deposition [Ebe+14; Cha+21], and subsequent dicing, rather than the lithographic fabrication scheme of FZPs [Moh+15]. A multilayer optical element is hence based on the same optical principle as a classical FZP: An incoming x-ray beam is diffracted by a zone, or in our case a layer structure, where the radial distance r_m of the m^{th} layer is defined by:

$$r_m = \sqrt{m \cdot \lambda f + \left(\frac{m \cdot \lambda}{2}\right)^2}.$$

The diffracted wavefield constructively interferes behind the optical element at a distance f, the focal length. λ denotes the wavelength of the radiation. The layer width is defined as $\Delta_m = r_m - r_{m-1}$, with the cases of the innermost layer (largest width) defined as $\max(\Delta_m)$ and the outermost layer (smallest width) as $\min(\Delta_m)$. The NA of the optical element and thus the size of the focus is a function of the outermost layer width $\min(\Delta_m)$, respectively for off-axis optics defined by the focal length divided by the size of the illuminated area. A planar structure of layers can be used to focus to a 1D line focus, for a 2D point focus the diffractive element needs to have a radial symmetry around the optical axis. Alternatively a point focus can be generated by a pair of two planar structures arranged in a crossed geometry. For the case of multilayer optics, planar structures are referred to as MLLs and radial symmetric structures as MZPs. Given the low absorption of hard x-rays, the depth of the multilayer structure is used to modulate the wavefield (e.g shifting the phase between neighbouring layers by π), rather than creating a binary structure of opaque and transparent layers as is the case with FZPs.

The description of multilayer optics by the kinematic diffraction theory is insufficient when the layer width is reduced to few nanometers and the depth is increased to several micrometers [Mas+04; Kan+05]. For clarity, we use the term width for the transverse extent of the simulated and discussed layers and the term depth for their extent along the optical axis. In multilayer optics with higher diffraction efficiencies and smaller focus sizes than achievable with classical FZPs [Sch06] one commonly encounters volume effects due to multiple scattering, such as waveguiding or the formation of standing waves resulting in the *Pendellösung* period [Aut06].

For higher focusing efficiency, the layers can be tilted into the direction of the focus. One has to differentiate between the tilted geometry, where all layers have the same tilt angle, and the wedged geometry, where all layers are tilted differently based on the Bragg angle $\theta_{\text{Bragg}} = \lambda/4\Delta_{\text{m}}$ [Yan+07]. The latter is more challenging in fabrication but results in higher diffraction efficiencies. For many experiments, a central beam stop in front of the MZP together with an order sorting aperture behind the MZP is required to block the 0^{th} order beam. Alternatively, with an off-axis illumination the focus generated by the $+1^{\text{st}}$ diffraction order can be separated from other diffraction orders. This is the case for most MLLs, with layers only on one side of the optical axis. For MZPs, off-axis illumination can be realized by illuminating only one side of the MZP [Sol+21a]. This configuration results in a point focus without the necessity of a pair of crossed MLLs, as later shown in Fig. 3.5 (II).

The simulations presented in this manuscript are based on parameters of existing multilayer optics. As a representative example, we use the material combination and geometry corresponding to recent MZPs fabricated by pulsed laser deposition [Ebe+14], with following parameters: The MZP has an outermost layer width $\min(\Delta_m)$ of 5 nm, a total number of layers M_{layer} of 784 layers, and a depth depending on the experimental setup between 2 µm for a photon energy of 8 keV and up to 30 µm for photon energies of 100 keV [Dör+13; Ost+17b]. For a photon energy of 13.8 keV, the focal length f is about 1 mm. The material combination of the layers is ZrO_2 and Ta_2O_3. This combination of materials has shown advantageous growth properties in the manufacturing process (in particular concerning surface roughness), and a sufficiently large difference of the refractive indizes. As an example for a crossed pair of MLLs we take the values of [Cha+21], with an outer most layer width of $\min(\Delta_m) = 4.31$ nm, $M_{\text{layers}} = 2759$ layers and a focal length of 2.13 mm for a photon energy of 17.4 keV. It should be noted, that with pairs of one-dimensional multilayer optics wavefront aberration cannot be completely avoided [CB20]. This becomes of importance for focus sizes below 1 nm.

3.3 Simulation framework

In this section, we briefly recapitulate the fundamentals of the different simulation approaches. The methods under discussion are all scalar and frequency-domain approaches, so that the simulated quantity is one spectral component of the time-independent wavefield $\psi(x, y, z)$. In the following, z denotes the optical axis and x, y correspondingly span the transverse (lateral) plane. The simulation approaches solve the following *propagation problem*. Given some initial wavefield $\psi(x, y, z_0)$ and some distribution of the complex refractive index $n_\lambda(x, y, z)$, find the wavefield $\psi(x, y, z_1)$ for $z_1 > z_0$ or, more generally, for all $z \in [z_0, z_1]$. All simulation approaches discussed in this section are implemented and made available under an open license at `https://gitlab.gwdg.de/irp/fresnel`. Other numerical approaches of interest are referenced in section 3.1.

The starting point is the Helmholtz equation (or stationary wave equation) [Pag06]

$$\left[\nabla^2 + k^2 n^2\,(x, y, z)\right] \psi\,(x, y, z) = 0\,, \tag{3.1}$$

where ∇^2 denotes the Laplace operator, and $k = 2\pi/\lambda$ is the wavenumber in free-space for wavelength λ. The refractive index $n = 1 - \delta + i\beta$ includes the terms accounting for phase shifts δ and an absorption β. Given a well-defined optical axis, the Helmholtz equation is commonly solved by applying a separation ansatz $\psi(x, y, z) = \tilde{\psi}(x, y, z)\,\exp(ikz)$, splitting the envelope $\tilde{\psi}(x, y, z)$ from the plane-wave carrier $\exp(ikz)$.

3.3.1 Free-space propagation

In free-space, or more generally in regions with constant refractive index, the solution $\psi_\lambda(x, y, z_1)$ can be calculated in a single step for any z_1. A plethora of methods exist that implement some discretized version of the Rayleigh-Sommerfeld or the Fresnel diffraction integrals, either as real-space convolutions or in Fourier space [Goo17; Zha+20]. Different approaches can be chosen, depending on the propagation distance $z_1 - z_0$, the sampling, and the lateral size of the simulation domain. For a detailed review, we refer to [VR09; Zha+20]. In this work, we use the Fresnel transfer-function (Fresnel-TF) and the Fresnel impulse-response (Fresnel-IR) approaches for shorter and longer propagation distances, respectively.

For very large propagation distances, the Rayleigh-Sommerfeld integral simplifies

to the Fraunhofer integral and can be computed by a single Fourier transform. The far-field detector images in the following applications are therefore calculated by a single fast fourier transform (FFT).

If both the initial field $\psi_\lambda(x, y, z_0)$ and the refractive-index distribution $n(x, y, z)$ are circularly symmetric with respect to the optical axis, then the propagated field will also have circular symmetry (CS). Since the diffraction integral can be conveniently expressed in cylindrical coordinates, we can omit the angular component in this case so that the 3-dimensional problem is reduced to a 2-dimensional one. For circular-symmetric optics, we use a CS Fresnel propagator, which is based on the discrete Hankel transform [GG04; LJ15]. Note that this method can simulate normal illumination only, because otherwise the initial field would not be of circular symmetry.

3.3.2 Multi-slice propagation

The multi-slice (MS) method was originally developed for electron diffraction (see [Cow95] and the references therein) but is well-established in x-ray optics nowadays [Pag06]. To account for multiple diffraction, the propagation through an extended object is partitioned into small steps. Each step consists of (i) multiplication of the transmission function of the respective slice to account for its refractive index using the projection approximation and (ii) free-space propagation.

For (ii), the angular spectrum method (see [Zha+20] for a recent review; also known as exact transfer function approach [Goo17]) is commonly used [Pag06; LWJ17]. As a consequence, the MS method inherits some features of the angular spectrum method. First, the FFT-based diffraction implicitly imposes periodic boundary conditions. Second, it is very sensitive to the sampling intervals for both the longitudinal coordinate z and lateral coordinates x, y, as well as the lateral extent of the computational domain as outlined in [Zha+20]. Finally, sub-step (ii) requires 2 FFTs per step, so that the computational complexity of a single step scales with $\mathcal{O}(N_{\text{px}} \cdot \log N_{\text{px}})$, with N_{px} being the total number of samples in each plane. The computational complexity of sub-step (i), on the other hand, scales with $\mathcal{O}(N_{\text{px}})$ and is hence irrelevant.

3.3.3 Finite-difference propagation

Finite-difference propagation (FD) methods, an entirely different approach, solve the paraxial Helmholtz equation in real space by discretizing the differential operators and solving a sparse linear system of equations. These methods have been well-established

for the simulation of optical waveguides for decades (see for example [Oka06] and the references therein) and have proven reliable for x-ray optics [FS05; FS06a; HS16; MS17].

In contrast to MS methods, FD methods work entirely in real space and, as such, do not inherit any boundary conditions. Instead, one has to impose explicit boundary conditions to obtain a unique solution. In fact, the solutions obtained by FD methods depend sensitively on the choice of boundary conditions. In the visible regime, often so-called transparent boundary conditions or absorbing boundary conditions in the form of perfectly matched layers are introduced, which minimize reflections at the boundaries of the computational domain. For hard x-rays, on the other hand, it usually suffices to specify approximate boundary values (Dirichlet boundary conditions) and extend the computational field beyond the region-of-interest, so that waves that are reflected at the boundaries are quickly dissipated due to the significantly higher absorption losses.

Here, we essentially follow earlier work [FS05; FS06a] but use a modern implementation in C++ and Python. We have implemented FD propagators for 2D, 3D, and CS geometries. The latter is based on earlier work by Melchior [MS17] but with improved treatment of the inner boundary. In each step, a system of linear equations (compare appendix 3.10) is solved. Finding the solution requires only a small fixed number of passes, so that the computational complexity scales with $\mathcal{O}(N_{\mathrm{px}})$. The 3D geometry uses dimensional splitting to uncouple the two transversal derivatives, so that the computational complexity is only doubled.

To summarize, in comparison to MS, FD propagation does not require special sampling conditions, does not impose periodic boundary conditions, and is considerably less computationally complex.

3.3.4 Combined approaches

As illustrated in Fig. 3.1, many imaging setups consist of multiple elements (e.g. optics, samples, detectors) separated by free-space. To cope with these different geometries with different sampling constraints, the presented methods can be combined. This is especially relevant for the simulation of wavefields propagating through an optical element and subsequent in free-space to a distant focal spot or sample, as discussed in section 3.6 for the focus characterization of MZPs and MLLs, and in section 3.7 for the simulation of an entire imaging scheme.

In this work we use FD to simulate the propagation through the optical elements.

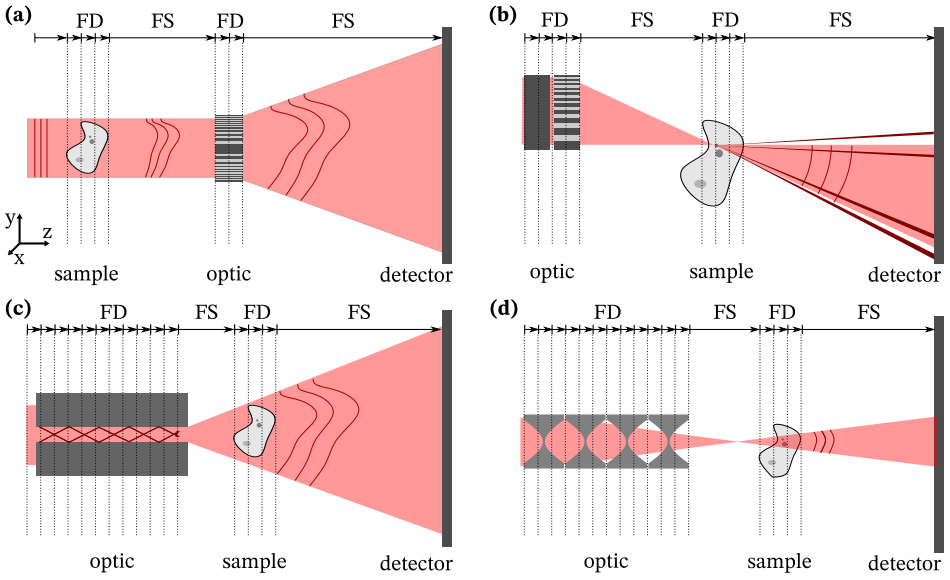

Fig. 3.1: Experimental geometries and simulation schemes. (a) Objective x-ray microscope. A sample is illuminated by a parallel beam. The modulated wavefield is magnified by an MZP and propagates in free-space to the detector. (b) A pair of crossed MLLs focus an incoming beam onto a sample, the wavefield gets diffracted by the sample and propagates to the detector. (c) A WG generates a strongly divergent cone beam illumination. The sample is positioned close to the WG-exit in the divergent beam. The beam is modulated by the sample and propagates in free-space to the detector. (d) A stack of compound refractive lenses (CRL) focus an incoming beam. A sample is positioned in the vicinity of the focus, modulates the wavefield and subsequently propagates to the detector. In all cases the interaction of matter with the x-ray wavefield can be simulated using the FD method. For the free-space propagation (FS) the Fresnel-TF or the Fresnel-IR approach is used respectively. Furthermore, the propagation to the far-field, in the cases here the propagation to the detector, is computed using the FFT. As illustrated the FD propagations are performed in small sub-steps to cover multi-scattering. The FS propagations are performed in a single step.

For propagation through free-space (FS), we use the strategy described in section 3.3.1, namely Fresnel-TF and Fresnel-IR for shorter and longer propagation distances, respectively. The far-field intensity distribution, where needed, is computed using FFT [Goo17].

3.3.5 Computational consumption

The simulations were computed on a dual-CPU server with two Intel Xeon E5-2650v3 (Haswell microarchitecture from 2014, 10 cores each). We note that only FFT, FS, and 3D-propagation are parallelized, whereas the CS and 2D propagation were run on a single core. Memory consumption was insignificant, since only a few slices need to be kept in main memory. Propagating a wave-field in 2D was executed within minutes, and in 3D within hours.

3.4 Convergence properties

Before we simulate 'real' optical elements, we study the convergence properties of the FD propagation as a function of spatial sampling by simulating a thick multilayer structure under plane-wave illumination at the Bragg angle of the structure. The material composition of the structure is similar to recent experiments using MZP optics [Ebe+14]. The multilayer structure is shown in Fig. 3.2 (a) together with the intensity distribution of the propagating wavefield. The simulated multilayer structure approximates an infinite number of bilayers. The bilayers are composed of alternating high density Ta_2O_3 and low density ZrO_2 layers of equal depth and a layer width of $\min(\Delta_m) = 4.5\,\text{nm}$. The depth in z is $\Lambda = 15.1\,\mu\text{m}$. It is illuminated by a plane wave under an angle of $\theta_m = 5.0\,\text{mrad}$ relative to the layer orientation, corresponding to the Bragg angle (θ_{Bragg}) of the multilayer at a photon energy is 13.8 keV.

The simulation is set up in 2D as follows. The coordinate system is defined by the optical axis z, which is parallel to the layers, and the transverse axis x, which is normal to the layers. The incoming plane wave is described at $z = 0$ with a unit amplitude and a linearly varying phase. The computational field-of-view is 8 µm. The boundaries are padded with 2 µm of Pb. Furthermore the Dirichlet boundary is set to a zero amplitude. To mitigate the influence of the boundaries, only a central region-of-interest with an extent of 409.6 nm (or 2^{10} grid points with a 0.4 nm distance) is used for further analysis. We have simulated the system for different pixel sizes in longitudinal (Δ_z)

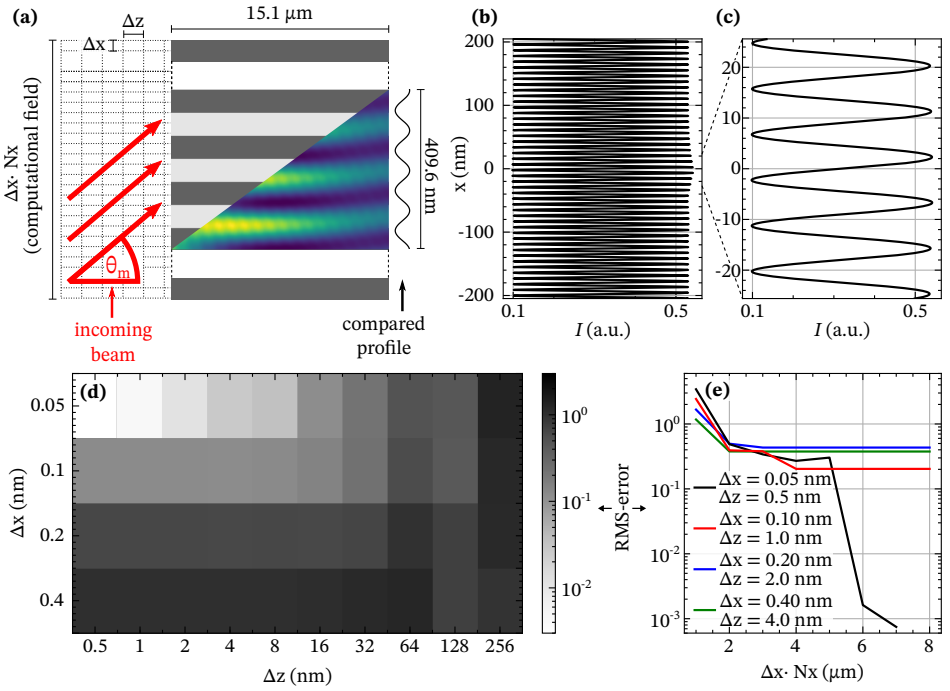

Fig. 3.2: Convergence of the FD as a function of the simulation parameters. (a) The setup of the simulation shows a multilayer structure with a layer width $\min(\Delta_m) = 4.5\,\text{nm}$, illuminated under an angle of $\theta_m = 5\,\text{mrad}$ and a depth of 15.1 μm. The material density and the wavefield intensity modulation inside the structure is indicated. The varied parameters are depicted: the propagation step size Δ_z, the lateral grid size Δ_x, the size of the computational field $N_x \cdot \Delta_x$. (b) Simulation results of the multilayer exit intensity profile of the region-of-interest with a width of 409.6 nm used for the further analysis. The simulation parameters are: $\Delta_z = 0.5\,\text{nm}$ and $\Delta_x = 0.05\,\text{nm}$. (c) Center region of the multilayer exit intensity profile shown in (b). (d) RMS-error as a function of the propagation step size Δ_z and the lateral grid size Δ_x. (e) RMS-error as a function of the computational field $\Delta_x \cdot N_x$.

Table 3.1: Parameters of the presented simulations depending on the dimension (D).

D	Δ_x, Δ_y	Δ_z
2D	0.1 nm	1 nm
3D	0.35 nm	50 nm
CS	0.1 nm	1 nm

and transverse (Δ_x) direction and simulated it for different computational field of views ($\Delta_x \cdot N_x$).

Figure 3.2(b-e) shows the wavefield simulations. In (b) the region-of-interest of the compared intensity profile is shown and in (c) a magnified section of the profile. The simulation grid was sampled with a propagation step size of $\Delta_z = 0.5\,\text{nm}$ and a lateral grid spacing of $\Delta_x = 0.05\,\text{nm}$, corresponding to the finest sampling interval in the comparison shown below in (d,e).

Next, we investigate how the resulting intensity profiles depend on the pixel size and how the accuracy of the FD converges. To this end, we take the highest sampled simulations as reference and plot the RMS-error of the residual as a function of Δ_z and Δ_x (d). The residual is evaluated only in the central part of the computational field-of-view, in a region-of-interest of 409.6 nm, to avoid boundary effects. The effect of the computational field is evaluated in (e), by plotting the RMS-error as a function of the lateral computational field-of-view. Four different parameter sets were simulated from $\Delta_z = 0.5\,\text{nm}$, $\Delta_x = 0.05\,\text{nm}$ to $\Delta_z = 4.0\,\text{nm}$, $\Delta_x = 0.4\,\text{nm}$. The lead Pb padding was set to 25 % of the computational field-of-view on each side.

In view of the results of the FD simulation accuracy, we adopted the following simulation strategy for the work presented below: For simulations in 2D, the grid spacings are kept constant, namely $\Delta_x^{\text{2D}} = 0.1\,\text{nm}$ in the lateral direction, and $\Delta_z^{\text{2D}} = 1\,\text{nm}$ along the propagation axis. Due to the larger computational effort in 3D, the lateral grid spacing will be increased to $\Delta_x^{\text{3D}} = 0.35\,\text{nm}$ and the propagation step size to $\Delta_z^{\text{3D}} = 50\,\text{nm}$. The parameters are summarized in Tab. 3.1.

3.5 Propagation through regular multilayers

3.5.1 Volume and dynamical diffraction effects

In this section, we present simulations of wave propagation in regular multilayers with plane waves coupling through the front. We compare a system with large periodicity ($\Delta_m = 25$ nm) with a system with small periodicity ($\Delta_m = 3$ nm). The latter corresponds approximately to the smallest layer widths currently fabricated for multilayer optics. The two periodicities demonstrate the transition from a regime that can be described by guiding modes to one that can be described by dynamical diffraction theory. The numerical calculations were performed in 2D with the simulation parameters shown in Tab. 3.1 and the parameters of the structure shown in Tab. 3.2.

Figure 3.3 shows wavefields propagating through multilayer structures illuminated by plane waves, comparing (a,b) normal-incidence illumination ($\theta_m = 0$), and (c,d) illumination under the Bragg angle ($\theta_m = \theta_{\text{Bragg}}$), both for (a,c) large periodicity and (b,d) small periodicity, respectively. The multilayer is in all cases 45.3 μm thick. The simulation includes 10 μm vacuum in front and behind the structure. The structure begins at the position $z = 0$. The photon energy and material combination is the same as above in the section 3.4. The different rows show (I) intensity, (II) phase, (III) the angular spectrum, and (IV) the zero and first order diffraction intensity, as a function of the propagation distance z. The angular spectrum in (III) is calculated by performing a Fourier transformation for each wavefield with respect to the x coordinate. This is equivalent to a far-field pattern of the multilayer exit wavefield, if it were cut at position z.

We first discuss the results for (a) $\Delta_m = 25$ nm and $\theta_m = 0$. The wavefield intensity, shown in (a,I), is attenuated in the layers of higher electron density (Ta_2O_3) and intensity maxima (guiding modes) form in the layers of lower electron density (ZrO_2). The formation of guiding modes in the material of lower electron density is well known from x-ray waveguides. The number of modes N_{modes} can be calculated by $N_{\text{modes}} = \lceil \sqrt{2\delta_2 - 2\delta_1} k \Delta_m / \pi \rceil$, where $\lceil \cdot \rceil$ denotes rounding up to the next integer. For normal-incidence illumination, only symmetric modes (even order) are populated. For the parameters of (a), this results in only the 0^{th} mode to be populated, in line with the simulation result. The phase modulation of the wavefield is shown in (a,II). The phase of the propagating wavefield is shifted differently in adjacent layers, due to the difference in the real part of the index of refraction δ. The angular spectrum, plotted in (a,III), shows multiple diffraction peaks of even and odd diffraction orders. While

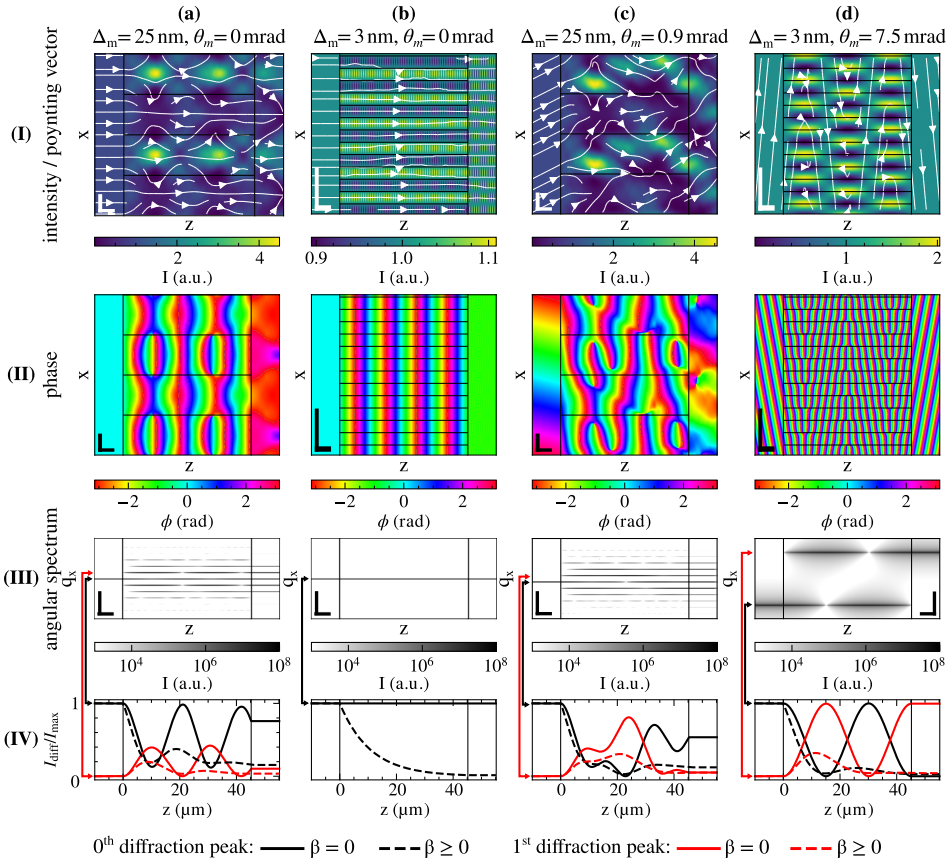

Fig. 3.3: Volume and dynamical diffraction effects of different multilayer structures and different illumination direction. The multilayer structures have layer widths of (a,c) $\Delta_m = 25\,\text{nm}$ and (b,d) $\Delta_m = 3\,\text{nm}$ and are illuminated by a plane under normal incidence (a,b) and under the corresponding Bragg angle (c,d). (I) Intensity modulation of the propagated wavefield, with the corresponding Poynting vectors (white). The layer edges are indicated by black lines. (II) Phase of the propagated wavefield. (III) Angular spectrum or far-field diffraction pattern as a function of the depth of the multilayer structure. (IV) Intensity modulation of the 0^{th} and 1^{st} diffraction peak as a function of the depth. The corresponding diffraction peak in (III) is indicated by arrows. In general the structure consists of a material combination of ZrO_2 and Ta_2O_3, and has a total depth of 45 μm padded by 10 μm vacuum before and after the structure. In (I)-(III) the material was considered as non absorbing ($\beta = 0$). In (IV) $\beta = 0$ and $\beta \geq 0$ is shown. The simulations were performed in 2D using FD. In case of (d) the half Pendellösung period is $\Lambda_{\text{Pendel}/2} = 15.1\,\mu\text{m}$. The simulation parameters are shown in Tab. 3.2. Scalebars vertical: (I,II) 10 nm, (III) scattering vector $q = 0.25\,\text{nm}^{-1}$, horizontal: 5 μm.

the odd orders are formed at the beginning of the multilayer structure, the even orders build up after a propagation distance of $z > 250\,\text{nm}$. This is in contrast to the analytical solution of an infinitesimally thin structure (projection approximation) [Pag06], where only odd-order diffraction peaks are described. Even diffraction orders occur due to volume diffraction effects. This has been observed also experimentally for multilayer systems [Mas+04]. A first maximum of the first order diffraction peak is formed at $z = 10.1\,\mu\text{m}$, which is only slightly larger than an odd multiple of a π phase shift between two adjacent layers with $9.6\,\mu\text{m}$. For no absorption ($\beta = 0$), the diffraction efficiency of the first maximum of the first order diffraction is 39.6 %, which is in line with the analytical solution of a multilayer system of 41.5 % [Pag06]. Including the absorption of ZrO_2 and Ta_2O_3 ($\beta \geq 0$), the efficiency is reduced to 19.9 %.

Next, we discuss the results for (b) $\Delta_m = 3\,\text{nm}$ and $\theta_m = 0$. The intensity modulation is much smaller (b,I), and a phase modulation is not noticeable (b,II). The angular spectrum, shown in (b,III,IV), shows only the 0^{th} diffraction order. If absorption is taken into account ($\beta > 0$), the intensity decays approximately with the mean absorption coefficients of ZrO_2 and Ta_2O_3. In contrast to the regime characterized by the formation of well-separated modes, as in (a), here in (b) the guided modes from adjacent 'guiding layers' have significant overlap and the approximation of separate waveguides is no longer valid. As a result, multilayer structures of such small layer widths can not be used as focusing optics since no phase modulation occurs.

We now turn to oblique incidence under the Bragg angle, shown in (c) for $\Delta_m = 25\,\text{nm}$ and $\theta_m = 0.9\,\text{mrad}$. In (c,I) the formation of two modes can be observed in the intensity field. This is different from the parallel illumination case and results from the non-symmetric overlap integral in coupling the incident beam to the modal profiles [FS06b]. This less symmetric pattern is also observed in the phase modulation (c,II) and the angular spectrum (c,III). In (c,IV) the formation of a strong maximum of the $+1^{\text{st}}$ order diffraction peak can be seen. However, the propagation distance after which this peak forms sensitively depends on the 'zone width' Δ_m, which makes it impractical to design focusing multilayer optics based on this reflection peak, since this would require different depth for each layer.

Finally, (d) shows a multilayer structure with $\Delta_m = 3\,\text{nm}$ under Bragg incidence $\theta_m = 7.4\,\text{mrad}$ (θ_{Bragg}). Panel (d,I) exhibits the formation of intensity maxima that can be described by standing waves, similar to the guiding modes shown at (a,I). The anti-nodes of the standing waves are positioned at the material boundaries and, in contrast to guiding modes, not in the center of a layer. This formation is well known from

dynamical diffraction theory and is denoted as *Pendellösung* [Aut06] for thick crystals illuminated in Laue geometry. The Pendellösung describes the oscillation of a wavefield by multiple diffraction inside a crystal. It has also been observed experimentally in a system similar to the simulated one [Kan+05]. Here, it can be most clearly observed by following the Poynting vectors in (d,I) and by the phase modulation inside the multilayer in (d,II). In the angular spectrum, this phase modulation results in the formation of two diffraction peaks oscillating exactly out of phase (d,III,IV). The Pendellösung period depends on the interfacial reflectivity, but not on the layer depth (for the layers of $\Delta_m = 25\,\text{nm}$ the Pendellösung effect is not prominent enough to be observed). The exit wavefront after half a Pendellösung period ($\Lambda_{\text{Pendel}/2}$) is opposite to the angle of incidence. For multilayers, one finds $\Lambda_{\text{Pendel}/2} = \pi\lambda/2\,|\delta_2 - \delta_1|$ [Kan+05]. Which is $\Lambda_{\text{Pendel}/2} = 15.1\,\mu\text{m}$, for the given parameters and is in perfect agreement with the simulations. The independence of $\Lambda_{\text{Pendel}/2}$ on the layer width Δ_m and the high diffraction efficiency of nearly up to 100 % (here: 99.6 % in the absence of absorption) makes it the optimal depth for multilayer focusing optics. When absorption is taken into account (d,IV), the maximum diffraction efficiency of the Bragg peak decreases, for the material combination here down to 32.1 % (see dashed line). Unlike for the guiding modes of $\Delta_m = 25\,\text{nm}$, the effective absorption is for the Pendellösung with $\Delta_m = 3\,\text{nm}$ no longer dominated by the layers with low electron density, but by a weighted mean of both layers resulting in an higher absorption.

In conclusion, we have shown that multilayer structures with large periodicity (here $\Delta_m = 25\,\text{nm}$) could be used for focusing of incident wavefields (shown in (a)). The diffraction efficiency can be further increased when the multilayer structure is illuminated under the corresponding Bragg angle (shown in (c)). Contrarily, multilayer structures with small periodicity (here $\Delta_m = 3\,\text{nm}$) illuminated in normal-incidence ($\theta_m = 0$) can not be used as focusing multilayer optics, since the phase modulation of the wavefield in the multilayer structure is negligible (shown in (b)). But, if the multilayer structure is illuminated under the corresponding Bragg angle the formation of standing waves can be observed, this effect is known as *Pendellösung*. When this effect is exploited, diffraction efficiencies of (nearly) up to 100 % are achievable (shown in (d)).

3.5.2 Real-structure effects

In this section, we consider the sensitivity to imperfections of multilayers with small periodicity, so called *real-structure effects*. Figure 3.4 illustrates the effect of different

Table 3.2: Parameters of the simulated multilayer structures in Fig. 3.3 and 3.4. The simulations were performed in 2D with a FOV of 8 µm and $80 \cdot 10^3$ lateral grid points. In all cases the photon energy is $E = 13.8$ keV and the layer materials are ZrO_2 and Ta_2O_3. Δ_m defines the layer width, θ_m the illumination incidence angle and Λ_t the depth of the structure.

Fig.	Δ_m	θ_m	Λ_t
3.3 (a)	25 nm	0.0 mrad	45.3 µm
3.3 (b)	3 nm	0.0 mrad	45.3 µm
3.3 (c)	25 nm	0.9 mrad	45.3 µm
3.3 (d)	3 nm	7.4 mrad	45.3 µm
3.4(a-d)	3 nm	7.4 mrad	45.3 µm

non-idealities that occur in non-perfect multilayer structures. We have simulated the following imperfections: in (a) the perfect binary material is replaced by a sinusoidal density profile; in (b) the interface between the low and high density layer has a small inter-layer (constant gradient) representing for example inter-diffusion or a smooth transition regime in the growth process; in (c) a layer sequence with random and uncorrelated width errors of 0.4 nm standard deviation has been simulated, and in (d) randomized surface height fluctuations representing interfacial roughness, here with RMS-roughness of $\sigma = 0.45$ nm. Row (I) shows a zoom into the different multilayer structures where the gray value encodes the decrement of the local refractive index δ. For all cases, the periodicity is $\Delta_m = 3$ nm and the illumination angle is $\theta_m = 7.4$ mrad (θ_{Bragg}). All other simulation parameters are identical to Fig. 3.3. A list of the basic simulation parameters can be found in Tab. 3.2.

Strictly speaking, the sinusoidal material profile shown in (a) is not an unwanted real-structure effect, as a perfect sinusoidal profile would offer optimum focusing properties without higher orders and focus side-maxima [Pag06]. The resulting far-field diffraction pattern (a,II,III) is similar to the perfect binary structure shown in Fig. 3.3 (d), with the difference that $\Lambda_{\text{Pendel}/2}$ is increased by 4.1 µm. The presence of absorption ($\beta \geq 0$) reduces the maximum diffraction efficiency to 24.1 % compared to 32.1 % for the perfect binary structure. The same applies for the inter-layer with linear profile (b). Such interfacial gradients can occur in deposition processes and result in lower effective reflectivities, increasing $\Lambda_{\text{Pendel}/2}$ by 1.6 µm and reducing the diffraction efficiency to 28.6 %.

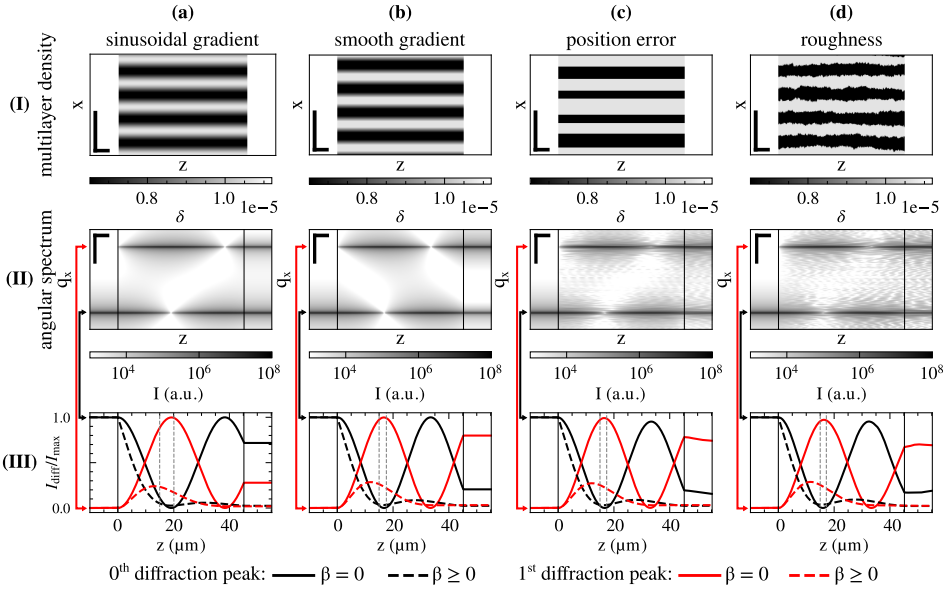

Fig. 3.4: Real structure effects. Multilayer structures with different layer transitions with a layer width of $\Delta_m = 3\,\text{nm}$ and an illumination under the Bragg angle ($\theta_m = 7.4\,\text{mrad}$). (a) Layer transition with a sinusoidal profile, (b) a linear gradient layer transition over a length of 1.5 nm, (c) a multilayer with a mean error of 0.35 nm in the width of the layers and (d) a multilayer with a surface roughness RMS = 0.45 nm [DeG+97]. (I) Zoom in of the decrement of the multilayer structure. Color scaling indicates the phase shifting part δ of the refractive index. (II) The angular spectrum as a function of the depth of the multilayer structure. (III) The intensity modulation of the 0^{th} and 1^{st} diffraction peak as a function of the depth. The corresponding diffraction peak in (II) is indicated by arrows. The half Penedellösung period is for (a) 19.2 µm, (b) 16.7 µm, (c) 16.5 µm and (d) 16.3 µm which was 15.1 µm for the perfect multilayer structure in Fig. 3.3 (d) 15.1 µm. The difference of the Pendellösungs periods are indicated by the grey vertical dotted lines. The parameters of the multilayer structure are equivalent to the simulations shown in Fig. 3.3. The parameters are listed in Tab. 3.2. Scalebars vertical: (I) 10 nm, (II) scattering vector $q = 0.25\,\text{nm}^{-1}$, horizontal: 5 µm

Table 3.3: Parameters of the simulated multilayer optics in Fig. 3.5 and 3.6 (a,b). The simulations were performed in 3D with a FOV of $9.45 \times 9.45\,\mu\text{m}^2$ and 27×10^3 grid points in each lateral direction. The photon energy is $E = 13.8\,\text{keV}$, the focal length is $f = 1\,\text{mm}$ and the multilayer depth is $\Lambda_t = 15.1\,\mu\text{m}$. NA defines the numerical aperture, $\max(\Delta_m)$ the largest and $\min(\Delta_m)$ the smallest layer width. The total number of layers is given by M_{layers}.

Fig.	geometry	NA	$\max(\Delta_m)$	$\min(\Delta_m)$	M_{layers}
3.5 (I), 3.6 (a,b)	MZP	$4.5 \cdot 10^{-3}$	50 nm	10 nm	216
3.5 (II), 3.6 (a,b)	off-axis MZP	$4.1 \cdot 10^{-3}$	50 nm	5 nm	890
3.5 (III), 3.6 (a,b)	MLL pair	$4.1 \cdot 10^{-3}$	50 nm	5 nm	890

For (c) the layer positioning error and (d) the interfacial roughness, $\Lambda_{\text{Pendel}/2}$ is also increased, namely by 1.4 µm and 1.2 µm, respectively. The layer positioning error and the interfacial roughness result in more diffuse far-field pattern in between the Bragg peaks (c,d,II). Both, position errors and the roughness, only have small effects on the diffraction efficiency, namely 97.3 % and 99.2 %, respectively without absorption ($\beta = 0$), and 27.3 % and 28.8 %, respectively including absorption ($\beta > 0$). Interestingly, in all cases the effects are relatively small and the diffraction efficiency seems robust at the level of realistic 'real-structure' parameters.

3.6 Multilayer focusing optics

We present simulations of focusing multilayer optics to show the possibilities and constraints to generate small focal spot sizes. We simulate fully illuminated MZPs, off-axis-illuminated MZPs, single MLLs, and a pair of crossed MLLs. We are particularly interested in the shape and size of the respective focus.

All simulated optics have a wedged geometry (the layers are matched to the local Bragg angles), a depth corresponding to $\Lambda_{\text{Pendel}/2}$, and were illuminated by normally incident plane waves. The outermost layer widths $\min(\Delta_m)$ for the optics was set such that all have similar NAs. The parameters are tabulated in Tab. 3.3. The fully illuminated MZP, the off-axis illuminated MZP and the crossed MLLs were simulated in 3D. Additionally, we performed simulations with even larger NAs of a single MLL and an MZP in 2D and CS, respectively.

Figure 3.5 shows the intensity of the diffracted wavefields propagating in 3D of (I) an

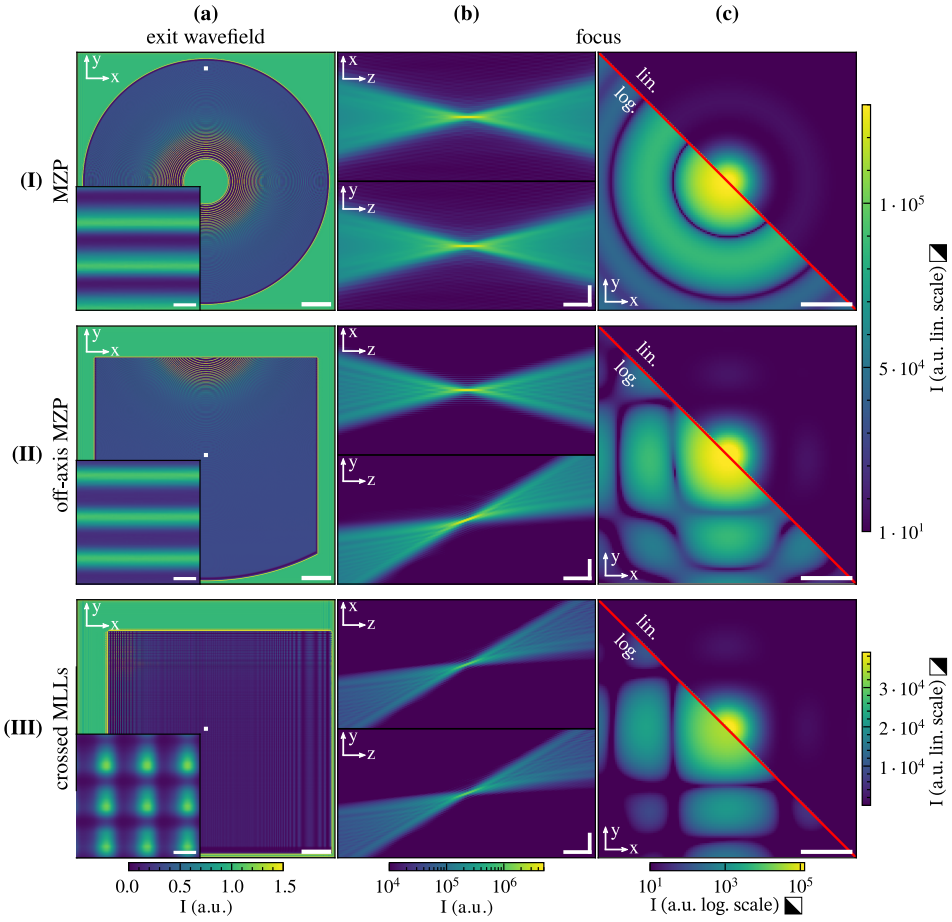

Fig. 3.5: Simulations in 3D of the multilayer optics. The diffracted wavefields of (I) an MZP with $\max(\Delta_m) = 50\,\text{nm}$, $\min(\Delta_m) = 10\,\text{nm}$ corresponding to an NA $= 4.5 \times 10^{-3}$, (II) an off-axis MZP with $\max(\Delta_m) = 50\,\text{nm}$, $\min(\Delta_m) = 5\,\text{nm}$ corresponding to an NA $= 4.1 \times 10^{-3}$ and (III) two crossed MLLs with $\max(\Delta_m) = 50\,\text{nm}$, $\min(\Delta_m) = 5\,\text{nm}$ corresponding to an NA $= 4.1 \times 10^{-3}$. The focal length is in all cases $f = 1\,\text{mm}$. (a) Intensity of the exit wavefield directly behind the multilayer optics, with an inset showing a zoom in, the position is indicated by the white square. (b) Focus profiles in propagation direction integrated over the lateral axes. (c) Lateral focus shape in logarithmic (lower left) and linear (upper right) color scaling. A list of the basic simulation parameters can be found in Tab. 3.3. Scalebars: (a) 1 µm, inset 10 nm, (b) vertical 0.1 µm and horizontal 10 µm, (c) 10 nm

MZP, (II) an off-axis MZP, and (III) a pair of crossed MLLs. (a) Shows the intensity distribution in the plane directly behind the structure, (b) the integrated longitudinal focus profile, and (c) the transverse focus profile. The intensity distribution behind the different lenses (a) shows characteristic differences: Firstly, we have full radial symmetry with respect to the optical axis for (I,a) the MZP. On the other hand, the center is shifted to the top and the top right of the FOV, for (II,a) off-axis MZP and (III,a) crossed MLL, respectively. Regarding (II), the multilayer structure itself was clipped, i.e. corresponding to only a section of a complete MZP. The same results (apart from apodization effects) could also be obtained by clipping the illumination. Regarding (III), two subsequent MLLs are needed to achieve a point focus. The lateral focus position differs in all three cases. The exit wavefield intensity for the pair of MLLs is lower than in (I,II,a) due to absorption in two subsequent multilayer structures instead of only one. The insets in (a) display a small magnified region of the respective exit wavefield. Note that the curvature of the layers in (I,II,a) is not visible on these small scales. The exit wavefield of the pair of the crossed MLLs (III,a) shows a grid-line intensity pattern, as both MLLs focus in one direction only. In (b), we show the longitudinal intensity profiles integrated over x and y, respectively. The on-axis and off-axis focusing shows different propagation directions. In (c), the corresponding lateral focal spot is shown in a linear and a logarithmic color scaling. In contrast to the circular-symmetric focal distribution of the MZP (I,c), and the axis-symmetric focal distribution of the MLL (III,c), for the off-axis MZP (II,c) no 2D symmetric focal distribution is observed. More interestingly, also the pattern of side maxima in the focal plane differs, according to the different pupil geometry.

In Fig. 3.6 (a,b), the corresponding line profiles of the focal planes are plotted. In (a,b) all optics simulated in 3D – MZP, off-axis MZP and crossed MLL – show a point focus of comparable size (full width at half max (FWHM) of 10 ± 0.1 nm). This is a result of the similar NAs of all three multilayer optics. Still, they differ in peak intensity and focusing efficiency, which is 21.4 % for the MZP, 23.7 % for the off-axis MZP, and 6.5 % for the MLLs (if absorption is neglected, $\beta = 0$, the focusing efficiencies are 52.9 % for the MZP, 75.7 % for the off-axis MZP, and 61.9 % for the MLLs). The efficiency is calculated using the intensity of the focus in the region between the first minima divided by the intensity in the structured area of the multilayer optics. The difference of the focusing efficiencies between the MZP and the off-axis MZP results from the smaller outermost layer width $\min(\Delta_m)$ of the off-axis MZP. Small layers have the highest focusing efficiency for the given depth of $\Lambda_{\text{Pendel}/2}$ due to the Pendellösung effect discussed above. Regarding the MLLs, the area of a single layer is decreasing

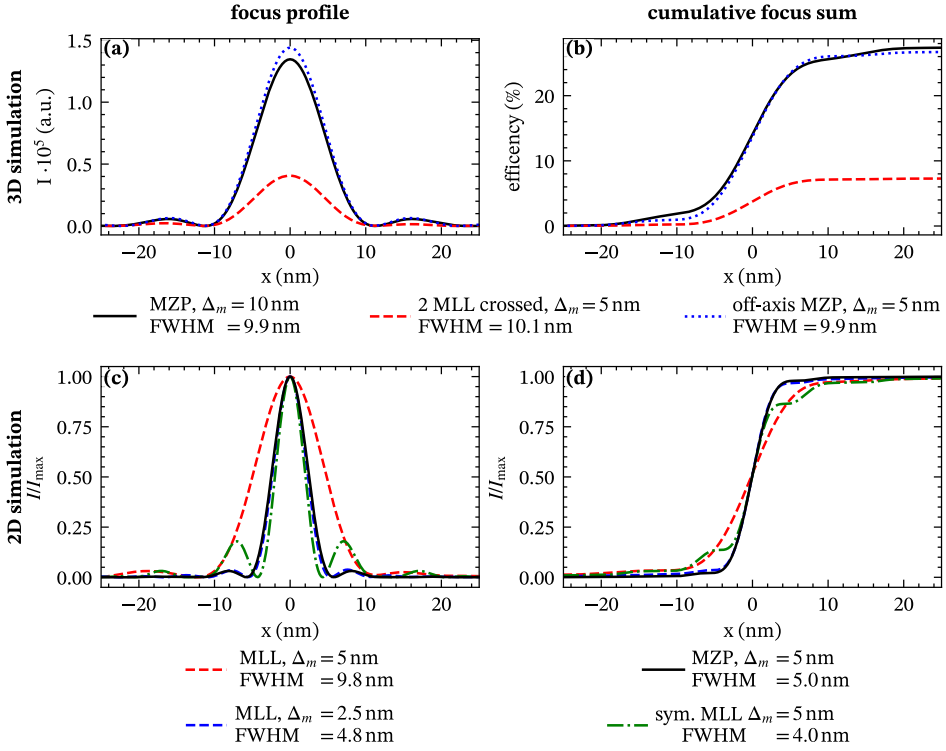

Fig. 3.6: (a) Focus profiles of the 3D simulations shown in Fig. 3.5 and (b) the cumulative sum of the focus profiles. (c) The normalized 2D focus profiles of the MLLs and an MZP simulated in a 2D Cartesian and circular-symmetric (CS) coordinate system, respectively. The results show simulations for one-sided (conventional) MLLs and symmetric (two-sided) MLLs. The latter is often used in the theoretical description of MLLs but has not been experimentally realized. (d) The normalized cumulative sum of the focus profiles. The simulation parameters are listed in Tab. 3.3, and 3.4 respectively.

Table 3.4: Parameters of the simulated multilayer optics in 2D shown in Fig. 3.6 (c,d). The simulations were performed with a FOV of 60 µm and 0.6×10^6 lateral grid points, an exception is the MZP with a FOV of 30 µm and 0.3×10^6 lateral grid points. The photon energy is $E = 13.8$ keV, the focal length is $f = 1$ mm and the multilayer depth is $\Lambda_t = 15.1$ µm. NA defines the numerical aperture, $\max(\Delta_m)$ the largest and $\min(\Delta_m)$ the smallest layer width. The total number of layers is given by M_{layers}.

Fig.	geometry	NA	$\max(\Delta_m)$	$\min(\Delta_m)$	M_{layers}
3.6 (c,d)	MLL	$4.1 \cdot 10^{-3}$	50 nm	5 nm	890
3.6 (c,d)	MLL	$8.6 \cdot 10^{-3}$	50 nm	2.5 nm	3585
3.6 (c,d)	symmetric MLL	$4.5 \cdot 10^{-3}$	50 nm	5 nm	890
3.6 (c,d)	MZP	$4.5 \cdot 10^{-3}$	50 nm	5 nm	890

with decreasing layer width, contrarily the area of a single layer of the MZP and off-axis MZP is constant with decreasing layer width. Since the highest focusing efficiency is given for the smaller layer widths, the difference in the geometry has an effect on the overall focusing efficiency of the MLL. Nevertheless, the main difference between the efficiency of the MZPs and the crossed MLLs results from the absorption by two subsequent optics.

Finally, Fig. 3.6 (c,d) show the focus profiles of multilayer optics with even larger NAs of up to 8.6×10^{-3} for sub-5 nm focusing. To simulate the large numerical apertures with sufficient accuracy at reasonable numerical expense, we have performed the simulations in 2D. In total, 4 multilayer optics have been simulated: an MZP, two MLLs with different NAs and one symmetric MLL with layers on both sides of the optical axis. Although the latter has been discussed previously [Yan+07], to our knowledge it has never been realized experimentally. The parameters are tabulated in Tab. 3.4. In (c), the different normalized focal intensity profiles are shown for comparison. As expected, the FWHM is a function of the numerical aperture. The often-used approximation that the outermost layer width $\min(\Delta_m)$ is about equal to the focus size is only valid for the on-axis optics (MZP, symmetric MLL). For on-axis MZPs, the side maxima can also increase if large areas of the inner layers are blocked, e.g. by a central beam stop [SM84]. Within the simulations, the smallest focal points with a FWHM of approximately 5 nm are generated by the MLL with $\min(\Delta_m) = 2.5$ nm and the MZP with $\min(\Delta_m) = 5.0$ nm. Both show similar focus profiles. This demonstrates that specific geometries of multilayer optics for point-focusing can be approximated

Table 3.5: Parameters of the simulated imaging setup in Fig. 3.7. The simulation was performed in 3D with a FOV of $10.15 \times 10.15\,\mu\text{m}^2$ and 29×10^3 grid points in each lateral direction. The pixel size in the sample plane is 0.35 nm and in the detector plane 44.25 µm. The photon energy is $E = 13.8\,\text{keV}$, the focal length is $f = 1\,\text{mm}$. Δ_{beam} defines the FWHM of the Gaussian illumination, Λ_{sample} the depth of the sample and z_{detector} the distance of MZP to the detector. NA defines the numerical aperture, $\max(\Delta_m)$ the largest and $\min(\Delta_m)$ the smallest layer width. The total number of layers is given by M_{layers} and the depth of the MZP by Λ_t.

	Setup parameters		Δ_{beam} (FWHM)	Λ_{sample}	z_{detector}	
			1.0 µm	0.25 µm	5 m	
MZP parameters	geometry	NA	$\max(\Delta_m)$	$\min(\Delta_m)$	M_{layers}	Λ_t
	off-axis	8.6×10^{-3}	25 nm	5 nm	863	2.5 µm

by simulations in the 2D or CS coordinate system.

In conclusion, we have shown that different kinds of optics can be used for point focusing. However, for two crossed MLLs, the absorbing material is doubled since two subsequent optics are needed. Further, the relation between the focus size and the outermost zone width is only valid for on-axis illuminations. For off-axis illuminated optics, on the other hand, the illumination NA is the decisive parameter.

3.7 Coherent diffractive imaging with a multilayer zone plate

In Fig. 3.7, we present the simulation of an entire imaging setup. The setup, sketched in row (I), shows an x-ray microscope with an MZP as an objective lens to magnify the object. An incident Gaussian beam is modulated by a phase-shifting and absorbing sample, diffracted by the MZP, and detected in the far-field.

We use the combined approach introduced in section 3.3.4 to simulate the imaging setup. The parameters are tabulated in Tab. 3.5. In an exemplary setup, where the detector is positioned in a distance of $z_{\text{detector}} = 5\,\text{m}$ to the sample, the simulated diffraction patterns correspond to a detector pixel size of 45.25 µm. The sample is modeled as a pure absorption object in the shape of the letter 'A', and a pure phase object in the shape of the letter 'P', positioned at four (a-d) different distances in front of

the MZP. The corresponding diffraction patterns are shown in (II) and the empty-beam divided patterns are shown in (III). In all diffraction patterns, the parallel non-diffracted beam — the 0^{th} order — illuminates only a few pixels in the center, whereas the rest of the image corresponds to the diffraction signal. The diffraction signal of the $+1^{st}$ and -1^{st} order can be observed in the upper and lower half of (II), respectively, and clearly shows a magnified copy of the incident beam including the modulation by the sample. The modulations of the sample can be observed even clearer in the empty-beam divided images shown in (III). These kind of modulations are well known from in-line holography, and referred to as holograms. In classical TXM [NRS76; Mül+14] with zone plate lenses to magnify the object, the sample is positioned at a distance of about one focal length, here position (c). With the off-axis MZP simulated here, the $+1^{st}$ diffraction order then shows a sharp magnified image of the pure absorption object (A) while the pure phase object (P) is barely visible in this position. Shifting the object along the optical axis (defocus position), enables propagation-based phase contrast at selectable propagation distances, or Fresnel numbers, up to the deeply holographic regime. Importantly, at each position, holographic images can be recorded at two different Fresnel numbers, given a sufficiently large detector, as simulated here. It can also be noted as a curious consequence of the holographic self-interference in the $+1^{st}$ and -1^{st} diffraction orders of the off-axis MZP, that high spatial frequencies are encoded in the diffraction signal around the 0^{th} order in the center of the detector, while lower and medium spatial frequencies are well encoded in the holographic signals appearing at higher angles.

At first, this configuration seems identical or similar to the classical TXM, but some important differences apply. Instead of recording the intensity pattern on the detector as 'the image', the coherent illumination allows for quantitative phase retrieval as in CDI. If the transfer function of the MZP is known, based on simulations and/or experimental measurements, one could develop a phase retrieval approach for an aberration free image reconstruction, similar to [Rob+15; HS17b]. Compared to the classic (incoherent) TXM, coherent imaging with an MZP objective lens, also allows for better image quality concerning both resolution and contrast. Resolution can be increased, since the full diffraction pattern can be included in phase retrieval. Concerning contrast, both phase and absorption can be retrieved quantitatively, without additional elements such as a Zernike phase plate. The relative contrast strength of absorption and phase can be systematically varied by the defocus distance. In contrast to pure CDI or ptychography, the holographic nature of the signal within the $+1^{st}$ and -1^{st} diffraction order encodes especially the low and moderate spatial frequencies, and

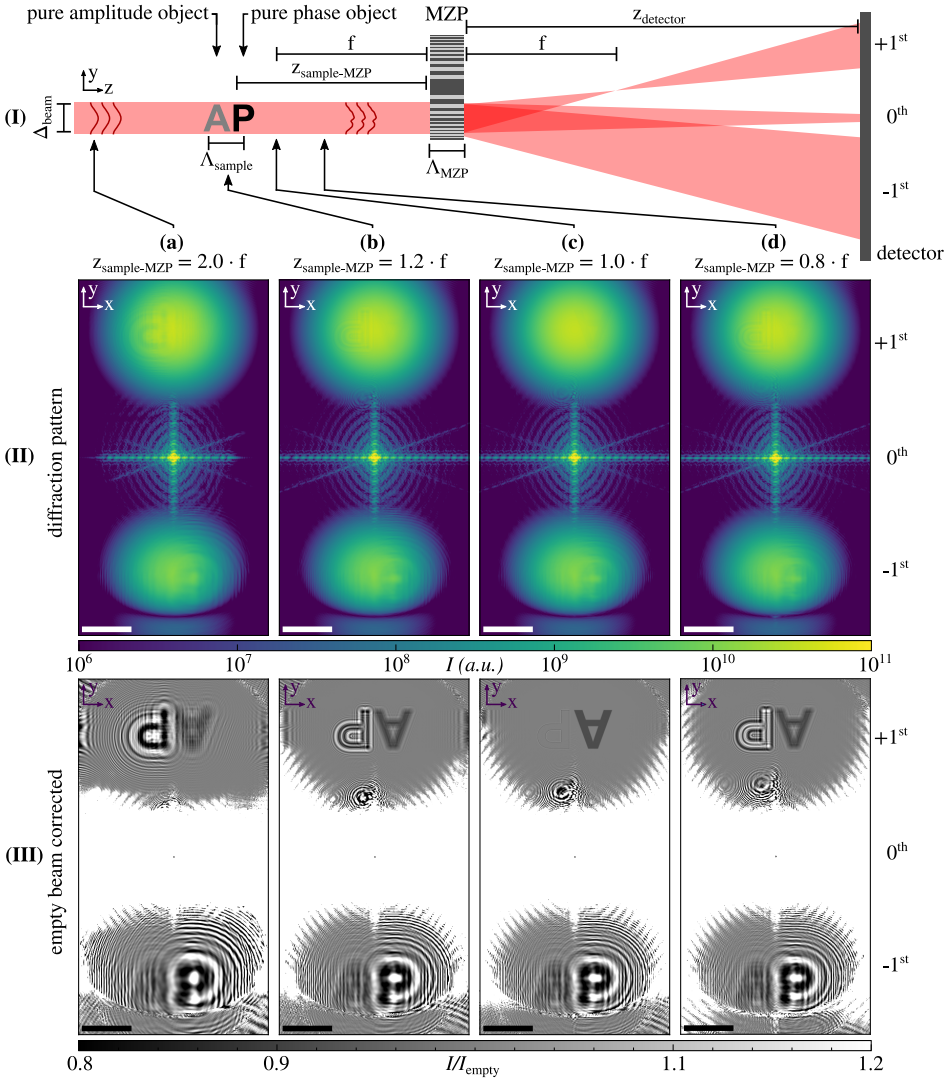

Fig. 3.7: *(caption next page)*

Fig. 3.7 *(previous page)*: 3D simulations of an x-ray microscope using an MZP as an objective lens. An incident Gaussian beam is modulated by a sample, diffracted by the MZP, and detected in the far-field. (I) Illustration of the experimental setup. MZP diffracts the beam in multiple diffraction orders, most prominent 0^{th}, $+1^{\text{st}}$, and -1^{st}. The samples are a pure absorption object 'A' and a pure phase object 'P'. The FWHM of the incident beam is denoted by Δ_{beam}, the depth of the sample by Λ_{sample}, the depth of the MZP by Λ_{MZP} and the focal length of the MZP by f. A list of the simulation parameters can be found in Tab. 3.3. (II) Diffraction pattern of the wavefield and (III) empty-beam divided diffraction pattern, highlighting the wave modulation. The corresponding diffraction order is indicated on the right side. (a-d) different positions $z_{\text{sample}-\text{MZP}}$ between the sample in units of focal length. In case of (c) with the sample positioned in the focal plane the pure phase object is in the $+1^{\text{st}}$ diffraction order almost not observable, only a light edge enhancement. The hologram of both objects is visible in every other distance and within the other diffraction orders. Scalebars: 200 px corresponding to a scattering vector $q = 0.125\,\text{nm}^{-1}$.

results in a particularly well posed problem for phase retrieval [Mar18]. These spatial frequencies are therefore easily phased based on the enlarged holographic signal in the $+1^{\text{st}}$ and -1^{st} diffraction orders. At the same time, high spatial frequencies are encoded within the diffracted signal around the center 0^{th} order. Interestingly, the presence of the $+1^{\text{st}}$ and -1^{st} diffraction orders also means that near-field holographic images at two different Fresnel numbers are recorded simultaneously. Furthermore, compared to the classical TXM scheme, this approach makes much more efficient use of the diffracted photons, by using the full diffraction pattern, and not only the $+1^{\text{st}}$ diffraction order. An image reconstruction approach could be kept similar to the algorithm presented in chapter 5, which jointly phases holographic and diffractive components. Advantages of using a known transfer function (modulator) in a three plane CDI setup has also been shown in [Zha+16], an has been denoted as coherent modulation imaging . A *modulator* consisting of randomly distributed equal sized pillars is positioned between the sample and the detector, equivalent to the MZP. The purpose of the modulator is to overcome inherent ambiguities in the phase retrieval process. By deploying an MZP, we redefine the purpose of the modulator by exploiting the magnifying capabilities of the MZP, as we already suggested in [Rob+15]. Thereby high spatial frequencies of weakly scattering samples can be recorded. Furthermore, by recording also the low spatial frequencies in the holographic components of the $+1^{\text{st}}$ and -1^{st} diffraction orders, the usual sampling constraints can be overcome extending the possible field of view, similar to chapter 5. The detailed implementation of the reconstruction approach using an MZP and its experimental verification exceeds the

scope of the present manuscript, and will be pursued in forthcoming work.

3.8 Conclusion

In summary, we showed that the FD approach is well-suited for numerical wavefield propagation through multilayer optics with large aspect-ratios of layer width to depth. The FD approach yields accurate wavefields, with no artifacts resulting from the periodic boundary conditions. Further, the computational field of view can be kept small, reducing the computation time, which is especially relevant for 3D simulations. Note that the results obtained here, by FD simulations of multilayer optics, are in line with previous investigations of the FD for the case of WG propagation [MS17].

Further, we studied the transition from a regime of guiding modes, observed at larger layer width, to the pronounced coupling of layers and formation of standing waves at small layer width observed in particular for oblique incidence. The latter phenomenon is well known as Pendellösung from the analytical theory of dynamical diffraction. By the present numerical simulations, the Pendellösung effects can be studied beyond approximations. Next, we have provided detailed 3D simulations comparing three different multilayer implementations, MZP, off-axis MZP and crossed MLLs. All three configurations are relevant in view of the ongoing developments in this field and the respective constraints of fabrication. The simulations clearly show that in all cases small focal points can be achieved. Particularly high focusing efficiencies are achieved when the fraction of the illuminated area structured by small layers is highest, such as in off-axis MZP. This results from the fact that the incidence angle and Pendellösung effect can then be optimized to a smaller range of layer widths. In addition when using a pair of MLLs for point focusing, the focusing efficiency is reduced by the doubled absorption since two subsequent optics are needed. Despite these differences, we can conclude that in principle all focal spots presented in this work are suitable for imaging applications, either in scanning or in full field.

After studying specific properties of isolated multilayer optics, we have extended the simulation to an imaging scheme combining multilayer optics with free-space propagation and diffraction. Different coherent imaging schemes can be conceived and treated by the present simulation approach. Correspondingly, Fig. 3.7 can be considered as just one example of many, where the optical design requires simulation of illumination, object, objective optics, and detection. Almost always, the simulation of the forward problem is an useful if not indispensable setup before a full phase

retrieval and imaging scheme can be implemented. However, it is a further goal of this work to also propose a specific coherent imaging scheme, based on an off-axis MZP (or FZP) objective lens, as presented in Fig. 3.7. This example also shows that full experimental setups can be simulated by FD, which hence can help to identify new imaging schemes for high resolution and optimized contrast. Altogether, this opens a brilliant perspective for coherent x-ray imaging, well suited for the current developments of multilayer focusing optics with higher NA and advanced iterative reconstruction algorithms.

Funding

German Federal Ministry of Education and Research (BMBF) through grant No. 05K19MG2 and the Deutsche Forschungsgemeinschaft grant SFB 1456/C03 'Mathematics of Experiment: The challenge of indirect measurements in the natural sciences'.

Acknowledgments

We thank Jan Goeman for discussion and advice in computing. L.M.L. and T.S. are members of the Max Planck School of Photonics supported by BMBF, Max Planck Society, and Fraunhofer Society.

3.9 Supplementary materials

3.10 Additional information on the finite-difference propagators

For reference, we briefly describe the FD propagators. Starting from the Helmholtz equation (3.1), we write the wavefield ψ as $\psi = u\exp(ikz)$ and write the Laplace operator as $\nabla^2 = \partial_z^2 + \nabla_\perp^2$. Neglecting $\partial_z^2 u$ (slowly varying envelope approximation) yields to a parabolic differential equation for the envelope,

$$2ik\partial_z u = \left(-\nabla_\perp^2 + k^2(1-n^2)\right) u, \tag{3.2}$$

the paraxial Helmholtz equation (PHE).

3.10.1 Elimination of units

We bring (3.2) into one standard form for the different geometries. For numerical computation, we express all distances as multiples of the mean wavelength λ_0. Define

$$A = i/(2k\lambda_0), \qquad F(x,z) = -ik\lambda_0(1-n^2)/2.$$

1D geometry: The lateral derivative is $\nabla_\perp^2 = \partial_x^2$. Then (3.2) becomes

$$\lambda_0 u_z = A\lambda_0^2 u_{xx} + Fu. \tag{3.3}$$

2D geometry: The lateral derivate is $\nabla_\perp^2 = \partial_x^2 + \partial_y^2$. Then (3.2) becomes

$$\lambda_0 u_z = A\lambda_0^2 u_{xx} + A\lambda_0^2 u_{yy} + Fu.$$

CS geometry: The lateral derivative is $\nabla_\perp^2 = \partial_x^2 + \frac{1}{x}\partial_x + \frac{1}{x^2}\partial_\varphi^2$. Assuming circular symmetry, $\partial_\varphi^2 u = 0$, yields

$$\lambda_0 u_z = A\lambda_0^2 u_{xx} + A\lambda_0^2 \frac{1}{x} u_x + Fu. \tag{3.4}$$

It has an apparent singularity at the origin. However, the second term stays finite in the limit $x \to 0$, because, using the symmetry

$$u(x) = u(-x)$$

we obtain

$$\lim_{x\to 0} \frac{u_x(x)}{x} = \lim_{x\to 0} \frac{u_x(x) - u_x(-x)}{2x} = u_{xx}(0).$$

Hence, (3.4) becomes

$$\lambda_0 u_z = \begin{cases} 2A\lambda_0^2 u_{xx} + Fu, & x = 0 \\ A\lambda_0^2 u_{xx} + A\lambda_0^2 \frac{1}{x} u_x + Fu, & x > 0. \end{cases} \tag{3.5}$$

3.10.2 Discretization

For each z, the scalar fields u and F are sampled on a discrete grid of size $(N+2)$ for 1D, $(N+1)$ for CS, and $(N+2)\times(M+2)$ for 2D. Let Δx, Δy, and Δz be the

sampling intervals in units of λ_0. Here we briefly describe the 1D and CS geometry in more detail. The 2D geometry is very similar but lengthier, so that we refer to [FS06a].

1D geometry: We approximate u_{xx} by second order central finite differences as

$$u_{xx}(x_i) \approx \frac{u_{i+1} + u_{i-1} - 2u_i}{\Delta x^2}.$$

Applying the Crank-Nicolson method on (3.3) yields

$$-au_{i-1}^{m+1} + \left(2 + 2a - f_i^{m+1}\right) u_i^{m+1} - au_{i+1}^{m+1} = au_{i-1}^{m} + \left(2 - 2a + f_i^{m}\right) u_i^{m} + au_{i+1}^{m}.$$

for $i \in \{1, \ldots, N\}$, where

$$\begin{aligned} a &= A\Delta z/\Delta x^2, \\ f_i^m &= F(x_i, z_m)\Delta z. \end{aligned}$$

The boundary values u_0 and u_{N+1} are given. We have a sparse system of N linear equations for N unknowns, $u_1^{m+1}, \ldots, u_N^{m+1}$, which can be solved.

CS geometry: The approach for circularly-symmetric functions is similar. Since (3.5) explicitly depends on x, we have to define the grid points. Here, we use integer grid points, $x_i = i\Delta x$ with $i \in \{0, \ldots, N\}$. Similar to u_{xx}, we approximate

$$u_x(x_i) \approx \frac{u_{i+1} - u_{i-1}}{2\Delta x}.$$

Using the Crank-Nicolson method on (3.5) yields

$$\begin{aligned} -\left(1 - \frac{1}{2i}\right) au_{i-1}^{m+1} + \left(2 + 2a - f_i^{m+1}\right) u_i^{m+1} - \left(1 + \frac{1}{2i}\right) au_{i+1}^{m+1} \\ = +\left(1 - \frac{1}{2i}\right) au_{i-1}^{m} + \left(2 - 2a + f_i^{m}\right) u_i^{m} + \left(1 + \frac{1}{2i}\right) au_{i+1}^{m}, \end{aligned}$$

for $i \in \{1, \ldots, N-1\}$, where a and f are defined as in the 1D geometry. For $i = 0$, the equation is different. Using symmetry, $u_{-1} = u_1$, we obtain

$$\left(2 + 4a - f_0^{m+1}\right) u_0^{m+1} - 4au_1^{m+1} = \left(2 - 4a + f_0^{m}\right) u_0^{m} + 4au_1^{m}.$$

The boundary values u_N are given. Here, we again have a sparse system of N linear equations for N unknowns, $u_0^{m+1}, \ldots, u_{N-1}^{m+1}$, which can be solved.

Note that we exploited the symmetry condition to avoid specifying the boundary values at the origin.

Off-axis multilayer zone plate with 16 nm x 28 nm focus for high resolution x-ray beam induced current imaging

4

Jakob Soltau, Lert Chayanun, Mikhail Lyubomirskiy, Jesper Wallentin, and Markus Osterhoff

reproduced[1] *from Journal of Synchrotron Radiation, 28, 5, 1573-1582 (2021)* [Sol+21a]

Using multilayer zone plates (MZP) as two-dimensional optics, focal spot sizes of less than 10 nm can be achieved, as we show here with a focus of 8.4 x 9.6 nm^2, but the need for order sorting apertures prohibits practical working distances. To overcome this issue, we introduce an off-axis illumination of a circular MZP to trade-off between working distance and focal spot size. By this, we can more than double the working distance between order sorting aperture and sample. Exploiting a 2D focus of 16 x 28 nm^2, we demonstrate real-space 2D mapping of local electric fields and charge carrier recombination using x-ray beam induced current (XBIC) in a single InP nanowire. Simulations show that a dedicated off-axis MZP can reach sub-10 nm focusing combined with reasonable working distances and low background, which could be used for in operando imaging of composition, carrier collection and strain in nanostructured devices.

[1] subject to minor corrections

4.1 Introduction

For hard x-ray imaging of bulk materials and biological specimens, the development of diffractive optics such as zone plates or multilayer lenses has been transformative in recent years [Dör+13; Moh+17; Baj+18]. Samples can now be probed in-situ or in-vivo with nanometer resolution [Vic+18]. In optics with large numerical apertures (NA), used to obtain the smallest focal spot sizes, the diffractive elements need to be scaled down since the size of the smallest structure corresponds directly to the size of the focal spot. The most common diffractive optics for focusing x-rays are Fresnel zone plates (FZP) which are fabricated using lithography. FZPs were developed for the focusing of soft x-rays [NRS74; Sch98; Gor+19; Rös+20] where zone widths of down to 8 nm were achieved. But for hard x-rays lithographic fabrication methods are limited to approximately 20 nm smallest structure sizes [CS14]. A smaller focal spot can be achieved by using double sided FZPs, for x-ray wavelengths of several nanometer and down to one angstrom [Moh+17]. In contrast, multilayer zone plates (MZP) are diffractive optics with smallest structure elements of down to 5 nm [Ebe+14], achieved using pulsed laser deposition (PLD). However the focal length of currently 1 mm at 15 keV results in short working distances. On the other hand, the fabrication allows the usage of MZPs at energies up to 100 keV [Ost+17b].

Beside a small focus size a low background signal is of importance in most experiments such as x-ray fluorescence (XRF) [Yan+16; Den+17], ptychography [Hol+14; Shi+19], scanning SAXS or WAXS [RBR19], for new imaging schemes such as Compton x-ray microscopy [VBC18] or, as shown in this manuscript, for x-ray beam induced current (XBIC) [Buo+03]. Unfortunately, when using diffractive x-ray optics, photons are diffracted into several orders (negative or positive) and some photons are undiffracted (zeroth order), resulting in a background signal and affecting the sensitivity and contrast of many measurements. The standard procedure to prevent this is blocking "unwanted" photons by a pair of apertures. Therefore a first central stop is positioned in-front of the optics, and a pinhole is used as an order sorting aperture (OSA) positioned between the optics and the sample in the vicinity of the focal spot (see Fig. 4.1(a)). The working distance z_{WD} is the distance between the OSA and the focal spot. It depends on the radius of the central stop. A small z_{WD} imposes strong restrictions on the study of samples. Due to volume diffraction effects in multilayer optics also even diffraction orders occur [Mas+04], resulting in the formation of a second order focus at the position of half the focallength, reducing z_{WD} even further. To increase z_{WD}, the radius of the central stop needs to be enlarged and thereby more inner zones

of the optic are not illuminated. This results in a loss of photon flux. However, the maximum length of z_{WD} is generally limited to half the focal length by the position of the second-order focus.

An alternative approach to a large central stop for filtering the beam from photons of unwanted diffraction orders is to separate the focused x-rays from the optical axis of the incoming beam, which could be advantageous for three important reasons: (i) The central part of the beam no longer needs to be blocked and therefore the central stop can be omitted or replaced by a simple pinhole. This results in an increased efficiency since the highest photon flux is in the center of the beam. (ii) Beside a reduced efficiency, the height of the focus side maxima is dependent on the ratio of the blocked area relative to the illuminated area [SM84]. This is not the case for an off-axis illumination, as shown in chapter 4.5.5 of the supplementary materials using finite-difference simulations. The simulations show an increased focus side maxima intensity by factor of 2.3 for the case of a fully illuminated MZP and an off-axis MZP with the same NA. Strong focus side maxima are reducing the effective resolution. And (iii) in case of the off-axis illumination, the OSA can be placed further upstream (see Fig. 4.1(b)), even beyond the second-order focus, without the limitations (i) and (ii), leaving more space for the sample. The compromise when it is placed further upstream is the reduced numerical aperture, thus the ratio of the outermost zone width to the possible focus size is no longer given. Nevertheless, this off-axis configuration is used in most experiments using a pair of one dimensional optics such as multilayer Laue lenses (MLL) [Mor+15]. The reduced dimensions of one dimensional optics imposes the disadvantage that for generating a 2D focus, two optics are required. Since the two MLLs need to be aligned in close distance, the complexity of the setup is further increased. In addition, the MLLs must be aligned that both focal planes match. When the photon energy changes, readjustment becomes necessary, which limits the flexibility in an experiment.

In this manuscript, we show that for high-resolution x-ray microscopy, this off-axis configuration is not limited to a pair of 1D lenses, but is also possible for a single circular diffractive optical element. We compare the off-axis geometry with a classical zone plate geometry and evaluate them using ptychography and finite-difference simulations. In section 4.3.2 we show that using an off-axis illuminated MZP it is possible to focus x-rays to a focal point separated from the beam. We measure focus sizes of $16.2 \times 27.9\,\mathrm{nm}^2$ and $8.4 \times 9.6\,\mathrm{nm}^2$ for the off-axis and the classic geometries, respectively (see section 4.3.1).

Fig. 4.1 ***(next page)*:** Two setups using an MZP in combination with apertures. Both are illuminated by an x-ray beam pre-focussed using CRLs. (a) Classic setup with a fully illuminated MZP and a central stop combined with a OSA to block background photons. The OSA is positioned to block the second order focus. (b) Setup with an off-axis illuminated MZP. Note that the pinhole can be omitted if the incoming beam is already confined by optics upstream. The contacted nanowire (NW) is depicted at the focal plane. The OSA is positioned to block the second order focus. (c) Scanning electron microscopy (SEM) image of the MZP mounted on a Si_3N_4-window. (d) SEM image of the outer zones of the MZP, showing a width of down to 5 nm. (e) Photograph (side-view) of the off-axis setup at the P10 beamline. The pinhole and the OSA are visible, the Si_3N_4-window where the MZP is mounted (not visible) and the nanowire sample with the bond wires. (f) SEM of the nanowire devices and the star shaped test structures, both created using lithography. (a,b) Not to scale. Scalebars: (c) 5 μm, (d) 50 nm, (e) 250 μm (f) 100 μm.

Crucially, the off-axis geometry more than doubles the distance between the OSA and the focus, increasing the working distance from 0.18 mm to 0.44 mm. We take advantage of the improved working distance and reduced background to perform simultaneous high-resolution XBIC real-space mapping and holographic, ptychographic or scanning transmission imaging of semiconductor nanowires, as shown in section 4.3.3. Finally, we use the nanowire as a detector to measure the intensity distributions along the optical axis of an off-axis illuminated MZP in section 4.3.4.

4.2 Methods

4.2.1 The multilayer zone plate

The MZP was fabricated using the technique of pulsed laser deposition (PLD), following the Fresnel zone plate formula with an outermost layer thicknesses of 5 nm, a diameter of 15.6 μm, 784 zones and a thickness of 2.4 μm (see Fig. 4.1(c,d)). The Fresnel zone plate formula defines the radius of a zone as $r \approx \sqrt{n\lambda f}$ with the wavelength λ, the focal length f and n the index of the zone. The outermost zone width Δr_N defines the maximum diffraction angle of the first order, which limits NA of the optics and the size of the focal spot as a result. Therefore Δr_N is almost equivalent to the theoretical focal spot size. MZPs have been used for focusing x-rays in an energy range from 8 keV [Dör+13] up to 100 keV [Ost+17b].

A round glass wire of diameter 2.1 μm was used as a substrate for the deposition process.

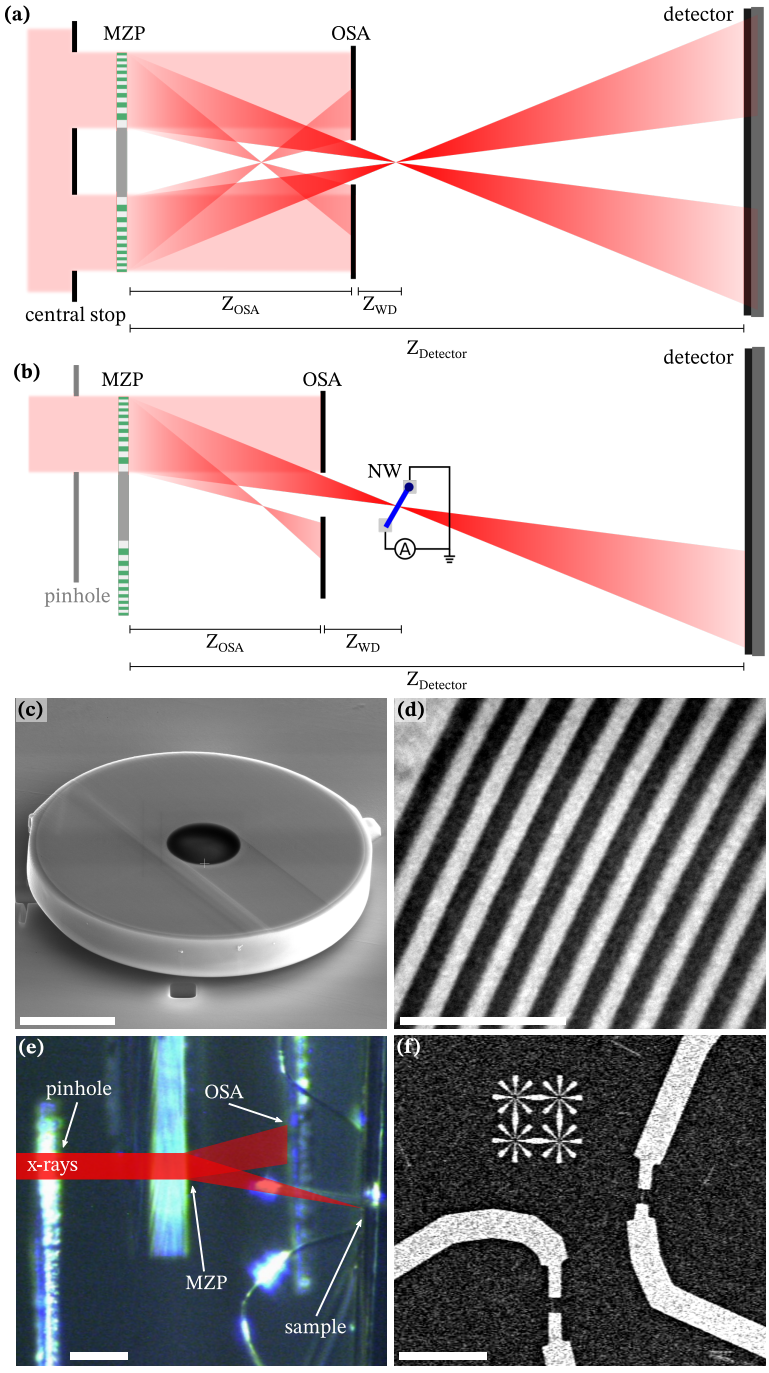

Fig. 4.1: *(caption previous page)*

Within our parameters, the glass wire corresponds to first thirteen zones, which therefore are missing. By using tapered fibers with an opening angle of 2.5 mrad the zones become tilted relative to the beam axis and in direction of the focus. This enhances the x-ray focusing efficiency [Yan+10]. In the case of the MZP used here, simulations show that this increases the focusing efficiency by almost a factor of 3 (see chapter 4.5.6 in the supplementary materials). In the fabrication process, the slice position is determined on the basis of the outer radius of the MZP. As materials for the zones, Ta_2O_5 and ZrO_2 were used. One advantage of PLD over other sputtering techniques originates in the energetic bombardment, resulting in cumulative smoothing [RLK10] which decreases roughness and distortions [Ebe+14].

The mounting of the MZP was modified compared to previous experiments, to achieve a better long-term stability during the measurements and to simplify the alignment process. In previous experiments the MZP was mounted on a tungsten tip, but here the MZP was mounted flat with three contacts on a Si_3N_4-window (thickness 1 µm) using a focused ion beam (FIB) setup (see Fig. 4.1(c)). The Si_3N_4-window enables the precise pre-alignment of the MZP using the reflection on the window by a laser beam which is aligned parallel to the x-ray beam. Further the flat mounting on the Si_3N_4-window fixed by three contacts increases the stability against potential oxidation processes at the contacts.

4.2.2 X-ray beam induced current

X-ray beam induced current (XBIC) can be used to measure local electric fields and charge carrier recombination conditions. Compared to scanning photocurrent microscopy (SPCM) [Ahn+07], a smaller diffraction limit allows for higher spatial resolution [Cha+19b]; compared to electron beam induced current (EBIC) [Han80], a higher penetration depth allows to characterise thicker samples [Stu+15]. Thus, complete devices can be investigated in operando.

In XBIC, an absorbed x-ray photon excites secondary electrons in semiconductors through a cascade process, which then thermalize to the band edge of the semiconductor [Rod97; GK17]. These secondary charges are collected under an applied or built-in electric field within the measured device. The XBIC signal is therefore dependent on the local electric field and carrier recombination conditions, and by scanning the sample in an x-ray focus the XBIC technique can be used to map the local charge transport and charge collection properties of semiconductor devices. For the XBIC measurements at the `GINIX` beamline, see below, the XBIC measurement system was

integrated into the control system at the instrument, as described previously [Cha+19b]. Nanowire devices were fabricated on an Si_3N_4 window, wire bonded and mounted in a special sample holder with electrical connections. Test structures, similar to Siemens stars, were also deposited on the Si_3N_4 window next to the nanowire device. The structure was used for a characterization of the off-axis beam path by ptychography. The smallest features of the star shaped test pattern were 100 nm.

4.2.3 P10-GINIX setup

The off-axis configuration of the MZP and XBIC measurements were performed at the GINIX instrument [Kal+11] at the coherence beamline P10, at the PETRA III storage ring (Hamburg, Germany). The experimental setup is depicted in Fig. 4.1(b). The undulator beam at the P10 beamline was monochromatized (Si(111) channel-cut monochromator) to a photon energy of 13.8 keV and pre-focused by a compound refractive lens (CRL). The MZP, apertures, and nanowire device were mounted on the high-resolution stage of the instrument [Ost+17a] for fly-scans and reduced vibrations, especially with respect to each other. As depicted in Fig. 4.1(b), the pinhole was mounted in front of the MZP and the OSA was carefully aligned between the MZP and the sample. The diameters of the apertures were 5.6 µm for the pinhole and 3.5 µm for the OSA. The focal length of the MZP at 13.8 keV is 0.92 mm. The maximum distance between the OSA and the focus is 0.44 mm. A picture of the setup is shown in Fig. 4.1(e). The pinhole was installed to decouple from vibrations of the incoming beam. The diffraction patterns of the x-ray beam were recorded using a single photon counting pixel detector (Eiger 4M, Dectris Ltd. Switzerland) positioned at $z_{\mathrm{DE}} = 5.1\,\mathrm{m}$. The detector has 2162×2068 pixels of size $\Delta_{\mathrm{px}} = 75\,\mu\mathrm{m}$.

4.2.4 P06-Nanoprobe setup

In addition to the measurement at the GINIX setup using an off-axis illuminated MZP, a second measurement was performed to determine the focus size of a fully illuminated MZP as a reference. Since the OSA had to be aligned at close distance to a test structure for this purpose, the measurement was realized in a separate experiment. This experiment was realized using the PtyNAMI instrument [Sch+20] at the Hard x-ray Micro/Nano-Probe at the beamline P06, which is also positioned at the PETRA III storage ring (see [Sch+16] for details). The MZP had the same zone parameters as the one used at the GINIX setup. The undulator beam was monochromatized (Si(111)

channel-cut monochromator) to a photon energy of 15 keV, and then pre-focused using a CRL optic with the MZP positioned in its focal plane. The size of the CRL focus was larger than the diameter of the MZP to prevent a decrease in intensity at the outer MZP-zones.

In Fig. 4.1(a) the experimental setup of the fully illuminated MZP is depicted. Despite the two setups being quite similar, they differ in two important points: (1) the shape of the first aperture. The aperture in this configuration is a solid central stop of 6 µm diameter for blocking the photons. (2) The smallest possible distance between the OSA and the focus is in the full-illumination configuration 0.18 mm, less than half the distance as in the off-axis geometry. At a greater distance between the OSA and the focal plane the OSA would cut into the beam. The focal length of the MZP at 15 keV is slightly larger with a length of 1.0 mm. As a sample a Siemens star test structure with 50 nm smallest feature size was positioned at a distance of 1.07 mm relative to the MZP and 0.25 mm relative to OSA. The diffraction patterns of the x-ray beam were recorded using a single photon counting pixel detector (Pilatus 300k, Dectris Ltd. Switzerland) positioned at a distance relative to the optic of $z_{\mathrm{DE}} = 3.43\,\mathrm{m}$. The detector has 619×487 pixels and a pixel size of $\Delta_{\mathrm{px}} = 172\,\mu\mathrm{m}$. A list of the parameters can be seen in Tab. 4.1.

4.3 Results

4.3.1 Beam characterization with fully illuminated MZP

The focus size and beam path of the MZP were characterized using ptychography [Rod+07]. As mentioned, the experiment using the fully illuminated MZP was performed at the P06 nanoprobe instrument. The sample (Siemens star) was scanned with 25×51 scan points at 0.2 s acquisition time per frame. The reconstruction was performed using the ptychography code of the beamline based on the ePIE algorithm [MR09]. The pixel size in the object plane was 3.2 nm.

Figure 4.2(a,b) shows the reconstructed and back propagated probe in the vicinity of the focus. The corresponding reconstructed object and probe can be found in the chapter 4.5.3.1in the supplementary materials. The focus is shown in Fig. 4.2(c-e) and has a FWHM of $8.4 \times 9.6\,\mathrm{nm}^2$. The FWHM was computed using the python `scipy.signal.peak_widths` [Vij+20]. The corresponding mean recorded detector field is shown in Fig. 4.2(f), showing the highly divergent beam. The focusing efficiency

Table 4.1: Basic parameters of the two beamline endstations where the experiments were performed. The distance of the detector to the MZP is defined as Δ_{Detector}. The focal length of the MZP is defined as f_{MZP} and the maximum distance between the OSA and the focus of the MZP is defined as $\Delta_{\text{OSA-focus}}$. The size of the OSA is given by D_{OSA}.

Beamline	E	monochromator	prefocus	Δ_{Detector}	f_{MZP}	$\Delta_{\text{OSA-focus}}$	D_{OSA}
P10-GINIX	13.8 keV	Si(111) pair channel-cut	CRL	5.10 m	0.92 mm	0.44 mm	3.5 µm
P06-Nanoprobe	15.0 keV	Si(111) pair channel-cut	CRL	3.43 m	1.00 mm	0.18 mm	3 µm

of the fully illuminated MZP was determined to be 7.3 %.

Note that the photon-flux density of the back-propagated probe is not evenly distributed, since the limited commissioning beam time did not allow for better alignment of the MZP. Nevertheless, the distance between the OSA and the focus is fairly short ($< 180\,\mu m$), preventing the alignment of the nanowire device for XBIC measurements due to bond wires protruding from the substrate.

The measurements were compared with simulations, which were performed using a finite differences (FD) solver [MS17] in three dimensions. Dynamical diffraction effects such as multiple diffractions and volume effects were considered. The parameters of the simulated MZP were equivalent to the specifications of the MZP used in the XBIC experiment. The far-field pattern shows the strongly divergent beam (see Fig.4.2(g)) and is similar to the far-field pattern measured in the experiment (see Fig.4.2(f)). While the diffracted photons are distributed over the full detector, the non diffracted photons are detected in only one pixel, which in a real detector pixel would result in beam damage, showing the necessity of apertures or beamstops. A characterization of the simulated focal spot gives a FWHM of $5.9 \times 5.9\,nm^2$ (see inset Fig. 4.2(g)). Thus, the simulations give a similar focus size as the outermost zone width, and agree reasonably well with the measurements. The difference can be attributed to the slight misalignment already mentioned, as well as to possible local manufacturing deviations from the ideal shape.

4.3.2 Beam characterization with off-axis illuminated MZP

The beam characterization of the off-axis illuminated MZP was performed at the `GINIX` endstation at the P10 beamline. The scan for ptychography reconstruction was done with 41×41 scan points and an 1.0 s acquisition time per frame. For reconstruction our own ptychography code based on the ePIE [MR09] algorithm was used. The pixel size in the object plane was 3.0 nm. The star shaped test structure on the Si_3N_4-window of the nanowire device was used as a sample. Figure 4.3(a,b) show the reconstructed and back propagated probe. Whereas the off-axis illumination in the vertical direction is only marginal visible (see Fig. 4.3(b)), the horizontal angle of the beam relative to the initial beam axis is clearly visible (see Fig. 4.3(a)).

The corresponding reconstructed object and probe can be found in the chapter 4.5.3.2 in the supplementary materials. The focal spot has a FWHM of $16.2 \times 27.9\,nm^2$ (see Fig. 4.3(c-e)). The reconstruction reveals an astigmatism based on a small misalignment of the focused x-ray beam. The difference in the focal plane positions in the vertical

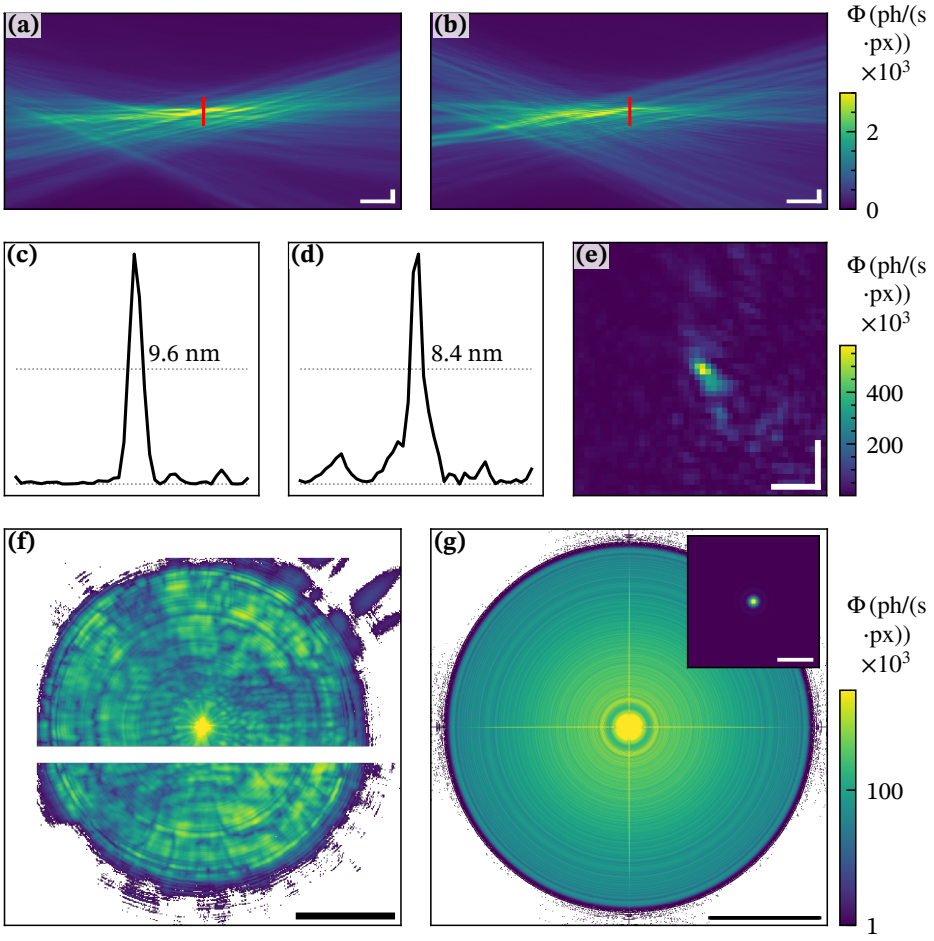

Fig. 4.2: Ptychographic reconstruction of the fully illuminated MZP. The pixel size was 3.2 nm. (a,b) Back-propagated wave fields. (c,d) Line profiles showing a FWHM of 8.4 nm × 9.6 nm. (e) Intensity distribution in the focal plane. (f) Measured mean far field intensity. The white bar is due to a detector gap. (g) Far field intensity distribution obtained by FD-simulations. The inset shows the simulated focal spot with a FWHM of 5.9 nm × 5.9 nm. The color bar of (f,g) is scaled logarithmically. Scalebars: (a,b) vertical 50 nm, horizontal 10 µm, (c-e) 25 nm, (f,g) $q = 0.26\,\mathrm{nm}^{-1}$, inset (g) 25 nm.

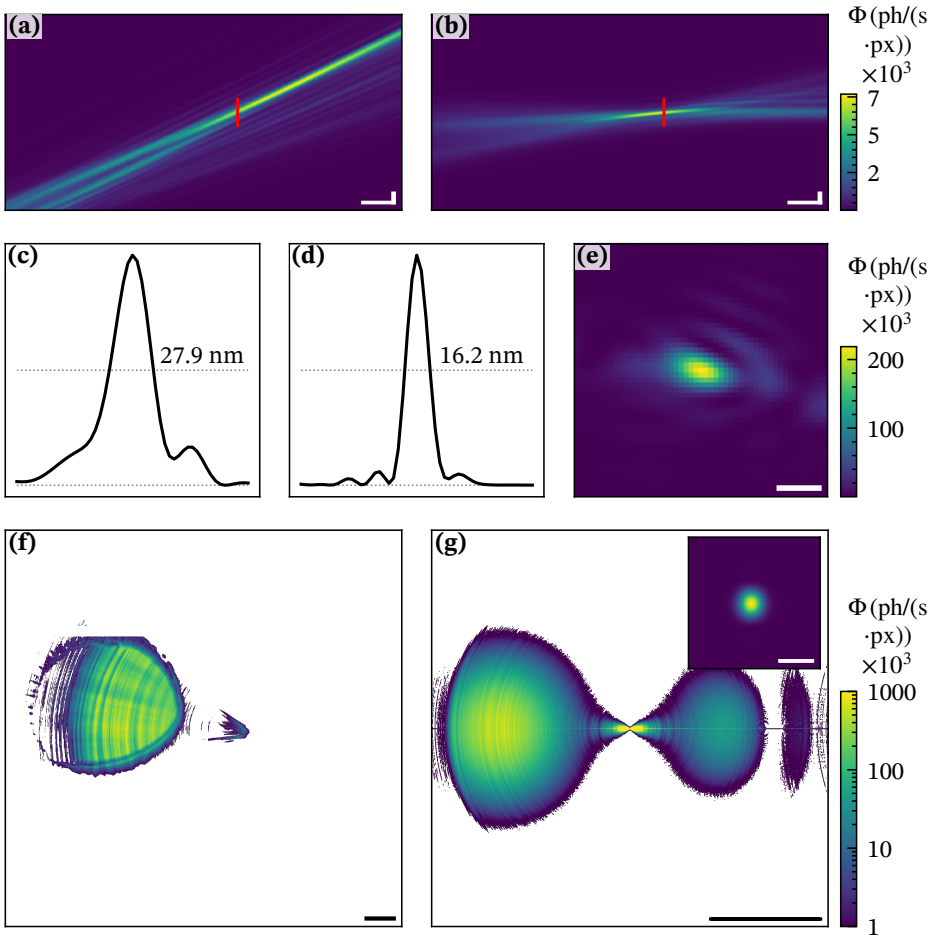

Fig. 4.3: Ptychographic reconstruction of the off-axis illuminated MZP. The pixel size was 3.0 nm. (a) and (b) Back-propagated wave field. (c) and (d) Line profiles from the same plane showing a FWHM of 16.2 nm × 27.9 nm and (e) Intensity distribution in the focal plane. (f) Measured mean far field intensity distribution. (g) Far field intensity distribution obtained by FD-simulations without apertures. On the left side the focused beam of the positive first order is seen, while on the right side the divergent beam of the negative first order. The inset shows the simulated focal spot with a FWHM of 12.1 nm × 15.4 nm. The color bar of (f,g) is scaled logarithmically. Scalebars: (a,b) vertical 50 nm, horizontal 10 µm, (c-e) 25 nm, (f) $q = 0.10\,\mathrm{nm}^{-1}$, (g) $q = 0.26\,\mathrm{nm}^{-1}$, inset (g) 25 nm.

and horizontal directions can be estimated from Fig. 4.3 (a) and (b) to be $\sim 16\,\mu m$. The corresponding mean detector image is shown in Fig. 4.3(f). The focused and thereby enlarged beam can be seen on the detector (left side) separated from some residual photons on the initial beam axis (center). The focusing efficiency of the off-axis illuminated MZP was determined to be 8.4 %.

Equivalent to the fully illuminated MZP, FD-simulations were performed for the off-axis illuminated MZP. In Fig. 4.3(g) the simulated far-field diffraction pattern is shown. In the left part of the far-field area the diffraction pattern of the positive first order can be seen, which generates the focal spot. In the right part the negative first order is visible and in between the non-diffracted photons of the zeroth diffraction order. The latter two diffraction orders justify the need for the OSA, and are therefore not visible in the measured detector image in Fig. 4.3(f). In contrast to the fully illuminated MZP, the pattern of the negative and positive diffraction orders do not overlap and can be distinguished.

The simulated focal spot has a width of $12.1 \times 15.4\,nm^2$. The difference compared with the measured data can be explained by the astigmatism of the beam. Nevertheless by using the off-axis illumination of the MZP the distance between the OSA and the sample was more than doubled, enabling the alignment of the nanowire device in the focal plane.

Before analysing the XBIC measurements, other off-axis x-ray optics will be addressed for comparison. KB-mirrors are the most common off-axis optics for hard x-rays which focus the incoming beam by total reflection and obtain thereby high focusing efficiencies. Since their surface roughness is quite sensitive KB-mirrors are usually stored in vacuum tanks, which are permanently installed. To compensate for side maxima of the focus, KB-mirrors are often used in combination with apertures. Unlike diffractive optics, KB mirrors cannot be used for direct imaging and are therefore only used for probing the sample. The focus size of KB-mirrors is limited by the critical angle of reflection which can only be overcome by coating the mirrors with a multilayer structure. Using a coated KB mirror a focus of $12 \times 13\,nm^2$ at an x-ray energy of 33.6 keV was achieved [Ces+17]. But, the efficiency of diffractive multilayer optics can be further improved by using a wedge geometry, where all layers are tilted according to the Bragg-law. As a result, the focusing efficiency is no longer limited mainly by the diffraction efficiency itself, but only by the absorption within the multilayer optics [Yan+07]. First characterizations of wedged multilayer optics in one dimension has been performed, resulting in an efficiency of 69 % [Baj+18]. For off-axis MZPs

Fig. 4.4 ***(next page)*:** High-resolution XBIC maps using the off-axis illuminated MZP with a step size of 20 nm. (a) STXM image of a single nanowire device. Next to the STXM image is a schematic of a nanowire roughly indicating the doping segments. (b) XBIC maps from the sketched red square in (a), using different x-ray fluxes of a transmission of 0.6 %, 2.5 %, 17.2 %, and 100 % of the maximum x-ray photon flux ($\Phi = 2.41 \times 10^7$ ph/s). Scalebars: 250 nm. The horizontally dashed lines indicate the doping junctions. (c) Axial and radial XBIC profiles, in logarithmic scale. (d) XBIC maps at different applied biases using $\Phi = 4.14 \times 10^6$ ph/s .(e) Axial and radial XBIC profiles, extracted from the XBIC maps in (d). Scalebars: 250 nm.

manufactured in the future, the already tilted geometry can be changed to a wedge geometry, to further increase the focusing efficiency.

4.3.3 Characterization of the nanowire device

XBIC has been used to investigate the nanoscale carrier dynamics in many types of semiconductors, using established x-ray focusing methods [Zap+20; Cha+19a; Stu+17]. The spatial resolution is limited by the x-ray focus size, reaching around or slightly below 50 nm with established optics, and it is highly desirable to base XBIC on novel high-resolution optics such as MZPs. Therefore, the off-axis illuminated MZP was used to investigate single contacted p-i-n doped InP nanowire devices using XBIC at the P10-`GINIX` instrument. The nanowires were similar to the devices in our previous publication [Cha+19a], and were synthesized at Lund NanoLab, Lund University, Sweden, for advanced solar cells [Otn+18]. We used the above-mentioned investigations to validate the present XBIC measurements using the new off-axis MZP configuration. The nanowire diameter is 180 nm, with a length of $\sim$ 3.3 µm. The nanowires themselves consist of three differently doped segments (p,i,n) which have a length of about 1.1 µm, see Fig. 4.4(a). Nanowires were transferred from the growth substrate onto a pre-defined Si_3N_4 membrane substrate. Then, they were turned into a single contacted nanowire device using electron beam lithography and metal evaporation [Cha+19a].

The geometry and sample we used allowed simultaneous collection of scanning transmission x-ray microscopy (STXM) and XBIC maps. Figure 4.4(a) shows a STXM image and Fig. 4.4(b) shows the corresponding 2D-XBIC maps at different photon fluxes (step size 20 nm, 0.1 s per point, fly-scan). The two contacts and the nanowire are resolved, and the sketch and the dashed lines indicate the segment junctions. Most of the XBIC signal (I_{XBIC}) was detected within the intrinsic middle segment of the

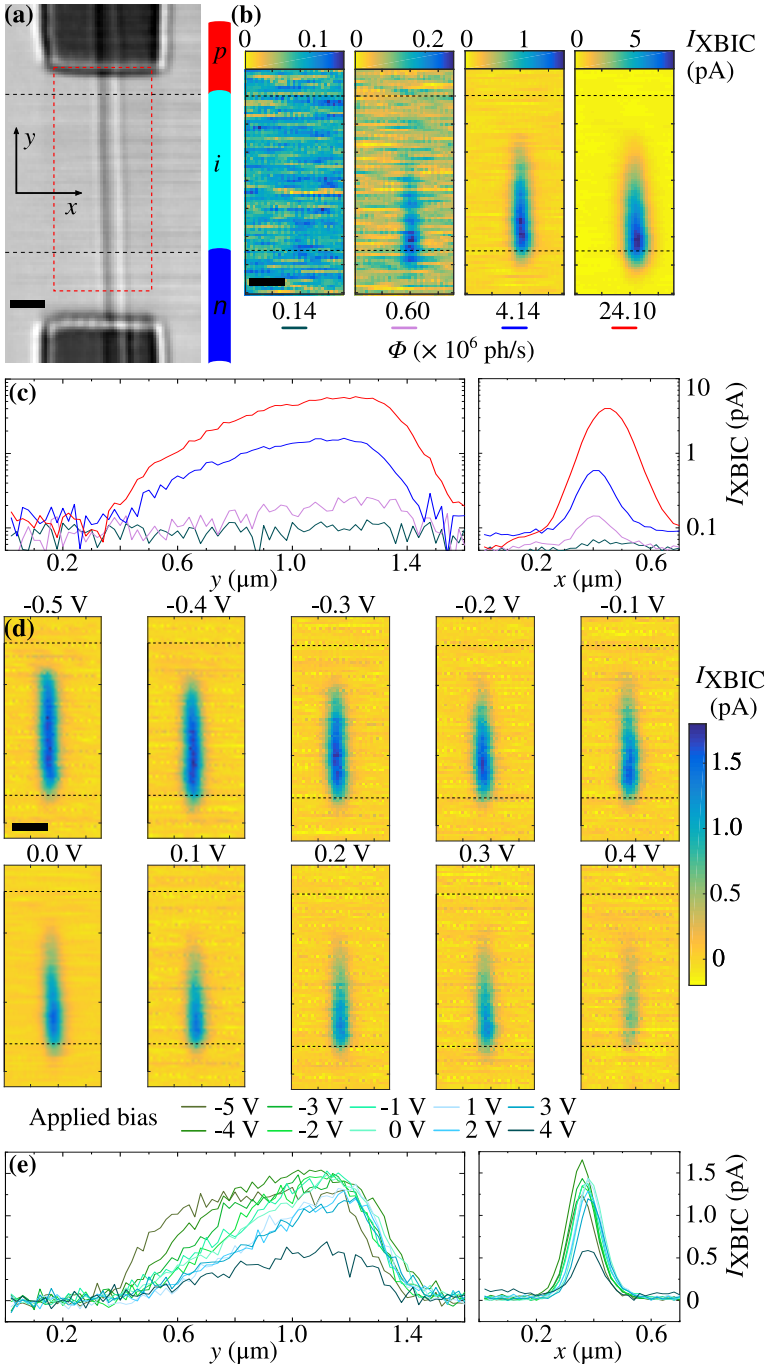

Fig. 4.4: *(caption previous page)*

nanowire (see Fig. 4.4(b)), where there is a build-in electric field as a result of a depletion region. The x-ray flux variation measurement was performed at zero bias (0 V). The transmission, T, of 0.6 %, 2.5 %, 17.2 %, and 100 % of the maximum x-ray photon flux ($\Phi = 2.41 \times 10^7$ ph/s) was changed by using attenuation filters. Φ was measured with the photon counting pixel detector.

We extracted the profiles of the integrated I_{XBIC} in the axial (z-axis) and radial (y-axis) directions of the nanowire, shown in Fig.4.4(c) and (e), respectively. The axial I_{XBIC} profile in Fig.4.4(c) is similar to our previous report [Cha+19a]. The characteristic decay length of the slopes on both sides (left $\sim$ 500 nm, and right $\sim$ 120 nm) of these profiles corresponds to the charge transport within the nanowires [Moh+12; Gut+12]. The longer decay on the left slope is the result of the gradient p-i junction caused by the memory effect during the nanowire growth [Cha+19a]. Our previous investigations analyzed these axial profiles in detail, while the spatial resolution was insufficient for the radial direction. Here, we can reveal I_{XBIC} profiles in the radial direction of the nanowire with several data points in Fig.4.4(c). These radial profiles at different Φ were fitted with the Gaussian distribution function in which their full-width-half-maximum ($\mathrm{FWHM}_{\mathrm{XBIC}}$) almost linearly increases with I_{XBIC} (see chapter 4.5.8 in the supplementary materials). The measured $\mathrm{FWHM}_{\mathrm{XBIC}}$ are lower than the nanowire diameter, which may seem unreasonable. However, the XBIC signal is reduced by secondary photons and electrons that escape the sample [Cha+19a; Stu+15], and this effect is stronger near the surface of the nanowire.

The XBIC signal depends on the local electric field, which can be systematically varied by applying an external bias [Cha+19a]. Therefore, we performed bias dependent XBIC measurements using $\Phi = 4.14 \times 10^6$ ph/s ($T = 17.2\,\%$). Figure 4.4(d) shows the XBIC maps of the nanowire, at applied biases ranging from -0.5 V to 0.4 V , while Fig.4.4(e) shows the axial and radial profiles. Generally, I_{XBIC} increased from forward bias to reverse bias, similar to our previous investigations [Cha+19a]. The maximum I_{XBIC} saturates at negative bias, as is most clearly observed in the axial and radial I_{XBIC} profiles in Fig.4.4(e). The reverse bias enhances the built-in electric field in the diode, and it becomes so strong that all generated carriers are collected. The opposite effect is observed with forward bias, where the reduced electric field in the depletion region leads to a lower charge collection efficiency (CCE). Moreover, the XBIC area is reduced along the axial direction and shifted toward the n-segment (see Fig.4.4(d)). Measurements using XRF [Tro+18] as well as the computer simulations [Cha+19a] show that an unintentional p-doping in the middle segment causes this asymmetric change of the XBIC area. Here, we can observe a complete two-dimensional charge

collection map of a single nanowire using the high-resolution MZP optics.

As a comparison, XBIC scans using a fully illuminated MZP without a central stop and an OSA can be found in chapter 4.5.9.1 in the supplementary materials. The measurements using the off-axis illuminated MZP benefits from a constant background independent of the applied voltage, absent of background photons, which allows the use of an uniform color scaling. With the fully illuminated MZP without a central stop and an OSA, the background signal is changing between the scans. Further, despite the nominally higher resolution of a fully illuminated MZP, the corresponding XBIC maps of the nanowire have a lower resolution due to photons coming from different diffraction orders (see chapter 4.5.9.1 in the supplementary materials).

4.3.4 Mapping the MZP focus with the nanowire device

Nanowire diodes are sufficiently small to be used as single pixel detector at a far better resolution than conventional detectors. We have previously used nanowire devices to map the Kirkpatrick-Baez mirror focus at the P10-`GINIX` [Wal+14b] and the NanoMax [Cha+20] beamlines. Here, the nanowire device was used to map the MZP beam path by using it as an 1D detector, in the direction across the nanowire. Figure 4.5(a) shows the beam path of the focused x-rays along the z-axis (propagation direction) and x-axis (horizontal plane). The map was recorded by scanning a vertical nanowire along both axis and performed using the off-axis illuminated MZP. The illumination time was 0.1 s, the step size in z-direction was 2 µm and the step size in x-direction was 10 nm again in fly-scan operation. An equivalent measurement using a fully illuminated MZP without a central stop and an OSA can be found in the chapter 4.5.9.2 in the supplementary materials. The XBIC measurements of the beam path focused by the off-axis illuminated MZP resolves the divergent angle of the beam relative to the beamline orientation, the rising intensity in the vicinity of the focus and a small side maximum in the focal plane. Also, it shows a decrease in the XBIC signal on the left side where the nanowire is no longer in the focal plane. Further, along the beam path small movements of approx. 20 nm of the beam relative to the nanowire can be observed.

The measured XBIC line profile can be calculated as the convolution of the nanowire profile with the x-ray beam. Figure 4.5(b) shows the calculated convolution for a 180 nm nanowire profile with the ptychographically reconstructed x-ray beam shown in Fig.4.3(c). The XBIC measurement and the convolution are in good agreement. The convolution shows a divergence and a rising side maximum which is also apparent in

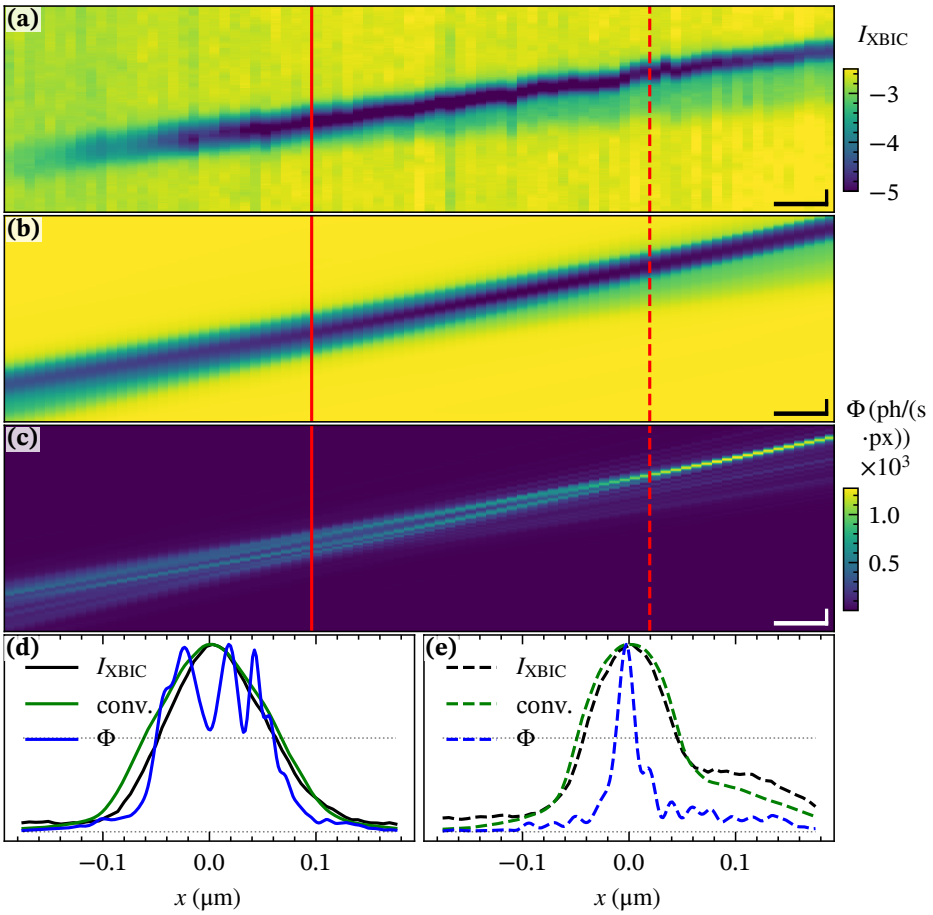

Fig. 4.5: Comparison of the x-ray beam path using XBIC and ptychography. (a) XBIC measurement of an off-axis illuminated MZP with apertures. (b) Convolution of the ptychographically reconstructed probe with a nanowire profile. (c) The corresponding ptychographic reconstruction. Dashed line is plane of focus, solid line is plane of measurement. (d) Line profile in the focus plane and (e) the measurement plane. Scalebars (a-c) vertical 100 nm, horizontal 10 µm, (d,e) 100 nm

the XBIC measurement. A 2 mrad difference in the beam path angle can be related to a misalignment of the motor x-axis relative to the beam. The corresponding beam profile in the ptychographic focal plane is shown in Fig. 4.5(e). Nevertheless, the limit in resolution of the nanowire detector with respect to the very small focus from the MZP becomes apparent, which makes it challenging to determine the focal plane using only the XBIC-measurements. The comparison of the XBIC measurement and the subsequently performed ptychographic measurement shows that the nanowires were not measured in the optimal focal plane, but at a distance of 64 µm from it. In Fig. 4.5(d) the beam profile in this plane is shown with a width of 192 nm based on the ptychographic reconstruction. This corresponds to the width of the nanowire (180 nm) and its resolution threshold, being the reason for the incorrectly chosen measurement plane.

Although ptychography provides higher resolution in determining the probe, several constraints must be met for a successful reconstruction, such as coherence, compactness, sampling and high stability. As a result, ptychography is limited to dedicated setups and beamlines. In contrast the XBIC method measures photons directly in the object plane. In the present case, the orientation of the nanowire led to a limited spatial resolution and a weak signal. We have recently demonstrated that much better spatial resolution can be achieved by orienting the nanowire parallel with the beam [Cha+20]. This increases the resolution to 60 nm together with the photon sensitivity, since the absorption length is now given by the nanowire length rather than the diameter.

4.4 Conclusion and outlook

We have presented a new approach to implement an 2D focusing optics in an off-axis geometry, with the main advantage of more than doubling the useful working distance to the sample. The focus size of the off-axis illuminated MZP was determined with a FWHM of 16.2×27.9 nm. Even though the focus is larger than that of a fully illuminated MZP (8.4×9.6 nm), the increased distance to the nearest OSA is what makes it possible to perform experiments with complex samples in the focal plane in the first place. Thereby experiments to measure the XRF, STXM or XBIC signal with a small focus size and with a low background signal become possible. MZPs (and MLLs) have a very short focal depth, whether classic or off-axis, which makes optimal sample alignment challenging. Our results show that “real-time” ptychographic measurements can be very helpful in sample alignment.

In addition, the focus of an off-axis illuminated MZP can be further reduced if the area of illumination and thereby the NA is increased. In the case of the experiment performed, a large part of the MZP was not illuminated and therefore a large part of the possible NA was not used. An illumination of ellipsoidal shape using a larger area could increase the NA and would still result in a separation of the focused beam and the initial beam axis. However, to gain the full benefits of an off-axis illuminated MZP, specially designed off-axis MZPs should be fabricated. A specially designed off-axis MZP would have the advantage that the area which needs to be fabricated is reduced to only one side of the MZP. This enables the fabrication of larger optics with a smaller focal spot size, or alternatively, a larger focus length. An example simulation of a dedicated off-axis MZP with a focal length of 1.84 mm is provided in Fig. 4.9 in chapter 4.5.4 in the supplementary materials. The size of the resulting focal spot is $9.0 \times 10.5\,\mathrm{nm}^2$, whereby fabrication details are similar to current specifications, especially with regard to total size and outermost zone width.

The focused off-axis beam was used to perform a mapping of the charge carrier distribution using XBIC. The measurements benefited from a low background signal. We were able to perform for the first time a two dimensional mapping of the area of InP nanowires charge carrier collection under various flux and applied bias settings (see Fig. 4.4). By optimizing the MZP optics and sample alignment, it should become feasible to acquire XBIC maps at a spatial resolution of less than 10 nm. This is substantially better than electron-beam methods, which suffer from an inherent broadening due to electron-electron scattering [Stu+15]. The low background of the off-axis MZP approach also makes it highly suitable for x-ray fluorescence, x-ray diffraction and STXM, signals that in principle can be acquired simultaneously [Cha+19b]. The longer working distance could also allow more complex in situ and operando studies. The off-axis MZP is well suited for the current upgrades of synchrotron radiation sources to diffraction limited storage rings. Altogether, this opens a brilliant perspective for ultrahigh resolution multimode imaging of nanostructures.

Acknowledgements

We thank Christian Eberl for the fabrication and Mike Kanbach for the the mounting of the MZPs, Tim Salditt for continuous support and fruitful discussions, and Michael Sprung and Fabian Westermeier for help at the beamline P10. And we thank Magnus Borgström for the nanowire growth. Further we thank Martin Seyrich, Dennis Brückner and Johannes Hagemann for help at the beamline P06.

Funding

This project was funded by the Röntgen Ångström Cluster, grant number 2015-06125, by Deutsche Forschungsgemeinschaft, grant number SFB 755, by Bundesministerium für Bildung und Forschung, grant number 05K19MG2, as well as the Olle Engkvist foundation, NanoLund, and Marie Sklodowska Curie Actions Cofund, Project INCA 600398. This project has received funding from the European Research Council (ERC) under the European Union's Horizon 2020 research and innovation program (grant agreement No 801847).

4.5 Supplementary materials

4.5.1 P10-GINIX setup (more detailed)

The experiment using the off-axis illuminated MZP was performed at the Göttingen instrument of nano-imaging with x-rays (GINIX) at the coherence beamline P10 of the PETRA III storage ring (Hamburg, Germany) [Sal+15]. The beamline uses a 5 m long undulator positioned at a distance of 88.5 m from the experimental hutch. In the described experiment the undulator beam was monochromatized to 13.8 keV using a Si(111) channel-cut monochromator. The monochromator is positioned at a distance of 50 m from the experimental hutch. Using compound refractive lenses (CRL) installed in an ultra-high vacuum chamber in the experimental hutch the beam is pre-focused to about 16 µm in horizontal and vertical direction. The focal length of the used CRLs is about 1.9 m. A detailed analysis of the CRL efficiencies can be found in [Zoz+14]. The MZP and the nanowires are mounted on the high-resolution stage of the GINIX instrument. The sample stage is motorized using piezo scanner by Physik Instrumente Karlsruhe (PI), the MZP stage by stick-slip positioners by SmarAct (Oldenburg) for translations, and a piezo-driven Gimbal mount for rotations. For detailed information on the stability and scanning precision see [Ost+17a]. The pinhole and the OSA were mounted on piezo scanners by SmarAct (Oldenburg). The diameter of the pinhole was 5.6 µm, the diameter of the OSA was 3.5 µm. The distance of the OSA relative to the focus was 0.44 mm.

At a distance of 5.1 m behind the sample the detector was positioned. A single photon counting Eiger 4M (Dectris Ltd., Switzerland) detector was used with 2068×2162 pixels with a pixel size of 75 µm.

4.5.2 P06-Nanoprobe setup (more detailed)

The experiment using the fully illuminated MZP was performed at the PtyNAMI instrument [Sch+20] of the Hard x-ray Micro/Nano-Probe at the beamline P06, which is positioned at the PETRA III storage ring. The beamline uses a 2 m long undulator positioned at a distance of 97.5 m from the nanohutch where the experiment was preformed. The undulator beam was monochromatized using a Si(111) channel-cut monochromator to 15 keV. The monochromator is positioned at a distance of 59.1 m from the nanohutch. The distance of the CRLs to the nanohutch is 54 m. Using the PtyNAMI instrument the pinhole, OSA, MZP and sample were mounted on piezo stages by SmarAct (Oldenburg). The diameter of the central stop was 6 µm, the diameter of the OSA was 3 µm. The distance of the OSA relative to the focus was 0.25 mm.

The diffraction patterns were recorded at a distance of 3.43 m relative to the sample using a single photon counting pixel detector (Pilatus 300k, Dectris Ltd. Switzerland). The detector has 619×487 pixels and a pixel size of $\Delta_{\mathrm{px}} = 172\,\mu\mathrm{m}$.

4.5.3 Ptychographic reconstructions

4.5.3.1 Fully illuminated MZP

The probe of the fully illuminated MZP was characterized using ptychography. The measurement was performed at the P06-Nanoprobe beamline [Sch+16], as described in the manuscript. A scan was performed with 25×51 scan points and an illumination time per frame of 0.2 s. As a sample a Siemens star was used with a smallest feature size of 50 nm. The Siemens star was positioned at a distance of 70 µm relative to the focus. For the reconstruction the ptychography script of the beamline was used. The script is based on the ePIE algorithm [MR09]. In Fig. 4.6 the results of the ptychographic reconstruction are depicted. In (a) the probe in the object plane, in (b) the phase of the object and in (c) the absorption of the object is shown. The smallest features of the object are well resolved. Further sub-structures are visible in the center of the Siemens star. These sub-structures are not an artifact from the reconstruction process, but real and due to beam damage resulting from a previous experiment.

4.5.3.2 Off-axis illuminated MZP

The probe of the off-axis illuminated MZP was characterized using ptychography. The measurement was performed at the P10-`GINIX` beamline [Kal+11], as described in the

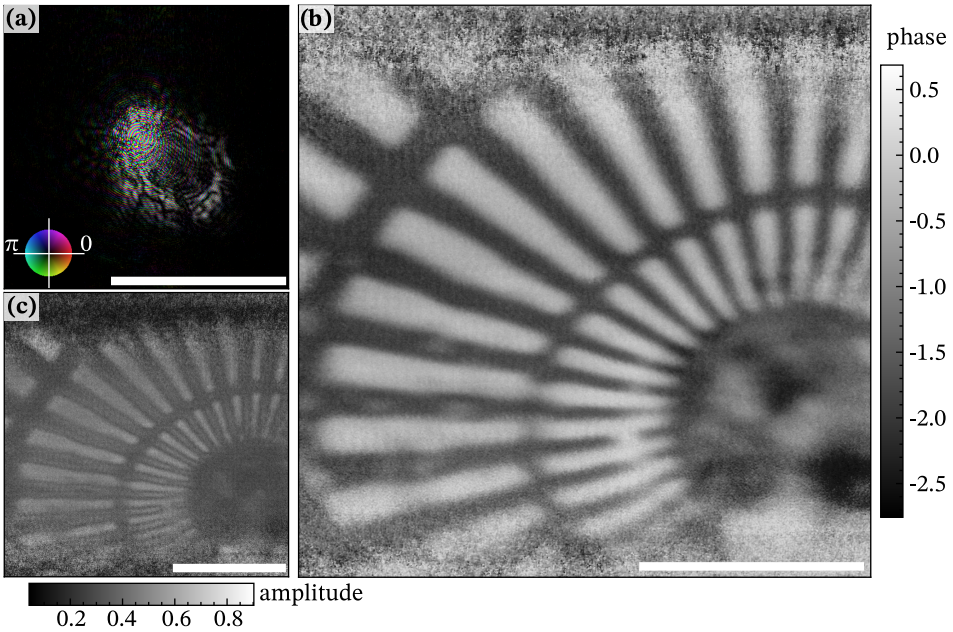

Fig. 4.6: Characterization of the fully illuminated MZP using ptychography. Ptychographic reconstruction of (a) the probe amplitude and phase in the sample plane. (b) The object phase and (c) the object amplitude. The object was a Siemens star with 50 nm smallest feature width. The sub-structures visible in the center of the Siemens star are not artifacts from the reconstruction process, but real structures due to beam damage from a previous experiment. Scalebars: 1 μm

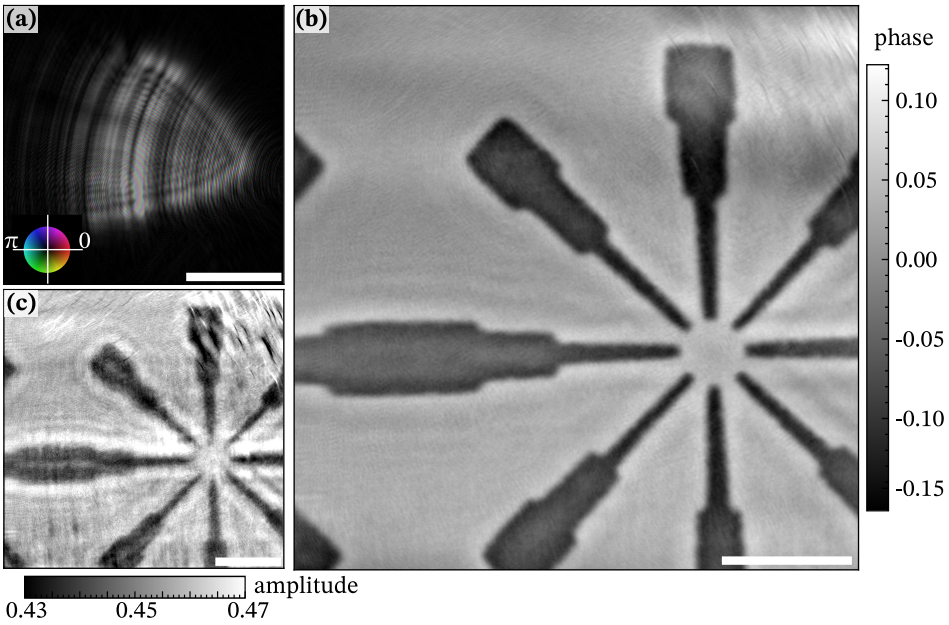

Fig. 4.7: Characterization of the off-axis illuminated MZP using ptychography. Ptychographic reconstruction of (a) the probe amplitude and phase in the sample plane. (b) The object phase and (c) the object amplitude. The object was a test pattern with 100 nm smallest feature width. Scalebars: 1 µm

manuscript. A scan was performed with 41×41 scan points and an illumination time per frame of 1.0 s. A lithographic test pattern with smallest structure size of 100 nm was used as a sample. The sample was positioned at a distance of 350 µm relative to the focus. The diameter of the beam in this plane was about 1.75 μm^2. For reconstruction our own ptychographic script was used. The script is based on the ePIE algorithm [MR09]. In Fig. 4.7 the results of the ptychographic reconstruction are depicted. In (a) the probe in the object plane, in (b) the phase of the object and in (c) the absorption of the object is shown. The smallest features of the object are well resolved. The shape of the probe is quiet similar to the shape measured at the detector. This is due to the relative large distance between the focus and the object.

4.5.4 Finite difference simulations

Simulations were performed to estimate the focusing properties of an MZP with the exact specifications as the one used in the experiments at the P10-GINIX instrument.

The parameters of the simulated MZP were: 0.92 mm focal length, 784 zones, first inner zone number 14 (equivalent to a diameter of 2.1 µm) 5 nm outermost zone width, 15.6 µm radial size, 2.4 µm optical thickness and a tilting angle of 2.5 mrad. The energy of the illumination was 13.8 keV. The simulations were based on a finite differences (FD) solver [MS17]. To account for the circular shape of the MZP the simulations were performed in three dimensions. The numerical grid parameters were $\Delta_{x,y} = 1$ nm and $\Delta_z = 10$ nm for the lateral and the propagation directions, respectively. In Fig. 4.8(a) the beam profile of an MZP fully illuminated by a plane wave is shown. No apertures (central stop and OSA) was simulated. This results in a background signal by the non-diffracted photons. In the inset the lateral extension of the focus is shown. The FWHM of the focus is $5.9 \times 5.9\,\text{nm}^2$. This is inline with the smallest outermost zone size of 5 nm. In Fig. 4.8(b) the far-field diffraction pattern can be seen. In the far-field pattern the non-diffracted photons are in the center pixels. The photons diffracted in the first positive and negative orders are distributed over the entire far-field. The diffraction patterns of both orders overlay each other and are therefore indistinguishable.

Next, the illumination of the MZP by an off-axis beam was simulated in the same configuration. The initial beam has a Gaussian shape with an FWHM of 4 µm and a lateral off-axis position of 6 µm. The propagation of the beam behind the MZP is shown in Fig. 4.8(c). Again no apertures (pinhole and OSA) were simulated. In the inset the focus extension in lateral dimension is shown. The FWHM of the focus is $12.1 \times 15.4\,\text{nm}^2$. The separation of the focus and the non-diffracted beam can be seen. A sample which would be positioned in the focus would not be penetrated by background photons. In Fig. 4.8(d) the far-field diffraction pattern of the simulated off-axis beam is shown. The photons diffracted in the plus first order are in the lower part, the photons of the negative first diffraction order are in the upper part and in the center the non-diffracted photons. In an actual experiment the photons of the non-diffracted beam and the first negative order would not be visible due to the positioning of the OSA. The difference in the size of the area of the photons diffracted in the negative and positive order, is due to the tilting of the individual zones and therefore different diffraction efficiencies.

Whereas the simulations in Fig. 4.8 are based on the specifications of an MZP which was already fabricated, is a potential dedicated off-axis MZP shown in Fig. 4.9. Since the total deposition process stability is the bottle neck in the fabrication of larger MZPs, the fabrication of an MZP with larger focal length is challenging. But by fabricating an MZP with zones on only one side, the deposition time per zone could be decreased and thus the total number of zones increased. The dedicated off-axis MZP simulated here

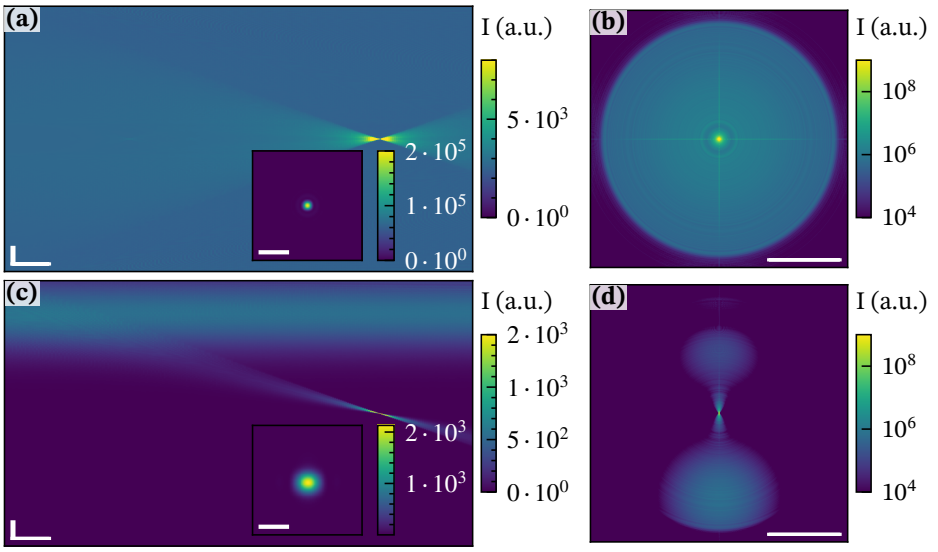

Fig. 4.8: Results of FD-simulations in three dimensions. (a) Shows the propagating wave field behind a fully illuminated MZP. At a distance of 1 mm the focus can be seen. The non-diffracted photons are generating a background signal. The inset shows the focal spot in its lateral extension. The focus has a FWHM of $5.9 \times 5.9\,\mathrm{nm}^2$. The corresponding far-field is shown in (b). (c) shows the propagating wave field behind an MZP illuminated by an off-axis Gaussian shaped beam. The focus at a distance of also 1 mm is clearly separated from the non-diffracted photons. The focus has a FWHM of $12.1 \times 15.4\,\mathrm{nm}^2$ and is shown in its lateral extension in the inset of the figure. The corresponding far-field is shown in (d). The positive and negative orders are separated and not overlapping. Scalebars: (a,c) vertical 100 µm and horizontal 1 µm, the insets 25 nm (b,d) $q = 0.26\,\mathrm{nm}^{-1}$

has the following parameters: 1568 zones (twice the number of zones as produced so far), 1.84 mm focal length, 5 nm outermost zone width. The size of the Gaussian shaped illumination was 15 µm with an off-axis position of 12 µm. The simulated beam path is shown in Fig. 4.9 with a focus FWHM of $9.0 \times 10.5\,\mathrm{nm}^2$ (see inset) positioned 1.84 mm behind the MZP, which is twice the length as the MZPs used in the described XBIC experiments. Conversely, it would also be possible to maintain the focal length but reduce the focus size.

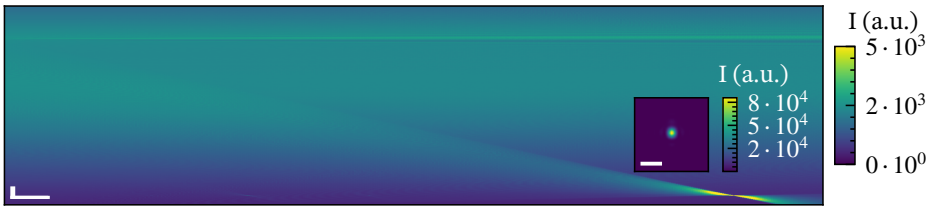

Fig. 4.9: Beam path simulation of a dedicated off-axis MZP with 1.84 mm focal length. This off-axis MZP has twice the number of zones compared to the MZP used in the experiment but is only one sided. The inset shows the lateral extension of the focus with $9 \times 10.5\,\mathrm{nm}^2$. Scalebars: vertical 100 µm and horizontal 1 µm, the inset 25 nm

4.5.5 Side maxima when center part is blocked

Figure 4.10 compares the height of the side maxima of a focus from a fully illuminated MZP with central stop and an off-axis illuminated MZP which has the same NA. As described by [SM84] for the case of round diffractive optics, focus side maxima increase the more zones in the center are not illuminated. Fig. 4.10 (a) shows the simulated focus of an MZP with the following parameters: photon energy 13.8 keV, focal length 0.92 mm, optical depth 2.5 µm, MZP diameter 16.5 µm, outer most layer width 5 nm, center stop diameter 8.24 µm. All layers are tilted according to the wedge geometry [Yan+07]. Fig. 4.10(b) shows the focus of an off-axis MZP with the same off-axis gap and the same diameter as the simulated MZP shown in (a). The only difference between the simulated MZP in (a) and (b) is the outer most layer width which is in case of (b) only 2 nm. This is due to the requirement for the simulation that both optics should have the same NA. The simulation were performed using the FD algorithm. In case of (a) the propagation of the field was simulated in a radial coordinate system [MS17], propagation step size was 10 nm and the lateral grid size was 0.1 nm. In case of (b) an 2D Cartesian coordinate system was used to simulate the propagation of the off-axis geometry. The simulation grid sizes were the same as in (a). The normalized focus profiles from (a) and (b) are shown in (c) for comparison. In case of the fully illuminated MZP with a central stop the side maxima have a height of 10.6 % of the maximum intensity of the focus, in contrast the side maxima peak height for the off-axis illuminated MZP is only 4.5 % of the maximum intensity. This result in a relative difference of the normalized side maxima by a factor of 2.31 between the off-axis illuminated MZP and the fully illuminated MZP. The large side maxima result in a reduced effective resolution of the focusing optic. Additionally, also the FWHM of the main focus is slightly smaller for the case of the off-axis illuminated MZP.

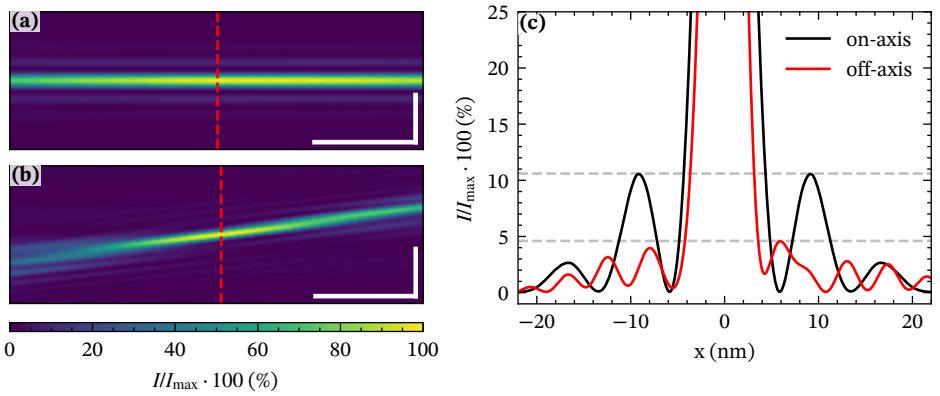

Fig. 4.10: Comparison of the focus side maxima for the case of (a) a full on-axis illuminated MZP with central stop and (b) an off-axis illuminated MZP. The NA of both configurations is the same with an illuminated area of 16.5 µm and a focal length of 0.92 mm at a photon energy of 13.8 keV. (c) the normalized intensity in the focal plane is plotted. In (a) and (b) the focal plane is indicated by the red dotted line. In (c) the height of the side maxima is indicated by the gray dotted line. The difference in the height is a factor of 2.3. Scalebars: (a,b) vertical 25 nm and horizontal 500 nm

4.5.6 Simulations of flat and tilted MZPs

Figure 4.11 shows the focal points of a flat MZP and the focal point of a tilted MZP. The intensity is normalized to the maximum intensity of the titled MZP. The focus was simulated using FD in a circular coordinate system [MS17]. The parameters of the simulated MZPs were: 0.92 mm focal length, 784 zones, 5 nm outermost zone width, 15.6 µm radial size, 2.5 µm optical thickness. The energy of the illumination was 13.8 keV. For the MZP in tilted geometry a tilting angle of 2.5 mrad was assumed. In Fig. 4.11(a,b) the intensity distributions of both focal points is shown with the same color scaling. The difference of the intensity of the focal spots is a factor of 2.9 as can be seen in the plotted focus profiles shown in Fig. 4.11(c). This demonstrates the improved focusing efficiency of an MZP based on the tilted geometry compared to an MZP in a flat geometry.

4.5.7 Comparison of on- and off-axis illuminated MZPs

A comparison of different central stop configurations of fully illuminated MZPs and configurations of off-axis illuminated MZPs is shown in Tab. 4.2. The comparison is performed regarding the focal spot size and the corresponding working distances

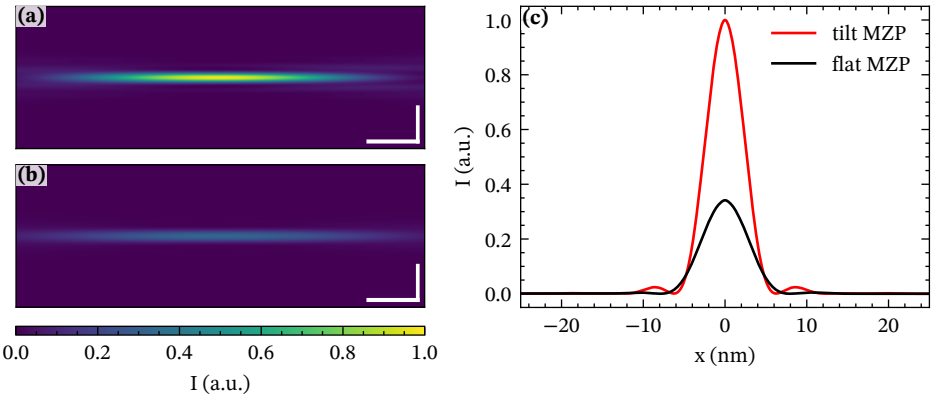

Fig. 4.11: Comparison of the focusing efficiency of an MZP in tilted and an MZP in flat geometry using FD-simulations. (a) shows the intensity distribution of the focus of a tilted MZP. (b) shows the equivalent intensity distribution of a flat MZP. In (a) and (b) the intensity is normalized by the peak intensity of the tilted MZP. (c) shows the focus profile of the flat and the tilted MZP. The maximum intensity of the flat and tilted MZP differ by a factor of 2.9. Scalebars: (a,b) vertical 25 nm and horizontal 0.5 µm

using finite difference simulations.

4.5.8 Flux dependence of the XBIC signal

In Fig.4.12(a) the maximum I_{XBIC} is plotted against the photon flux Φ, where the expected linear relation can be observed. Theoretically, I_{XBIC} can be estimated using the equation, $I_{\mathrm{XBIC}} = q\eta p_{|\Phi S(x,y,z)|}$, where q is the charge constant, η is the charge generation yield, $p_{|\Phi S(x,y,z)|}$ is the x-ray absorption probability, and $S\,(x, y, z)$ is the relative spatially dependent charge collection efficiency [Cha+19a]. The charge generation yield is the ratio between the energy of the x-rays, E, and the ionization energy of the semiconductor ϵ, so that $\eta = E/\epsilon$ [AB78]. In the case of a very thin sample, p_{abs} can be approximated from $p_{abs} = \mu d$, where μ is the absorption coefficient, and d is the thickness of the sample. At the maximum I_{XBIC} from the map, we can assume the maximum charge collection efficiency, and therefore $S\,(x, y, z) = 1$ [Cha+19a]. Consequently, I_{XBIC} as a function of Φ can be written as $I_{\mathrm{XBIC}} = 1.7062 \times 10^{-18} \cdot \Phi$ for the x-ray energy of 13.8 keV. This function is plotted in Fig.4.12 (a) as a red line. We can observe the difference between the maximum measured and the theoretically calculated I_{XBIC} from the plot in Fig. 4.12 (a). This low measured XBIC comparing to the calculation was evidenced before in the previous publication. In this experiment,

Table 4.2: Comparison of different central stop configurations of fully illuminated MZPs and configurations of off-axis illuminated MZPs. The NA of $8.7 \cdot 10^{-3}$ is equivalent to the fully illuminated MZP used for the experiments at 13.8 keV photon energy at the GINIX-P10 setup. D_{CS} is the size of the center stop, R_{off} is the radial off-axis position of the off-axis MZP. z_{WD} is the working distance between the focus and the OSA. A_{MZP}/A_{CS} is the area of the fully illuminated MZP which is covered by the central stop. In case of the off-axis illuminated MZP no central stop is required and therefore no area is covered. The focus FWHM d_{FWHM} was simulated using finite differences. It should be noted that additional parameters such as the intensity of the side maxima or in case of the on-axis illuminated MZPs with a central stop the flux density distribution, which is in most case of Gaussian shape, have an additional effect in selecting the best possible configuration for an experiment.

	MZP		off-axis MZP	
NA	$8.7 \cdot 10^{-3}$	$8.7 \cdot 10^{-3}$	$4.4 \cdot 10^{-3}$	$8.7 \cdot 10^{-3}$
D_{CS}	6 µm	12 µm	-	-
A_{MZP}/A_{CS}	86 %	44 %	-	-
R_{off}	-	-	6 µm	6 µm
z_{WD}	197 µm	276 µm	394 µm	251 µm
d_{FWHM}	4.8 nm	4.1 nm	8.0 nm	4.3 nm

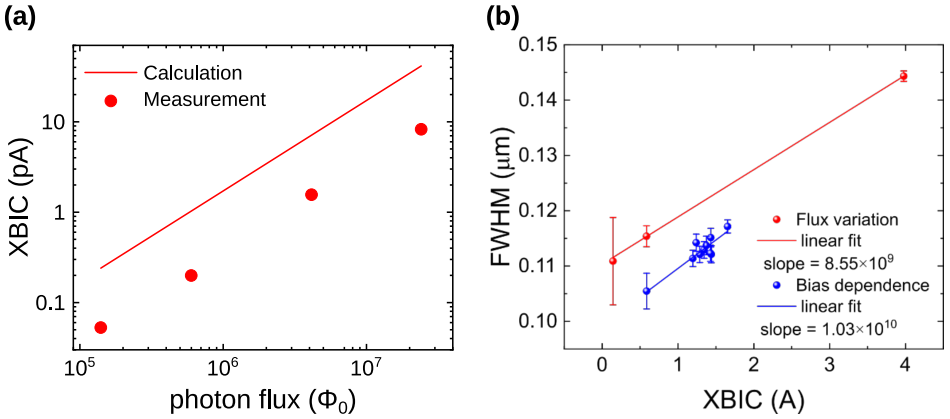

Fig. 4.12: (a) The plot of the maximum I_{XBIC} (red circle) and the calculated I_{XBIC} (red line) against the x-ray photon flux. (b) Comparisons of the different radial XBIC profiles. The FWHM of the radial XBIC profiles is plotted against the maximum XBIC signal from the x-ray photon flux variation and the bias-dependent XBIC measurements. The difference between the two measurements can be explained by variations in the intensity of the x-ray beam.

the measured I_{XBIC} is about 20 % of the theoretical calculation, which could attribute to the escaping of those secondary electrons from this nanostructure sample [Cha+19a; Stu+17]. Hence, we introduced the term for the new charge generation yield of the nanowire compensating the actual yield with the escaping secondary charges.

In Fig.4.12 (b) the radially profiles at different x-ray photon fluxes and bias-dependent XBIC measurements are compared. The profiles are fitted using the Gaussian distribution function and the full-width-half-maximum (FWHM) is defined. The FWHM increases almost linearly with the x-ray photon flux, respectively the XBIC signal. The same applies to the bias-dependent measurements.

4.5.9 XBIC by a fully illuminated MZP

4.5.9.1 Bias dependent measurements

Beside the XBIC measurements of the off-axis illuminated MZP described in the manuscript, measurements using a full-illuminated MZP at the P10 beamline were performed as well. Therefore the OSA (and the pinhole) were moved out of the beam, since the nanowire device needs more free space in the vicinity of the focus. For a fully illuminated MZP the maximum free space between the focus/sample and the

OSA would be below 180 μm, which is not enough for the positioning of the nanowire device.

Equivalent to the bias dependent measurements presented in the manuscript using an off-axis illuminated MZP, bias dependent measurements were performed using the fully illuminated MZP. The XBIC maps at different applied biases ranging from -0.5 V to 0.4 V with the increment of 0.1 V and are shown in Fig. 4.13. The scan was done with 20 nm step size and 0.1 s acquisition time. The I_{XBIC} presents the charge collection of the device. Just like in the figure in the main manuscript the range of the color bar is the same for all maps. For the fully illuminated MZP, this results in a bias dependent background signal. This is different for the measurements using the off-axis illuminated MZP presented in the main manuscript, where the color bar range is equal for all maps, and no bias-dependent background signal was observed.

Furthermore, in the case of the fully illuminated MZP, the shape of the nanowire XBIC signal, although similar, is much broader. This is contradictory at first, since the fully illuminated MZP produces a smaller focus. However this is due to the photons from different diffraction orders which also produce an XBIC signal, which then leads to the broadening of the nanowire signal.

This demonstrates for the case of the XBIC measurement in the described experiment, that the slightly larger focus of the off-axis MZP with OSAs and therefore negligible background photons is resulting in a better measurement as the smaller focus of the fully illuminated MZP without OSAs and therefore with a background signal.

4.5.9.2 Measurement of the beam path

Equivalent to the beam path characterization by using the nanowire device as an x-ray detector in the manuscript a second scan was performed using the fully illuminated MZP again with no apertures (central stop and OSA). The measured XBIC signal of the focused beam is shown in Fig. 4.14. Only few photons are detected in the region of the center, where the first zones are missing due to the glass wire. Similar to the measurement of the off-axis MZP a small miss alignment ($\approx$ 0.6 mrad) of the motor-axis relative to the propagation direction of the beam can be seen. Most photons are detected along the diffraction angles of 4.8 mrad. According to literature the best diffraction efficiency in the direction of the focus is achieved when the zones are tilted by half the diffraction angle [Yan+10]. This is consistent with the results measured with the nanowire instrument, as the zones of the MZP are tilted by $\approx$ 2.5 mrad.

From the XBIC measurement it is challenging to determine the size of the focus

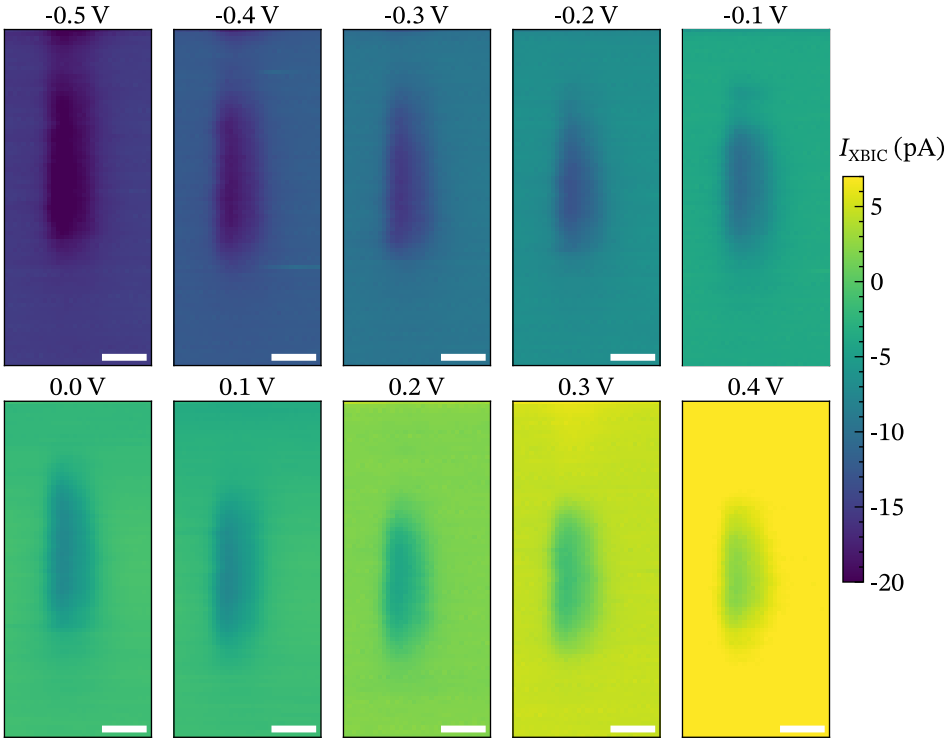

Fig. 4.13: Voltage variation from −0.5 V to 0.4 V with the increment of 0.1 V using the fully illuminated MZP with no apertures (central stop and OSA). The similar measurement but with an off-axis illuminated MZP can be found in Fig. 4.4. Scalebars: 100 nm

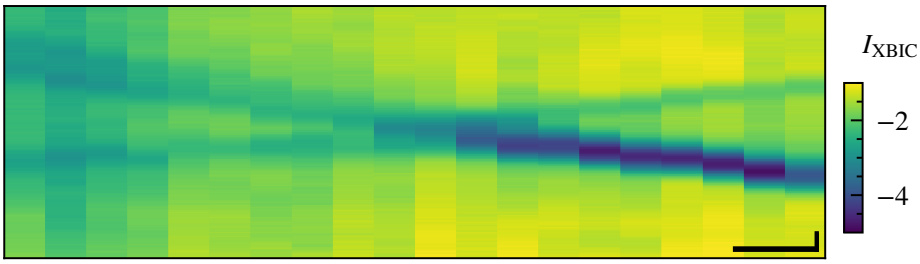

Fig. 4.14: XBIC measurements of the beam path of a fully illuminated MZP with no apertures (central stop and OSA). The similar measurement but with an off-axis illuminated MZP can be found in Fig. 4.5. Scalebar: vertical 100 nm, horizontal 10 µm

because first the background photons are generating an XBIC signal as well and second as mentioned in the manuscript the resolution of the nanowire device as a detector is limited by the width of the nanowire (180 nm). It should be noted that the measurement already gives a good impression of the beam path and reveals the position of the focal plane. In contrast, in this setup configuration a comparative determination of the beam path by using a ptychography is not possible due to the non-existence of a central stop and an OSA and therefore an unfulfilled sampling constraint [MSC98].

In-line holography with hard x-rays at sub-15 nm resolution

5

JAKOB SOLTAU, MALTE VASSHOLZ, MARKUS OSTERHOFF, AND TIM SALDITT

reproduced[1] from Optica 8, 818-823 (2021) [Sol+21b]

X-ray in-line holography is well suited for three-dimensional imaging since it covers a large field-of-view without the necessity of scanning. However, its resolution did not extend to the range covered by CDI or ptychography. In this work we show full-field holographic X-ray imaging based on cone-beam illumination, beyond the resolution limit given by the cone-beam numerical aperture. Image information encoded in far-field diffraction and in holographic self-interference is treated in a common reconstruction scheme, without the usual empty beam correction step of in-line holography. An illumination profile tailored by waveguide optics and exactly known by prior probe retrieval is shown to be sufficient for solving the phase problem. The approach paves the way towards high resolution and dose-efficient X-ray tomography, well suited for the current upgrades of synchrotron radiation sources to diffraction limited storage rings.

[1] subject to minor corrections

5.1 Introduction

Coherent X-ray optics has led to transformative progress in recent years [Ces+17; Baj+18; Moh+17], opening up novel opportunities to image matter at high resolution [Özt+18; Vil+18; Hol+19], with chemical sensitivity [Lim+16], and at ultra-fast time scales [Ayy+21; Wie+18]. For non-destructive imaging of three-dimensional (3D) bulk materials and biological specimen, hard X-ray in-line holography or propagation imaging is particularly suitable [Kua+20; Cro+18; Gar+19], since it offers a phase-sensitive imaging scheme which can cover large specimen in a full-field approach without the need for scanning. Contrast formation is based on wave propagation and self-interference of the scattered and primary beam behind the object. By illumination with a parallel beam, macroscopic scales can be covered, while illumination with a spherical beam behind a nanofocus optic enables nanoscale resolution [Wil+96; Mok+07; Bar+15]. In contrast to coherent diffractive imaging (CDI) the phase problem of holographic imaging is mathematically better posed [Mar15], due to the near-field interference between a scattered wave and a reference wave. Further, coherence requirements in near-field propagation imaging can be relaxed with respect to CDI [HS18], and phase retrieval neither requires the object nor the illumination field to be compactly supported [Clo+99; HTS18]. Based on its full-field nature and its dose efficiency, propagation imaging is well suited for 3D imaging of biological soft tissues [Khi+16; Töp+18; Ced+17; Khi+18], as well as for dynamic imaging [Wal+14a].

Unfortunately, the resolution of holographic imaging is limited by the source size of the cone-beam illumination, and does not reach the values in the sub-20 nm regime which are routinely achieved by ptychography [Hol+19; Pfe18; Özt+18] or CDI [Mia+15; Lo+18]. While one can improve focusing to increase the numerical aperture (NA), the finite source size will always impose a limit. Further, image reconstruction is inconsistently based on an illumination by a perfect point source, which is tacitly assumed when applying the Fresnel scaling theorem [Pag06]. The common procedure to deal with finite source size and wavefront aberrations is to divide the recorded hologram I_z by the measured intensity image of the empty beam I_z^E, and then treat $\bar{I}_z = I_z/I_z^E = |\mathcal{D}_z\{O\}|^2$ as the propagation of the object function O under the Fresnel propagator D_z. For sufficiently thin objects, O is given by a projection integral $O(x,y) = \exp[-i2\pi/\lambda \int_{-\Delta t}^{0}[\delta_\lambda(x,y,z) - i\beta_\lambda(x,y,z)]\mathrm{d}z]$ for the object of thickness Δt and refractive index $n(x,y,z) = 1 - \delta_\lambda(x,y,z) + i\beta_\lambda(x,y,z)$ at wavelength λ. Strictly speaking, this approach is valid only for the assumed idealized illumination conditions (ideal plane wave or ideal spherical wave). For general illumination (probe)

functions P, the relation $I_z := |\mathcal{D}_z\{P \cdot O\}|^2 \simeq |\mathcal{D}_z\{P\}|^2 \cdot |\mathcal{D}_z\{O\}|^2$ fails or is at best approximative. Instead of dividing intensities of the propagated wave in the detection plane (z_{De}), one should divide the object exit wave ψ by the complex-valued probe P in the object plane (z_{Ob}) to retrieve the object transmission function O without aberrations introduced by the illumination field. Even if the empty-beam approximation is justified, as for a Gaussian beam, the information contained in the scattered radiation is not exploited, resulting in an NA reduced to the divergence of the illuminating beam. In general, the empty beam division compromises resolution and image quality, and accounts for the fact that in-line holography often does not even reach the resolution given by the source size [Hom+15; Hag+14].

In this publication we extend full-field in-line holography to high resolutions and circumvent the spoiling effects of empty beam division. For this purpose, we adapt the principle of keyhole coherent diffractive imaging [Wil+06; Abb+08], which showed that iterative solutions to the phase problem are possible for extended objects with phase-curved incident illumination, if the illumination function is well known. We show that both ptychographic and single shot iterative probe reconstruction before recording of the object is greatly facilitated by the combination of high curvature in the object plane and high compactness of the probe in the source plane. At the same time, this waveguide illumination scheme also relaxes the constraints of a compact probe in the object plane, to the benefit of combining high resolution and large field-of-view.

5.2 Method

5.2.1 Algorithm

The basic concept of the high-resolution X-ray holography approach is outlined in Fig. 5.1. The concept is based on the propagation of the full wave field $\psi(x, y)$ between the object plane (z_{Ob}) and the detector plane (z_{De}). The approach uses the information provided by a single measurement of the holographic far-field intensities I_z at z_{De} and the known illumination function P at z_{Ob}. P is reconstructed by ptychography or by a single-frame inversion scheme, exploiting the high compactness in the waveguide exit plane (z_{WG}) due to the waveguide confinement. In the first case a short ptychography scan needs to be recorded before (or after) the holographic imaging of the samples (or a holo-tomography scan). Importantly, we find that I_z of a single distance recording and P are sufficient inputs for objects with either (i) vanishing absorption (pure phase-

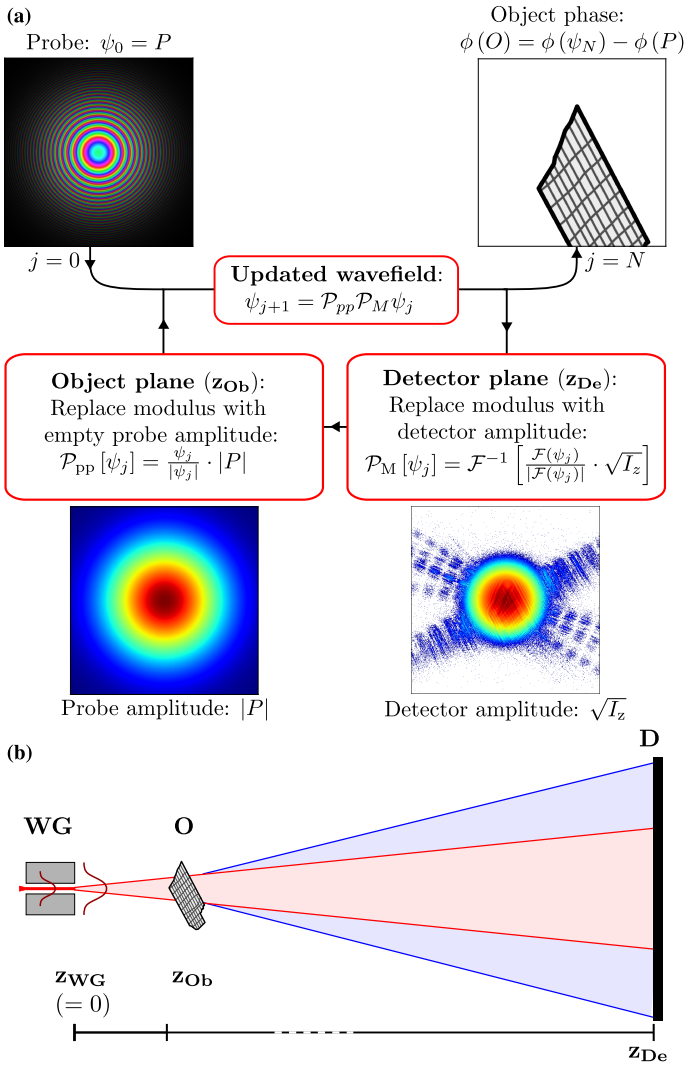

Fig. 5.1: (a) Outline of the X-ray holography algorithm. $\mathcal{P}_M$ denotes the magnitude and $\mathcal{P}_{pp}$ the pure phase object constraint. $\mathcal{F}$ and $\mathcal{F}^{-1}$ represent the forward and inverse FFT respectively. As initial ($j = 0$) wave field, the known illumination function P is used. The phase object O is calculated in the last iterative step ($j = N$) by subtracting the the phase of the probe P from the exit wave field. The object phase (top, right), which has been used in the simulation as an example, is given by a freely sketched cardiomyocyte image, inspired by the real cardiomyocyte imaged below, in Fig. 5.4. (b) Schematic of the experimental setup. A monochromatic hard X-ray beam is focused by KB mirrors onto a WG, which acts as a spatial and coherence filter. The object O is positioned in the divergent beam, at z_{Ob}. The different radiation cones indicate the WG illumination and the scattered photons. The detector D is positioned at z_{De}.

contrast samples), (ii) phase-amplitude coupling (homogeneous object composition), or (iii) for objects which are compactly supported. Due to the high wavefront curvature at z_{Ob} and hence the holographic nature of the far-field pattern in the center of the detector image, this set is sufficient for reconstruction. This holds even if P is more extended than the classical oversampling criterion [MSC98] would require for CDI phase retrieval. As usual, compatibility with the measured data is assured by applying the magnitude constraint: The solution must satisfy the measured intensity distribution of the recorded diffraction pattern I_z (see Fig. 5.1(a)). To this end, the wave field $\psi(x, y)$ is modified such that

$$\mathcal{P}_M\left[\psi(x,y)\right] = \mathcal{F}^{-1}\left[\frac{\mathcal{F}\left[\psi(x,y)\right]}{\left|\mathcal{F}\left[\psi(x,y)\right]\right|}\cdot\sqrt{I_z(x',y')}\right] .$$

In order to formulate phase retrieval only in terms of projections and to treat all constraints on equal footing, the propagation of the wave field between object and detector (and back) is incorporated into the projection operator. In contrast to typical X-ray holography experiments which describe image formation in an equivalent geometry after application of the Fresnel scaling theorem [Pag06], we calculate propagation from the object exit plane to the detector in the direct geometry via a numerical fast Fourier transformation (FFT). The holographic intensity in the detector plane is then written as $I_z(x', y') := |\mathcal{F}\{\psi(x, y)\}|^2$, where $\mathcal{F}$ is the Fourier operator. This replaces the use of the Fresnel operator in conventional cone-beam X-ray holography $\mathcal{D}_{z_{\text{eff}}}$ and the use of an effective distance $z_{\text{eff}} = z_{\text{De}}/M$, where $M = z_{\text{De}}/z_{\text{Ob}}$ is the magnification. Further, the assumption of an ideal point source illumination is made obsolete by the direct geometry, so that the reconstructed illumination P (at z_{Ob}) can be properly fed into the constraint scheme of the object plane without the necessity to use an effective probe. Depending on the available constraints, the object plane projector $\mathcal{P}_O$ is chosen

$$\mathcal{P}_O \in \{\mathcal{P}_{pp}, \mathcal{P}_r, \mathcal{P}_S, \mathcal{P}_{SH}, \mathcal{P}_h\} ,$$

where $\mathcal{P}_{pp}$ denotes a projector imposing a pure-phase constraint. Of course, the possible set of object projectors can be further extended by projectors implementing a range $\mathcal{P}_r$, support $\mathcal{P}_S$, shearlet (sparsity) $\mathcal{P}_{SH}$ or homogeneous object $\mathcal{P}_h$ constraints (see chapter 5.5.2 in the supplementary materials). In the present experimental demonstration, $\mathcal{P}_{pp}$ has been used, well justified for hard X-rays and unstained biological cells.

$\mathcal{P}_{pp}$ acts on $\psi\,(x,y)$ as

$$\mathcal{P}_{pp}\left[\psi(x,y)\right] = \frac{\psi(x,y)}{|\psi(x,y)|} \cdot |P\,(x,y)\,|\,.$$

The iterative phase retrieval algorithm can be implemented via different update schemes. Here we used either the simple error reduction (ER) as shown in Fig. 5.1(a)

$$\psi_{j+1} = \mathcal{P}_O \mathcal{P}_M \psi_j$$

or the more sophisticated relaxed averaged alternating reflector (RAAR) [Krü+12] scheme

$$\psi_{j+1} = \left[\frac{1}{2}\beta\left(\mathcal{R}_O\mathcal{R}_M + \mathcal{I}\right) + (1-\beta)\,\mathcal{P}_M\right]\psi_j\,,$$

employing not only projections but also reflection operators $\mathcal{R}$ defined as

$$\mathcal{R} = 2\mathcal{P} - \mathcal{I}\,,$$

where $\mathcal{I}$ is the identity. The parameter β controls the relaxation and can be optimized for convergence. In most cases, the differences in the resulting image quality between ER and RAAR were only minor.

In this way, we extend the classical work [Wil+06; Abb+08] by a few important modifications which result in significant improvements of the image quality: (1) we exchange the Fresnel zone plate (FZP) by an X-ray waveguide (WG) optic generating a compact source spot at the WG exit (z_{WG}), but a highly curved wavefront at z_{Ob}. (2) We reconstruct the probe P by ptychography before the single-frame acquisition of the object O, and (3) we use a modified reconstruction scheme which is not based on subtraction of the probe. We show that the usual sampling constraints can be overcome, i.e. the field-of-view (FOV) at z_{Ob} can be larger than the critical value calculated from the detector pixel size Δ_{px} according to the classical oversampling criterion [MSC98]. At the same time, we preserve the main advantage of the keyhole concept in achieving robust phase retrieval up to high spatial frequencies without restrictive object constraints. We demonstrate the method using a lithographic test pattern imaged at a (half-period) resolution of $\Delta = 11.2\,\mathrm{nm}$ and with FOV of $13 \times 13\,\mu\mathrm{m}^2$, within a single frame acquisition of down to 0.2 s illumination time. The potential for biological samples at sub-cellular level is shown by imaging a cardiac cell (cardiomyocyte) with a FOV of $50 \times 50\,\mu\mathrm{m}^2$. The dose efficiency of holographic imaging which does not require any optical element between object and detector has already been stressed in a recent

study [Bar+15]. Here we further improve the dose efficiency by using single photon counting pixel detectors with high quantum efficiency. The use of photon counting detectors with large pixel size becomes possible since reconstruction is neither limited by the oversampling criterion as in CDI or ptychography nor by the demagnified pixel size as in classical holography.

5.2.2 Experimental setup

The experiments were performed using the GINIX instrument [Kal+11] at the coherence beamline P10 of the PETRA III storage ring (Hamburg, Germany, see chapter 5.5.1 in the supplementary materials). The undulator beam was monochromatized ($Si(111)$ channel cut) to a photon energy of $E = 8\,\mathrm{keV}$ and focused by Kirkpatrick-Baez (KB) mirrors to about 300 nm in horizontal and vertical direction. A two-dimensional X-ray silicon WG was placed in the focal plane of the mirrors (see Fig. 5.1(b)), in order to reduce the source spot size and filter the coherence [OS11]. Objects were placed into the divergent wave field exiting the WG, at z_{Ob}, and the coherent diffraction pattern with holographic and CDI components was recorded with a single photon counting pixel detector (Eiger 4M, Dectris Ltd. Switzerland) positioned at $z_{\mathrm{De}} = 5.1\,\mathrm{m}$. The detector has 2162×2068 pixels and a pixel size of $\Delta_{\mathrm{px}} = 75\,\mu\mathrm{m}$. The WG was fabricated in silicon using electron-beam lithography and reactive ion etching (Eulitha, Switzerland) and was subsequently capped by wafer bonding in a clean room environment. The WG channels with a cross section of $89 \times 115\,\mathrm{nm}^2$ (horizontal $\times$ vertical) were cut to an optical length of 1 mm. The measured WG exit flux was 1.3×10^9 photons/s.

5.3 Results and discussion

First, we determine the complex-valued wave field of the probe P at z_{Ob} by a ptychographic reconstruction using the ePIE algorithm [MR09; MJL17]. A tantalum test object (NTT, Japan) including a Siemens star pattern with 50 nm smallest feature size was positioned and scanned in the WG beam. The ptychographic scan was performed with 16×16 scan points at $z_{\mathrm{Ob}} = 1.2\,\mathrm{mm}$, a step size of $0.2\,\mu\mathrm{m}$ and 0.2 s acquisition time per frame. The resulting probe P and phase objects are shown in Fig. 5.2(a,b). For comparison the probe is then back-propagated to its source plane at the WG exit (z_{WG} (c)), and compared with the wave field reconstructed from a single empty beam measurement (d), using a support constraint defined by the shape of the WG exit.

The resulting source sizes (FWHM) are (c) $29.1 \times 31.7\,\mathrm{nm}^2$, and (d) $27.7 \times 27.3\,\mathrm{nm}^2$, which is significantly smaller than the geometric channel dimensions of $89 \times 115\,\mathrm{nm}^2$. The smaller WG source size results from multi-modal interference, and is in line with finite difference (FD) simulations [MS17], shown in (e). The FD simulations yield to a FWHM of $31.8 \times 34.6\,\mathrm{nm}^2$ for the given parameters. For further details see chapter 5.5.1 in the supplementary materials.

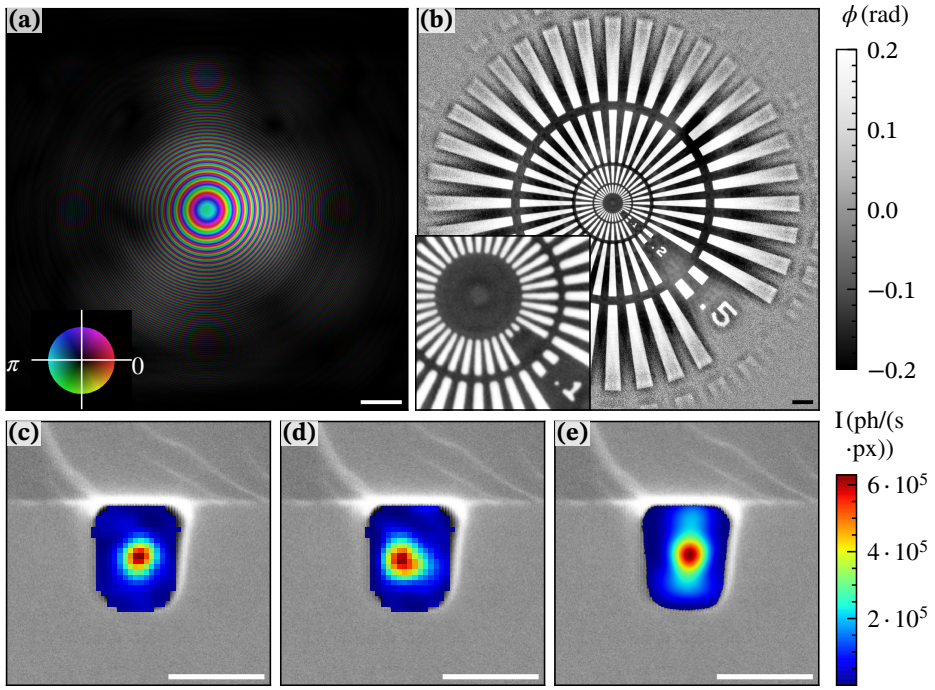

Fig. 5.2: Ptychographic reconstruction of (a) the probe P amplitude and phase and (b) the objects O phase with a pixel size $\delta_{\mathrm{px}} = 5.2\,\mathrm{nm}$. The inner radius of the Siemens star pattern corresponds to spokes with 50 nm feature size (see zoom in inset). (c-e) Intensity distributions at the WG exit, superimposed with a SEM image of the WG exit surface: (c) ptychographic reconstruction, (d) single shot reconstruction by the RAAR algorithm using a support constraint [Krü+12], and (e) FD-simulated intensity distribution. The source sizes (FWHM) are (c) $29.1 \times 31.7\,\mathrm{nm}^2$, (d) $27.7 \times 27.3\,\mathrm{nm}^2$, and (e) $31.8 \times 34.6\,\mathrm{nm}^2$. Scalebars: (a,b) 1 µm, (c-e) 100 nm.

Next, we use the pre-determined probe reconstructed by ptychography P (shown in Fig. 5.2(a)) at z_{Ob} to phase single-shot acquisitions of an object O illuminated by P. Here, no further scanning is required, in particular no overlap constraint as in ptychography. Neither do we require compactness of the object function O as in CDI.

Instead, the only constraint which we use, is the amplitude of the exit wave which we constrain to $|PO| = |P|$ for a pure phase object. This is well justified for the objects of interest here (nanostructures, biological cells) at the given photon energy. More generally, other constraints such as homogeneous object (i.e. coupled phase and amplitude), sparsity or simple range constraints (positive-definiteness of absorption) can already be sufficient, see the simulation for the range constraint $|PO| \leq |P|$, provided in chapter 5.5.3 in the supplementary materials. Importantly, the highly curved illumination enables reconstruction beyond the the classical oversampling criterion $o = z_{\mathrm{De}}\lambda/(\Delta_{\mathrm{px}}L) \geq 2$[MSC98], i.e. the illuminated area on the object can be larger than L calculated from $o = 2$. Note that this is not in contradiction to the Nyquist-Shannon theorem due to the holographic nature of the image formation.

Figure 5.3(a) proves this claim by presenting the reconstruction of a Siemens star from a single frame acquisition with 1 s exposure time (b), recorded with a FOV$= 13 \times 13\,\mu\mathrm{m}^2$. The spokes of the Siemens star are fully resolved in a region of $8.2 \times 8.2\,\mu\mathrm{m}^2$, corresponding to $o \simeq 1.3$. The high quality of the full-field image is demonstrated by the magnified region in the inset of (a). Note that the decay of the illumination function results in a decrease of the signal-to-noise towards the image boundaries. Surprisingly, even in regions which receive very low flux, the object can still be recognized, albeit with some artefacts (for further details see chapter 5.5.9 in the supplementary materials). The smallest features of the pattern are the 50 nm stripes in the center, which are clearly resolved. The high resolution is achieved here by photons diffracted by the object to large angles and detected out-of-the central radiation cone. At the same time, a decisive advantage over standard far-field diffraction in (nearly) plane wave illumination as typical for CDI or ptychography is the fact that low and moderate spatial frequencies are phased from the in-line holographic signal. Further, we could show a probe reconstruction of a single empty beam image is sufficient, given the compactness of the beam in the WG exit plane, see chapter 5.5.4 in the supplementary materials.

In order to further quantify the resolution we have analyzed the reconstruction of a pattern with 50 nm (half-period) lines and spaces, see Fig. 5.3(c-e). The reconstruction by the presented method shows higher resolution and image quality than the conventional reconstruction by the contrast-transfer-function (CTF) approach [Clo+99] after empty-beam division. Note, that the pixel size $\delta_{\mathrm{px}} = 5.2$ nm in the new method is determined by the detector NA, and no longer by the geometrically magnified pixel size $\delta^{\mathrm{M}}_{\mathrm{px}} = \Delta_{\mathrm{px}}/M = 17.3$ nm, as in the conventional reconstruction. The resolution of the holographic reconstruction was determined by Fourier ring correlation (FRC)

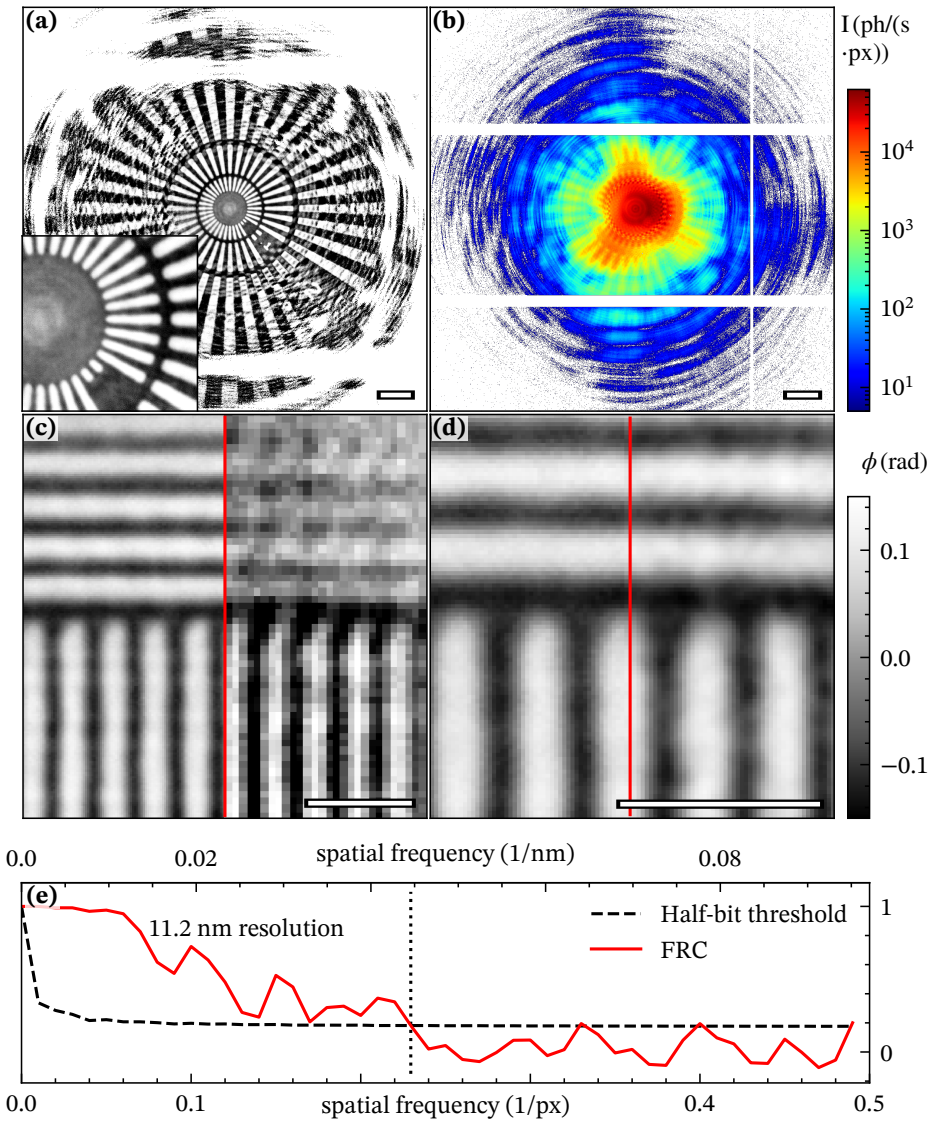

Fig. 5.3: *(caption next page)*

Fig. 5.3 *(previous page)*: In-line X-ray holography reconstructions of a test pattern at $z_{\mathrm{Ob}} = 1.2\,\mathrm{mm}$ with the detector at $z_{\mathrm{De}} = 5.1\,\mathrm{m}$. (a) Reconstructed Siemens star with δ_{px}=5.2 nm and 1 s acquisition time. The inner radius of the Siemens star pattern corresponds to spokes with 50 nm feature size (see zoom in inset). (b) The corresponding detector image. Reconstruction of a 50 nm lines and spaces structure: (c) Split-view, comparing reconstruction using the novel approach (δ_{px}=5.2 nm) with a reconstruction by empty beam division and CTF ($\delta_{\mathrm{px}}^{\mathrm{M}}$=17.3 nm). Both use the same data, recorded with an acquisition time of 2 s. (d) Split-view, comparing the reconstruction from data with 2 s to 0.2 s acquisition time, in a ROI of $0.5 \times 0.5\,\mu\mathrm{m}^2$. (e) FRC analysis of this ROI, correlating reconstructions of two independent measurements with an acquisition time of 2 s each, indicating a resolution (half-period) of $\Delta = 11.2\,\mathrm{nm}$. Scalebars: (a) 1 µm. (b) $100\,_{\mathrm{px}}$ corresponding to a scattering vector $q = 0.06\,\mathrm{nm}^{-1}$, (c,d) 250 nm.

[HS05], correlating the reconstructions of two different data sets, each with independent ptychographic reconstructions of P. The FRC indicates a resolution (half-period) of $\Delta = 11.2\,\mathrm{nm}$ (e). Further, we include a reconstruction from data with a shorter acquisition of 0.2 s which still shows well resolved lines and spaces, but with slightly more noise (d).

Next, the method was used to image an adult murine cardiomyocyte. The cardiac cells were isolated by dissociation of healthy mouse hearts, chemically fixed, dispersed on a silicon nitride window, plunge frozen and freeze dried [Rei+20]. The cells were imaged using the same setup described before. P was reconstructed from a ptychographic scan (of the same object) at $z_{\mathrm{Ob}} = 3.9\,\mathrm{mm}$ with 15×12 scan points of 1 s acquisition time and $\delta_{\mathrm{px}} = 10.2\,\mathrm{nm}$. Figure 5.4 presents reconstructions from single shot, for two different defocus planes. The larger defocus distance ($z_{\mathrm{Ob}} = 9.3\,\mathrm{mm}$) images shown in (a) result in a FOV of more than $50 \times 50\,\mu\mathrm{m}^2$. The flux density in the object plane was 1.4×10^6 photons/µm^2, corresponding to a dose of 1.6×10^4 Gy. Sub-cellular structures such as the nuclei, mitochondria and microfibrils and the sarcomeric architecture can be clearly identified. The brighter stripes perpendicular to the orientation of the cell's main axis exhibit a smaller phase shift/lower electron density and can be associated with the M-lines of the sarcomere. In (b), the same cell was recorded closer to the WG at $z_{\mathrm{Ob}} = 3.9\,\mathrm{mm}$. As a result of the increased flux density (8×10^6 photons/µm^2), the sub-cellular structure is now more clearly resolved and the electron dense z-discs within the individual sarcomeres become visible (b, red square). The thickness of the z-disk was determined to 105 nm (FWHM), in agreement with literature [FF11].

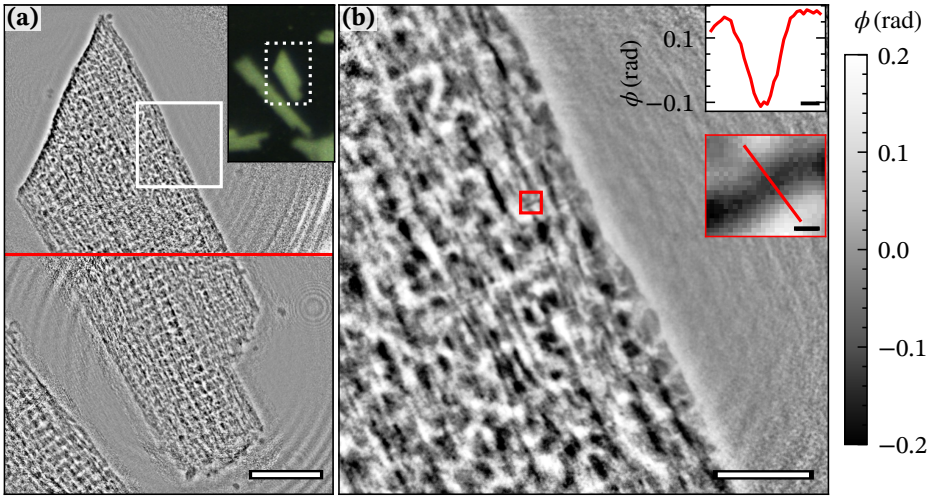

Fig. 5.4: (a) In-line X-ray holography reconstruction using our novel approach of an entire cardiomyocyte at $z_{Ob} = 9.3\,\text{mm}$, covered by two exposures at different sample positions. The combined FOV is $103 \times 49\,\mu\text{m}^2$ with $\delta_{px} = 10.2\,\text{nm}$ (for comparison: $\delta_{px}^{M} = 136.5\,\text{nm}$). The inset shows an optical microscope image of the cell. The X-ray FOV is marked by a dashed white rectangle. (b) Additional reconstruction measured at $z_{Ob} = 3.9\,\text{mm}$ with $\delta_{px} = 10.2\,\text{nm}$ (for comparison: $\delta_{px}^{M} = 57.3\,\text{nm}$). Position marked in (a) by solid white squares. Sub-cellular structures can be identified, e.g. the z-disc (red square). The line profile through the z-disk has an FWHM of 105 nm. Scalebars: (a) 10 µm, (b) 2.5 µm and insets 50 nm. A comparison of our novel in-line X-ray holography approach and ptychography is given in chapter 5.5.5 in the supplementary materials.

5.4 Conclusion

In conclusion, we have presented a new approach to image extended specimen with full-field single shot X-ray holography. In contrast to current X-ray holography, this approach offers super-resolution with respect to the illuminating NA. This was demonstrated by imaging a test structure with a resolution of 11.2 nm using a waveguide source size of 30.4 nm (FWHM), as shown in Fig. 5.3(e). In addition, the limitation of an effective pixel size by geometric magnification, as in in-line holography, does not apply. At the same time, the object's FOV can be larger than in CDI. In other words, with respect to the usual in-line holography approach based on the Fresnel scaling theorem and empty beam division, we observe a super-resolution effect (resolution better than NA of illuminating beam). And with respect to CDI we achieve sub-sampling capability. This is a result of the particular design of the illumination resulting in a diffraction pattern with the holographic contributions in the center and the coherent diffraction contributions in the annulus outside the primary beam. Note that the holographic pattern within the primary beam does not obey Friedel symmetry, i.e. even for weak phase objects the diffraction pattern is not centrosymmetric due to the curvature of the probe. In contrast to plane wave illumination, this 'phase-structured' illumination results in enhanced 'diversity' and less-redundant measurements. Altogether, this opens a brilliant perspective for high resolution and dose-effective X-ray tomography, well suited for the current upgrades of synchrotron radiation sources to diffraction limited storage rings.

Acknowledgment

We acknowledge DESY (Hamburg, Germany), a member of the Helmholtz Association HGF, for the provision of experimental facilities. We would like to thank Michael Sprung and Fabian Westermeier for assistance in using beamline P10 at PETRA III. We thank Mike Kanbach for WG fabrication and Bastian Hartmann for engineering help.

Funding

Financial support by German Federal Ministry of Education and Research (BMBF) through grant No. 05K19MG2 is gratefully acknowledged. We acknowledge funding by the Max Planck School of Photonics supported by BMBF, Max Planck Society, and Fraunhofer Society.

5.5 Supplementary materials

5.5.1 Experimental setup and waveguide optics

The experiment was performed with the Göttingen instrument of nano-imaging with X-rays (GINIX) at the coherence beamline P10 of the PETRA III storage ring (Hamburg, Germany) [Sal+15]. The undulator beam was monochromatized using a Si(111) monochromator to 8 keV, and focused by Kirkpatrick-Baez (KB) mirrors to about 300 nm in horizontal and vertical direction. At a distance of 5.1 m an Eiger 4M (Dectris Ltd., Switzerland) detector was positioned with a pixel size of $\Delta_{\mathrm{px}} = 75\,\mu\mathrm{m}$. The waveguide (WG) was positioned in the focal plane of the mirrors, and is used as a spatial and coherence filter [Kal+11; Krü+12]. The maximum WG-beam flux measured at the detector was 1.3×10^9 photons/s. The WG was fabricated in silicon using electron-beam lithography and reactive ion etching (Eulitha, Switzerland) and was subsequently capped by wafer bonding in a clean room environment. The WG channel has a cross section of $89 \times 115\,\mathrm{nm}^2$, with a total length of 1 mm.

Figure 5.5 shows the simulation of a wave field propagating through a silicon WG with the same parameters as in the experiment. A scanning electron micrograph of the WG exit was used as a template for the simulation. As initial condition, a plane wave was assumed. Simulations were performed using a Finite Difference (FD) solver [MS17], with the numerical grid parameters $\mathrm{px}_{\mathrm{x,y}} = 0.5\,\mathrm{nm}$ and $\mathrm{px}_{\mathrm{z}} = 0.1\,\mu\mathrm{m}$ for the lateral and the propagation directions, respectively. In (a) and (b) the wave field intensity inside the WG is shown. The dashed lines indicate the borders of the guiding channel. In (c) the simulated WG-exit field is propagated to the object plane, at a source-sample distance of $z_{01} = 1.2\,\mathrm{mm}$ using the Fresnel propagation [Pag06; Loh+20]. The wave field is compared to the near-field distribution obtained by ptychography at the same source-sample distance, shown in (d). The size and phase of both wave fields show only small deviations which can be attributed to differences of the initial illumination of the WG. In the experiment an highly focused beam by a pair of KB-mirrors was used, in contrast to the plane wave illumination used in the simulations. Furthermore, despite the use of the SEM cross section of the WG for simulation, differences to the exact shape of the WG are expected. For further comparison of the numerical aperture and divergence, the simulated wave field is propagated by fast Fourier transformation (FFT) to the detector plane at a distance of $z_{12} = 5.1\,\mathrm{m}$, as shown in (e). The far-field diffraction of the WG-beam (empty image) is shown in (f). While the divergence is in good agreement with the simulations, differences in the exact intensity distribution

again reflect the approximative nature of the simulation regarding the exact geometry and illumination.

Figure 5.6 shows the intensity distribution in the waveguide exit plane, comparing the exit intensity of the FD-simulations (a), to the experimental intensity distribution obtained from back-propagated ptychographic probe reconstruction (b), and the inversion of the far-field pattern of the empty waveguide beam, based on iterative projections onto the measured intensities (detection plane) and a support constraints (waveguide exit plane), implemented by a RAAR algorithm (c). The spot size is of particular importance for holographic resolution, and is determined to (a1,a2) $31.8 \times 34.6\,\mathrm{nm}^2$, (b1,b2) $29.1 \times 31.7\,\mathrm{nm}^2$, and (c1,c2) $27.7 \times 27.3\,\mathrm{nm}^2$, for the three cases, respectively. The values indicate the FWHM of the line profiles, computed using the python `scipy.signal.peak_widths` [Vij+20] function, and are in good agreement. Note that the source spot is significant smaller than the dimensions of the WG, which relaxes the requirements of lithography and also decreases the heat load in the waveguide cladding.

Experimental parameters for in-line X-ray holography are listed in Tab. 5.1.

Table 5.1: Experimental parameters for the in-line X-ray holography reconstructions presented in the main article.

Fig.	5.3 (a,b)	5.3 (c,d)	5.3 (d)	5.4 (a)	5.4 (b)
sample	Siemens Star	L&S	L&S	cardiomyocyte	
acquisition time (s)	1.0	2.0	0.2	1.0	1.0
pixel size δ_{px} (nm)	5.2	5.2	5.2	10.3	10.3
z_{Ob} (mm)	1.2	1.2	1.2	9.3	3.9
dose (Gy)	1.1×10^6	2.1×10^6	2.1×10^5	1.6×10^4	9.2×10^4
flux per frame (photons/ (μm$^2 \cdot$ frame))	5.0×10^7	1.0×10^8	1.0×10^7	1.4×10^6	8.0×10^6

5.5.2 Detailed information on the algorithm and constraints

Our approach of in-line holography uses the information provided by the measurements of the holographic far-field intensities $I_z(x', y')$ (detector plane) and the known

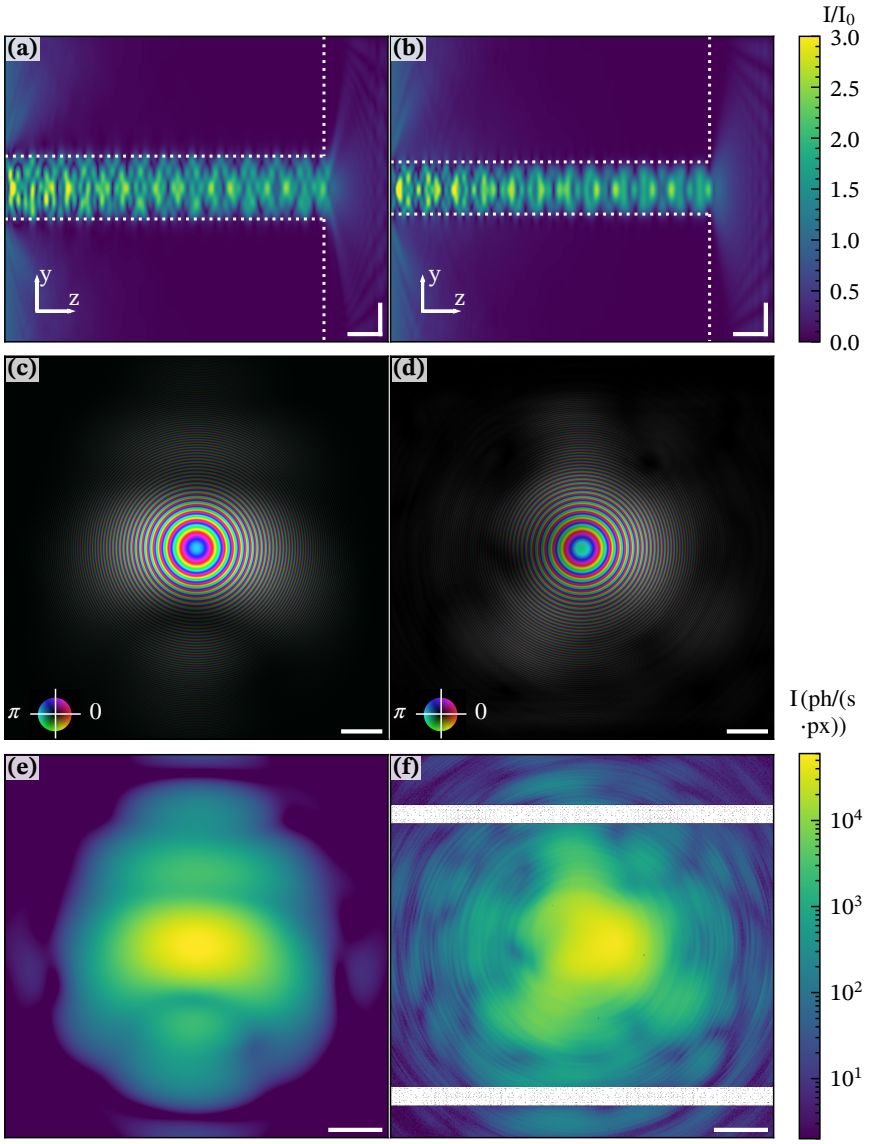

Fig. 5.5: (a,b) Intensity profiles along the two lateral center planes of a silicon-WG calculated by a Finite Difference simulation. (c,d) Comparison of the wave field (amplitude and phase) in the object plane for simulation (c) and the reconstructed field obtained by ptychography (d). Corresponding far-field intensity distributions for the simulation (e), and the waveguide beam recorded in the experiment (empty beam) (f). Scalebars: (a,b) horizontal 100 µm, vertical 50 nm, (c,d) 1 µm, corresponding to a scattering vector of $q = 0.034\,\mathrm{nm}^{-1}$, and (e,f) $100\Delta_{\mathrm{px}}$ with a size of 75 µm, corresponding to a scattering vector of $q = 0.06\,\mathrm{nm}^{-1}$.

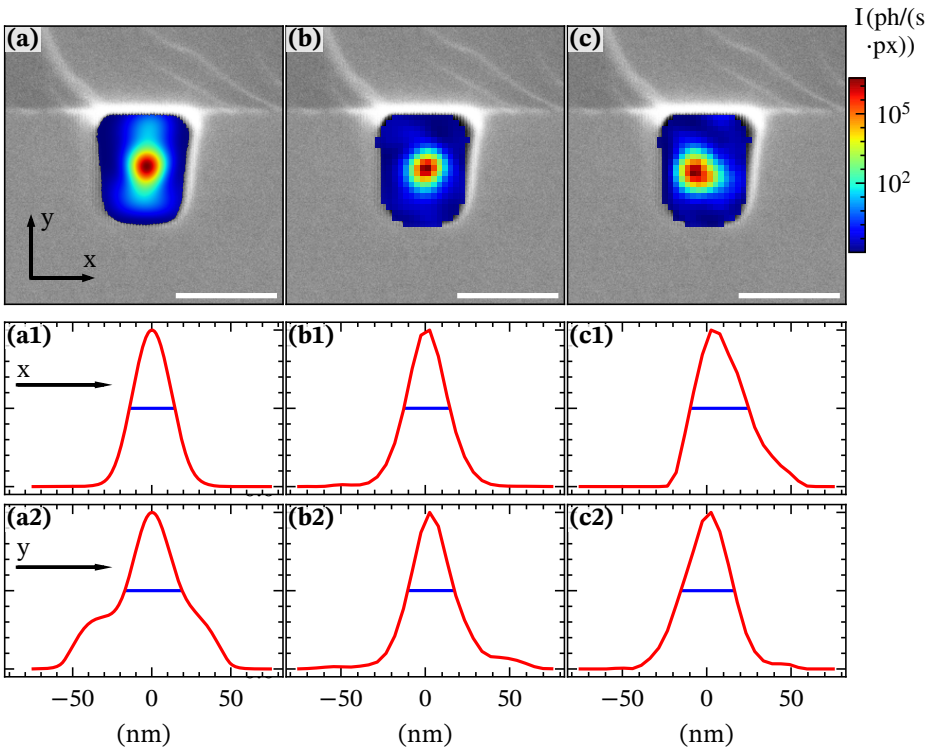

Fig. 5.6: The FWHM of the WG exit intensity, obtained from (a) FD-simulations, (b) the ptychographic reconstruction, and (c) the single frame far-field inversion based on the support constraint. The obtained values of (a1,a2) $31.8 \times 34.6\,\mathrm{nm}^2$, (b1,b2) $29.1 \times 31.7\,\mathrm{nm}^2$, and (c1,c2) $27.7 \times 27.3\,\mathrm{nm}^2$, are in good agreement, and prove that the probe required for the holographic imaging can be reconstructed from a single empty beam acquisition. Scalebars: 100 nm

illumination function (probe) $P(x, y)$ in the object plane. We present in the following the basic projectors. The measured data is assured by using the magnitude constraint $\mathcal{P}_M$. The solution must satisfy the measured intensity distribution of the hologram $I(x', y')$ in the detection plane. Therefore, $\mathcal{P}_M$ acts on the wave field $\psi(x, y)$ such that

$$\mathcal{P}_M\left[\psi(x,y)\right] = \mathcal{F}^{-1}\left[\frac{\mathcal{F}\left[\psi(x,y)\right]}{|\mathcal{F}\left[\psi(x,y)\right]|}\cdot\sqrt{I(x',y')}\right] .$$

The phase retrieval is formulated in terms of projections, to treat all constraints on equal footing, the propagation of the wave field between object and detector (and back) is incorporated into the projection operator.

Depending on the available constraints, the object plane projector is chosen

$$\mathcal{P}_O \in \{\mathcal{P}_{pp}, \mathcal{P}_r, \mathcal{P}_S, \mathcal{P}_{SH}, \mathcal{P}_h\} ,$$

where $\mathcal{P}_r, \mathcal{P}_{pp}, \mathcal{P}_S, \mathcal{P}_{SH}, \mathcal{P}_h$ denote projectors imposing range constraints, pure-phase constraint, support constraint, shearlet (sparsity) constraint and homogeneous object constraints. In the supplementary materials only $\mathcal{P}_{pp}$ has been used, with the exception of Fig. 5.9 where additionally the $\mathcal{P}_S$ and of Fig. 5.7 where in the object plane only the $\mathcal{P}_r$ were used.

But the most general constraint is the range constraint, which sets the magnitude ($|\psi|$) and phase ($\arg(\psi)$) behind the object equal or smaller to the magnitude and phase of the illumination field ϕ_0. This is justified, since the wave field amplitudes can only be smaller (absorbing components in the object) than or equal (transparent components), and the same is true for the phase due to positivity of the electron density. Accordingly, we can write

$$\mathcal{P}_r\left[\psi(x,y)\right] = \begin{cases} |\psi_0(x,y)|\exp(i\arg(\psi(x,y))) & \text{if } |\psi(x,y)| > |\psi_0(x,y)| \\ |\psi(x,y)|\exp(i\arg(\psi_0(x,y))) & \text{if } \arg(\psi(x,y)) > \arg(\psi_0(x,y)) \\ \psi(x,y) & \text{else.} \end{cases}$$

For hard X-rays and unstained biological specimen, objects are often well approximated as pure phase contrast

$$\mathcal{P}_{pp}\left[\psi(x,y)\right] = \frac{\psi(x,y)}{|\psi(x,y)|}\cdot|P\left(x,y\right)| .$$

As in CDI, the support constraint can also be used as a powerful constraint, if war-

ranted, but importantly it is not required in this approach due to the properties of the illumination. In this case, the reconstructed sample is only allowed to cover a limited part s of the field of view

$$\mathcal{P}_S\left[\psi(x,y)\right] = \begin{cases} \psi(x,y) & \text{if } (x,y) \in s \\ \psi_0(x,y). \end{cases}$$

The idea of the shearlet (sparsity) constraint $\mathcal{P}_{SH}$ is to perform a shearlet transform in the object plane, then cut off the shearlet coefficients with a small modulus up to a certain threshold and perform the inverse shearlet transformation. This is beneficial for the convergence of the iterative update process if the object possesses a sparse representation in a shearlet frame.

The homogeneous object constrain $\mathcal{P}_h$ is rigorously true for samples composed of a single material where the proportionality of the refraction index parameters δ and β can be assumed. Hence, the parameters of δ and β of the reconstructed object can be coupled in the reconstruction process.

5.5.3 Simultaneous reconstruction of sample phase and amplitude

Figure 5.7 presents simulations of our method for an object with phase (institute logo) and amplitude (cell phantom) contributions. See the simulated diffraction pattern shown in (a,b). The object is positioned at a source-sample distance of $z_{01} = 0.75\,\text{mm}$, far-field images are recorded at $z_{12} = 5.1\,\text{m}$ with a detector pixel size $\Delta_{\text{px}} = 75\,\mu\text{m}$. The pixel size in the sample plane given by the inverse fast Fourier transformation (FFT) is $\delta_{\text{px}} = 5.2\,\text{nm}$. Poisson noise is added to the simulated diffraction patterns, corresponding to a total photon number of 5×10^4 photons$/\Delta_{\text{px}}$. First, we reconstruct from a single acquisition, which corresponds to an under-determined problem, second from two images recorded with different Fresnel number F. The corresponding reconstructions (RAAR, $\mathcal{P}_r$) of amplitude and phase are shown in (c,d), and (e,f) for the single and the double acquisition, respectively. Even in the first case, the amplitude image (c) is reconstructed fairly well, and the phase image (d) is also distinguishable, but distorted by artifacts. In a possible tomographic imaging experiment the separation between phase and amplitude could be further increased by tomographic consistency constraints. The more straightforward solution is the two distance image acquisition, which immediately results in excellent reconstruction quality, as shown in (e) and (f).

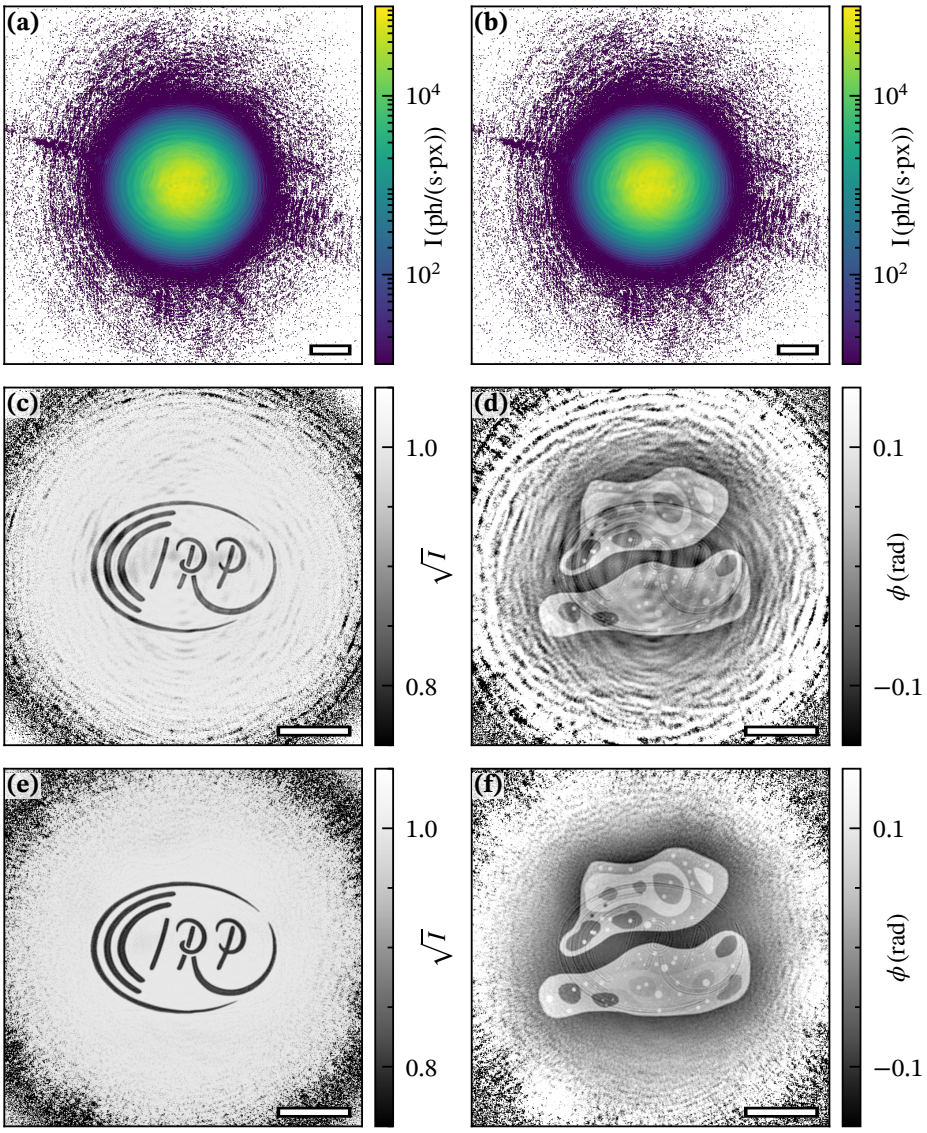

Fig. 5.7: (a,b) Simulated intensity distribution in the far-field for two different distances, namely (a) $z_{01} = 0.75\,\mathrm{mm}$ and (b) $z_{01} = 0.825\,\mathrm{mm}$. (c,d) Single image reconstructions of amplitude (c) and phase (d), from the far-field data in (b). (e,f) Two distance image reconstruction of amplitude (c) and phase (d), from both far-field patterns (a) and (b). Phase and amplitude are well distinguished and resolved. Scalebars: (a,b) $100\Delta_{\mathrm{px}}$, corresponding to a lateral momentum transfer (scattering vector) of $q = 0.06\,\mathrm{nm}^{-1}$, (c-f) $1\,\mu\mathrm{m}$.

5.5.4 Object reconstruction based on probe reconstructed from a single image

Figure 5.8 shows two reconstructions of the Siemens star test pattern, the first using a probe reconstructed from the ptychographic scan, the second reconstructed from a single acquisition far-field inversion (RAAR,$\mathcal{P}_S$), which imposes the support constraint in the waveguide exit plane and then yields the illumination by forward propagation to the the object plane. In both cases the same detector image for the sample reconstruction was used. The 50 nm features in the center of the Siemens star are well resolved in both cases. For the ptychographic probe, the reconstructed object is less noisy and the edges are more clearly defined. At the same time, the result shows that a single flat (empty) image is already sufficient to achieve the high resolution range. This demonstrates that the novel approach presented in this publication is not limited to probe reconstruction by ptychography, but can be extended to other methods.

5.5.5 Comparison of the novel approach and ptychography

Figure 5.9 shows the reconstruction of a cardiomyocyte cell using ptychography (a-c), and in-line holography (d-f) based on our novel approach. The same sample region as in Fig.5.4 of the main manuscript is shown, but here a support constraint was used in addition. The ptychographic reconstruction was performed on a scan of 15×12 points and an acquisition time of 1 s resulting in a dose of 1.7×10^7 Gy for the complete scan. For in-line holography, the acquisition time was 1 s and the deposited dose was (d) 1.6×10^4 Gy, and (e,f) 9.2×10^4 Gy, reflecting the different defocus distances $z_{01} = 9.3$ mm and $z_{01} = 3.9$ mm, respectively. In all six images the sub-cellular structure is resolved and small features such as mitochondria and m- and z-disk of sizes of ≈ 100 nm become visible.

5.5.6 Additional ptychographic dataset with 3x3 scan points

Figure 5.10 shows the wave field and object reconstructed from a scan using only 3×3 scan points with an acquisition time of 0.2 s per frame. Comparing the wave field with the results obtained from the 12×12 scan shown in the main manuscript (see Fig. 5.2), the probe and object are slightly more noisy. Nevertheless, it demonstrated that the scan time for the probe determination can be significantly reduced to scan times of below 2 s if needed.

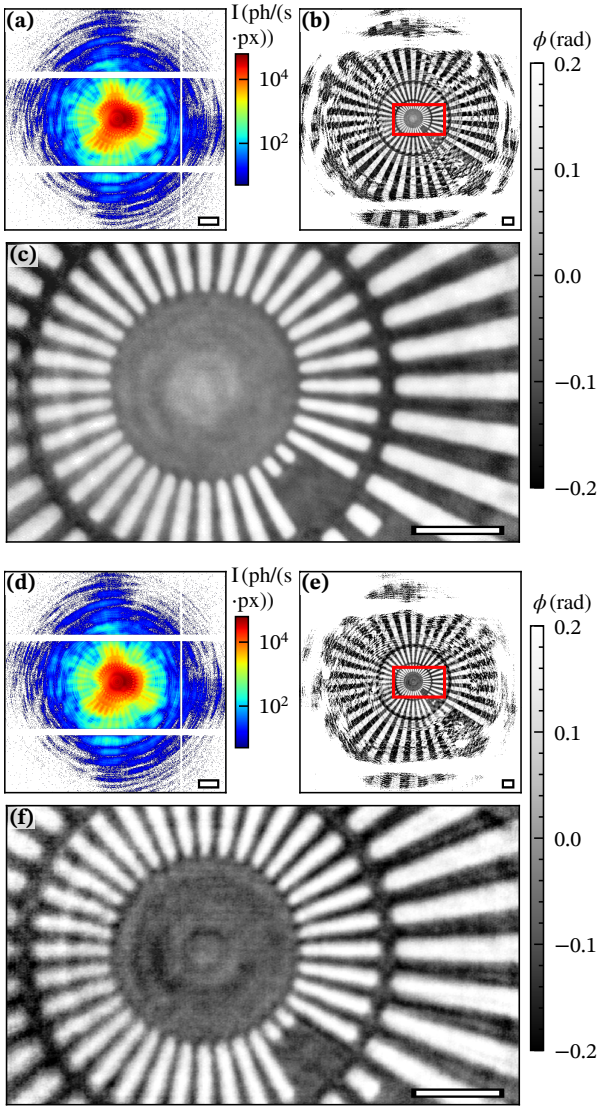

Fig. 5.8: Object reconstruction using a probe pre-reconstructed by ptychography (a-c), and a probe pre-reconstructed from a single-acquisition far-field pattern based on inversion using a compact support in the waveguide exit plane (d-f). (a,d) Intensity distribution in the detector plane (hologram). (b,e) Reconstructed phase in the object plane, and (c,f) magnified inset of the region marked by the red rectangle in (b,e). The fact that the (a-c) and (d-f) panels are consistent and of almost equal image quality demonstrates that a ptychographic scan is not required beforehand for probe reconstruction. Instead, the probe can also be reconstructed from a single empty beam acquisition.

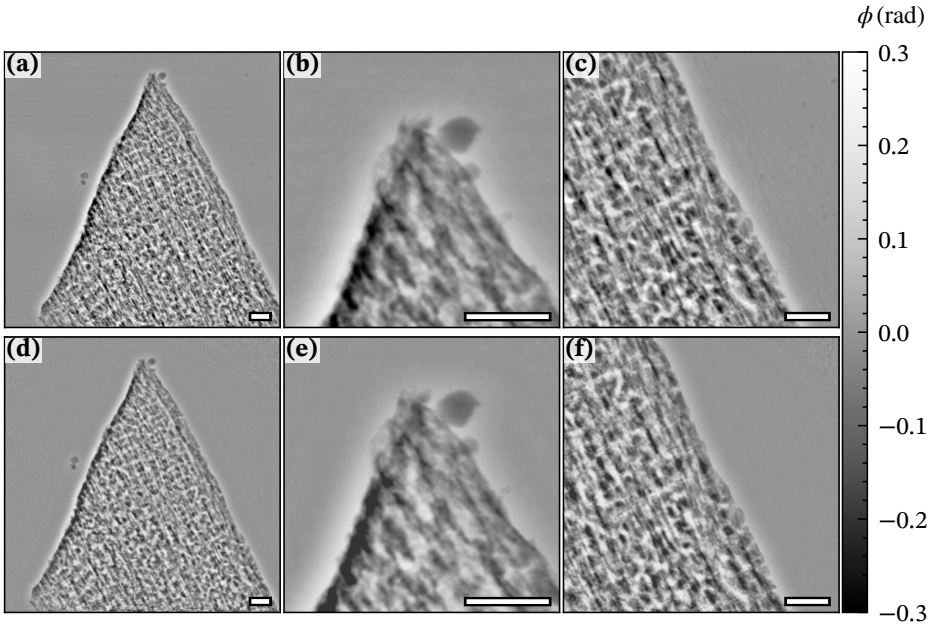

Fig. 5.9: Comparison of the ptychorgaphic reconstruction (a-c, ptychographic scan) to in-line holography based on the present approach (d-f, single frame acquisition) for the same cardiomyocyte. In contrast to Fig.5.4 of the main manuscript, a support mask was used for the reconstruction in regions without cell. The result hence shows that the present approach (with no scanning required) gives equivalent image quality compared to a ptychographic scan of the same object. Scalebars: 2 μm.

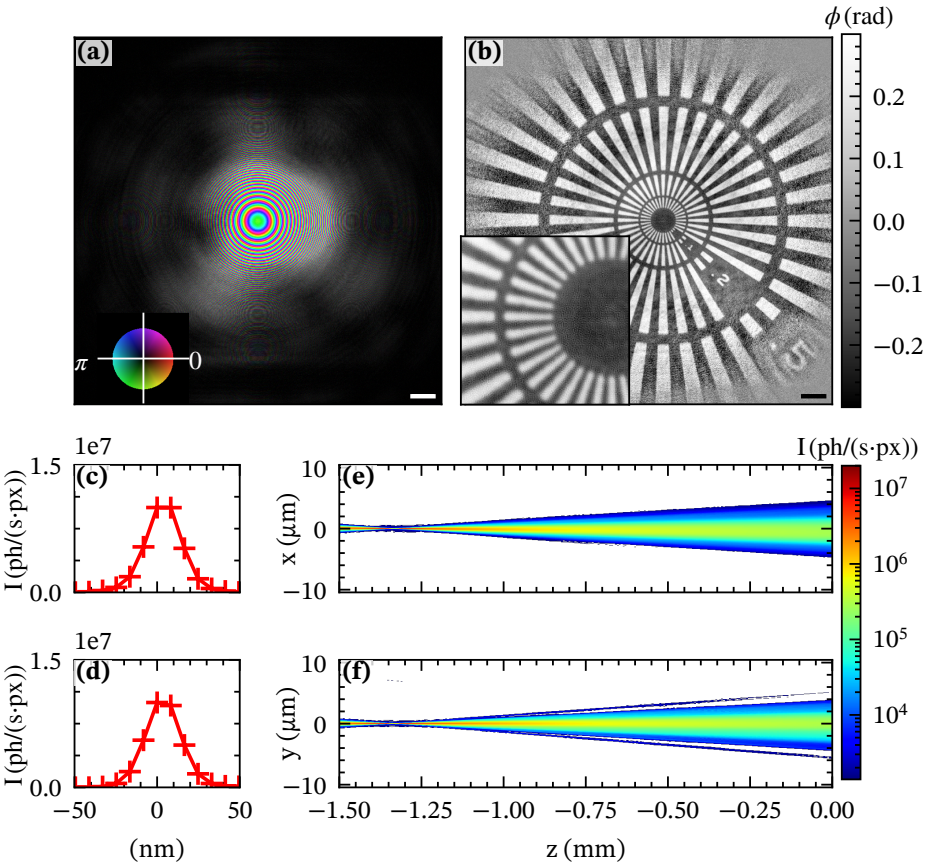

Fig. 5.10: Ptychographic reconstruction with pixel size $\delta_{\mathrm{px}} = 5.2\,\mathrm{nm}$ from a scan using only 3×3 scan points with an acquisition time of 0.2 s per frame, showing amplitude and phase of the probe in the sample plane (a), and the reconstructed phase of the object (b). The inner features of the Siemens star are spokes with a size of 50 nm feature size. (c) Horizonatal and (d) vertical intensity profile of the reconstructed probe back-propagated to the WG exit using the Fresnel propagator.(e,f) Corresponding longitudinal sections, showing the probe propagation. All scalebars: 1 μm.

5.5.7 Oversampling

Figure 5.11 shows the reconstruction of a simulated object (cardiomyocyte phantom) for different oversampling ratios o, comparing illuminations by (a,c) a divergent beam (b,d) a parallel beam. In (a,b) the diameter of the illumination is $L = 1000 \cdot \Delta_{\text{px}} = 5.1\,\mu\text{m}$, and in (c,d) $L = 3000 \cdot \Delta_{\text{px}} = 15.2\,\mu\text{m}$, resulting in oversampling ratio of $o = 2.1$ and $o = 0.7$, respectively. In both cases, the illumination is circular.

In case of the divergent beam, a Gaussian beam phase curvature is assumed, while the phase is assumed constant for the parallel beam. The sample distance z_{De}, wavelength λ, and detector pixel size Δ_{px}, which together with L determine the oversampling ratio $o = z_{\text{De}}\lambda/(\Delta_{\text{px}}L) \geq 2$ [MSC98], are identical to the parameters of the experiment. As object, a cardiomyocyte phantom was used as a pure phase object. The object field of view is shown in the first column, the illumnination is shown in the second column, and the corresponding far field diffraction pattern for each case are shown in the third column. The reconstruction algorithm is identically to the procedure described in Fig.5.1 of the main manuscript. The only exception is, that in case of the parallel beam a supporting mask in the sample plane was used. In contrast to the divergent beam, the parallel beam setting requires this constraint for successful phase retrieval. The last column shows the resulting reconstructions of the object phase. For $o = 2.1$, the object phase can be reconstructed using either the divergent or the parallel beam. Contrarily, for $o = 0.7$, only the divergent beam gives a satisfactory reconstruction. In the case of parallel beam simulation, the outline of the cell is still well represented due to the tight support, while the inner structure ('organelles') are blurred.

5.5.8 Alternative determination of the resolution

As an alternative to the FRC, the resolution was determined in Fig. 5.12 by the steepness of an object's edge. The reconstructed sample phase shown in Fig.5.3(c) of the main manuscript was used. The sample is a tantalum test object (NTT, Japan) with a pattern of lines and spaces of 50 nm (half-period). The sample was positioned at a distance of $z_{\text{Ob}} = 1.2\,\text{mm}$ relative to the waveguide. The aquisition time of the detector image was 2 s. The pixel size in the object plane is $\delta_{\text{px}} = 5.2\,\text{nm}$. The region of interest for the determination of the edge slope was 27×14 (vertical $\times$ horizontal) pixel (see Fig. 5.12(a)). The average slope is depicted in Fig. 5.12(b). The fit of an error function yields a half width at half maximum (HWHM) of 11.9 nm. This is in excellent agreement with the resolution determined in the main manuscript by FRC of 11.2 nm.

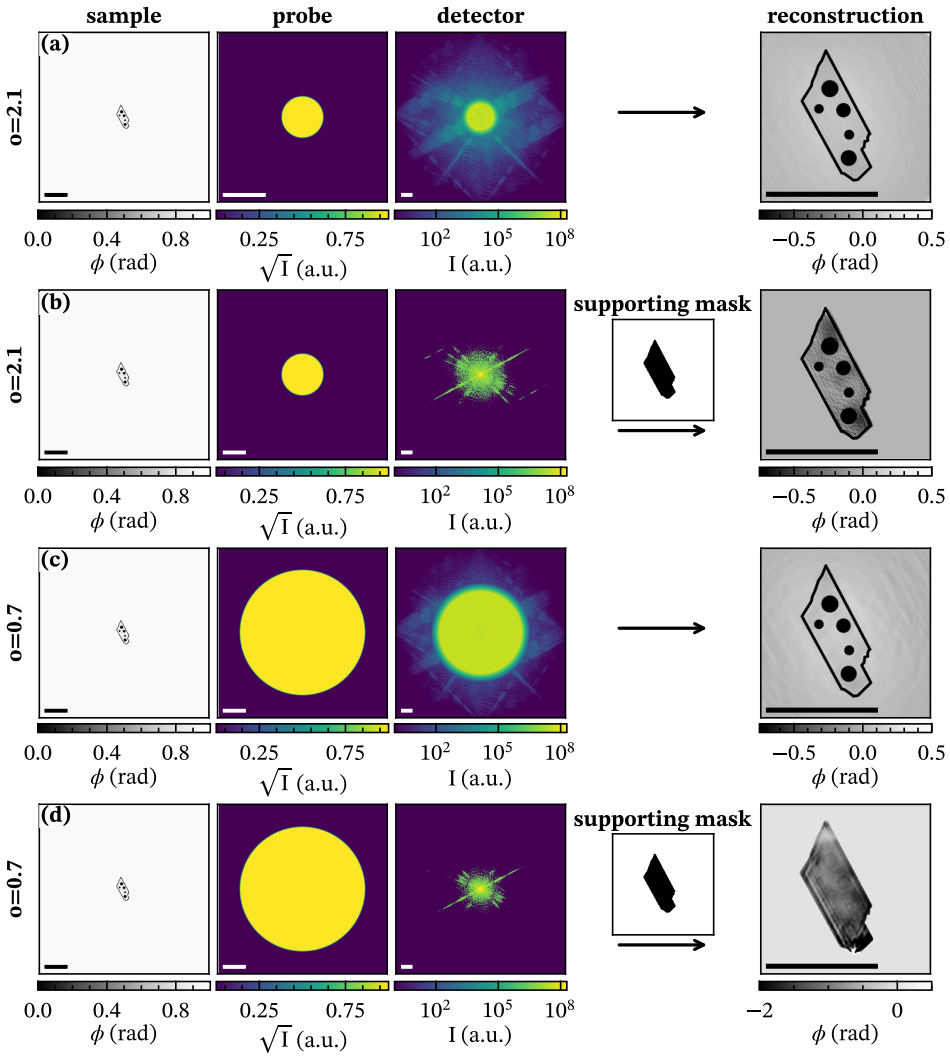

Fig. 5.11: *(caption next page)*

Fig. 5.11 ***(previous page)*****:** Reconstruction from simulated data, for different oversampling ratios, comparing illumination schemes of holography (divergent beam) and classical CDI (parallel beam). The algorithmic implementation proposed in the main text was used in both cases. A pure phase object was simulated (cardiomyocyte phantom), similar to Fig.5.1 of the main manuscript. The object is fully illuminated in both cases. The first column of the figure shows the sample, the second the probe, the third the detector in the far-field and the fourth the reconstructed phase of the object. (a) For the divergent beam illumination and $o = 2.1$, the novel holographic approach yields a successful reconstruction, even without support constraint. (b) For the parallel beam illumination and $o = 2.1$, a good reconstruction is obtained as well, but only when a tight support constraint is applied. The use of this support mask results in a flat background. (c) For the divergent beam illumination and $o = 0.7$, the novel holographic approach still yields a successful reconstruction. (d) For the parallel beam illumination and $o = 0.7$, however, the reconstruction fails, despite a tight support constraint. Scalebars: (detector) $100\Delta_{\mathrm{px}}$ corresponding to a scattering vector $q = 0.06\,\mathrm{nm}^{-1}$, other scalebars $2.5\,\mu\mathrm{m}$.

5.5.9 Probe profile in the sample plane

Figure 5.13 shows the reconstructed sample phase as shown in Fig.5.3(a) of the main manuscript, complemented by the vertical and horizontal probe intensity profiles in the sample plane. Furthermore, the oversampling criterion of $o = 2$ is indicated by the red dashed line/circle. It is apparent that the sample is not only reconstructed successfully in the center region of the probe but also in regions of low intensity towards the edges. This shows that a rather low dose is sufficient to successfully reconstruct the phase of the object using the proposed in-line holography approach. This experimental result is further corroborated with the simulated results shown in Fig. 5.11. The artefacts in the reconstruction of the Siemens star arise from: (i) the presence of detector gaps (inter-module gaps), (ii) low dose at the outer regions, and (iii) residual probe errors due to drift. Despite these effects and in particular low intensities at the boundaries of the field-of-view, even parts of the sample at a distance from the illumination center of up to $6.5\,\mu\mathrm{m}$ are still reconstructed. This corresponds to an oversampling ratio of $o = 0.8$. Within a radius of $4.1\,\mu\mathrm{m}$ from the illumination center, the Siemens star is well reconstructed, corresponding to an oversampling ratio of $o = 1.3$.

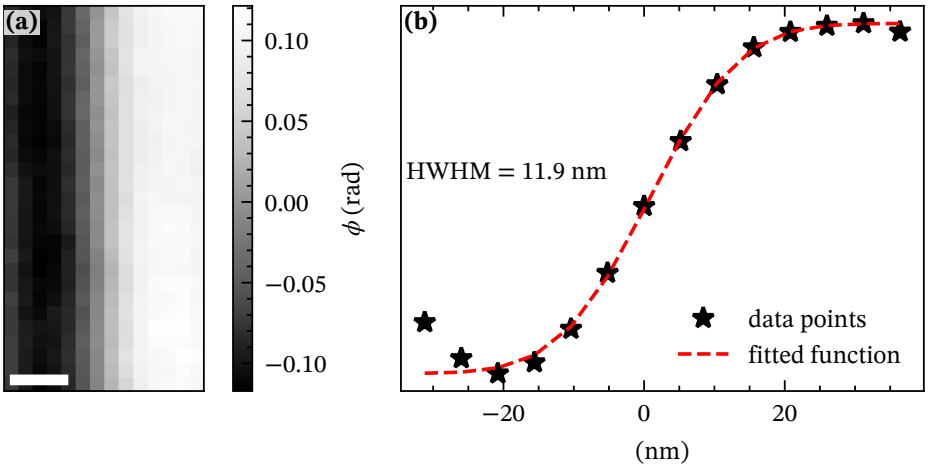

Fig. 5.12: Determination of the resolution based on the edge steepness. (a) Small region of interest of Fig.5.3(c) of the main manuscript. (b) The vertically averaged slope of (a). The resulting edge was fitted using an error function. The fit yields a half width at half maximum (HWHM) of 11.9 nm, in perfect agreement with the resolution determined by FRC in Fig. 5.3 (c) of the manuscript with 11.2 nm. Scalebar: 20 nm.

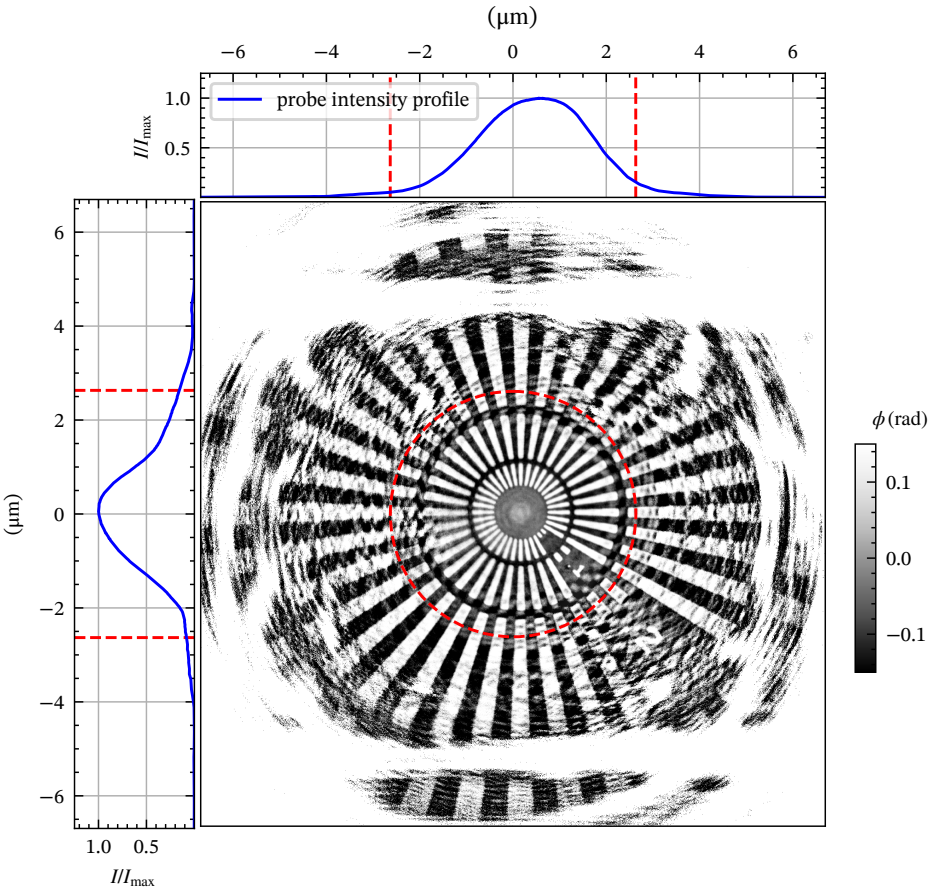

Fig. 5.13: The intensity profile of the probe in the object plane and the reconstructed phase of the object. Furthermore the oversampling condition of $o = 2$ is indicated by the dashed red lines/circle.

Coherent diffractive imaging with diffractive optics

6

JAKOB SOLTAU, MARKUS OSTERHOFF, AND TIM SALDITT

reproduced[1] from Phys. Rev. Lett. 128, 223901 (2022) [SOS22]

We present a novel approach to x-ray microscopy, based on a multilayer zone plate which is positioned behind a sample similar to an objective lens. However, unlike transmission x-ray microscopy, we do not content ourselves with a sharp intensity image instead we incorporate the multilayer zone plate transfer function directly in an iterative phase retrieval scheme to exploit the large diffraction angles of the small layers. The presence of multiple diffraction orders, which is conventionally a nuisance, now comes as an advantage for the reconstruction and photon efficiency. In a first experiment, we achieve sub-10 nm resolution and a quantitative phase contrast.

[1] subject to minor corrections

X-ray microscopy enables imaging of matter at high resolution down to the 10 nm range (see chapter 5 and [Özt+18; Vil+18; Hol+19; De +21]), with chemical sensitivity [Lim+16] and at ultrafast timescales [Ayy+21; Wie+18; Vas+21]. Above all, it offers unique advantages for nondestructive imaging of bulk and optically intransparent samples. For biological matter and complex nanomaterials full-field imaging is particularly suitable, since it can cover large specimens without the need for scanning. Conceptually, there are three very different approaches to full-field x-ray microscopy. The first modern x-ray microscopes, so-called transmission x-ray microscopes (TXMs), were developed in the 1970s. They used Fresnel zone plates (FZPs) as objective lenses to directly image and magnify the sample structure, relying on a sharp image in the detection plane [Sch+80]. To circumvent the problems associated with low diffraction efficiencies and imperfect FZP lenses, coherent diffractive imaging (CDI) was introduced [MSC98; Mia+15], replacing lens-based image formation by an iterative phase retrieval algorithm, to invert a coherent diffraction pattern of a compact sample. For extended samples, the ptychographic variant of CDI proved particularly well suited [Rod+07], which solves the phase problem based on partial overlap between subsequent acquisitions using a finite beam. Despite impressive progress in dose efficiency and fast scanning [Jia+21], overhead due to motor movement still imposes constraints on the scan time and limits the observation of fast dynamic processes. Furthermore, scanning is incompatible with single pulse imaging at free-electron lasers (FELs). The third full-field x-ray microscopy approach, finally, is based on inline holography in a cone-beam geometry (see chapter 5 and [Mok+07; Bar+15; Ces+17]). Because of its adjustable field-of-view (FOV) and resolution, and comparatively well-posed phase problem, it performs very well for tomography of weakly contrasted biological samples [Khi+16; Töp+18].

Notwithstanding the advantages of the more recent lensless approaches to microscopy, it is timely to revisit lens-based x-ray microscopy. Since CDI was proposed 20 years ago, significant progress in nanofabrication has resulted in high resolution and high efficiency zone plate optics, in particular, multilayer zone plates (MZPs) and one-dimensional multilayer Laue lenses (MLL), which can focus an x-ray beam to a size of sub-10 nm (full width at half maximum, FWHM) (see chapter 4 and [Dör+13; Baj+18]). Unfortunately, however, this focusing capability does not directly translate to an equivalent resolution in full-field imaging, due to a number of complications associated with multiple diffraction orders, volume diffraction, remaining aberrations, and the need of Zernike phase rings for phase contrast. At the same time, the recently achieved 10 nm resolution in absorption contrast shows the potential of high resolution

zone plate optics [De +21].

In this Letter we present a novel approach to full-field hard x-ray microscopy, combining conceptional aspects of all three major developments and their corresponding advantages. The proposed method is, in particular, applicable to high brilliance synchrotron sources and uniquely suited to implement high resolution single pulse imaging at FELs. We use an MZP as an objective lens to achieve high resolution, but do not content ourselves with a sharp intensity image; instead, we use a fully quantitative and iterative phase retrieval scheme to reconstruct the sample transmission function. To this end, we use the measured MZP transfer function. This liberates us from the requirement to use perfectly aligned, aberration- and distortion-free optics, and allows us to exploit the full information and numerical aperture (NA) of the diffraction pattern with the sample encoded in near- and far-field intensity distributions. Using this scheme, we experimentally demonstrate sub-10 nm resolution and quantitative contrast of the measured sample. We refer to the imaging scheme as *reporter-based imaging* (RBI), because in contrast to the conventional application of an objective lens to acquire a sharp image of the sample, we use the MZP as a reporter of the near-field behind the sample, rather than trying to obtain a sharp image in the detector plane.

Figure 6.1 illustrates the RBI scheme demonstrated experimentally at the `GINIX` instrument [Sal+15] of the coherence beamline P10 of the PETRA III storage ring (Hamburg, Germany). In Fig. 6.1 (a), the basic optical concept of RBI is shown, with the sample in plane z_{sam} illuminated by a coherent microfocus, with low divergence and a spot size defining the FOV. The reporter structure, here composed of an MZP with focal length f, is positioned behind the sample in plane z_{rep}. The MZP diffracts the incident beam, mostly to the zeroth, +first, and -first order. The zeroth order corresponds to a conventional CDI signal (without MZP). All signals are acquired by the same detector positioned in the far-field at z_{de}. Figures 6.1 (b) and 6.1 (c) show typical full-field diffraction images of the sample corresponding to the same exposure Fig. 6.1 (b) with and Fig. 6.1 (c) without empty beam division. With $|z_{\mathrm{de}} - z_{\mathrm{rep}}| \gg f$ the image plane of the MZP (z_{im}) is close to its focal plane. The distance of the sample to the image plane ($|z_{\mathrm{im}} - z_{\mathrm{sam}}|$) defines the defocus distance for the coherent imaging scheme. In other words, the MZP images the defocus plane onto the detector. This is visible in the empty beam divided detector image shown in Fig. 6.1 (b). Two magnified near-field intensity distributions (inline holograms) are recorded in different areas on the detector at different effective defocus distances corresponding to the +first (upper left corner) and -first (lower right corner) MZP diffraction order. The spatial separation of these signals on the detector is controlled by the off-axis translation of the MZP, as

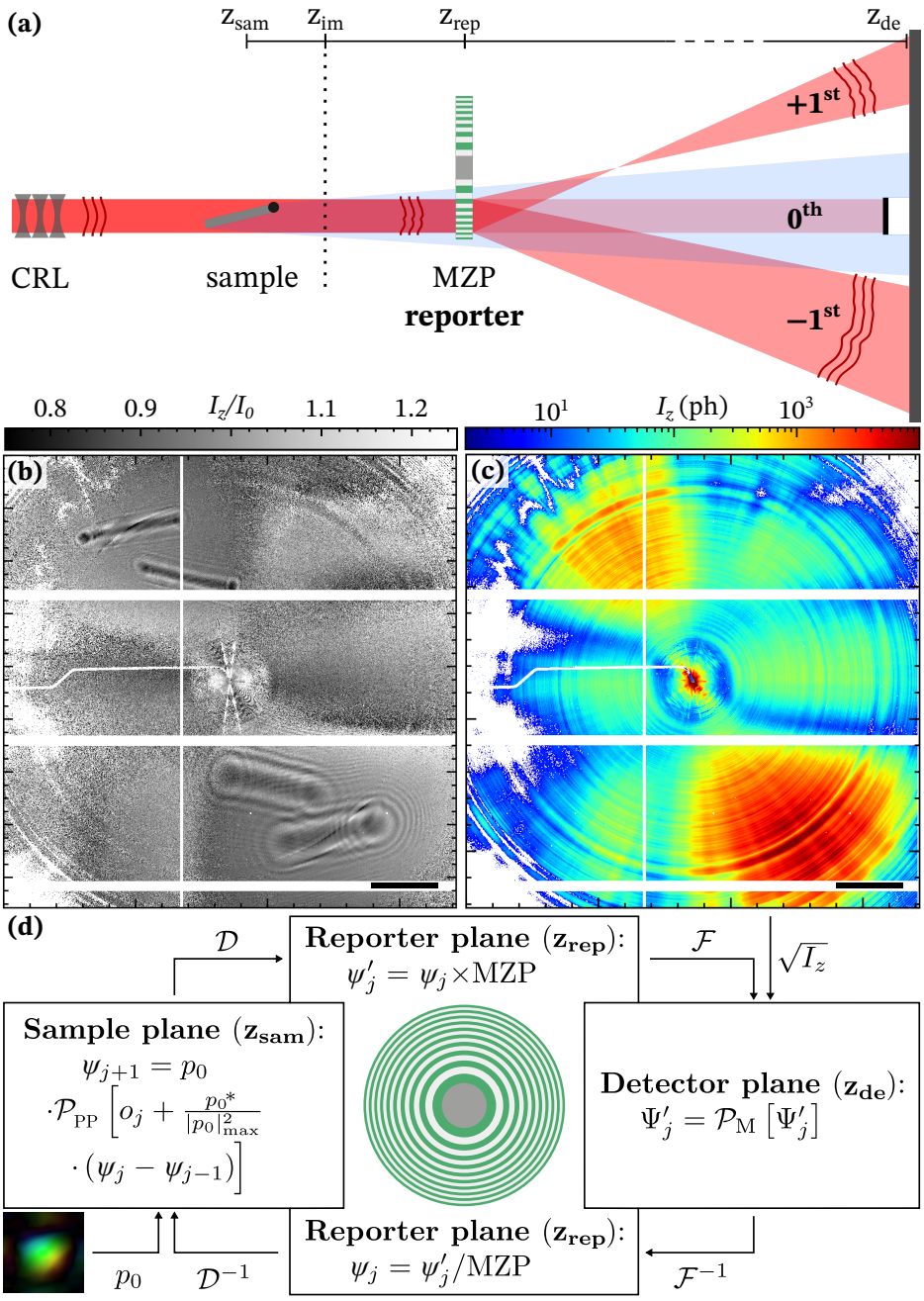

Fig. 6.1: *(caption next page)*

Fig. 6.1 *(previous page)*: (a) Schematic of the RBI setup. A coherent x-ray beam (red) is focused by CRLs onto the sample, here a nanowire (NW), and an MZP is positioned as a reporter in the near-field. The MZP diffracts the beam into the $-$first, $+$first and zeroth diffraction order recorded in the far-field. The blue color indicates the CDI diffraction signal of the sample. (b) The empty divided detector image indicating the three different sample (NW) signals (two holograms and one CDI signal) recorded in a single measurement (linear gray scale). (c) The intensity measurement with the sample (NW) in the beam. This single measurement is used for the sample reconstruction. The acquisition time was 5 s (logarithmic color scale). (d) Outline of the RBI algorithm. $\mathcal{D}$, $\mathcal{D}^{-1}$ denotes the near- and $\mathcal{F}$, $\mathcal{F}^{-1}$ far-field propagators, $\mathcal{P}_{\mathrm{PP}}$ the pure phase and $\mathcal{P}_{\mathrm{M}}$ the magnitude constraint, p_0 the incident illumination function and MZP the transfer function of the MZP. Scalebars: 250 pixels corresponding to a scattering vector $q = 0.15\,\mathrm{nm}^{-1}$.

illustrated in Fig. 6.1 (a). In Fig. 6.1 (c), showing the undivided detector image (I_z) on a logarithmic scale (acquisition time 5 s), the diffraction of the incident beam in the +first and -first order can be distinguished based on the corresponding high-flux areas (color code red). The concentric rings around the center are imprints of the zones of the MZP. Altogether the detector records three different but complementary signals of the sample in a single intensity measurement: a conventional CDI signal visible around the center, and in addition, holograms of the sample encoded in the divergent beams of the +first and -first MZP diffraction orders. The data were acquired at the following configuration and parameters: The undulator beam was monochromatized by a Si(111) channel-cut monochromator to a photon energy of 8 keV and focused by beryllium CRLs with a divergence of 0.05 mrad to a spot size of $3.0 \times 3.7\,\mu\mathrm{m}^2$ (FWHM) defining the FOV. The sample consisted of InP nanowires (NW) with a diameter of 200 nm and a length of $2.8\,\mu$m, terminated by an Au tip at one end, and was deposited on an Si_3N_4 window. The distance between the sample z_{sam} and the MZP z_{rep} was 878 μm. The position of the sample was chosen to be close but not equal to the imaging plane z_{im}. A more detailed discussion on the position z_{sam} can be found in the numerical simulations of chapter 3. The MZP was composed of 784 zones, an outermost zone width of 5 nm, and a focal length of 530 μm [Ebe+14]. The diameter of the MZP was $16.9\,\mu$m with an optical depth of $1.2\,\mu$m. The focus of a similar MZP was characterized by ptychography in chapter 4. The MZP was also mounted on an Si_3N_4 window. The coherent diffraction patterns were recorded with a single photon counting pixel detector (Eiger 4M, Dectris Ltd. Switzerland) positioned at a distance of 5.05 m behind the MZP, with 2167×2070 pixels and a pixel size of $75\,\mu$m.

Figure 6.1 (d) outlines the iterative RBI phase retrieval algorithm operating on a single intensity measurement I_z of the sample, such as the one shown in Fig. 6.1 (c). In addition to the input $\sqrt{I_z}$, the probe function illuminating the sample p_0 and the transfer function of the MZP were used. p_0 and the structure of the MZP were reconstructed by a prior ptychographic scan without sample (see Fig. 6.2). RBI is based on the propagation of the wave field ψ_j between the sample plane z_{sam} and the detector plane z_{de}. But unlike conventional approaches, the propagation is performed not in a single step using a near- or far-field propagator but in three substeps: (i) near-field propagation ($\mathcal{D}$) from z_{sam} to z_{rep} ($\psi_j = \mathcal{D}\left[\psi_j\right]$), (ii) multiplication of the reporter transfer function ($\psi'_j = \psi_j \times \text{MZP}$), and (iii) far-field propagation ($\mathcal{F}$) to z_{de} ($\Psi'_j = \mathcal{F}\left[\psi'_j\right]$). The three-step approach with applied knowledge in each field builds upon the seminal work [Qui+06] to reconstruct a divergent wave field and Ref. [Abb+08] for imaging. In both cases it has been shown that the use of multiple planes in a single-shot approach is beneficial for phase retrieval. As usual, compatibility with the measured data is assured in z_{de} by applying the magnitude constraint: $\mathcal{P}_M\left[\Psi'_j\right] = \sqrt{I_z} \times \Psi'_j/|\Psi'_j|$. The updated wave field (Ψ'_j) is backpropagated using the inverse operations: (iii) $\psi'_j = \mathcal{F}^{-1}\left[\Psi'_j\right]$, (ii) $\psi_j = \psi'_j/\text{MZP}$, and (i) $\psi_j = \mathcal{D}^{-1}\left[\psi_j\right]$. In z_{sam}, the object o_j and probe function p are separated. The separation and the update of o_j is performed equivalent to the standard extended ptychographic iterative engine update function (ePIE) [MR09] as written in Fig. 6.1 (d), in combination with a pure phase constraint P_{PP}, well justified for hard x-ray imaging of nanomaterials such as NWs. The P_{PP} acts on o_j as $\mathcal{P}_{\text{PP}}\left[o_j\right] = \exp\left[i\phi\left(o_j\right)\right]$. Alternatively, depending on the specific imaging problem, other object projectors could be implemented such as range, support, shearlet (sparsity), or homogeneous object constraints [SEL20]. The updated object (o_{j+1}) is multiplied with the initial (not updated) probe function p_0 to generate the updated wave field ψ_{j+1} for the next iteration. Besides the ePIE update scheme of the wave field, different approaches could be used such as alternating projections (AP) [Krü+12] or the relaxed averaged alternating reflector (RAAR) [Luk04]. But importantly, for the reconstruction of the object, the transfer function of the MZP and the probe illumination function have to be known. Both were obtained by ptychography before the single frame acquisition of the sample.

In Fig. 6.2 (a) the reconstructed probe and Fig. 6.2 (b) the phase of the reconstructed MZP are shown. The enlarged regions in Figs. 6.2 (c) and 6.2 (d) show the radially decreasing zone widths of the MZP. The pixel size of the reconstruction is 5.2 nm. The probe illumination function in Fig. 6.2 (a) shows a nearly flat phase in the maximum and side maxima of only low intensity. For the reconstruction, two ptychographic scans

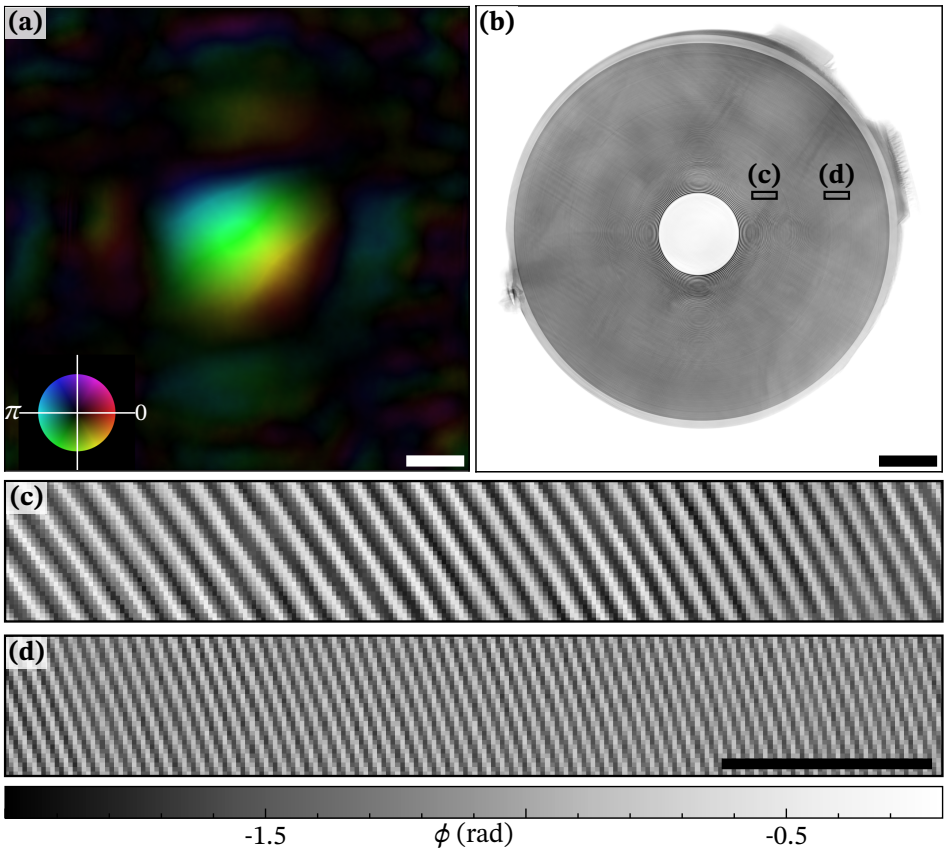

Fig. 6.2: (a) Ptychographic reconstruction of (a) the probe amplitude and phase at z_{rep} with a FWHM of the intensity profile of $3.0 \times 3.7\,\mu\mathrm{m}^2$ and (b) the MZP. The enlargements (c,d) show the radially decreasing zone widths. Scalebars: (a,b) 2.5 µm, (c,d) 250 nm.

(without the NWs) were recorded with 41×41 scan positions, one with a beamstop and high photon flux and one without but with a photon flux reduced by attenuators. The acquisition time per point was 3 s and 1 s for the scan without and with beamstop, respectively. A customized ptychographic code based on the ePIE update approach [MR09] was used. Both scans were used for the reconstruction of the probe and the object in a combined scheme, alternating between the wave field update using the detector image without and with the beamstop. This approach was chosen since the center beam contains primarily information of the probe, whereas the different diffraction orders of the MZP are recorded with a much higher signal-to-noise ratio using no attenuators (with a beamstop).

Figure 6.3 (a) shows the RBI reconstruction of the NWs. Both NWs are resolved, including the Au tip at the end of each wire. The blue circle indicates the area where the intensity of the incident illumination falls below 10 % of the maximum intensity. This results in a lower contrast, as can be seen by the Au tip of the left NW. One-hundred iterations were already sufficient for the reconstruction. Given the redundancy by the three diffraction signals, no artifacts of detector gaps appear in the reconstruction. The enlargement of the tip of the NW on the right side is presented in Fig. 6.3 (b). The round Au tip and the InP main part are resolved. Below the transition from the Au tip to the NW main part, a small change in contrast is visible, resembling rings around the NW (indicated by two blue arrows). With the current measurements, it is very plausible that theses fringes are not a reconstruction artifact but an effect of structural defects within the wires associated with rotational twinning. The observed rings are similar in appearance to scanning and transmission electron microscopy of similar InP NWs [Wal+10]. It should be noted that rotational twinning does not change the electron density, only the crystal structure. Although in coherent diffractive imaging the differences in the phase shift are attributed to a difference in the electron density, the diffraction of photons by small features beyond the NA of the detector could result in small variations in the reconstruction. The resolution of the phase image is determined by an edge fit. Since the NWs are cylindrically shaped objects, the steepest edge of the NW is the transition of the Au tip to the InP main part. The red rectangle in Fig. 6.3 (b) indicates the region of the edge fit. The result is shown in Fig. 6.3 (c) indicating a steepness (half width at half maximum, HWHM) and thus a resolution of 9.8 nm. In Figs. 6.3 (d) and 6.3 (e) the phase shift of the reconstructed NW is compared to the phase shift of a phantom model using the NW design parameters to demonstrate that the phase shift reconstructed by RBI is in quantitative agreement with expectation, up to only a small deviation for the NW Au tip.

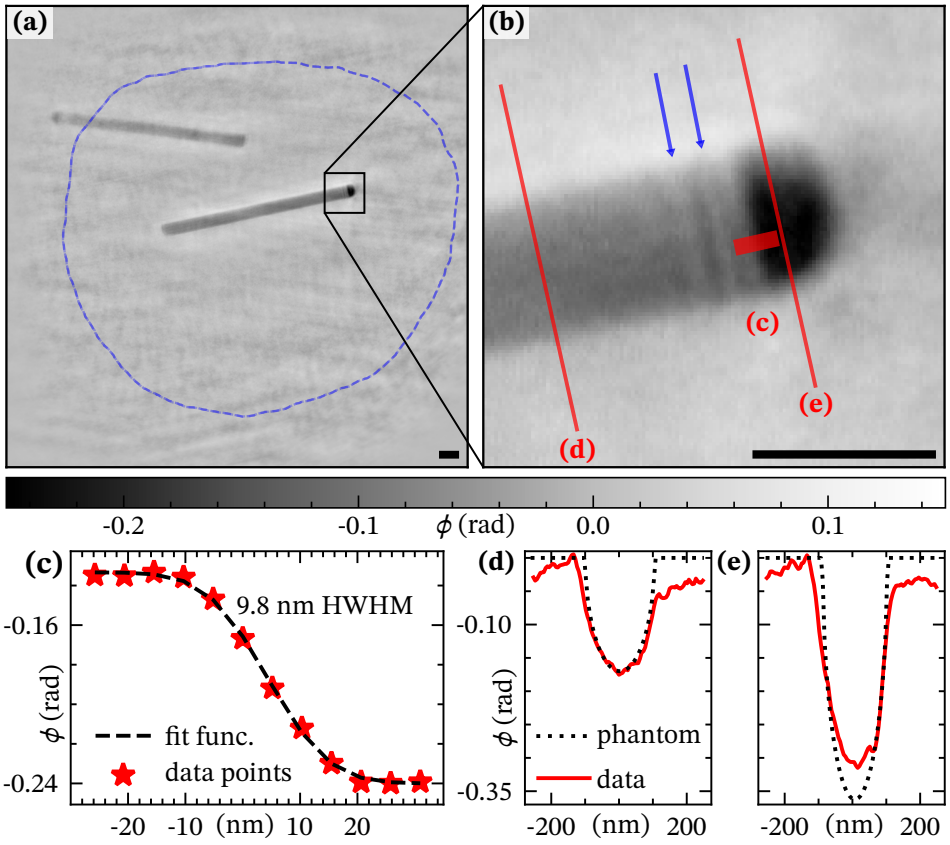

Fig. 6.3: (a) Reconstructed NWs using RBI using the detector image shown in Fig. 6.1 (d). The NWs have a 200 nm diameter and an Au tip at one end. The blue circle indicates the area where the relative intensity is below 10 %. (b) Enlarged region of one NW tip. (c) Error fit of the material edge indicated in (b), resulting in a resolution (half-period) of 9.8 nm. (d) Line profile of the InP main part of the NW and (e) of the Au tip compared with expected phase shifts of a NW phantom. Scalebars: 250 nm.

Next we discuss the RBI scheme, first in comparison to conventional CDI, then to TXM, and finally to inline holography. In comparison to CDI, RBI has the following advantages: (I) Given the strong signals of the MZP diffraction orders, the possible resolution is enhanced with respect to the CDI signal without the MZP which would be limited to a smaller NA for weakly scattering samples. (II) The low and moderate spatial frequencies are encoded not only in a few center pixels but are distributed over large detector areas due to the magnification by the MZP diffraction orders. The fact that the diffraction pattern is not centrosymmetric (broken Friedel symmetry) results in an enhanced 'diversity' and allows the reconstruction of extended samples without the necessity of a support mask. Additionally, at least three different images of the sample structure are encoded in a single diffraction pattern, the +first and -first MZP diffraction orders and the CDI signal. This gives a strong redundancy which can be exploited for the reconstruction and can compensate missing information due to intermodular gaps and a beamstop. In contrast to coherent modulation imaging [Zha+16], here we redefine the purpose of the modulator by exploiting the magnifying capabilities of the MZP given its outermost zone width of 5 nm, as we had already suggested in chapter 3 and [Rob+15]. Thereby we additionally relax the sampling constraint and achieve a high magnification of the sample. A comparison between a sample reconstructed with RBI and reconstructed with conventional CDI, in equal configurations is shown in chapter 6.1.3 in the supplementary materials. Notwithstanding the mentioned advantages of a reporter structure, it must be noted that the corresponding absorption (in the reporter) decreases the dose efficiency. By using an MZP with an optical depth of only 1.2 μm corresponding to an absorption of 13.1 %, we keep this effect at a tolerable level.

In comparison to conventional (incoherent) TXM, RBI has the following advantages: (i) The reconstruction from a single detector image is not limited to either phase or absorption contrast, and (ii) the reconstructed sample has a quantitative contrast. (iii) The best possible resolution is not solely defined by the NA of the reporter but by the maximum diffraction angle which is recorded by the detector. This is because in addition to the magnified near-field, the conventional CDI signal is also recorded. The CDI signal may dominate at high angles for strongly scattering samples and MZPs of moderate resolution. (iv) The full signal of diffracted and nondiffracted photons as well as positive and negative diffraction orders can be used for phase retrieval, increasing photon efficiency and reducing the sample dose. (v) Aberrations of the MZP do not result in distortions of the reconstructed sample structure. Note that unlike x-ray microscopes using point-to-point imaging optics, the depth of field limit

(of the sample) can be extended using multislice approaches similar to ptychography [Tsa+16]. At the same, time we do not want to conceal that TXMs are better suited for low coherence and have demonstrated impressive imaging results in material science with resolutions down to 10 nm in absorption contrast [De +21].

Finally, a discussion of RBI compared to inline holography. Inline holography is a phase-sensitive imaging scheme that can cover large specimens and is due to its dose efficiency well suited for imaging biological tissues [Töp+18]. The resolution of holographic imaging is limited by the source size of the illumination, which can be challenging with respect to wave front artifacts [Hag+17; Mor+20]. Novel approaches which can achieve superresolution with respect to the source spot NA depend on the application of waveguide filtering (see chapter 5). Since a focused beam needs to be coupled into the waveguide, typically with channel dimensions below 100 nm, this scheme is not easily implemented at FELs where high focus intensities could damage the waveguide. Contrarily, the MZP optic of the RBI scheme is illuminated over areas of several micrometers, resulting in lower peak intensities.

In conclusion, we have presented a novel coherent diffractive imaging approach using a reporter structure and achieving a sub-10 nm (half-period) resolution with quantitative phase contrast. The scheme is based on the coherent full-field illumination of a sample, an MZP positioned in the near-field, and the recording of the diffraction pattern in the far-field. We have shown that a single diffraction pattern recorded in this configuration encodes at least three complementary sample signals, the +first and -first MZP diffraction order and the CDI signal around the center beam. By treating all signals in a common reconstruction scheme, we have shown that the highest recorded diffraction angle can be exploited for high resolution, and the simultaneous presence of the positive and negative diffraction orders for a robust reconstruction which can be applied for isolated and nonisolated samples. By using the MZP transfer function directly within the iterative reconstruction scheme, we overcome limitations imposed by aberrations or distortions of the reporter structure. Further, sample to MZP distance allows for an additional control parameter for contrast variation. Finally, we stress that RBI does not require the use of point-to-point imaging optics as a reporter. Instead, the diffractive reporter structure could be favorably designed and generalized to a wider class of diffractive optics suitable to report the wave field.

Acknowledgment

We thank Christian Eberl for the fabrication and Mike Kanbach for the mounting of the MZP. Further, we thank Jesper Wallentin and Lert Chayanun for providing the NWs and the discussions on rotational twinning, as well as Lukas Hrachowina and Magnus Borgström for the NW fabrication. We also would like to thank Michael Sprung, Fabian Westermeier and Anna-Lena Robisch for assistance during the beamtime. Finally, we thank Jan Goeman for discussion and advice in computing.

Funding

Financial support by German Federal Ministry of Education and Research (BMBF) through grant No. 05K19MG2 and the Deutsche Forschungsgemeinschaft (DFG) grants No. SFB 755 and SFB 1456 was gratefully acknowledged.

6.1 Supplementary materials

6.1.1 Experimental setup

The experiment of reporter based imaging (RBI) using a multilayer zone plate (MZP) was performed at the Göttingen instrument of nano-imaging with X-rays (GINIX) at the coherence beamline P10 of the PETRA III storage ring (Hamburg, Germany) [Sal+15]. The 5 m long undulator source is located at a distance of 88.5 m from the experimental hutch. The undulator beam was monochromatized to 8 keV using a $Si(111)$ channel-cut monochromator. The monochromator is positioned at a distance of 50 m in front of the experimental hutch. Using Beryllium compound refractive lenses (CRL) installed in an ultra-high vacuum chamber, the beam is focused to spot size of $3.0 \times 3.7\,\mu m^2$ (Full width at half maximum, FWHM) in horizontal and vertical direction. A detailed analysis of the CRL efficiencies can be found in [Zoz+12]. The MZP was fabricated using the technique of pulsed laser deposition (PLD) [Ebe+14]. The MZP was composed of 784 zones, an outermost zone width of 5 nm and has a diameter of 16.9 µm with an optical depth of 1.2 µm. The MZP was mounted on a Si_3N_4-window. The naowires were also deposited on a a Si_3N_4-window. The MZP-Si_3N_4-window and the NWs-Si_3N_4-window were mounted on the high-resolution stage of the GINIX instrument. The MZP stage was motorized by stick-slip positioners by SmarAct (Oldenburg) for translations (SLC-1730), and a piezo-driven Gimbal mount

for rotations (STT-12.7). The sample stage was motorized using piezo scanner (M-686, N-765 and P-733) by Physik Instrumente Karlsruhe (PI). For detailed information on the stability and scanning precision see [Ost+17a]. The distance of the OSA relative to the focus was 878 µm. The detector was positioned at a distance of 5.05 m downstream from the MZP. A single photon counting Eiger 4m (Dectris Ltd., Switzerland) detector was used with 2068×2162 pixels with a pixel size of 75 µm.

6.1.2 Adjustment of the reconstructed probe amplitude for RBI

To ensure that the probe used as an input parameter for reporter based imaging (RBI), is of equal flux to the single recorded detector image, an update of the probe amplitude $|p_0|$ was performed. For the update we used an empty beam detector image with equal imaging parameters as the recording used for phase retrieval of the NWs and shown in Fig. 6.4 (a). Parameters which were changed with respect to the ptychographic scans were a longer acquisition time of 5 s, no attenuators and a smaller beam stop. The amplitude of the probe was updated by propagating ($\mathcal{F}$) the ptychographic reconstructed probe to the detector plane (z_{De}), performing a magnitude constraint using the empty beam detector image and subsequently propagating the probe back ($\mathcal{F}^{-1}$) to the MZP plane (z_{Rep}). A single iteration to update the amplitude of the probe was sufficient.

6.1.3 Comparison of RBI with conventional CDI

Figure 6.4 shows the comparison of an intensity measurement and its corresponding reconstruction in a coherent diffractive imaging (CDI) configuration (a,b) and in the proposed RBI configuration (c,d). In (a) only the sample (two NWs) is positioned in the beam. In (c) the sample (the same two NWs) and the reporter (MZP) are placed in the beam. Except for the reporter, the configuration and the image acquisition specifications are identical in (a) and (c). In both cases, the illumination time was 3 s, the other parameters can be found in the main manuscript and in section 6.1.1. The reconstruction of the sample structure using RBI (d) is described and discussed in detail in the main manuscript and shown here solely for comparison. The reconstructed NWs using conventional CDI are shown in (b). To achieve comparability, the reconstruction procedure is identical to RBI with the following three differences: (i) the propagation from the sample plane (z_{Sam}) to the detector plane (z_{De}) is performed in a single step using a Fourier-transformation (FFT). (ii) In the sample plane (z_{Sam}) an additional constraint is applied, the support constraint. The necessary mask was generated using

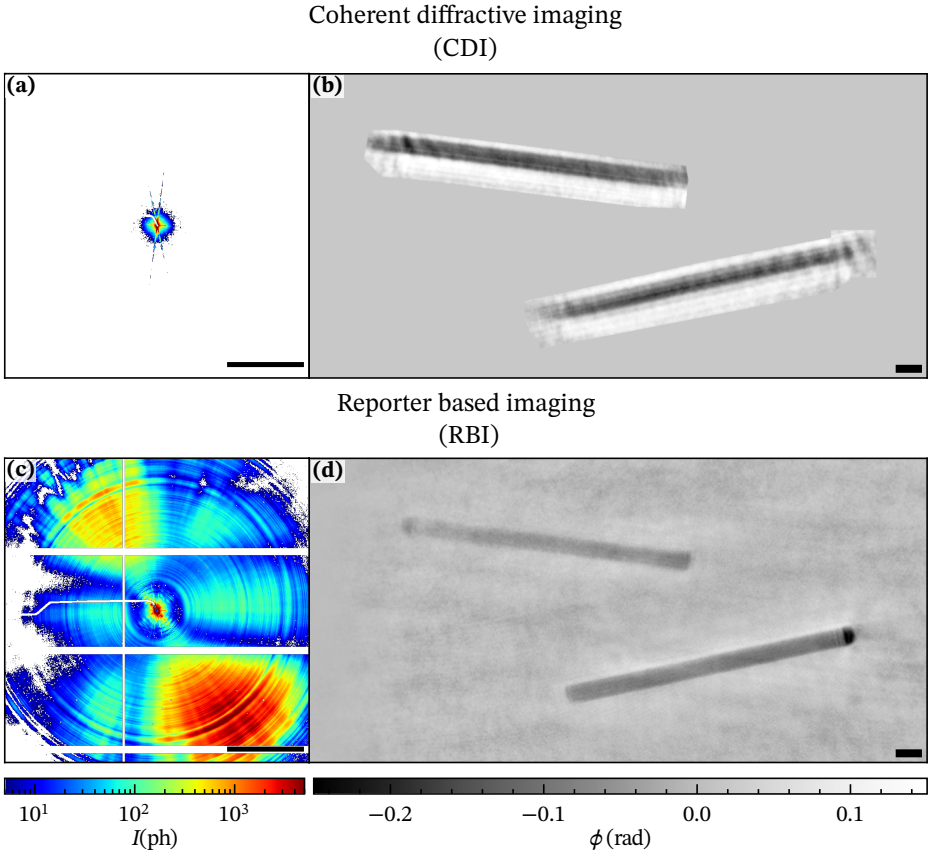

Fig. 6.4: (a) The intensity measurement in a conventional CDI configuration with only the sample (NW) in the beam. (b) The corresponding reconstruction of the sample structure using the CDI intensity pattern shown in (a). (c) The intensity measurement in the RBI configuration with the sample (NW) and the reporter (MZP) in the beam. (d) The corresponding reconstruction of the sample structure using the RBI intensity pattern shown in (c). In case (a) and (c) the illumination time was 3 s. (a,c) and (b,d) use the same colorbar. Scalebars: (a,c) 411 pixels, corresponding to a scattering vector $q = 0.25\,\mathrm{nm}^{-1}$, (b,d) 250 nm

prior knowledge given by the RBI reconstruction of the sample. Alternatively a shrink-wrap approach could be used as well [Mar+03]. All sample values outside the mask were set to exp $(i \cdot 0)$. (iii) 10000 iterations were performed (RBI 100 iterations). The CDI reconstruction of the two NWs shows that the strong diffraction signal along the longitudinal NWs edges results in a successful reconstruction of the InP-main part. Contrarily, the tip and the end of both NWs are not well resolved. The diffraction signal encoding their positions is superimposed by the non-diffracted photons of the parallel beam (e.g. side-maxima and air scattering). This also results in a blurry reconstruction of the Au-tip. Furthermore the InP-main part is not-homogeneous which is almost certainly a reconstruction artefact. In sharp contrast, the RBI-reconstruction (d) is sharp and homogeneous, even though no support constraint is used! The tips and ends are well resolved, and a quantitative separation of the Au-tip from the InP-main part can be seen.

6.1.4 Alternative treatment in terms of conventional inline holography

Figure 6.5 shows the results of the phase retrieval processes of (a,b) the magnified hologram in the -1st MZP diffraction order, and (c,d) using the RBI scheme as described in the main manuscript. The RBI reconstruction is shown here only for the comparison. In both cases shown in Fig. 6.5 the same intensity measurement of the sample was used with an acquisition time of 5 s. The only difference is, that for the case of (a,b) this intensity pattern was divided by an empty beam measurement. The reconstruction shown in (a,b) presents the case of idealising the MZP as magnifying optics to image the hologram of the sample. For the reconstruction of the near-field, a conventional holographic phase retrieval approach is chosen using the contrast transfer function (CTF) [Clo+99] scheme, but without using the MZP transfer function. Since the reconstruction is performed in an effective geometry, we content ourselves with the hologram of the -1st diffraction order. To cope with the apparent astigmatism of the MZP, two different Fresnel numbers for the vertical and horizontal axis are used, $\mathrm{Fr_v} = 2.85 \cdot 10^{-4}$ and $\mathrm{Fr_h} = 3.20 \cdot 10^{-4}$ respectively. Nevertheless an astigmatism in the reconstruction is still apparent. Additionally the reconstruction has a low signal-to-noise ratio since only one MZP diffraction order is used. For the reconstruction using RBI, the full detector signal was used. The result is shown in Fig. 6.5 (c,d) with a resolution of sub-10 nm as discussed in the main manuscript. This demonstrates that if the MZP is used to generate a magnified hologram, the large numerical aperture of

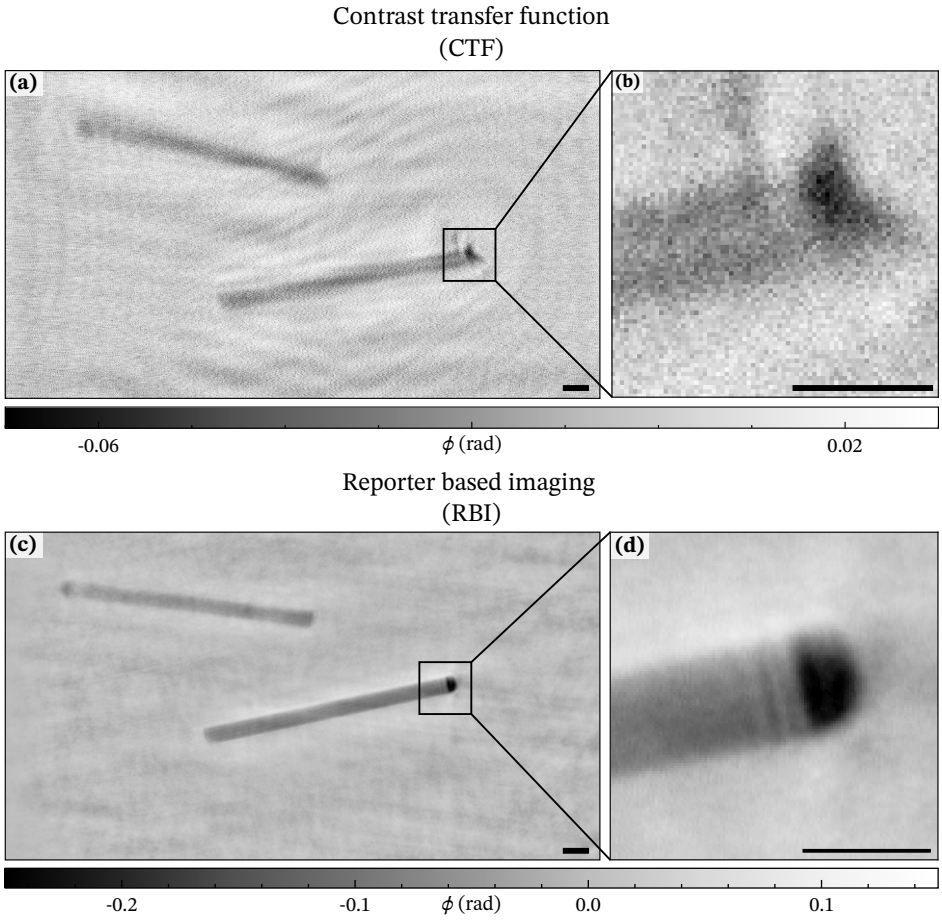

Fig. 6.5: (a) NWs reconstructed using a conventional phase retrieval process based on the contrast transfer function (CTF). The reconstruction is performed based on the empty beam divided detector image shown in Fig. 6.1 (b) in the main manuscript. As a hologram, the area of the -1st MZP diffraction order was used. The NWs have a 200 nm diameter and a Au-tip at one end. (b) Enlarged region of one NW tip shown in (a). (c) The same NWs, but reconstructed using RBI and the single intensity pattern shown in Fig. 6.1 (c) in the main manuscript. (d) Enlarged region of one NW tip shown in (c). Pixel size (a,b) 7.9 nm and (c,d) 5.2 nm. Scalebars: 250 nm.

the MZP and its small layers can not be exploited, given the substantial aberrations and distortions. Furthermore, it should be noted that the reconstructed phase contrast is far from being quantitative. At the same time it must be mentioned that the MZP was not designed as an objective lens and that we used the MZP in an off-axis geometry which can cause astigmatism [CB20]. However, for the optic and parameters of the present experiment, comparing Fig. 6.4 (b) and Fig. 6.5 (a,b) indicates the advantages of encoding different sample information in a single diffraction pattern acquired in the RBI scheme.

Conclusion

7

In this thesis we have developed novel imaging schemes for hard x-ray microscopy. We have simulated the novel techniques and demonstrated sub-10 nm spatial resolution experimentally. We have performed experiments using two different concepts of x-ray microscopy, firstly scanning the sample with a small focal spot, and secondly coherent full-field imaging.

In chapter 3 we have investigated recently developed MZPs and their one dimensional counterpart MLLs which are able to focus hard x-rays to small focal spot sizes given their large numerical aperture (NA). We simulated the propagation of an x-ray wavefield inside multilayer structures using the finite difference method. The simulated MZPs and MLLs had smallest zone widths of down to 2.5 nm and a thickness in propagation direction of up to 15 μm. With the help of simulations, we have shown that the application of the 'classical' zone plate structure cannot simply be adapted for multilayer optics with smallest zone widths. The structure needs to be adapted to volume diffraction effects to reach smallest focal spot sizes and to achieve high efficiencies. We have studied these volume effects, and have shown the transition from a regime of guiding modes observed at larger zone widths (25 nm) to the formation of standing waves at small zone widths (3 nm). The standing waves are well known as *Pendellösung* from the analytical theory of dynamical diffraction. Furthermore, we have shown that an MZP with wedged geometry and an optical depth of half the Pendellösung period can reach high focusing efficiencies. Simulations of periodic multilayer structures have indicated that diffraction efficiencies can go up to nearly 100 %[1] in only one diffraction order. The latter is especially of interest for x-ray optics as it would eliminate the necessity of using apertures between the optics and the sample, such as the order sorting aperture (OSA). Furthermore, we have shown that point focusing of the incident beam can be achieved not only using a fully illuminated MZP or two crossed MLLs, but also using an MZP illuminated in an off-axis geometry. The off-axis configuration has the advantage that the focus is separated from the non-diffracted primary beam, which is beneficial in terms of contrast. In all cases, we showed that the

[1] If absorption is neglected.

size of the focus is a function of the NA of the illuminated multilayer optics, with only small variations in the focusing efficiency. This changes, however, when absorption is taken into account. In this case, the efficiency of the MLLs is reduced by about a factor of two compared to MZPs since MLLs need two subsequent optics for point focusing.

In chapter 4, we have performed experiments to characterize the focus of a fully illuminated MZP and an MZP illuminated in an off-axis geometry. In both cases the outermost zone width was 5 nm, and in both cases we have performed the characterization using the well established method of ptychography. For the case of the fully illuminated MZP we have measured a focus size of $8.4 \times 9.6\,\mathrm{nm}^2$ at a photon energy of 15 keV. For the case of the off-axis illuminated MZP we measured a focus size of $16 \times 28\,\mathrm{nm}^2$ at a photon energy of 13.8 keV. Despite the fact that both optics have the same outermost zone width, the extent of the illuminated area differs (i.e. the NA) which results in the difference in the focus size. The advantage of the off-axis configuration, however, is the extended working distance between the sample and the OSA. Additionally, no beam stop is needed in the center, which is usually the area of the highest photon flux. This will become even more relevant when highly efficient MZPs with only one diffraction order will be fabricated. This would enable imaging without any further aperture. In a first step, we have established the approach of the off-axis illuminated MZP to increase the distance between the OSA and a sample of nanowires. The nanowires were contacted by bond wires protruding from the substrate, and thereby further reducing the already small working distance. This made a scanning experiment in the configuration of a fully illuminated MZP impossible. We measured the x-ray beam induced current (XBIC) in single nanowires, a measurement which benefits from a low background signal. For the first time we have recorded a two dimensional mapping of the InP nanowires charge carrier distribution under various flux and applied bias settings. The measurement benefited from the small focal spot size, demonstrating it's superiority over electron-beam induced current (EBIC), where the resolution is inherently limited by the electron-electron scattering rather than the focus size of the beam [Stu+15]. The low background of the off-axis MZP makes it highly suitable for x-ray fluorescence, diffraction and STXM measurements. We have demonstrated the feasibility and advantages of the off-axis illumination configuration and provided experimental evidence for a dedicated off-axis MZP, combining the advantages of off-axis illuminated optics, such as MLLs, and single point focusing optics, such as MZPs.

In chapter 5 we have developed and demonstrated the novel concept of super-resolution x-ray in-line holography. X-ray holography is well suited for three-dimensional imaging

since it covers a large field of view without the necessity of scanning, as shown in several applications [Töp+18; Eck+20]. Furthermore, the single shot approach makes it also applicable for the quasi-instantaneous image acquisition of pulsed sources such as XFELs [Hag+21; Vas+21]. However, in-line holography is limited in resolution by the NA of the cone-beam. We have presented a novel in-line holography approach which offers super-resolution with respect to the NA of the illumination, and at the same time does not need the usual empty beam correction step of in-line holography. This was achieved by illuminating the sample with a strongly divergent cone beam emerging from a confined source spot. For the phase retrieval we have used the image information encoded in the coherent diffraction pattern outside of the primary beam and the image information encoded in the holographic self-interference in the center. Both signals have been treated in a common image reconstruction scheme. For the reconstruction it was sufficient to use only the constraint of a known probe, which we retrieved by using ptychography or alternatively in a single shot approach. We have demonstrated super-resolution in-line holography by imaging a test structure with a resolution of 11.2 nm (HWHM) using a waveguide source size of 30.4 nm (FWHM). In contrast to in-line holography this approach is not limited in its resolution by the geometric magnification, and with respect to CDI, we have achieved sub-sampling capability. This enables imaging with a large field of view (here $13 \times 13\,\mu\text{m}^2$) and without constraints for an isolated sample. We have shown that the acquisition time could be reduced down to 0.2 s without significant compromises in resolution. Furthermore, we have taken the first step for the application of super-resolution in-line holography for tomography of biological specimens, by imaging a cardiac cell with a large field of view of up to $50 \times 50\,\mu\text{m}^2$.

In chapter 6 we have demonstrated a second novel imaging approach by performing coherent diffractive imaging using an MZP similar to an objective lens. We refer this imaging scheme as reporter based imaging. We have iteratively reconstructed an image of two nanowires with a resolution of 9.8 nm (HWHM) at a photon energy of 8 keV. In the experiment, we have illuminated the nanowires with an incident beam of low divergence and have positioned an MZP (the reporter) in the near-field of the sample. The acquired far-field diffraction pattern encodes at least three different signals: The direct CDI signal of the sample, and the $+1^{\text{st}}$ and -1^{st} diffraction order of the MZP imprinted with the holographic self-interference of the sample. The encoded low and moderate spatial frequencies can be observed in the acquired detector images as well as in the simulations performed in chapter 3. As in super-resolution in-line holography, we can exploit the redundancy of the signals to image non-isolated samples. In addition,

we have reconstructed the transfer function of the MZP using ptychography. By using the obtained transfer function within the iterative phase retrieval process, we can reconstruct the sample without any distortions or artifacts introduced by aberrations of the MZP, or individual zones of the MZP imprinted in the diffraction pattern. This liberates us from recording a sharp image, as it is the case for a conventional TXM or an optical microscope. Furthermore, the possible image resolution is defined by the detector NA and no longer limited by the NA of the MZP.

In chapter 5 and 6 we have presented two novel coherent full-field imaging schemes, super-resolution in-line holography and reporter based imaging. In both schemes, we exploit the image information encoded in the far-field diffraction and in holographic self-interference, in a joint image reconstruction approach. We have shown that this is of advantage, as it allows to image non-isolated samples with a resolution limit defined by the highest diffraction angle.

The two full-field imaging schemes presented here, super-resolution in-line holography and reporter based imaging, have the potential to be further improved by reconstructing different diffraction patterns of a subsequent measurement in a joint approach. In the presented reconstruction scheme the probe is determined at the beginning or at the end of a scan. The advantage of a joint reconstruction scheme, however, would be that the probe can be adjusted to fluctuations of the illumination which can occur during a scan. Furthermore the probe can be reconstructed with a higher precision and a better signal-to-noise ratio. This is especially of interest for tomographic data sets, as these contain subsequent images of the same sample each under a different orientation. One could develop this approach even further, by reconstructing the full sample volume in a joint scheme as already shown for in-line holography in [Ruh+14; RS16]. Advanced propagation methods, such as the introduced finite-difference methods, could enable imaging of samples with multiple scattering.

In conclusion, we have presented an off-axis configuration of the MZP for probing samples with a small x-ray focus suitable for high-resolution mapping using the contrast diversity of STXM. Additionally, we have presented two novel full-field imaging approaches with resolutions only limited by the highest diffraction angle, and suitable to imaging non-isolated samples. Altogether, this opens a brilliant perspective for x-ray imaging with the current progress in coherent x-ray sources such as free-electron lasers and diffraction limited storage rings.

Appendix

A.1 Selection of source code for chapter 3

Source code for *Python 3.7*.

A.1.1 Simulation of a wavefield propagating through an MZP

Numerical implementation of a wavefield diffracted by a multilayer zone plate.

```
import numpy as np
import xraylib as xrl
import matplotlib.pyplot as plt
from tqdm import tqdm
import fresnel.propagate as propagate
import fresnel.vacuum as vac
import fresnel.hankel

% Link to implementation of the fresnel code in C++ and Python, which is
    made available under an open license at https://gitlab.gwdg.de/irp/
    fresnel.

% The simulation is performed in units of wavelength

def braggAngle(mlWidth):
    '''

    returns the Bragg angle for a given layer width
    mlWidth: layer width


    '''
    return 0.25/mlWidth

def getMaxPos(a):
    '''

    calculates the position of the maximum value in an arras
```

```
    a: input array

    '''
    return np.unravel_index(np.argmax(a, axis=None), a.shape)

def cropToCenter2D(a,cropx,cropy):
    '''

    crops an array to a specific size around the center
    a: input array
    cropx: crop in x direction
    cropy: crop in y direction

    '''
    y,x = a.shape
    startx = x//2-(cropx//2)
    starty = y//2-(cropy//2)
    return a[starty:starty+cropy,startx:startx+cropx]

def zonePlateRadius(zoneNumber,focallength,geometry='flat',zStep=0,
    tiltAnlge=0):
    '''

    calculates the radius of a zone plate
    zoneNumber: zone number of the zone plate
    focallength: focal length of the zone plate
    geometry: geometry of the zone plate (flat,tilt,wedge)
    zStep: position of depth in propagation direction
    tiltAnlge: if the geometry is tilt, then the specific tilt angle
    zoneRadius: radius of the zone

    '''
    zoneRadius    = np.sqrt(zoneNumber*focallength + (zoneNumber/2)**2)
    if geometry == 'tilt':
        zoneRadius = zoneRadius - (zStep*np.arctan(tiltAngle))
    elif geometry == 'wedge':
        zoneRadius = zoneRadius - (zStep*zoneRadius/(2*focallength))
    return zoneRadius

def zonePlateNumber(zoneRadius,focallength,geometry='flat',zStep=0,
    tiltAngle=0):
    '''

    calculates the number of the zone as a function of the radius
    zoneRadius: radius of the zone plate
```

```
70      focallength: focal length of the zone plate
71      geometry:  geometry of the zone plate (flat,tilt,wedge)
72      zStep: position of depth in propagation direction
73      tiltAngle: if the geometry is tilt, then the specific tilt angle
74
75      '''
76      if geometry == 'tilt':
77          zoneRadius = zoneRadius + (zStep*np.arctan(tiltAngle))
78      elif geometry == 'wedge':
79          zoneRadius = zoneRadius + (zStep*zoneRadius/(2*focallength))
80      zoneNumber = (2*(np.sqrt(focallength**2+zoneRadius**2)-focallength))
81      return zoneNumber.astype(dtype=np.uint16)
82
83  def createZonePlateIndex3D(zp0,zpN,focallength,Ny,Nx,dy,dx,geometry='flat'
        ,zStep=0,tiltAnlge=0):
84      '''
85
86      creates a 2D array for a binary zone plate, for the 3D simulation
87      zp0: smallest zone number of the zone plate
88      zpN: largest zone number of the zone plate
89      focallength: focal length of the zone plate
90      Ny: number of pixels of the simulated array in y
91      Nx: number of pixels of the simulated array in x
92      dy: pixel size in y
93      dx: pixel size in x
94      geometry: geometry of the zone plate (flat,tilt,wedge)
95      zStep: position of depth in propagation direction
96      tiltAnlge: if the geometry is tilt, then the specific tilt angle
97
98      '''
99      materialIndex = np.ones((Nx,Ny),dtype=np.int8)
100     x = abs((np.linspace(0,Nx-1,Nx)-int(Nx*0.5)))*dx
101     y = abs((np.linspace(0,Ny-1,Ny)-int(Ny*0.5)))*dy
102     xx, yy = np.meshgrid(x, y, sparse=True)
103     radiusIndex = np.sqrt(xx**2 + yy**2)
104
105     nmIndex = np.zeros((Nx,Ny),dtype=np.uint16)
106     nmIndex = zonePlateNumber(radiusIndex,focallength,geometry,zStep)
107
108     rLw = zonePlateRadius(zp0,focallength,zStep=zStep,geometry=geometry)
109     rUp = zonePlateRadius(zpN,focallength,zStep=zStep,geometry=geometry)
110
111     #materialIndex[nmIndex%2 == 0] = 2
112     materialIndex.fill(2)
113     materialIndex[nmIndex%2 == 1] = 3
```

```
114     materialIndex[np.logical_or(radiusIndex<rLw, radiusIndex>rUp)] = 0
115
116     return materialIndex
117
118 #### Basic simulation script for the propagation of a wavefield through an
        MZP ####
119
120 # basic setup parameters
121 energy     = 13.8 # keV
122 wavelength = 1.2398 / (energy * 1e3) *1e-6 # m
123
124 # specifications of the material
125 density_ZrO2  = 6.2 #xrl.ElementDensity(xrl.SymbolToAtomicNumber('ZrO2'))
126 density_Ta2O3 = 12.16#xrl.ElementDensity(xrl.SymbolToAtomicNumber('Ta2O3')
      )
127 n_ZrO2  = xrl.Refractive_Index('ZrO2', energy, density_ZrO2)
128 n_Ta2O3 = xrl.Refractive_Index('Ta2O3', energy, density_Ta2O3)
129
130 # calculation of the the half Pendellösung period
131 pendelLength = np.pi*wavelength/(4*abs(np.real(n_ZrO2)-np.real(n_Ta2O3)))
132
133 ######### FULL MZP #########
134 ## simulation box basics
135 # pixel sizes
136 dx = 0.35e-9/wavelength
137 dy = np.copy(dx)
138 dz = 50e-9/wavelength
139
140 # size of he computational field of view
141 Lx = 9.5e-6/wavelength
142 Ly = np.copy(Lx)
143 Lz = pendelLength/wavelength
144
145 # calculation of the number of pixels
146 Nx = int(Lx/dx)
147 if Nx % 2:
148     Lx = (dx+Lx)
149     Nx = int(Lx/dx)
150 Ny = np.copy(Nx)
151 Nz = int(Lz/dz)
152
153 # specifications of the MZP
154 innerZoneWidth = 50e-9/wavelength
155 outerZoneWidth = 10e-9/wavelength
156 focallength    = 1e-3/wavelength
```

```
157
158 # calculate the zone plate number from the zone width
159 zp0 = int(focallength/(2*innerZoneWidth)**2)
160 zpN = int(focallength/(2*outerZoneWidth)**2)
161
162 ## Define the incident illumination as plane wave
163 u0 = np.ones((Nx,Ny),dtype=np.complex128)
164 materialArrayZP = np.ones((Nx,Ny),dtype=np.complex128)
165
166 zStep   = 0
167
168 # create an index array of the MZP
169 zpIndex = createZonePlateIndex3D(zp0,zpN,focallength,Ny,Nx,dy,dx,zStep=
        zStep,geometry='wedge')
170
171 # create a material array of the MZP
172 materialArrayZP = np.zeros((Nx,Ny),dtype=np.complex128)
173 materialArrayZP = np.piecewise(materialArrayZP, [zpIndex==1 , zpIndex==2,
        zpIndex==3, zpIndex==0], [1,n_ZrO2,n_Ta2O3,1])
174
175 # define the FD propagtor for the MZP
176 propMat = propagate.FDPropagator3d(materialArrayZP, u0, dz, dy, dx)
177 field   = np.zeros((Nx,Ny), dtype=np.complex128)
178 field[...] = u0
179
180 # propagate the wavefield through the MZP
181 for iz in tqdm(range(1, Nz),position = 0):
182     boundary = (0, 0, 0, 0)
183     zStep   = iz*dz
184     zpIndex = createZonePlateIndex3D(zp0,zpN,focallength,Ny,Nx,dy,dx,zStep
        =zStep,geometry='wedge')
185     materialArrayZP = np.piecewise(materialArrayZP, [zpIndex==1 , zpIndex
        ==2, zpIndex==3, zpIndex==0], [1,n_ZrO2,n_Ta2O3,1])
186     field   = propMat.step(materialArrayZP, boundary)
187
188 # define the propagation distance in the vicinity of the focal spot
189 Lz = focallength*0.9
190 Nz = 1
191 dz = Lz/Nz
192 # calculate the fresnel number
193 frNum = dx**2/dz
194
195 # chose the fresnel propagator with the suitable sampling constraint
196 if dx**2 > dz/Nx:
197     print('TF')
```

```
    propVac = vac.FresnelTFPropagator(field.shape, frNum)
elif  dx**2 < dz/Nx:
    print('IR')
    propVac = vac.FresnelIRPropagator(field.shape, frNum)
else:
    print('TF or IF')

# propagate wave field to the vicinity of the focal spot
for iz in tqdm(range(Nz),position = 0):
    field = propVac(field)

# parameters for propagating IN the vicinity of the focal spot
Lz = focallength*0.2
Nz = 200
dz = Lz/Nz
frNum = dx**2/dz
Nx2 = 2048*3

fieldVa2 = np.copy(cropToCenter2D(field,Nx2,Nx2))

# chose the fresnel propagator with the suitable sampling constraint
if dx**2 > dz/Nx2:
    print('TF')
    propVac = vac.FresnelTFPropagator(fieldVa2.shape, frNum)
elif  dx**2 < dz/Nx2:
    print('IR')
    propVac = vac.FresnelIRPropagator(fieldVa2.shape, frNum)
else:
    print('TF or IF')

intVaSave  = np.zeros((fieldVa2[::,::].shape[0],fieldVa2[::,::].shape[1],
    Nz), dtype=np.float64)
intVaSave[::,::,0] = np.copy(abs(fieldVa2[::,::])**2)

# propagate in the vicinity of the focal spot
for iz in tqdm(range(Nz),position = 0):
    fieldVa2 = propVac(fieldVa2)
    intVaSave[::,::,iz] = np.copy(abs(fieldVa2[::,::])**2)


# save the different fields of the focus
[yMaxPos,xMaxPos,zMaxPos] = getMaxPos(intVaSave)
np.save('MZPIntFocus_CutSum0', np.squeeze((abs(intVaSave[yMaxPos,::]))))
np.save('MZPIntFocus_CutSum1', np.squeeze((abs(intVaSave[::,xMaxPos]))))
np.save('MZPIntFocus_ProfileSum0', np.squeeze(np.sum(abs(intVaSave),0)))
```

```
np.save('MZPIntFocus_ProfileSum1', np.squeeze(np.sum(abs(intVaSave),1)))
[yMaxPos,xMaxPos,zMaxPos] = getMaxPos(intVaSave)
np.save('MZPIntFocus_Center', abs(intVaSave[::,::,zMaxPos]))
```

A.2 Selection of source code for chapter 5

Source code for *MATLAB 2020b*.

A.2.1 Implementation of the iterative reconstruction of the waveguide exit wavefield

The reconstruction approach is similar to [Krü+12] and [Mar07].

```
function [uOutWG] = startField(detectorAmp,SupportWG,SupportFF,lambda,Ni)

% Function for the basic iterative reconstruction
% of the waveguide exit wavefield
% The approach is based on the error reduction scheme
%
% detectorAmp: amplitude of the detector
% SupportWG: support/mask in the waveguide exit plane
% SupportFF: support/mask in the detector plane (e.g. detector gaps, beam
    stop)
% zGau: the dis
% Ni: number of iterations
% uOutWG: reconstructed wavefield
%

% defining the initial parameters
detectorAmp = single(ifftshift(ifftshift(detectorAmp,1),2));
uOutWG      = complex(zeros(size(SupportWG),'single'));
uOutWG      = PMwithMask(uOutWG,SupportFF,detectorAmp);
uOutWG      = ifft2(uOutWG);
SupportFF   = ifftshift(ifftshift(SupportFF,1),2);

% iterative reconstruction
tic
for ii = 1:Ni
    uOutWG  = fft2(uOutWG);
    uOutWG  = PMwithMask(uOutWG,SupportFF,detectorAmp);
    uOutWG  = ifft2(uOutWG);
    uOutWG  = PS(uOutWG,SupportWG);
```

```
    uOutWG  = (fliplr(uOutWG) + uOutWG)*0.5;
    fprintf(' %d ',ii); toc
end

end
```

```
function [uOut] = PMwithMask(uIn,Mask,Amplitude)

% Preform of the magnitude constraint with a mask
% to be used in the detector plane
%
% uIn: input wavefield
% Mask: field of the mask
% Amplitude: array of the amplitude for the update
% uOut: updated output field

uOut = uIn;
uOut(Mask==1) = Amplitude(Mask==1).*exp(1i.*angle(uIn(Mask==1)));

end
```

```
function [uOut] = PS(uIn,Mask)

% Preform of the support constraint with a mask
% to be used in the sample plane
%
% uIn: input wavefield
% Mask: field of the mask (e.g. the shape of the waveguide exit)
% uOut: updated output field

uOut = uIn;
uOut = uOut.*Mask;


end
```

A.2.2 Basic implementation of ePIE ptychography

A different example for the ptychographic implementation in Matlab can be found in [HS19].

```
function [uOut] = PM(uIn,Amplitude)

    % Preform of the magnitude constraint without a mask
```

```
    % to be used in the detector plane
    %
    % uIn: input wavefield
    % Amplitude: array of the amplitude for the update
    % uOut: updated output field

    uOut = Amplitude.*exp(1i.*angle(uIn));
end
```

```
function [UpdateOut] = UpdateFunction(UpdateIn,TheOtherIn,Field,uField,
    alpha,typePIE)

% update function for ptychography
% based on: "further improvements to the ptychographical iterative
% engine" by A. Maiden
% doi = 10.1364/OPTICA.4.000736
% UpdateIn = example the object
% ProbeIn  = Probe for start
% Field    = Field before modulus update
% uField   = Backpropagated Field after modulus update
% alpha    = alpha or beta from
% type     = (PIE = 1, ePIE = 2, rPIE = 3.)

maxIntBIn = max(abs(TheOtherIn),[],'all').^2;

if typePIE == 1
    UpdateOut = UpdateIn + ...
        (abs(TheOtherIn) .* conj(TheOtherIn) .* (uField-Field)) ...
        ./ (sqrt(maxIntBIn) * (abs(TheOtherIn).^2 + alpha*maxIntBIn));
elseif typePIE == 2
   UpdateOut = UpdateIn + ...
       (alpha .* conj(TheOtherIn) ./ maxIntBIn) ...
       .*(uField - Field);
elseif typePIE == 3
    UpdateOut = UpdateIn + ...
        (conj(TheOtherIn) .* (uField-Field)) ...
        ./ ( (1-alpha).*(abs(TheOtherIn).^2) + alpha*maxIntBIn );
else
    disp('wrong type')
end
```

```
function [pos01,img01] = loadDataForMyPtycho(Nvertical,Nhorizontal,
    motorVertical,motorHorizontal,ScanName,PathToEigerFolder,ScanNumber)

%
```

```
% Simple function to load the
% Nvertical: number of vertical scan positions
% Nhorizontal: number of horizontal scan positions
% motorVertical: name of the vertical motor
% motorHorizontal: name of the horizontal motor
% ScanName: name of the scan
% PathToEigerFolder: path to the Eiger files
% ScanNumber: number of the scan
%
% All Units are in meter


% Numbers of scan positions
Ny = Nvertical;
Nx = Nhorizontal;
Ni = Ny*Nx;

% arrays where the detector images and the motor positions are stored
img01  = zeros(2167,2070,Ni,'single');
pos01  = zeros(Ni,2);

ii = 1;

% Load all detector images and the corresponding motor positions
while ii <= Ni
    if mod(ii,Nx) == 1
        subScan = zeros(2167,2070,Nx);
        FileName   = sprintf('PathToEigerFiles');
        subScan(:,:,:) = single(LoadEigerImage(FileName,1,1,1,-1,-1,Nx,2))
    ;
        iLineStart = floor((ii-1)/Nx)*Nx+1;
        img01(:,:,iLineStart:(iLineStart+Nx-1)) = subScan;
    end
    motPath     = sprintf('PathToMotorFiles');
    dumpfile    = wwas(motPath);
    pos01(ii,1) = -1*dumpfile.(motorVertical)*1e-3;
    pos01(ii,2) = -1*dumpfile.(motorHorizontal)*1e-3;
    fprintf(sprintf(' %d %d ',ii)); toc;
    ii = ii +1;
end
end


function [probe,object,pxSF] = simpleMyPtycho(listWithImages,
    listOfMotorPositions,...
    zWgSmpl,zSmplDet,NpxProbe,w0Gau,lambda,NumItt,upsamplingFactor,
```

```
    centerPxVer,centerPxHor,pxDetector,updateObj,updatePrb,...
    useGpu,purePhaseObject,xyPosRefinement,saveName,saveVersion,
    liveShowModulo,saveFilesOn,startProbe)


%
% function for an ePIE ptychographic reconstruction
%
% based on: "further improvements to the ptychographical iterative
% engine" by A. Maiden
% doi = 10.1364/OPTICA.4.000736
%
% A detailed theory about ptychography can be found in the handbook of
    microscopy by Hawkes and Spence
%
% The HoloTomoToolbox is needed during the recosntruction
%
% All Units are in meter
%
% listWithImages: array with the detector images
% listOfMotorPositions: array with the Motor positions
% zWgSmpl: distance between the WG exit and the sample (object)
% zSmplDet: distance between the sample (object) and the detector
% NpxProbe: number of pixels for the reconstruction
% w0Gau: FWHM of the guessed initial Gaussian beam
% lambda: wavelength
% NumItt: number of iterations
% upsamplingFactor: upsampling for a large FOV
% centerPxVer: position of the beam center pixel in vertical
% centerPxHor: position of the beam center pixel in horizontal
% pxDetector: detector pixel size
% updateObj: update strength of the object (often denoted as alpha)
% updatePrb: update strength of the probe (often denoted as beta)
% useGpu: should the GPU be used for a faster reconstruction
% purePhaseObject: should the pure phase constraint be used in the sample
    plane
% xyPosRefinement: should a refinement of the motor positioned be
    performed
% saveName: the name at which the reconstructed object and probe should be
     saved
% saveVersion: if multiple versions of the same reconstruction exist
% liveShowModulo: should during the iterative reconstruction updates of
    the object and probe be shown?
% saveFilesOn: should during the iterative reconstruction updates of the
    object and probe be saved as tiff?
```

```
% startProbe: if from a subsequent reconstruction a probe already exist,
    it can be useed as a start guess
%

MotorPos    = listOfMotorPositions;
pxFF        = pxDetector;
scNi        = size(listWithImages,3);
scNy        = round(sqrt(scNi));
scNx        = scNy;
%
% Crop and pad Detector Images
InputFF = zeros(NpxProbe,NpxProbe,scNi,'single');
tic
fprintf(' crop and pad Detector Images \n');
for ii = 1:scNi
    centerPxY   = centerPxVer  + round(NpxProbe*0.5);
    centerPxX   = centerPxHor  + round(NpxProbe*0.5);
    singleDetectorImg    = padToSize(listWithImages(:,:,ii),[size(
    listWithImages,1)+NpxProbe,size(listWithImages,2)+NpxProbe],'both');
    InputFF(:,:,ii)      = singleDetectorImg(centerPxY-NpxProbe*0.5+1:
    centerPxY+NpxProbe*0.5,centerPxX-NpxProbe*0.5+1:centerPxX+NpxProbe
    *0.5);
    fprintf(' %d ',ii); toc
end
%
% Upsampling of the detector images
NpxProbe     = NpxProbe*upsamplingFactor;
pxFF         = pxFF/upsamplingFactor;

% calculation of the sample field pixel size
pxSF         = lambda*zSmplDet/(pxFF*NpxProbe);
NpxO         = round(max(abs(MotorPos/pxSF-mean(MotorPos/pxSF,1)),[],'all'
    )*2+NpxProbe*1.1);
meanScanImg  = mean(InputFF,3);
%
% Random way to use diff.-Paterns
Randii       = zeros(scNi,NumItt,'double');
for jj = 1:1:NumItt
    Randii(:,jj)       = randperm(scNi);
end

% Define Object and Probe
Object       = ones(NpxO,NpxO);
Probe        = gaussianBeam(NpxProbe,NpxProbe,lambda/pxSF,zWgSmpl/pxSF,
    w0Gau/pxSF);
```

```
%
% Scale the Probe
ProbeFF       = fftshift(fft2(ifftshift(Probe)));
scaleFactor   = 1/sum(abs(ProbeFF),'all');
BackProbeFF   = fftshift(ifft2(ifftshift(ProbeFF*(scaleFactor))));
scaleFactor   = (sum(abs(BackProbeFF),'all')/sum(abs(Probe),'all'));
Probe         = scaleFactor*gaussianBeam(NpxProbe,NpxProbe,lambda/pxSF,
    zWgSmpl/pxSF,w0Gau/pxSF);
if sum(abs(startProbe),'all') >0; Probe = startProbe; end

% define which process is calculated on the GPU
if useGpu == 2
    useGpuArrayAmp  = @(f) gpuArray(f);
    useGpuArrayRest = @(f) gpuArray(f);
elseif useGpu == 1
    useGpuArrayAmp  = @(f) gather(f);
    useGpuArrayRest = @(f) gpuArray(f);
else
    useGpuArrayAmp  = @(f) gather(f);
    useGpuArrayRest = @(f) gather(f);
end

% bring everything to GPU
clear gpuAmpFF
gpuAmpFF         = sqrt(useGpuArrayAmp(InputFF));

gpuMotorPos      = useGpuArrayRest(MotorPos);
meanPosY         = mean(gpuMotorPos(:,1));
meanPosX         = mean(gpuMotorPos(:,2));
%
gpuObject        = useGpuArrayRest(single(Object));
gpuProbe         = useGpuArrayRest(single(Probe));
%
% Define the update functions
typePIE          = 2;
PDataFFcdi       = @(f,g) PM(f,g);
fUpdateObj       = @(f,g,Field,uField) UpdateFunction(f,g,Field,uField,
    updateObj,typePIE);
fUpdatePrb       = @(f,g,Field,uField) UpdateFunction(f,g,Field,uField,
    updatePrb,typePIE);
%
% Start Ptychography
fprintf(' start reconstruction \n');
tic
for jj = 1:1:NumItt
```

```
122     for ii = 1:1:scNi
123         iiR = Randii(ii,jj);
124         % Selects range in Object to be updated
125         relPosY  = round((gpuMotorPos(Randii(ii,jj),1)-meanPosY)/pxSF);
126         relPosX  = round((gpuMotorPos(Randii(ii,jj),2)-meanPosX)/pxSF);
127         rangePxY = round(NpxO*0.5)-relPosY + (1-floor(NpxProbe*0.5):floor(
    NpxProbe*0.5));
128         rangePxX = round(NpxO*0.5)-relPosX + (1-floor(NpxProbe*0.5):floor(
    NpxProbe*0.5));
129 
130         gpuDetectorAmplitude = imresize(useGpuArrayRest(gpuAmpFF(:,:,iiR))
    ,upsamplingFactor,'bicubic');
131         % normalize the images can be uncommented in some cases
132         gpuDetectorAmplitude = gpuDetectorAmplitude./sum(
    gpuDetectorAmplitude,'all');
133         gpuDetectorAmplitude = ifftshift(ifftshift(gpuDetectorAmplitude,1)
    ,2);
134         gpuSubObejct         = gpuObject(rangePxY,rangePxX);
135 
136         % preform position refinement
137         if xyPosRefinement
138             pcShift = zeros(9,2);
139             errorPC = zeros(9,1,'single');
140             pc = 0;
141             gpuProbeFieldFarField = fft2(gpuProbe);
142             for pcY = -1:1
143                 for pcX = -1:1
144                     pc = pc+1;
145                     pcShift(pc,1)        = pcY;
146                     pcShift(pc,2)        = pcX;
147                     gpuSubObejct         = gpuObject(rangePxY+pcShift(pc
    ,1),rangePxX+pcShift(pc,2));
148                     gpuWaveField         = gpuProbe.*gpuSubObejct;
149                     gpuWaveFieldFarField = fft2(gpuWaveField);
150                     errorArray  = abs(abs(gpuWaveFieldFarField)-abs(
    gpuDetectorAmplitude));
151                     errorPC(pc) = gather(sum(((errorArray)).^2,'all'));
152                 end
153             end
154             [~,indexPC] = min(errorPC);
155             correctShift = pxSF;
156             gpuMotorPos(iiR,1) = gpuMotorPos(iiR,1) - pcShift(indexPC,1)*
    correctShift;
157             gpuMotorPos(iiR,2) = gpuMotorPos(iiR,2) - pcShift(indexPC,2)*
    correctShift;
```

```
158             gpuSubObejct   = gpuObject(rangePxY,rangePxX);
159         end
160 
161         %%%% ptycho reconstruction
162         gpuWaveField         = gpuProbe.*gpuSubObejct;
163         gpuUpdateWaveField   = ifft2(PDataFFcdi(fft2(gpuWaveField),
    gpuDetectorAmplitude));
164         gpuSubObejct         = fUpdateObj(gpuSubObejct,gpuProbe,
    gpuWaveField,gpuUpdateWaveField);
165         gpuProbe             = fUpdatePrb(gpuProbe,gpuSubObejct,
    gpuWaveField,gpuUpdateWaveField);
166         if purePhaseObject
167             updatePrbDeltaRatio  = 0;
168             gpuSubObejct         = exp((1i+updatePrbDeltaRatio).*angle(
    gpuSubObejct));
169         end
170         gpuObject(rangePxY,rangePxX) = gpuSubObejct;
171     end
172 
173     % Show during the iterative reconstruction the object and the probe
174     fprintf(' %d ',jj); toc
175     if mod(jj-1,liveShowModulo)==0
176         subplot(2,2,1); imagesc(abs(gpuProbe)); axis image; title(sprintf(
    'Probe - Amplitude (of iteration %d) ',jj)); colorbar;
177         subplot(2,2,3); imagesc(angle(gpuProbe./useGpuArrayRest(Probe)));
    axis image; title(sprintf('Probe - Phase (of iteration %d) ',jj));
    colorbar;
178         subplot(2,2,2); imagesc(cropToCenter(abs(gpuObject),[NpxProbe,
    NpxProbe])); axis image; title(sprintf('Object - Amp (of iteration %d
    ) ',jj)); colorbar;
179         subplot(2,2,4); imagesc(cropToCenter(angle(gpuObject),[NpxProbe,
    NpxProbe])); axis image; title(sprintf('Object - Phase (of iteration
    %d) ',jj)); colorbar;
180         drawnow
181     end
182 
183     % Save during the iterative reconstruction the object and the probe
184     if saveFilesOn
185         if jj == 1; jjj = 1; end
186         if mod(jj,2^jjj)==1
187             jjj = jjj+1;
188             imwrite_tiff(gather(angle(gpuObject)),sprintf('%s_ObjectPha_
    %04d_Scan_%04d_%s.tif',saveName,jj,NpxProbe,saveVersion));
189             imwrite_tiff(gather(abs(gpuProbe)),sprintf('%s_ProbeAmp_%04
    d_Scan_%04d_%s.tif',saveName,jj,NpxProbe,saveVersion));
```

```
            imwrite_tiff(gather(angle(gpuProbe)),sprintf('%s_ProbePha_%04d_Scan_%04d_%s.tif',saveName,jj,NpxProbe,saveVersion));
        end
    end
end

end
%%


%% Load the HoloTomoToolbox first
addpath(genpath('PathTo/holotomotoolbox/functions/'));
%% Load Data
% Number of scan points in vertical and horizontal direction
Nvertical            = 21;
Nhorizontal          = 21;
 % if Motor units are NOT mm than multiply with factor
motorVertical        = 'motorVertical';
% if Motor units are NOT mm than multiply with factor
motorHorizontal      = 'motorHorizontal';
ScanName             = 'ScanName';
PathToEigerFolder    = 'PathTODetectorImages';
% can be found in the Eiger file folder
ScanNumber           = 2;

% Load the data for ptychography
[pos01,img01] = loadDataForMyPtycho(Nvertical,Nhorizontal,motorVertical,motorHorizontal,ScanName,PathToEigerFolder,ScanNumber);

%% Do Ptychography, Tiff files are stored in increasing steps
% list of eiger images
listWithImages       = img01;
% list of positions of motor
listOfMotorPositions = pos01;
% can very good be defined by CTF
zWgSmpl              = 10e-3;
% 5.1m bei run96
zSmplDet             = 5.10;
% 512 bis 2048 kann gewählt werden
NpxProbe             = 2048;
% 30nm works good for WGs
w0Gau                = 30e-9;
% 1.55e-10m = 8KeV, 8.98e-11m = 13.8KeV
lambda               = 1.55e-10;
% Number of Itteration
NumItt               = 51;
```

```
% uneven upsampling sometimes don't work
upsamplingFactor     = 8;
% uneven pixel works better most of the time
centerPxVer          = 1366-1;
% uneven pixel works better most of the time
centerPxHor          = 632-1;
% 75µm Eiger pixel size 75µm
pxDetector           = 75e-6;
% 1.0  best works for WG-Ptycho
updateObj            = 1.0;
% 0.2  best works for WG-Ptycho
updatePrb            = 0.2;
% 2 all on GPU, 1 part on GPU, 0 all on CPU
useGpu               = 0;
purePhaseObject      = true;
% true very time consuming but worth it for final rec
xyPosRefinement      = false;
% can be freely choosen good practice use a folder
saveName             = sprintf('results/%s',ScanName);
% if more scans of same sample are done
saveVersion          = 'v01';
% which pixel should be shown
liveShowModulo       = 2;
% saves files each (1+2^ii)
saveFilesOn          = true;

% if zero array than new Probe, if from a different scan already a probe
    for a start guess is used
startProbe           = probeIn;

% Finally make ptychography
[probeNew,object,pxSF] = simpleMyPtycho(listWithImages,
    listOfMotorPositions,...
    zWgSmpl,zSmplDet,NpxProbe,w0Gau,lambda,NumItt,upsamplingFactor,
    centerPxVer,centerPxHor,pxDetector,updateObj,updatePrb,...
    useGpu,purePhaseObject,xyPosRefinement,saveName,saveVersion,
    liveShowModulo,saveFilesOn,startProbe);
%%
% Save the reconstructed Object and Probe
imwrite_tiff(gather(angle(object)),'PathToObjectPhase.tif');
imwrite_tiff(gather(abs(object)),'PathToObjectAmplitude.tif');
imwrite_tiff(gather(abs(probeNew)),'PathToProbeAmplitude.tif');
imwrite_tiff(gather(angle(probeNew)),'PathToProbePhase.tif');
```

A.2.3 Basic implementation of super-resolution in-line holography

```
function [uOut] = PMwithFFT(uIn,Amplitude)

% Magnitude constraint (without an mask for detector gaps, could be added)
% Projector in the detector plane
% Propagates the wavefield from the sample plane to the detector plane
% Sets a magnitude constraint
% Back-propagates the wavefield from the detector plane to the sample
    plane
%
% uIn: input wavefield
% Amplitude: array of the amplitude for the update
% uOut: updated output field

uIn  = fftshift(fft2(ifftshift(uIn)));
uOut = Amplitude.*exp(1i.*angle(uIn));
uOut = fftshift(ifft2(ifftshift(uOut)));

end
```

```
function [uOut] = PS(uIn,RefWave)

% Projector in the sample plane
% Sets a pure phase constraint

uObj   = ones(size(uIn),'single','gpuArray');
uObjPh = uIn./RefWave;
uObj   = ones(size(uObj)).*exp(1i.*angle(uObjPh));
uOut   = RefWave.*uObj;

end
```

```
function reconstructionEngine = generateReconstructionEngine(
    itterativeEngine,beta)

%
% Generates the reconstruction algorithm either based on GS or on RAAR
%
% A nice overview to different algorithms and how to implement can be
% found in:
% S. Marchesini. "Invited Article: A unified evaluation of iterative
    projection
```

```
% algorithms for phase retrieval". In: Rev. Sci. Instrum. 78.1 (2007), p. 011301.
% doi: 10.1063/1.2403783.
%
% itterativeEngine: chose the iterative update approach, GS or RAAR
% beta: if the RAAR approach is used set here a suitable weighting value (0-1)
% reconstructionEngine: a function for the iterative update reconstruction
%
%

if nargin <= 1; beta = 0; end

% projector for the Sample plane
PDataConstrSF               = @(uIn,constSF) PS(uIn,constSF);
RPDataConstrSF              = @(uIn,constSF) 2*PDataConstrSF(uIn,constSF) - uIn;
% projector for the Detector plane
PDataConstrFF           = @(uIn,ampDet) PMwithFFT(uIn,ampDet);
RPDataConstrFF          = @(uIn,ampDet) 2*PDataConstrFFfft(uIn,ampDet) - uIn;

% define a function for the update process
switch itterativeEngine
    case 'GS'
        reconstructionEngine = @(uIn,ampDet,constSF) PDataConstrSF(PDataConstrFF(uIn,ampDet),constSF);
    case  'RAAR'
        reconstructionEngine = @(uIn,ampDet,constSF) (0.5*beta)*(RPDataConstrSF(RPDataConstrFF(uIn,ampDet),constSF) + uIn) + (1-beta)*PDataConstrFF(uIn,ampDet);
end
end
```

```
function [EigerImage] = LoadEigerImage(FileName,FirstPixelHor,FirstPixelVer,FirstImageNum,NumPixelHor,NumPixelVer,NumImages,ImageSizeModus)

% Basic function to load the Eiger 4M images
% the detector gaps get a zero value
%
% FileName: Name of the  file including the path
% FirstPixelHor: first pixel in the horizontal axis
% FirstPixelVer: first pixel in the vertical axis
% FirstImageNum: first image of the h5 file
% NumPixelHor: Size of the ROI to be loaded
```

```
% NumPixelVer: Size of the ROI to be loaded
% NumImages: Number of image of the h5 file to be loaded
% ImageSizeModus: 1 (int16) or 2 (int32), depends on the acquisition time
%

if NumPixelHor < 0
    NumPixelHor = 2070;
end
if NumPixelVer < 0
    NumPixelVer = 2167;
end

% int16
if ImageSizeModus == 1
    EigerImage =  uint16(flipud(rot90(h5read(FileName, '/entry/data/data',
     ...
        [FirstPixelHor FirstPixelVer FirstImageNum],[NumPixelHor
    NumPixelVer NumImages])));
    EigerImage(EigerImage>=65535)=0;
    EigerImage(EigerImage<0)=0;
    EigerImage(isnan(EigerImage)) = 0;
    EigerImage(isinf(EigerImage)) = 0;
% int32
elseif ImageSizeModus == 2
    EigerImage =  uint32(flipud(rot90(h5read(FileName, '/entry/data/data',
     ...
        [FirstPixelHor FirstPixelVer FirstImageNum],[NumPixelHor
    NumPixelVer NumImages])));
    EigerImage(EigerImage>=4.294967295e9)=0;
    EigerImage(EigerImage<0)=0;
    EigerImage(isnan(EigerImage)) = 0;
    EigerImage(isinf(EigerImage)) = 0;
end
end
```

```
%%
% Basic script for super-resolution in-line holography
% Constraints are:
%   - prior knowledge about the probe
%   - Pure phase object
%
% All units in SI
%

%% Load HoloTomoToolbox
addpath(genpath('PathToHoloTomoToolbox'));
```

```
12
13 %% Load the prior reconstructed Probe
14 fileNamePha = Tiff('PathToThePhaseOfTheProbe','r');
15 fileNameAmp = Tiff('PathToThePhaseOfTheAmplitude','r');
16
17 %% Calculate the Probe for initialization of the iterative reconstruction
18 PhaseProbe  = read(fileNamePha);
19 AmpliProbe  = read(fileNameAmp);
20 ProbeFieldStart = AmpliProbe.*exp(1i.*PhaseProbe);
21
22 %% Set basic input parameters
23 % the wavelength
24 lambda            = 1.545-10;
25 % number of pixel used for the reconstrutction
26 Np                = 2048;
27 % upscaling of the detector pixels for larger FOV in the sample plane
28 upScaleFac        = 2;
29 % vertical position of the center pixel
30 centerPxDetectorY = 1341;
31 % horizontal position of the center pixel
32 centerPxDetectorX =  652;
33 %% Load the detector images (here from an Eiger 4m)
34 % name of the scan
35 ScanName   = 'ScanName';
36  % scan number
37 ScanNum    = 4;
38 % number of the image
39 ImageNum   = 1;
40 % number of images (if subsequent images are recorded for a better SNR)
41 Nx         = 10;
42 % path to the detector file
43 FileName   = sprintf('PathToH5FileName');
44 % loading the detector images
45 Img(:,:)   = mean(single(LoadEigerImage(FileName,1,1,ImageNum,-1,-1,Nx,2))
       ,3);
46 %% Centering the detector images and upscaling
47 % calculate the vertical center pixel position
48 centerPxY   = centerPxDetectorY  + round(Np*0.5);
49 % calculate the horizontal center pixel position
50 centerPxX   = centerPxDetectorX  + round(Np*0.5);
51 %
52 % In the two subsequent steps, centering and upscaling of the input
       detector image
53 singleDetectorImg = padToSize(Img,[size(Img,1)+Np,size(Img,2)+Np],'both');
54 DetectorAmp       = sqrt(imresize(singleDetectorImg(centerPxY-Np*0.5+1:
```

```
    centerPxY+Np*0.5,centerPxX-Np*0.5+1:centerPxX+Np*0.5),upScaleFac,'
    bicubic'));

%% Set reconstruction algorithm
% set reconstruction algorithm (GS,RAAR)
itterativeEngine  = 'GS';
% if RAAR is chosen than set here the regularization parameter
beta              = 0.25;
% gives a function for the propagation and reconstruction
recEngine         = generateReconstructionEngine(itterativeEngine,beta);
% number of iterations for reconstruction
Ni = 101;
% set the start Field for the reconstruction
uField    = gpuArray(ProbeFieldStart);

%% Iterative reconstruction of the wavefield
tic
for ii = 1:1:Ni
    % update step
    [uField] = recEngine(uField,DetectorAmp,ProbeFieldStart);
    fprintf(' %d ',ii); toc
end

%% Calculate the sample phase from the reconstructed wavefield and plot
    and save it
samplePhase = angle(exp(1i.*(angle(uField)-angle(ProbeFieldStart))));
subplot(1,1,1); imagesc(samplePhase); axis image; colorbar;
imwrite_tiff(gather(samplePhase),'PathForSaveReconstructedSamplePhase');
%%
```

Bibliography

[Abb73] E. Abbe. “Beiträge zur Theorie des Mikroskops und der mikroskopischen Wahrnehmung.” In: *Archiv für mikroskopische Anatomie* 9.1 (1873), pp. 413–468.

[Abb+08] B. Abbey, K. A. Nugent, G. J. Williams, J. N. Clark, A. G. Peele, M. A. Pfeifer, M. de Jonge, and I. McNulty. “Keyhole coherent diffractive imaging.” In: *Nat. Phys.* 4 (2008), pp. 394–398. DOI: 10.1038/nphys896.

[Ahn+07] Y. Ahn, A. Tsen, B. Kim, Y. W. Park, and J. Park. “Photocurrent imaging of p- n junctions in ambipolar carbon nanotube transistors.” In: *Nano letters* 7.11 (2007), pp. 3320–3323.

[AB78] R. Alig and S. Bloom. “Secondary-electron-escape probabilities.” In: *Journal of Applied Physics* 49.6 (1978), pp. 3476–3480.

[AM11] J. Als-Nielsen and D. McMorrow. *Elements of modern X-ray physics*. John Wiley & Sons, 2011.

[AK74] S. Aoki and S. Kikuta. “X-Ray Holographic Microscopy.” In: *Jpn. J. Appl. Phys.* 13.9 (1974), pp. 1385–1392. DOI: 10.1143/jjap.13.1385.

[Ard39] M. von Ardenne. “Zur Leistungsfähigkeit des Elektronen-Schattenmikroskopes und über ein Röntgenstrahlen-Schattenmikroskop.” In: *Naturwissenschaften* 27.28 (1939), pp. 485–486. DOI: 10.1007/BF01489234.

[Att00] D. Attwood. *Soft x-rays and extreme ultraviolet radiation: principles and applications*. Cambridge university press, 2000.

[Aut06] A. Authier. “Dynamical theory of X-ray diffraction.” In: *International Tables for Crystallography* (2006), pp. 626–646.

[Ayy+21] K. Ayyer et al. “3D diffractive imaging of nanoparticle ensembles using an x-ray laser.” In: *Optica* 8.1 (2021), pp. 15–23. DOI: 10.1364/OPTICA.410851.

[Baj+18] S. Bajt et al. “X-ray focusing with efficient high-NA multilayer Laue lenses.” In: *Light Sci. Appl.* 7 (2018), p. 17162. DOI: 10.1038/lsa.2017.162.

[Bar+15] M. Bartels, M. Krenkel, J. Haber, R. N. Wilke, and T. Salditt. “X-Ray Holographic Imaging of Hydrated Biological Cells in Solution.” In: *Phys. Rev. Lett.* 114.4 (2015), p. 048103. DOI: 10.1103/PhysRevLett.114.048103.

[Beh21] R. Behling. *Modern diagnostic x-ray sources: technology, manufacturing, reliability*. CRC Press, 2021.

[BKV03] C. Bergemann, H. Keymeulen, and J. F. van der Veen. “Focusing X-Ray Beams to Nanometer Dimensions.” In: *Phys. Rev. Lett.* 91.20 (2003), p. 204801. DOI: 10.1103/PhysRevLett.91.204801.

[BW13] M. Born and E. Wolf. *Principles of optics: electromagnetic theory of propagation, interference and diffraction of light*. Elsevier, 2013.

[Bra12] W. L. Bragg. “The Specular Reflection of X-rays.” In: *Nature* 90.2250 (1912), pp. 410–410.

[Buo+03] T. Buonassisi, M. Heuer, O. Vyvenko, A. Istratov, E. Weber, Z. Cai, B. Lai, T. Ciszek, and R. Schindler. “Applications of synchrotron radiation X-ray techniques on the analysis of the behavior of transition metals in solar cells and single-crystalline silicon with extended defects.” In: *Physica B: Condensed Matter* 340 (2003), pp. 1137–1141.

[Ced+17] A. Cedola, A. Bravin, I. Bukreeva, M. Fratini, A. Pacureanu, A. Mittone, L. Massimi, P. Cloetens, P. Coan, G. Campi, R. Spanò, F. Brun, V. Grigoryev, V. Petrosino, C. Venturi, M. Mastrogiacomo, N. K. de Rosbo, and A. Uccelli. “X-Ray Phase Contrast Tomography Reveals Early Vascular Alterations and Neuronal Loss in a Multiple Sclerosis Model.” In: *Sci. Rep.* 7.5890 (2017), pp. 1–11. DOI: 10.1038/s41598-017-06251-7.

[Ces+17] J. Cesar da Silva, A. Pacureanu, Y. Yang, S. Bohic, C. Morawe, R. Barrett, and P. Cloetens. “Efficient concentration of high-energy x-rays for diffraction-limited imaging resolution.” In: *Optica* 4.5 (2017), pp. 492–495. DOI: 10.1364/OPTICA.4.000492.

[CS14] C. Chang and A. Sakdinawat. “Ultra-high aspect ratio high-resolution nanofabrication for hard X-ray diffractive optics.” In: *Nature communications* 5.1 (2014), pp. 1–7.

[CB20] H. N. Chapman and S. Bajt. “A ray-trace analysis of x-ray multilayer Laue lenses for nanometer focusing.” In: *J. Opt.* 22.11 (2020), p. 115610. DOI: 10.1088/2040-8986/abb9c2.

[Cha+21] H. N. Chapman, M. Prasciolu, K. T. Murray, J. L. Dresselhaus, and S. Bajt. “Analysis of X-ray multilayer Laue lenses made by masked deposition.” In: *Optics express* 29.3 (2021), pp. 3097–3113.

[Cha96] H. N. Chapman. “Phase-retrieval X-ray microscopy by Wigner-distribution deconvolution.” In: *Ultramicroscopy* 66.3 (1996), pp. 153–172. DOI: 10.1016/S0304-3991(96)00084-8.

[Cha19] H. N. Chapman. “X-Ray Free-Electron Lasers for the Structure and Dynamics of Macromolecules.” In: *Annu. Rev. Biochem.* 88.1 (2019), pp. 35–58. DOI: 10.1146/annurev-biochem-013118-110744.

[CN10] H. N. Chapman and K. A. Nugent. “Coherent lensless X-ray imaging.” In: *Nat. Photonics* 4 (2010), pp. 833–839. DOI: 10.1038/nphoton.2010.240.

[Cha+19a] L. Chayanun, G. Otnes, A. Troian, S. Hammarberg, D. Salomon, M. T. Borgström, and J. Wallentin. “Nanoscale mapping of carrier collection in single nanowire solar cells using X-ray beam induced current.” In: *J. Synchrotron Radiat.* 26.1 (2019), pp. 102–108. DOI: 10.1107/S1600577518015229.

[Cha+19b] L. Chayanun, S. Hammarberg, H. Dierks, G. Otnes, A. Björling, M. T. Borgström, and J. Wallentin. “Combining Nanofocused X-Rays with Electrical Measurements at the NanoMAX Beamline.” In: *Crystals* 9.8 (2019), p. 432.

[Cha+20] L. Chayanun, L. Hrachowina, A. Björling, M. T. Borgström, and J. Wallentin. “Direct Three-Dimensional Imaging of an X-ray Nanofocus Using a Single 60 nm Diameter Nanowire Device.” In: *Nano letters* 20.11 (2020), pp. 8326–8331.

[Che+08] Y. T. Chen, T. N. Lo, C. W. Chiu, J. Y. Wang, C. L. Wang, C. J. Liu, S. R. Wu, S. T. Jeng, C. C. Yang, J. Shiue, C. H. Chen, Y. Hwu, G. C. Yin, H. M. Lin, J. H. Je, and G. Margaritondo. “Fabrication of high-aspect-ratio Fresnel zone plates by e-beam lithography and electroplating.” In: *J. Synchrotron Radiat.* 15.2 (2008), pp. 170–175. DOI: 10.1107/S0909049507063510.

[Clo+99] P. Cloetens, W. Ludwig, J. Baruchel, D. Van Dyck, J. Van Landuyt, J. P. Guigay, and M. Schlenker. "Holotomography: Quantitative phase tomography with micrometer resolution using hard synchrotron radiation x rays." In: *Appl. Phys. Lett.* 75.19 (1999), pp. 2912–2914. DOI: 10.1063/1.125225.

[Cos65] V. E. Cosslett. "X-ray microscopy." In: *Reports on Progress in Physics* 28.1 (1965), pp. 381–409. DOI: 10.1088/0034-4885/28/1/311.

[Cos59] V. Cosslett. "Microscopy with X-Rays." In: *Nature* 183.4673 (1959), pp. 1423–1427.

[Cow95] J. Cowley. *Diffraction Physics*. North-Holland Personal Library. Elsevier Science, 1995. ISBN: 9780080530390.

[Cro+18] L. C. P. Croton, K. S. Morgan, D. M. Paganin, L. T. Kerr, M. J. Wallace, K. J. Crossley, S. L. Miller, N. Yagi, K. Uesugi, S. B. Hooper, and M. J. Kitchen. "In situ phase contrast X-ray brain CT." In: *Sci. Rep.* 8.11412 (2018), pp. 1–12. DOI: 10.1038/s41598-018-29841-5.

[Dar12] O. Darrigol. *A history of optics from Greek antiquity to the nineteenth century*. Oxford University Press, 2012.

[De +21] V. De Andrade, V. Nikitin, M. Wojcik, A. Deriy, S. Bean, D. Shu, T. Mooney, K. Peterson, P. Kc, K. Li, S. Ali, K. Fezzaa, D. Gürsoy, C. Arico, S. Ouendi, D. Troadec, P. Simon, F. De Carlo, and C. Lethien. "Fast X-ray Nanotomography with Sub-10 nm Resolution as a Powerful Imaging Tool for Nanotechnology and Energy Storage Applications." In: *Adv. Mater.* 33.21 (2021), p. 2008653. DOI: 10.1002/adma.202008653.

[DeG+97] E. P. DeGarmo, J. T. Black, R. A. Kohser, and B. E. Klamecki. *Materials and process in manufacturing*. Prentice Hall Upper Saddle River, 1997.

[Den+18] J. Deng, Y. H. Lo, M. Gallagher-Jones, S. Chen, A. Pryor, Q. Jin, Y. P. Hong, Y. S. G. Nashed, S. Vogt, J. Miao, and C. Jacobsen. "Correlative 3D x-ray fluorescence and ptychographic tomography of frozen-hydrated green algae." In: *Sci. Adv.* 4.11 (2018), eaau4548. DOI: 10.1126/sciadv.aau4548.

[Den+17] J. Deng, D. J. Vine, S. Chen, Q. Jin, Y. S. Nashed, T. Peterka, S. Vogt, and C. Jacobsen. "X-ray ptychographic and fluorescence microscopy of frozen-hydrated cells using continuous scanning." In: *Scientific Reports* 7.1 (2017), pp. 1–10.

[Don+20] C. Donnelly, S. Finizio, S. Gliga, M. Holler, A. Hrabec, M. Odstrčil, S. Mayr, V. Scagnoli, L. J. Heyderman, M. Guizar-Sicairos, and J. Raabe. "Time-resolved imaging of three-dimensional nanoscale magnetization dynamics." In: *Nat. Nanotechnol.* 15 (2020), pp. 356–360. DOI: 10.1038/s41565-020-0649-x.

[Dör+13] F. Döring, A. L. Robisch, C. Eberl, M. Osterhoff, A. Ruhlandt, T. Liese, F. Schlenkrich, S. Hoffmann, M. Bartels, T. Salditt, and H. U. Krebs. "Sub-5 nm hard x-ray point focusing by a combined Kirkpatrick-Baez mirror and multilayer zone plate." In: *Opt. Express* 21.16 (2013), pp. 19311–19323. DOI: 10.1364/OE.21.019311.

[Ebe15] W. Eberhardt. "Synchrotron radiation: A continuing revolution in X-ray science - Diffraction limited storage rings and beyond." In: *J. Electron Spectrosc. Relat. Phenom.* 200 (2015), pp. 31–39. DOI: 10.1016/j.elspec.2015.06.009.

[Ebe16] C. Eberl. "Multilagenzonenplatten für die Mikroskopie mit harter Röntgenstrahlung." PhD thesis. 2016.

[Ebe+14] C. Eberl, F. Döring, T. Liese, F. Schlenkrich, B. Roos, M. Hahn, T. Hoinkes, A. Rauschenbeutel, M. Osterhoff, T. Salditt, et al. "Fabrication of laser deposited high-quality multilayer zone plates for hard X-ray nanofocusing." In: *Applied surface science* 307 (2014), pp. 638–644.

[Eck+20] M. Eckermann, J. Frohn, M. Reichardt, M. Osterhoff, M. Sprung, F. Westermeier, A. Tzankov, C. Werlein, M. Kühnel, D. Jonigk, et al. "3D virtual pathohistology of lung tissue from Covid-19 patients based on phase contrast X-ray tomography." In: *Elife* 9 (2020), e60408.

[EFR95] P. Engström, S. Fiedler, and C. Riekel. "Microdiffraction instrumentation and experiments on the microfocus beamline at the ESRF." In: *Rev. Sci. Instrum.* 66.2 (1995), pp. 1348–1350. DOI: 10.1063/1.1145971.

[Eve+21] J. Everett, F. Lermyte, J. Brooks, V. Tjendana-Tjhin, G. Plascencia-Villa, I. Hands-Portman, J. M. Donnelly, K. Billimoria, G. Perry, X. Zhu, P. J. Sadler, P. B. O'Connor, J. F. Collingwood, and N. D. Telling. "Biogenic metallic elements in the human brain?" In: *Sci. Adv.* 7.24 (2021), eabf6707. DOI: 10.1126/sciadv.abf6707.

[FR04] H. M. L. Faulkner and J. M. Rodenburg. “Movable Aperture Lensless Transmission Microscopy: A Novel Phase Retrieval Algorithm.” In: *Phys. Rev. Lett.* 93.2 (2004), p. 023903. DOI: 10.1103/PhysRevLett.93.023903.

[Fie78] J. R. Fienup. “Reconstruction of an object from the modulus of its Fourier transform.” In: *Optics letters* 3.1 (1978), pp. 27–29.

[FF11] D. Frank and N. Frey. “Cardiac Z-disc Signaling Network∗.” In: *J. Biol. Chem.* 286.12 (2011), pp. 9897–9904. DOI: 10.1074/jbc.R110.174268.

[FKL12] W. Friedrich, P. Knipping, and M. v. Laue. *Interferenz-Erscheinungen bei Röntgenstrahlen*. München, 1912.

[FOS06] C. Fuhse, C. Ollinger, and T. Salditt. “Waveguide-Based Off-Axis Holography with Hard X Rays.” In: *Phys. Rev. Lett.* 97.25 (2006), p. 254801. DOI: 10.1103/PhysRevLett.97.254801.

[Fuh+04] C. Fuhse, A. Jarre, C. Ollinger, J. Seeger, T. Salditt, and R. Tucoulou. “Front-coupling of a prefocused x-ray beam into a monomodal planar waveguide.” In: *Appl. Phys. Lett.* 85.11 (2004), pp. 1907–1909. DOI: 10.1063/1.1791736.

[FS05] C. Fuhse and T. Salditt. “Finite-difference field calculations for one-dimensionally confined X-ray waveguides.” In: *Physica B: Condensed Matter* 357.1-2 (2005), pp. 57–60.

[FS06a] C. Fuhse and T. Salditt. “Finite-difference field calculations for two-dimensionally confined x-ray waveguides.” In: *Applied optics* 45.19 (2006), pp. 4603–4608.

[FS06b] C. Fuhse and T. Salditt. “Propagation of x-rays in ultra-narrow slits.” In: *Optics communications* 265.1 (2006), pp. 140–146.

[Gab48] D. Gabor. “A New Microscopic Principle.” In: *Nature* 161 (1948), pp. 777–778. DOI: 10.1038/161777a0.

[Gar+19] F. García-Moreno, P. H. Kamm, T. R. Neu, F. Bülk, R. Mokso, C. M. Schlepütz, M. Stampanoni, and J. Banhart. “Using X-ray tomoscopy to explore the dynamics of foaming metal.” In: *Nat. Commun.* 10.3762 (2019), pp. 1–9. DOI: 10.1038/s41467-019-11521-1.

[Ge+18] M. Ge, D. S. Coburn, E. Nazaretski, W. Xu, K. Gofron, H. Xu, Z. Yin, and W.-K. Lee. “One-minute nano-tomography using hard X-ray full-field transmission microscope.” In: *Appl. Phys. Lett.* 113.8 (2018), p. 083109. DOI: 10.1063/1.5048378.

[GK17] A. Gektin and M. Korzhik. “Inorganic scintillators for detector systems.” In: (2017).

[GS72] R. W. Gerchberg and W. O. Saxton. “A practical algorithm for the determination of phase from image and diffraction plane pictures.” In: *Optik* 35 (1972), pp. 237–246.

[Gie+10] K. Giewekemeyer, H. Neubauer, S. Kalbfleisch, S. P. Krüger, and T. Salditt. “Holographic and diffractive x-ray imaging using waveguides as quasi-point sources.” In: *New J. Phys.* 12.3 (2010), p. 035008. DOI: 10.1088/1367-2630/12/3/035008.

[Goo17] J. Goodman. *Introduction to Fourier Optics, 4W. H.* 2017.

[Gor+19] S. Gorelick, M. De Jonge, C. Kewish, and A. De Marco. “Ultimate limitations in the performance of kinoform lenses for hard x-ray focusing.” In: *Optica* 6.6 (2019), pp. 790–793.

[GG04] M. Guizar-Sicairos and J. C. Gutiérrez-Vega. “Computation of quasi-discrete Hankel transforms of integer order for propagating optical wave fields.” In: *JOSA A* 21.1 (2004), pp. 53–58.

[Gut+12] C. Gutsche, R. Niepelt, M. Gnauck, A. Lysov, W. Prost, C. Ronning, and F.-J. Tegude. “Direct determination of minority carrier diffusion lengths at axial GaAs nanowire p–n junctions.” In: *Nano letters* 12.3 (2012), pp. 1453–1458.

[Hag+14] J. Hagemann, A.-L. Robisch, D. R. Luke, C. Homann, T. Hohage, P. Cloetens, H. Suhonen, and T. Salditt. “Reconstruction of wave front and object for inline holography from a set of detection planes.” In: *Opt. Express* 22.10 (2014), pp. 11552–11569. DOI: 10.1364/OE.22.011552.

[HS17a] J. Hagemann and T. Salditt. “The fluence–resolution relationship in holographic and coherent diffractive imaging.” In: *J. Appl. Crystallogr.* 50.2 (2017), pp. 531–538. DOI: 10.1107/S1600576717003065.

[HTS18] J. Hagemann, M. Töpperwien, and T. Salditt. “Phase retrieval for near-field X-ray imaging beyond linearisation or compact support.” In: *Appl. Phys. Lett.* 113.4 (2018), p. 041109. DOI: 10.1063/1.5029927.

[Hag+21] J. Hagemann, M. Vassholz, H. Hoeppe, M. Osterhoff, J. M. Rosselló, R. Mettin, F. Seiboth, A. Schropp, J. Möller, J. Hallmann, C. Kim, M. Scholz, U. Boesenberg, R. Schaffer, A. Zozulya, W. Lu, R. Shayduk, A. Madsen, C. G. Schroer, and T. Salditt. "Single-pulse phase-contrast imaging at free-electron lasers in the hard X-ray regime." In: *J. Synchrotron Radiat.* 28.1 (2021), pp. 52–63. DOI: 10.1107/S160057752001557X.

[Hag+17] J. Hagemann, A.-L. Robisch, M. Osterhoff, and T. Salditt. "Probe reconstruction for holographic X-ray imaging." In: *Journal of Synchrotron Radiation* 24.2 (2017), pp. 498–505. DOI: 10.1107/S160057751700128X.

[HS17b] J. Hagemann and T. Salditt. "Divide and update: towards single-shot object and probe retrieval for near-field holography." In: *Optics express* 25.18 (2017), pp. 20953–20968.

[HS18] J. Hagemann and T. Salditt. "Coherence-resolution relationship in holographic and coherent diffractive imaging." In: *Opt. Express* 26.1 (2018), pp. 242–253. DOI: 10.1364/OE.26.000242.

[Han80] J. Hanoka. "Electron-beam-induced current characterization of polycrystalline silicon solar cells." In: *Solar Cells* 1.2 (1980), pp. 123–139.

[HS19] P. Hawkes and J. C. H. Spence. *Springer Handbook of Microscopy*. Cham, Switzerland: Springer International Publishing, 2019. ISBN: 978-3-030-00068-4. DOI: 10.1007/978-3-030-00069-1.

[HS05] M. van Heel and M. Schatz. "Fourier shell correlation threshold criteria." In: *J. Struct. Biol.* 151.3 (2005), pp. 250–262. DOI: 10.1016/j.jsb.2005.05.009.

[HH70] R. Hegerl and W. Hoppe. "Dynamische Theorie der Kristallstrukturanalyse durch Elektronenbeugung im inhomogenen Primärstrahlwellenfeld." In: *Ber. Bunsenges. Phys. Chem.* 74.11 (1970), pp. 1148–1154. DOI: 10.1002/bbpc.19700741112.

[HOH03] O. Hemberg, M. Otendal, and H. M. Hertz. "Liquid-metal-jet anode electron-impact x-ray source." In: *Appl. Phys. Lett.* 83.7 (2003), pp. 1483–1485. DOI: 10.1063/1.1602157.

[HGD93] B. L. Henke, E. M. Gullikson, and J. C. Davis. "X-ray interactions: photoabsorption, scattering, transmission, and reflection at E= 50-30,000 eV, Z= 1-92." In: *Atomic data and nuclear data tables* 54.2 (1993), pp. 181–342.

[Hig+03] O. Hignette, P. Cloetens, W.-K. Lee, W. Ludwig, and G. Rostaing. “Hard X-ray microscopy with reflecting mirrors status and perspectives of the ESRF technology.” In: *J. Phys. IV France.* 104 (2003), pp. 231–234. DOI: 10.1051/jp4:200300068.

[Hig+05] O. Hignette, P. Cloetens, G. Rostaing, P. Bernard, and C. Morawe. “Efficient sub 100nm focusing of hard x rays.” In: *Rev. Sci. Instrum.* 76.6 (2005), p. 063709. DOI: 10.1063/1.1928191.

[HS16] S. Hoffmann-Urlaub and T. Salditt. “Miniaturized beamsplitters realized by x-ray waveguides.” In: *Acta Crystallographica Section A: Foundations and Advances* 72.5 (2016), pp. 515–522.

[Hol+14] M. Holler, A. Diaz, M. Guizar-Sicairos, P. Karvinen, E. Färm, E. Härkönen, M. Ritala, A. Menzel, J. Raabe, and O. Bunk. “X-ray ptychographic computed tomography at 16 nm isotropic 3D resolution.” In: *Sci. Rep.* 4.3857 (2014), pp. 1–5. DOI: 10.1038/srep03857.

[Hol+17] M. Holler, M. Guizar-Sicairos, E. H. R. Tsai, R. Dinapoli, E. Müller, O. Bunk, J. Raabe, and G. Aeppli. “High-resolution non-destructive three-dimensional imaging of integrated circuits.” In: *Nature* 543 (2017), pp. 402–406. DOI: 10.1038/nature21698.

[Hol+19] M. Holler, M. Odstrcil, M. Guizar-Sicairos, M. Lebugle, E. Müller, S. Finizio, G. Tinti, C. David, J. Zusman, W. Unglaub, O. Bunk, J. Raabe, A. F. J. Levi, and G. Aeppli. “Three-dimensional imaging of integrated circuits with macro- to nanoscale zoom.” In: *Nat. Electron.* 2 (2019), pp. 464–470. DOI: 10.1038/s41928-019-0309-z.

[Hom+15] C. Homann, T. Hohage, J. Hagemann, A.-L. Robisch, and T. Salditt. “Validity of the empty-beam correction in near-field imaging.” In: *Phys. Rev. A* 91.1 (2015), p. 013821. DOI: 10.1103/PhysRevA.91.013821.

[Hon+18] A.-P. Honkanen, C. Ferrero, J.-P. Guigay, and V. Mocella. “A finite-element approach to dynamical diffraction problems in reflection geometry.” In: *Journal of Applied Crystallography* 51.2 (2018), pp. 514–525. DOI: 10.1107/S1600576718001930.

[HH72] P. Horowitz and J. A. Howell. “A Scanning X-Ray Microscope Using Synchrotron Radiation.” In: *Science* 178.4061 (1972), pp. 608–611. DOI: 10.1126/science.178.4061.608.

[IBP11] G. E. Ice, J. D. Budai, and J. W. L. Pang. “The Race to X-ray Microbeam and Nanobeam Science.” In: *Science* 334.6060 (2011), pp. 1234–1239. DOI: 10.1126/science.1202366.

[Ice+00] G. E. Ice, J.-S. Chung, J. Z. Tischler, A. Lunt, and L. Assoufid. “Elliptical x-ray microprobe mirrors by differential deposition.” In: *Rev. Sci. Instrum.* 71.7 (2000), pp. 2635–2639. DOI: 10.1063/1.1150668.

[IH96] A. Iida and K. Hirano. “Kirkpatrick-Baez optics for a sub-μm synchrotron X-ray microbeam and its applications to X-ray analysis.” In: *Nucl. Instrum. Methods Phys. Res., Sect. B* 114.1 (1996), pp. 149–153. DOI: 10.1016/0168-583X(96)00138-3.

[Jar+05] A. Jarre, C. Fuhse, C. Ollinger, J. Seeger, R. Tucoulou, and T. Salditt. “Two-Dimensional Hard X-Ray Beam Compression by Combined Focusing and Waveguide Optics.” In: *Phys. Rev. Lett.* 94.7 (2005), p. 074801. DOI: 10.1103/PhysRevLett.94.074801.

[Jia+21] Y. Jiang, J. Deng, Y. Yao, J. A. Klug, S. Mashrafi, C. Roehrig, C. Preissner, F. S. Marin, Z. Cai, B. Lai, and S. Vogt. “Achieving high spatial resolution in a large field-of-view using lensless x-ray imaging.” In: *Applied Physics Letters* 119.12 (2021), p. 124101. DOI: 10.1063/5.0067197.

[Kal+11] S. Kalbfleisch, H. Neubauer, S. P. Krüger, M. Bartels, M. Osterhoff, D. D. Mai, K. Giewekemeyer, B. Hartmann, M. Sprung, and T. Salditt. “The Göttingen Holography Endstation of Beamline P10 at PETRA III/DESY.” In: *AIP Conference Proceedings* 1365.1 (2011), pp. 96–99. DOI: 10.1063/1.3625313.

[Kan+06] H. C. Kang, J. Maser, G. B. Stephenson, C. Liu, R. Conley, A. T. Macrander, and S. Vogt. “Nanometer Linear Focusing of Hard X Rays by a Multilayer Laue Lens.” In: *Phys. Rev. Lett.* 96.12 (2006), p. 127401. DOI: 10.1103/PhysRevLett.96.127401.

[Kan+05] H. Kang, G. Stephenson, C. Liu, R. Conley, A. Macrander, J. Maser, S. Bajt, and H. Chapman. “High-efficiency diffractive x-ray optics from sectioned multilayers.” In: *Applied physics letters* 86.15 (2005), p. 151109.

[Kan+08] H. C. Kang, H. Yan, R. P. Winarski, M. V. Holt, J. Maser, C. Liu, R. Conley, S. Vogt, A. T. Macrander, and G. B. Stephenson. “Focusing of hard x-rays to 16 nanometers with a multilayer Laue lens.” In: *Appl. Phys. Lett.* 92.22 (2008), p. 221114. DOI: 10.1063/1.2912503.

[Kau96] B. Kaulich. “Phasenzonenplatten für die Röntgenmikroskopie im Photonenenergiebereich von 2-8 keV.” PhD thesis. University of Göttingen, 1996.

[Kel32] G. Kellström. “Experimentelle Untersuchungen über Interferenz- und Beugungserscheinungen bei langwelligen Röntgenstrahlen.” In: *Nova Acta Regia Societatis Scientiarum Upsaliensis* 8 (1932), pp. 1–66.

[Ker+84] D. Kern, P. Coane, R. Acosta, T. Chang, R. Feder, P. Houzego, W. Molzen, J. Powers, A. Speth, and R. Viswanathan. “Electron beam fabrication and characterization of Fresnel zone plates for soft x-ray microscopy.” In: *Science with Soft X-rays*. Vol. 447. International Society for Optics and Photonics. 1984, pp. 204–213.

[Khi+18] A. Khimchenko, C. Bikis, A. Pacureanu, S. E. Hieber, P. Thalmann, H. Deyhle, G. Schweighauser, J. Hench, S. Frank, M. Müller-Gerbl, G. Schulz, P. Cloetens, and B. Müller. “Hard X-Ray Nanoholotomography: Large-Scale, Label-Free, 3D Neuroimaging beyond Optical Limit.” In: *Adv. Sci.* 5.6 (2018), p. 1700694. DOI: 10.1002/advs.201700694.

[Khi+16] A. Khimchenko, H. Deyhle, G. Schulz, G. Schweighauser, J. Hench, N. Chicherova, C. Bikis, S. E. Hieber, and B. Müller. “Extending two-dimensional histology into the third dimension through conventional micro computed tomography.” In: *Neuroimage* 139 (2016), pp. 26–36. DOI: 10.1016/j.neuroimage.2016.06.005.

[Krü+10] S. P. Krüger, K. Giewekemeyer, S. Kalbfleisch, M. Bartels, H. Neubauer, and T. Salditt. “Sub-15 nm beam confinement by two crossed x-ray waveguides.” In: *Opt. Express* 18.13 (2010), pp. 13492–13501. DOI: 10.1364/OE.18.013492.

[Krü+12] S. P. Krüger, H. Neubauer, M. Bartels, S. Kalbfleisch, K. Giewekemeyer, P. J. Wilbrandt, M. Sprung, and T. Salditt. “Sub-10 nm beam confinement by X-ray waveguides: design, fabrication and characterization of optical properties.” In: *J. Synchrotron Radiat.* 19.2 (2012), pp. 227–236. DOI: 10.1107/S0909049511051983.

[Kua+20] A. T. Kuan, J. S. Phelps, L. A. Thomas, T. M. Nguyen, J. Han, C.-L. Chen, A. W. Azevedo, J. C. Tuthill, J. Funke, P. Cloetens, A. Pacureanu, and W.-C. A. Lee. *Dense neuronal reconstruction through X-ray holographic*

nano-tomography. Tech. rep. 2020, pp. 1637–1643. DOI: 10.1038/s41593-020-0704-9.

[KP02] A. N. Kurokhtin and A. V. Popov. "Simulation of high-resolution x-ray zone plates." In: *J. Opt. Soc. Am. A* 19.2 (2002), pp. 315–324. DOI: 10.1364/JOSAA.19.000315.

[Lag+97] S. Lagomarsino, A. Cedola, P. Cloetens, S. Di Fonzo, W. Jark, G. Soullié, and C. Riekel. "Phase contrast hard x-ray microscopy with submicron resolution." In: *Appl. Phys. Lett.* 71.18 (1997), pp. 2557–2559. DOI: 10.1063/1.119324.

[Len+99] B. Lengeler, C. G. Schroer, M. Richwin, J. Tümmler, M. Drakopoulos, A. Snigirev, and I. Snigireva. "A microscope for hard x rays based on parabolic compound refractive lenses." In: *Appl. Phys. Lett.* 74.26 (1999), pp. 3924–3926. DOI: 10.1063/1.124225.

[Len+98] B. Lengeler, J. Tümmler, A. Snigirev, I. Snigireva, and C. Raven. "Transmission and gain of singly and doubly focusing refractive x-ray lenses." In: *J. Appl. Phys.* 84.11 (1998), pp. 5855–5861. DOI: 10.1063/1.368899.

[LJ15] K. Li and C. Jacobsen. "Rapid calculation of paraxial wave propagation for cylindrically symmetric optics." In: *JOSA A* 32.11 (2015), pp. 2074–2081.

[LWJ17] K. Li, M. Wojcik, and C. Jacobsen. "Multislice does it all—calculating the performance of nanofocusing x-ray optics." In: *Optics express* 25.3 (2017), pp. 1831–1846.

[Lim+16] J. Lim, Y. Li, D. H. Alsem, H. So, S. C. Lee, P. Bai, D. A. Cogswell, X. Liu, N. Jin, Y.-s. Yu, N. J. Salmon, D. A. Shapiro, M. Z. Bazant, T. Tyliszczak, and W. C. Chueh. "Origin and hysteresis of lithium compositional spatiodynamics within battery primary particles." In: *Science* 353.6299 (2016), pp. 566–571. DOI: 10.1126/science.aaf4914.

[Lo+19] Y. H. Lo, C.-T. Liao, J. Zhou, A. Rana, C. S. Bevis, G. Gui, B. Enders, K. M. Cannon, Y.-S. Yu, R. Celestre, K. Nowrouzi, D. Shapiro, H. Kapteyn, R. Falcone, C. Bennett, M. Murnane, and J. Miao. "Multimodal x-ray and electron microscopy of the Allende meteorite." In: *Sci. Adv.* 5.9 (2019), eaax3009. DOI: 10.1126/sciadv.aax3009.

[Lo+18] Y. H. Lo, L. Zhao, M. Gallagher-Jones, A. Rana, J. J. Lodico, W. Xiao, B. C. Regan, and J. Miao. "In situ coherent diffractive imaging." In: *Nat. Commun.* 9.1826 (2018), pp. 1–10. DOI: 10.1038/s41467-018-04259-9.

[Loh+20] L. M. Lohse, A.-L. Robisch, M. Töpperwien, S. Maretzke, M. Krenkel, J. Hagemann, and T. Salditt. "A phase-retrieval toolbox for X-ray holography and tomography." In: *J. Synchrotron Radiat.* 27.3 (2020), pp. 852–859. DOI: 10.1107/S1600577520002398.

[Luk04] D. R. Luke. "Relaxed averaged alternating reflections for diffraction imaging." In: *Inverse Problems* 21.1 (2004), pp. 37–50. DOI: 10.1088/0266-5611/21/1/004.

[MJL17] A. Maiden, D. Johnson, and P. Li. "Further improvements to the ptychographical iterative engine." In: *Optica* 4.7 (2017), pp. 736–745. DOI: 10.1364/OPTICA.4.000736.

[MR09] A. M. Maiden and J. M. Rodenburg. "An improved ptychographical phase retrieval algorithm for diffractive imaging." In: *Ultramicroscopy* 109.10 (2009), pp. 1256–1262. DOI: 10.1016/j.ultramic.2009.05.012.

[Mar07] S. Marchesini. "Invited Article: A unified evaluation of iterative projection algorithms for phase retrieval." In: *Rev. Sci. Instrum.* 78.1 (2007), p. 011301. DOI: 10.1063/1.2403783.

[Mar+03] S. Marchesini, H. He, H. N. Chapman, S. P. Hau-Riege, A. Noy, M. R. Howells, U. Weierstall, and J. C. H. Spence. "X-ray image reconstruction from a diffraction pattern alone." In: *Phys. Rev. B* 68 (14 2003), p. 140101. DOI: 10.1103/PhysRevB.68.140101.

[Mar15] S. Maretzke. "A uniqueness result for propagation-based phase contrast imaging from a single measurement." In: *Inverse Prob.* 31.6 (2015), p. 065003. DOI: 10.1088/0266-5611/31/6/065003.

[Mar18] S. Maretzke. "Locality estimates for Fresnel-wave-propagation and stability of x-ray phase contrast imaging with finite detectors." In: *Inverse Problems* 34.12 (2018), p. 124004.

[Mas+04] J. Maser, G. B. Stephenson, S. Vogt, W. Yun, A. Macrander, H. C. Kang, C. Liu, and R. Conley. "Multilayer Laue lenses as high-resolution x-ray optics." In: *Design and microfabrication of novel X-ray optics II*. Vol. 5539. International Society for Optics and Photonics. 2004, pp. 185–194.

[MS92] J. Maser and G. Schmahl. “Coupled wave description of the diffraction by zone plates with high aspect ratios.” In: *Opt. Commun.* 89.2 (1992), pp. 355–362. DOI: 10.1016/0030-4018(92)90182-Q.

[MS17] L. Melchior and T. Salditt. “Finite difference methods for stationary and time-dependent X-ray propagation.” In: *Opt. Express* 25.25 (2017), pp. 32090–32109. DOI: 10.1364/OE.25.032090.

[MSC98] J. Miao, D. Sayre, and H. N. Chapman. “Phase retrieval from the magnitude of the Fourier transforms of nonperiodic objects.” In: *J. Opt. Soc. Amer. A* 15.6 (1998), pp. 1662–1669. DOI: 10.1364/JOSAA.15.001662.

[Mia+99] J. Miao, P. Charalambous, J. Kirz, and D. Sayre. “Extending the methodology of X-ray crystallography to allow imaging of micrometre-sized non-crystalline specimens.” In: *Nature* 400.6742 (1999), pp. 342–344. DOI: 10.1038/22498.

[Mia+15] J. Miao, T. Ishikawa, I. K. Robinson, and M. M. Murnane. “Beyond crystallography: Diffractive imaging using coherent x-ray light sources.” In: *Science* 348.6234 (2015), pp. 530–535. DOI: 10.1126/science.aaa1394.

[Mim+10] H. Mimura, S. Handa, T. Kimura, H. Yumoto, D. Yamakawa, H. Yokoyama, S. Matsuyama, K. Inagaki, K. Yamamura, Y. Sano, et al. “Breaking the 10 nm barrier in hard-X-ray focusing.” In: *Nature physics* 6.2 (2010), pp. 122–125.

[Mim+08] H. Mimura, S. Morita, T. Kimura, D. Yamakawa, W. Lin, Y. Uehara, S. Matsuyama, H. Yumoto, H. Ohashi, K. Tamasaku, Y. Nishino, M. Yabashi, T. Ishikawa, H. Ohmori, and K. Yamauchi. “Focusing mirror for x-ray free-electron lasers.” In: *Rev. Sci. Instrum.* 79.8 (2008), p. 083104. DOI: 10.1063/1.2964928.

[Moh+15] I. Mohacsi, I. Vartiainen, M. Guizar-Sicairos, P. Karvinen, V. A. Guzenko, E. Müller, E. Färm, M. Ritala, C. M. Kewish, A. Somogyi, and C. David. “High resolution double-sided diffractive optics for hard X-ray microscopy.” In: *Opt. Express* 23.2 (2015), pp. 776–786. DOI: 10.1364/OE.23.000776.

[Moh+17] I. Mohacsi, I. Vartiainen, B. Rösner, M. Guizar-Sicairos, V. A. Guzenko, I. McNulty, R. Winarski, M. V. Holt, and C. David. “Interlaced zone plate optics for hard X-ray imaging in the 10 nm range.” In: *Sci. Rep.* 7.43624 (2017), pp. 1–10. DOI: 10.1038/srep43624.

[Moh+12] A. Mohite, D. Perea, S. Singh, S. Dayeh, I. Campbell, S. Picraux, and H. Htoon. “Highly efficient charge separation and collection across in situ doped axial VLS-grown Si nanowire p–n junctions.” In: *Nano letters* 12.4 (2012), pp. 1965–1971.

[Mok+07] R. Mokso, P. Cloetens, E. Maire, W. Ludwig, and J.-Y. Buffière. “Nanoscale zoom tomography with hard x rays using Kirkpatrick-Baez optics.” In: *Appl. Phys. Lett.* 90.14 (2007), p. 144104. DOI: 10.1063/1.2719653.

[Mor+20] A. J. Morgan, K. T. Murray, M. Prasciolu, H. Fleckenstein, O. Yefanov, P. Villanueva-Perez, V. Mariani, M. Domaracky, M. Kuhn, S. Aplin, I. Mohacsi, M. Messerschmidt, K. Stachnik, Y. Du, A. Burkhart, A. Meents, E. Nazaretski, H. Yan, X. Huang, Y. S. Chu, H. N. Chapman, and S. Bajt. “Ptychographic X-ray speckle tracking with multi-layer Laue lens systems.” In: *Journal of Applied Crystallography* 53.4 (2020), pp. 927–936. DOI: 10.1107/S1600576720006925.

[Mor+15] A. J. Morgan, M. Prasciolu, A. Andrejczuk, J. Krzywinski, A. Meents, D. Pennicard, H. Graafsma, A. Barty, R. J. Bean, M. Barthelmess, D. Oberthuer, O. Yefanov, A. Aquila, H. N. Chapman, and S. Bajt. “High numerical aperture multilayer Laue lenses.” In: *Sci. Rep.* 5.9892 (2015), pp. 1–14. DOI: 10.1038/srep09892.

[Mül+14] M. Müller, T. Mey, J. Niemeyer, and K. Mann. “Table-top soft x-ray microscope using laser-induced plasma from a pulsed gas jet.” In: *Optics express* 22.19 (2014), pp. 23489–23495.

[NRS76] B. Niemann, D. Rudolph, and G. Schmahl. “X-ray microscopy with synchrotron radiation.” In: *Applied Optics* 15.8 (1976), pp. 1883–1884.

[NRS74] B. Niemann, D. Rudolph, and G. Schmahl. “Soft x-ray imaging zone plates with large zone numbers for microscopic and spectroscopic applications.” In: *Optics Communications* 12.2 (1974), pp. 160–163.

[Oka06] K. Okamoto. *Fundamentals of optical waveguides*. Amsterdam Boston: Elsevier, 2006. ISBN: 9780080455068.

[Oku+20] T. Okumura, N. Yamaguchi, H. Suga, Y. Takahashi, H. Segawa, and T. Kogure. “Reactor environment during the Fukushima nuclear accident inferred from radiocaesium-bearing microparticles - Scientific Reports.” In: *Sci. Rep.* 10.1352 (2020), pp. 1–9. DOI: 10.1038/s41598-020-58464-y.

[Ost+15] M. Osterhoff, C. Eberl, F. Döring, R. N. Wilke, J. Wallentin, H.-U. Krebs, M. Sprung, and T. Salditt. "Towards multi-order hard X-ray imaging with multilayer zone plates." In: *J. Appl. Crystallogr.* 48.1 (2015), pp. 116–124. DOI: 10.1107/S1600576714026016.

[Ost+17a] M. Osterhoff, C. Eberl, J. Soltau, and H.-U. Krebs. "Preparing for hard x-ray microscopy with Multilayer Zone Plates." In: *J. Phys. Conf. Ser.* 849.1 (2017), p. 012049. DOI: 10.1088/1742-6596/849/1/012049.

[Ost+12] M. Osterhoff, C. Morawe, C. Ferrero, and J.-P. Guigay. "Wave-optical theory of nanofocusing x-ray multilayer mirrors." In: *Opt. Lett.* 37.17 (2012), pp. 3705–3707. DOI: 10.1364/OL.37.003705.

[Ost+13] M. Osterhoff, C. Morawe, C. Ferrero, and J.-P. Guigay. "Optimized x-ray multilayer mirrors for single nanometer focusing." In: *Opt. Lett.* 38.23 (2013), pp. 5126–5129. DOI: 10.1364/OL.38.005126.

[OS11] M. Osterhoff and T. Salditt. "Coherence filtering of x-ray waveguides: analytical and numerical approach." In: *New J. Phys.* 13.10 (2011), p. 103026. DOI: 10.1088/1367-2630/13/10/103026.

[Ost+17b] M. Osterhoff, J. Soltau, C. Eberl, and H.-U. Krebs. "Ultra-high-aspect multilayer zone plates for even higher x-ray energies." In: *Advances in X-Ray/EUV Optics and Components XII*. Vol. 10386. International Society for Optics and Photonics. 2017, p. 1038608.

[Ote+08] M. Otendal, T. Tuohimaa, U. Vogt, and H. M. Hertz. "A 9keV electron-impact liquid-gallium-jet x-ray source." In: *Rev. Sci. Instrum.* 79.1 (2008), p. 016102. DOI: 10.1063/1.2833838.

[Otn+18] G. Otnes, E. Barrigón, C. Sundvall, K. E. Svensson, M. Heurlin, G. Siefer, L. Samuelson, I. Aberg, and M. T. Borgström. "Understanding InP nanowire array solar cell performance by nanoprobe-enabled single nanowire measurements." In: *Nano letters* 18.5 (2018), pp. 3038–3046.

[Özt+18] H. Öztürk, H. Yan, Y. He, M. Ge, Z. Dong, M. Lin, E. Nazaretski, I. K. Robinson, Y. S. Chu, and X. Huang. "Multi-slice ptychography with large numerical aperture multilayer Laue lenses." In: *Optica* 5.5 (2018), pp. 601–607. DOI: 10.1364/OPTICA.5.000601.

[Pag06] D. Paganin. *Coherent X-ray optics*. 6. Oxford University Press on Demand, 2006.

[Par+08] D. Y. Parkinson, G. McDermott, L. D. Etkin, M. A. Le Gros, and C. A. Larabell. "Quantitative 3-D imaging of eukaryotic cells using soft x-ray tomography." In: *J. Struct. Biol.* 162.3 (2008), p. 380. DOI: 10.1016/j.jsb.2008.02.003.

[Pat+17] J. Patommel, S. Klare, R. Hoppe, S. Ritter, D. Samberg, F. Wittwer, A. Jahn, K. Richter, C. Wenzel, J. W. Bartha, M. Scholz, F. Seiboth, U. Boesenberg, G. Falkenberg, and C. G. Schroer. "Focusing hard x rays beyond the critical angle of total reflection by adiabatically focusing lenses." In: *Appl. Phys. Lett.* 110.10 (2017), p. 101103. DOI: 10.1063/1.4977882.

[Pfe+06] F. Pfeiffer, C. David, J. F. van der Veen, and C. Bergemann. "Nanometer focusing properties of Fresnel zone plates described by dynamical diffraction theory." In: *Phys. Rev. B* 73 (24 2006), p. 245331. DOI: 10.1103/PhysRevB.73.245331.

[Pfe18] F. Pfeiffer. "X-ray ptychography." In: *Nat. Photonics* 12 (2018), pp. 9–17. DOI: 10.1038/s41566-017-0072-5.

[Qui+06] H. M. Quiney, A. G. Peele, Z. Cai, D. Paterson, and K. A. Nugent. "Diffractive imaging of highly focused X-ray fields." In: *Nat. Phys.* 2 (2006), pp. 101–104. DOI: 10.1038/nphys218.

[Rar+80] R. Rarback, J. Kenny, J. Kirz, X. Xie, and E. Ash. *Scanned image microscopy*. Vol. 1980. Academic press, 1980.

[Reh+15] S. Rehbein, A. Lyon, R. Leung, M. Feser, and G. Schneider. "Near field stacking of zone plates for reduction of their effective zone period." In: *Opt. Express* 23.9 (2015), pp. 11063–11072. DOI: 10.1364/OE.23.011063.

[Rei+20] M. Reichardt, C. Neuhaus, J.-D. Nicolas, M. Bernhardt, K. Toischer, and T. Salditt. "X-Ray Structural Analysis of Single Adult Cardiomyocytes: Tomographic Imaging and Microdiffraction." In: *Biophys. J.* 119.7 (2020), pp. 1309–1323. DOI: 10.1016/j.bpj.2020.08.019.

[RBR19] C. Riekel, M. Burghammer, and M. Rosenthal. "Nanoscale X-ray diffraction of silk fibers." In: *Frontiers in Materials* 6 (2019), p. 315.

[RFM97] M. S. del Rio, C. Ferrero, and V. Mocella. "Computer simulation of bent perfect crystal diffraction profiles." In: *High Heat Flux and Synchrotron Radiation Beamlines*. Ed. by A. T. Macrander and A. M. Khounsary. Vol. 3151. International Society for Optics and Photonics. SPIE, 1997, pp. 312–323. DOI: 10.1117/12.294490.

[Rob+15] A. Robisch, K. Kröger, A. Rack, and T. Salditt. “Near-field ptychography using lateral and longitudinal shifts.” In: *New Journal of Physics* 17.7 (2015), p. 073033.

[RF04] J. M. Rodenburg and H. M. L. Faulkner. “A phase retrieval algorithm for shifting illumination.” In: *Appl. Phys. Lett.* 85.20 (2004), pp. 4795–4797. DOI: 10.1063/1.1823034.

[Rod+07] J. M. Rodenburg, A. C. Hurst, A. G. Cullis, B. R. Dobson, F. Pfeiffer, O. Bunk, C. David, K. Jefimovs, and I. Johnson. “Hard-X-Ray Lensless Imaging of Extended Objects.” In: *Phys. Rev. Lett.* 98.3 (2007), p. 034801. DOI: 10.1103/PhysRevLett.98.034801.

[RLK10] J. Röder, T. Liese, and H.-U. Krebs. “Material-dependent smoothing of periodic rippled structures by pulsed laser deposition.” In: *Journal of Applied Physics* 107.10 (2010), p. 103515.

[Rod97] P. A. Rodnyi. *Physical processes in inorganic scintillators*. Vol. 14. CRC press, 1997.

[Rön95] W. C. Röntgen. “Aus den sitzungsberichten der würzburger physik.-medic.” In: *Würzburg: Gesellschaft* (1895), pp. 137–147.

[Rös+20] B. Rösner, S. Finizio, F. Koch, F. Döring, V. A. Guzenko, M. Langer, E. Kirk, B. Watts, M. Meyer, J. L. Ornelas, et al. “Soft x-ray microscopy with 7 nm resolution.” In: *Optica* 7.11 (2020), pp. 1602–1608.

[Rud+84] D. Rudolph, B. Niemann, G. Schmahl, and O. Christ. “The Göttingen x-ray microscope and x-ray microscopy experiments at the BESSY storage ring.” In: (1984), pp. 192–202.

[Ruh+14] A. Ruhlandt, M. Krenkel, M. Bartels, and T. Salditt. “Three-dimensional phase retrieval in propagation-based phase-contrast imaging.” In: *Phys. Rev. A* 89.3 (2014), p. 033847. DOI: 10.1103/PhysRevA.89.033847.

[RS16] A. Ruhlandt and T. Salditt. “Three-dimensional propagation in near-field tomographic X-ray phase retrieval.” In: *Acta Crystallogr., Sect. A: Found. Adv.* 72.2 (2016), pp. 215–221. DOI: 10.1107/S2053273315022469.

[RS19] A. Ruhlandt and T. Salditt. “Time-resolved x-ray phase-contrast tomography of sedimenting micro-spheres.” In: *New J. Phys.* 21.4 (2019), p. 043017. DOI: 10.1088/1367-2630/ab13c8.

[SA10] A. Sakdinawat and D. Attwood. “Nanoscale X-ray imaging.” In: *Nat. Photonics* 4 (2010), pp. 840–848. DOI: 10.1038/nphoton.2010.267.

[Sal+15] T. Salditt, M. Osterhoff, M. Krenkel, R. N. Wilke, M. Priebe, M. Bartels, S. Kalbfleisch, and M. Sprung. "Compound focusing mirror and X-ray waveguide optics for coherent imaging and nano-diffraction." In: *J. Synchrotron Radiat.* 22.4 (2015), pp. 867–878. DOI: 10.1107/S1600577515007742.

[SEL20] T. Salditt, A. Egner, and D. R. Luke. *Nanoscale Photonic Imaging*. Springer Nature, 2020.

[Say80] D. Sayre. "Prospects for long-wavelength X-ray microscopy and diffraction." In: *Imaging Processes and Coherence in Physics*. Springer, 1980, pp. 229–235.

[Say52] D. Sayre. "Some implications of a theorem due to Shannon." In: *Acta Crystallogr.* 5.6 (1952), p. 843. DOI: 10.1107/S0365110X52002276.

[SO91] R. Scarmozzino and R. M. Osgood. "Comparison of finite-difference and Fourier-transform solutions of the parabolic wave equation with emphasis on integrated-optics applications." In: *JOSA A* 8.5 (1991), pp. 724–731.

[SM12] I. Schlichting and J. Miao. "Emerging opportunities in structural biology with X-ray free-electron lasers." In: *Curr. Opin. Struct. Biol.* 22.5 (2012), p. 613. DOI: 10.1016/j.sbi.2012.07.015.

[SR69] G. Schmahl and D. Rudolph. "High power zone plates as image forming systems for soft X-rays." In: *Optik* 29 (1969), pp. 577–585.

[Sch+80] G. Schmahl, D. Rudolph, B. Niemann, and O. Christ. "Zone-plate X-ray microscopy." In: *Quarterly Reviews of Biophysics* 13.3 (1980), pp. 297–315. DOI: 10.1017/S0033583500001700.

[Sch98] G. Schneider. "Cryo X-ray microscopy with high spatial resolution in amplitude and phase contrast." In: *Ultramicroscopy* 75.2 (1998), pp. 85–104. DOI: 10.1016/S0304-3991(98)00054-0.

[Sch+16] C. G. Schroer, C. Baumbach, R. Döhrmann, S. Klare, R. Hoppe, M. Kahnt, J. Patommel, J. Reinhardt, S. Ritter, D. Samberg, M. Scholz, A. Schropp, F. Seiboth, M. Seyrich, F. Wittwer, and G. Falkenberg. "Hard x-ray nanoprobe of beamline P06 at PETRA III." In: *AIP Conference Proceedings* 1741.1 (2016), p. 030007. DOI: 10.1063/1.4952830.

[Sch+03] C. G. Schroer, M. Kuhlmann, U. T. Hunger, T. F. Günzler, O. Kurapova, S. Feste, F. Frehse, B. Lengeler, M. Drakopoulos, A. Somogyi, A. S. Simionovici, A. Snigirev, I. Snigireva, C. Schug, and W. H. Schröder. "Nanofocusing parabolic refractive x-ray lenses." In: *Appl. Phys. Lett.* 82.9 (2003), pp. 1485–1487. DOI: 10.1063/1.1556960.

[Sch+05] C. G. Schroer, O. Kurapova, J. Patommel, P. Boye, J. Feldkamp, B. Lengeler, M. Burghammer, C. Riekel, L. Vincze, A. van der Hart, and M. Küchler. "Hard x-ray nanoprobe based on refractive x-ray lenses." In: *Appl. Phys. Lett.* 87.12 (2005), p. 124103. DOI: 10.1063/1.2053350.

[Sch06] C. G. Schroer. "Focusing hard x rays to nanometer dimensions using Fresnel zone plates." In: *Phys. Rev. B* 74.3 (2006), p. 033405. DOI: 10.1103/PhysRevB.74.033405.

[Sch+20] A. Schropp, R. Döhrmann, S. Botta, D. Brückner, M. Kahnt, M. Lyubomirskiy, C. Ossig, M. Scholz, M. Seyrich, M. E. Stuckelberger, et al. "PtyNAMi: ptychographic nano-analytical microscope." In: *Journal of applied crystallography* 53.4 (2020), pp. 957–971.

[Sei+11] M. M. Seibert et al. "Single mimivirus particles intercepted and imaged with an X-ray laser." In: *Nature* 470 (2011), pp. 78–81. DOI: 10.1038/nature09748.

[Sha+79] D. C. Shaver, D. C. Flanders, N. M. Ceglio, and H. I. Smith. "X-ray zone plates fabricated using electron-beam and x-ray lithography." In: *Journal of Vacuum Science and Technology* 16.6 (1979), p. 1626. DOI: 10.1116/1.570258.

[She+15] Y. Shechtman, Y. C. Eldar, O. Cohen, H. N. Chapman, J. Miao, and M. Segev. "Phase Retrieval with Application to Optical Imaging: A contemporary overview." In: *IEEE Signal Process. Mag.* 32.3 (2015), pp. 87–109. DOI: 10.1109/MSP.2014.2352673.

[Shi+19] X. Shi, N. Burdet, B. Chen, G. Xiong, R. Streubel, R. Harder, and I. K. Robinson. "X-ray ptychography on low-dimensional hard-condensed matter materials." In: *Applied Physics Reviews* 6.1 (2019), p. 011306.

[SM84] M. Simpson and A. Michette. "Imaging properties of modified Fresnel zone plates." In: *Optica Acta: International Journal of Optics* 31.4 (1984), pp. 403–413.

[Sni+96] A. Snigirev, V. Kohn, I. Snigireva, and B. Lengeler. "A compound refractive lens for focusing high-energy X-rays." In: *Nature* 384 (1996), pp. 49–51. DOI: 10.1038/384049a0.

[Sol+21a] J. Soltau, L. Chayanun, M. Lyubomirskiy, J. Wallentin, and M. Osterhoff. "Off-axis multilayer zone plate with 16 nm x 28 nm focus for high-resolution X-ray beam induced current imaging." In: *J. Synchrotron Radiat.* 28.5 (2021). DOI: 10.1107/S1600577521006159.

[Sol+21b] J. Soltau, M. Vassholz, M. Osterhoff, and T. Salditt. "In-line holography with hard x-rays at sub-15 nm resolution." In: *Optica* 8.6 (2021), pp. 818–823. DOI: 10.1364/OPTICA.420060.

[Sol+21c] J. Soltau, L. M. Lohse, M. Osterhoff, and T. Salditt. "Finite-difference propagation for the simulation of x-ray multilayer optics." In: *Opt. Express* 29.25 (2021), pp. 41932–41953. DOI: 10.1364/OE.445300.

[SOS22] J. Soltau, M. Osterhoff, and T. Salditt. "Coherent Diffractive Imaging with Diffractive Optics." In: *Phys. Rev. Lett.* 128 (22 2022), p. 223901. DOI: 10.1103/PhysRevLett.128.223901.

[Stu+15] M. Stuckelberger, B. West, S. Husein, H. Guthrey, M. Al-Jassim, R. Chakraborty, T. Buonassisi, J. M. Maser, B. Lai, B. Stripe, et al. "Latest developments in the x-ray based characterization of thin-film solar cells." In: *2015 IEEE 42nd Photovoltaic Specialist Conference (PVSC)*. IEEE. 2015, pp. 1–6.

[Stu+17] M. Stuckelberger, B. West, T. Nietzold, B. Lai, J. M. Maser, V. Rose, and M. I. Bertoni. "Engineering solar cells based on correlative X-ray microscopy." In: *Journal of Materials Research* 32.10 (2017).

[Thi+08] P. Thibault, M. Dierolf, A. Menzel, O. Bunk, C. David, and F. Pfeiffer. "High-resolution scanning x-ray diffraction microscopy." In: *Science* 321.5887 (2008), pp. 379–382.

[TE10] P. Thibault and V. Elser. "X-Ray Diffraction Microscopy." In: *Annu. Rev. Condens. Matter Phys.* 1.1 (2010), pp. 237–255. DOI: 10.1146/annurev-conmatphys-070909-104034.

[Töp+18] M. Töpperwien, F. van der Meer, C. Stadelmann, and T. Salditt. "Three-dimensional virtual histology of human cerebellum by X-ray phase-contrast tomography." In: *Proc. Natl. Acad. Sci. U.S.A.* 115.27 (2018), pp. 6940–6945. DOI: 10.1073/pnas.1801678115.

[Tro+18] A. Troian, G. Otnes, X. Zeng, L. Chayanun, V. Dagyto, S. Hammarberg, D. Salomon, R. Timm, A. Mikkelsen, M. T. Borgström, et al. “Nanobeam X-ray fluorescence dopant mapping reveals dynamics of in situ Zn-doping in nanowires.” In: *Nano letters* 18.10 (2018), pp. 6461–6468.

[Tsa+16] E. H. R. Tsai, I. Usov, A. Diaz, A. Menzel, and M. Guizar-Sicairos. “X-ray ptychography with extended depth of field.” In: *Opt. Express* 24.25 (2016), pp. 29089–29108. DOI: 10.1364/OE.24.029089.

[Ung89] P. Unger. “Herstellung von Fresnel-Zonenplatten für die Röntgenmikroskopie durch Strukturierung im Nanometerbereich.” PhD thesis. University of Göttingen, 1989.

[Van+17] G. Van der Snickt, H. Dubois, J. Sanyova, S. Legrand, A. Coudray, C. Glaude, M. Postec, P. Van Espen, and K. Janssens. “Large-Area Elemental Imaging Reveals Van Eyck’s Original Paint Layers on the Ghent Altarpiece (1432), Rescoping Its Conservation Treatment.” In: *Angewandte Chemie International Edition* 56.17 (2017), pp. 4797–4801.

[Vas+21] M. Vassholz, H. P. Hoeppe, J. Hagemann, J. M. Rosselló, M. Osterhoff, R. Mettin, T. Kurz, A. Schropp, F. Seiboth, C. G. Schroer, M. Scholz, J. Möller, J. Hallmann, U. Boesenberg, C. Kim, A. Zozulya, W. Lu, R. Shayduk, R. Schaffer, A. Madsen, and T. Salditt. “Pump-probe X-ray holographic imaging of laser-induced cavitation bubbles with femtosecond FEL pulses.” In: *Nat. Commun.* 12.3468 (2021), pp. 1–11. DOI: 10.1038/s41467-021-23664-1.

[Vas21] M. Vassholz. “A matter of brightness: table-top X-ray generation inside waveguides and X-ray holography with single free-electron laser pulses.” PhD thesis. University of Göttingen, 2021.

[Vic+18] T. W. Victor, L. M. Easthon, M. Ge, K. H. O’Toole, R. J. Smith, X. Huang, H. Yan, K. N. Allen, Y. S. Chu, and L. M. Miller. “X-ray fluorescence nanotomography of single bacteria with a sub-15 nm beam.” In: *Scientific Reports* 8.1 (2018), pp. 1–8.

[Vij+20] A. Vijaykumar et al. “SciPy 1.0: fundamental algorithms for scientific computing in Python.” In: *Nat. Methods* 17 (2020), pp. 261–272. DOI: 10.1038/s41592-019-0686-2.

[Vil+11] J. Vila-Comamala, A. Diaz, M. Guizar-Sicairos, A. Mantion, C. M. Kewish, A. Menzel, O. Bunk, and C. David. "Characterization of high-resolution diffractive X-ray optics by ptychographic coherent diffractive imaging." In: *Opt. Express* 19.22 (2011), pp. 21333–21344. DOI: 10.1364/OE.19.021333.

[Vil+21] P. Villanueva-Perez, H. Fleckenstein, M. Prasciolu, K. T. Murray, M. Domaracký, K. Gregorič, V. Mariani, L. Gelisio, M. Kuhn, J. Hannappel, O. Yefanov, N. Ivanov, I. Sarrou, D. Pennicard, J. Becker, M. von Zimmermann, O. Gutowski, A.-C. Dippel, H. N. Chapman, and S. Bajt. "Scanning Compton X-ray microscopy." In: *Opt. Lett.* 46.8 (2021), pp. 1920–1923. DOI: 10.1364/OL.421232.

[Vil+18] P. Villanueva-Perez, B. Pedrini, R. Mokso, P. Vagovic, V. A. Guzenko, S. J. Leake, P. R. Willmott, P. Oberta, C. David, H. N. Chapman, and M. Stampanoni. "Hard x-ray multi-projection imaging for single-shot approaches." In: *Optica* 5.12 (2018), pp. 1521–1524. DOI: 10.1364/OPTICA.5.001521.

[VBC18] P. Villanueva-Perez, S. Bajt, and H. Chapman. "Dose efficient Compton X-ray microscopy." In: *Optica* 5.4 (2018), pp. 450–457.

[VR09] D. G. Voelz and M. C. Roggemann. "Digital simulation of scalar optical diffraction: revisiting chirp function sampling criteria and consequences." In: *Applied Optics* 48.32 (2009), p. 6132. DOI: 10.1364/ao.48.006132.

[Wal+14a] S. M. Walker, D. A. Schwyn, R. Mokso, M. Wicklein, T. Müller, M. Doube, M. Stampanoni, H. G. Krapp, and G. K. Taylor. "In Vivo Time-Resolved Microtomography Reveals the Mechanics of the Blowfly Flight Motor." In: *PLoS Biol.* 12.3 (2014), e1001823. DOI: 10.1371/journal.pbio.1001823.

[Wal+10] J. Wallentin, M. Ek, L. R. Wallenberg, L. Samuelson, K. Deppert, and M. T. Borgström. "Changes in Contact Angle of Seed Particle Correlated with Increased Zincblende Formation in Doped InP Nanowires." In: *Nano Letters* 10.12 (2010), pp. 4807–4812. DOI: 10.1021/nl101747z.

[Wal+14b] J. Wallentin, M. Osterhoff, R. N. Wilke, K.-M. Persson, L.-E. Wernersson, M. Sprung, and T. Salditt. "Hard X-ray detection using a single 100 nm diameter nanowire." In: *Nano letters* 14.12 (2014), pp. 7071–7076.

[Wan+20] Y. Wang, L. Hu, B. Zhang, L. Zhou, Y. Tao, M. Li, and Q. Jia. "Finite-element simulation for X-ray volume diffractive optics based on the wave optical theory." In: *Opt. Express* 28.23 (2020), pp. 34973–34993. DOI: 10.1364/OE.409961.

[Wie+18] M. O. Wiedorn et al. "Megahertz serial crystallography." In: *Nat. Commun.* 9.4025 (2018), pp. 1–11. DOI: 10.1038/s41467-018-06156-7.

[Wil+96] S. W. Wilkins, T. E. Gureyev, D. Gao, A. Pogany, and A. W. Stevenson. "Phase-contrast imaging using polychromatic hard X-rays." In: *Nature* 384 (1996), pp. 335–338. DOI: 10.1038/384335a0.

[Wil+06] G. J. Williams, H. M. Quiney, B. B. Dhal, C. Q. Tran, K. A. Nugent, A. G. Peele, D. Paterson, and M. D. de Jonge. "Fresnel Coherent Diffractive Imaging." In: *Phys. Rev. Lett.* 97.2 (2006), p. 025506. DOI: 10.1103/PhysRevLett.97.025506.

[Yan+18] H. Yan, N. Bouet, J. Zhou, X. Huang, E. Nazaretski, W. Xu, A. P. Cocco, W. K. S. Chiu, K. S. Brinkman, and Y. S. Chu. "Multimodal hard x-ray imaging with resolution approaching 10 nm for studies in material science." In: *Nano Futures* 2.1 (2018), p. 011001. DOI: 10.1088/2399-1984/aab25d.

[Yan+10] H. Yan, H. C. Kang, R. Conley, C. Liu, A. T. Macrander, G. B. Stephenson, and J. Maser. "Multilayer Laue lens: a path toward one nanometer x-ray focusing." In: *X-ray Optics and Instrumentation* 2010 (2010).

[Yan+07] H. Yan, J. Maser, A. Macrander, Q. Shen, S. Vogt, G. B. Stephenson, and H. C. Kang. "Takagi-Taupin description of x-ray dynamical diffraction from diffractive optics with large numerical aperture." In: *Phys. Rev. B* 76.11 (2007), p. 115438. DOI: 10.1103/PhysRevB.76.115438.

[Yan+16] H. Yan, E. Nazaretski, K. Lauer, X. Huang, U. Wagner, C. Rau, M. Yusuf, I. Robinson, S. Kalbfleisch, L. Li, et al. "Multimodality hard-x-ray imaging of a chromosome with nanoscale spatial resolution." In: *Scientific Reports* 6.1 (2016), pp. 1–7.

[Yan+19] Y. Yang, R. Xu, K. Zhang, S.-J. Lee, L. Mu, P. Liu, C. K. Waters, S. Spence, Z. Xu, C. Wei, D. J. Kautz, Q. Yuan, Y. Dong, Y.-S. Yu, X. Xiao, H.-K. Lee, P. Pianetta, P. Cloetens, J.-S. Lee, K. Zhao, F. Lin, and Y. Liu. "Quantification of Heterogeneous Degradation in Li-Ion Batteries." In: *Adv. Energy Mater.* 9.25 (2019), p. 1900674. DOI: 10.1002/aenm.201900674.

[Yun+99] W. Yun, B. Lai, A. A. Krasnoperova, E. Di Fabrizio, Z. Cai, F. Cerrina, Z. Chen, M. Gentili, and E. Gluskin. “Development of zone plates with a blazed profile for hard x-ray applications.” In: *Rev. Sci. Instrum.* 70.9 (1999), pp. 3537–3541. DOI: 10.1063/1.1149956.

[Zap+20] M. Zapf, M. Ritzer, L. Liborius, A. Johannes, M. Hafermann, S. Schönherr, J. Segura-Ruiz, G. Martínez-Criado, W. Prost, and C. Ronning. “Hot electrons in a nanowire hard X-ray detector.” In: *Nature communications* 11.1 (2020), pp. 1–7.

[Zha+16] F. Zhang, B. Chen, G. R. Morrison, J. Vila-Comamala, M. Guizar-Sicairos, and I. K. Robinson. “Phase retrieval by coherent modulation imaging - Nature Communications.” In: *Nat. Commun.* 7.13367 (2016), pp. 1–8. DOI: 10.1038/ncomms13367.

[Zha+20] W. Zhang, H. Zhang, C. J. Sheppard, and G. Jin. “Analysis of numerical diffraction calculation methods: from the perspective of phase space optics and the sampling theorem.” In: *JOSA A* 37.11 (2020), pp. 1748–1766.

[Zoz+12] A. Zozulya, S. Bondarenko, A. Schavkan, F. Westermeier, G. Grübel, and M. Sprung. “Microfocusing transfocator for 1D and 2D compound refractive lenses.” In: *Optics express* 20.17 (2012), pp. 18967–18976.

[Zoz+14] A. Zozulya, A. Shabalin, H. Schulte-Schrepping, J. Heuer, M. Spiwek, I. Sergeev, I. Besedin, I. Vartanyants, and M. Sprung. “Wavefront preserving channel-cut optics for coherent x-ray scattering experiments at the P10 beamline at PETRAIII.” In: *Journal of Physics: Conference Series*. Vol. 499. 1. IOP Publishing. 2014, p. 012003.

Author contributions

Author contributions chapter 3: The manuscript was mainly written by J. Soltau, L.M. Lohse, and T. Salditt with substantial input from M. Osterhoff. The finite difference solver was written by L.M. Lohse. The simulation code was written by J. Soltau. The data analysis was performed by J. Soltau. The data analysis was discussed by J. Soltau, L.M. Lohse M. Osterhoff and T. Salditt. All authors read and approved the manuscript.

Author contributions chapter 4: The manuscript was mainly written by J. Soltau and L. Chayanun with substantial input from J. Wallentin and M. Osterhoff. The beamtime at the P06 was initialized by M. Lyubomirskiy . The beamtime at the P10 was applied by M. Osterhoff, J. Soltau, L. Chayanun and J. Wallentin. The nanowires were contacted and organized by L. Chayanun and J. Wallentin. The following participated at the beamtime at P06: J. Soltau, M. Lyubomirskiy, M. Osterhoff, M. Seyrich, D. Brückner and J. Hagemann. The following participated at the beamtime at P10: J. Soltau, M. Osterhoff, L. Chayanun, and J. Wallentin. The MZP were fabricated by C. Eberl and mounted from M. Kanbach. The MZP off-axis illumination approach was mainly developed by J. Soltau with substantial input from M. Osterhoff. The code for the P06 data analysis was provided by the P06 beamline. The code for the P10 data analysis was written by J. Soltau. The diffraction data was analyzed by J. Soltau. The XBIC data was analyzed by L. Chayanun. The diffraction data was discussed by J. Soltau and M. Osterhoff. All authors read and approved the manuscript.

Author contributions chapter 5: The manuscript was mainly written by J. Soltau and T. Salditt with substantial input from M. Vassholz and M. Osterhoff. The following participated at the beamtime: J. Soltau, M. Vassholz, M. Osterhoff, and T. Salditt. The waveguides were mounted by M. Kanbach. The super-resolution in-line holography approach was mainly developed by J. Soltau and T. Salditt with substantial input from M. Vassholz and M. Osterhoff. The code for the data analysis was written by J. Soltau. The diffraction data was analyzed by J. Soltau. The diffraction data was discussed by J.

Soltau, M. Vassholz, M. Osterhoff, and T. Salditt. All authors read and approved the manuscript.

Author contributions chapter 6: The manuscript was written by J. Soltau. The following participated at the beamtime: J. Soltau, A.L. Robisch, M. Osterhoff and T. Salditt. The reporter based imaging approach was mainly developed by J. Soltau and T. Salditt. The code for the data analysis was written by J. Soltau. The diffraction data was analyzed by J. Soltau. The diffraction data was discussed by J. Soltau, M. Osterhoff, and T. Salditt. The MZP were fabricated by C. Eberl and mounted from M. Kanbach.

List of publications

1. Coherent diffractive imaging with diffractive optics. J. Soltau, M. Osterhoff, and T. Salditt. In: *Phys. Rev. Lett.*, 128, 223901 (2022).
   doi: 10.1103/PhysRevLett.128.223901.
2. Finite-difference propagation for the simulation of x-ray multilayer optics. J. Soltau, L. M. Lohse, M. Osterhoff, and T. Salditt. In: *Opt. Express*, 25, 29, 41932-41953, (2021).
   doi: 10.1364/OE.445300.
3. Off-axis multilayer zone plate with 16 nm x 28 nm focus for high-resolution X-ray beam induced current imaging. J. Soltau, L. Chayanun, M. Lyubomirskiy, J. Wallentin, and M. Osterhoff. In: *J. Synchrotron Radiat.*, 28, 5, (2021).
   doi: 10.1107/S1600577521006159.
4. In-line holography with hard x-rays at sub-15 nm resolution. J. Soltau, M.Vassholz, M. Osterhoff, and T. Salditt. In: *Optica*, 8, 6, 818-823, (2021).
   doi: 10.1364/OPTICA.420060.
5. Focus characterization of the NanoMAX Kirkpatrick Baez mirror system. M. Osterhoff, A.-L. Robisch, J. Soltau, M. Eckermann, S. Kalbfleisch, D. Carbone, U. Johansson, and T. Salditt. In: *J. Synchrotron Radiat.*, 26, 4, 1173-1180, (2019).
   doi: 10.1107/S1600577519003886.
6. A zone-plate-based two-color spectrometer for indirect X-ray absorption spectroscopy. F. Döring, M. Risch, B. Rösner, M. Beye, P. Busse,K. Kubicek, L. Glaser, P.S. Miedema, J. Soltau, D. Raiser, V.A. Guzenko, L. Szabadics, L. Kochanneck, M. Baumung, J. Buck, C. Jooss, S. Techert, and C. David. In: *J. Synchrotron Radiat.*, 26, 4, 1266-1271, (2019).
   doi: 10.1107/S1600577519003898.
7. ID-Full Field Microscopy of Elastic and Inelastic Scattering with Transmission off-axis Fresnel Zone Plates. F. Döring, F. Marschall,Z. Yin,

B. Rösner, M. Beye, P. Miedema, K. Kubicek, L. Glaser,D. Raiser, J. Soltau, V.A. Guzenko, J. Viefhaus, J. Buck, M. Risch, S. Techert, and C. David. In: *Microsc. Microanal.*, 24, S2, 182-183, (2018).

DOI: 10.1017/S1431927618013260.

8. Ultra-high-aspect multilayer zone plates for even higher x-ray energies. M .Osterhoff, J. Soltau, C. Eberl, and H.-U. Krebs. In: *Advances in X-Ray/EUV Optics and Components XII*, 10386, 1038608, (2017).

   DOI: 10.1117/12.2271139.

9. Preparing for hard x-ray microscopy with Multilayer Zone Plates. M .Osterhoff, J. Soltau, C. Eberl, and H.-U. Krebs. In: *J. Phys. Conf. Ser.*, 849, 1, 012049 (2017).

   DOI: 10.1088/1742-6596/849/1/012049.

10. Controlled charge extraction-antiblooming capabilities in pnCCD imaging sensors. J. Schmidt, R. Hartmann, P. Holl, M. Huth, G. Lutz, U. Pietsch, H. Ryll, S. Send, M. Simson, H. Soltau, J. Soltau, D. Steigenhöfer, and L. Strüder. In: *J. Instrum.*, 11, 01, P01012, (2016).

    DOI: 10.1088/1748-0221/11/01/p01012.

11. Dynamic range of fully depleted pnCCDs: modeling and experimental confirmation. J .Schmidt, R. Hartmann, P. Holl, M. Huth,G. Lutz, J. Soltau, D. Steigenhöfer, H. Soltau, and L. Strüder. In: *High Energy, Optical, and Infrared Detectors for Astronomy VI*, 9154, (2014).

    DOI: 10.1117/12.2055343.

12. High Speed, High Throughput Two Dimensional Direct Electron Detector Based on the Concept of pnCCDs. L. Strüder, J. Soltau, J. Schmidt, R. Hartmann, M. Huth, H. Soltau, P. Holl, M. Simson, G. Lutz, and H. Ryll. In: *Microsc. Microanal.*, 20, S3, 392-393, (2014).

    DOI: 10.1017/S1431927614003687.

13. Extending the dynamic range of fully depleted pnCCDs J. Schmidt, R. Hartmann, P. Holl, M. Huth, G. Lutz, H. Ryll, S. Send, M. Simson, D. Steigenhöfer, J. Soltau, H. Soltau, and L. Strüder. In: *J. Instrum.*, 9, 10, P10008, (2014).

    DOI: 10.1088/1748-0221/9/10/p10008.

14. High Speed, High Resolution pnCCDs as Two Dimensional Imaging Spectrometers for X-rays and Electrons. H. Soltau, R. Hartmann, P.

Holl, S. Ihle, H. Ryll, M. Huth, J. Schmidt, R. Eckhardt, M. Simson, J. Soltau, C Thamm, and L. Strüder. In: *Microsc. Microanal.*, 20, S3, 652-653, (2014).
DOI: 10.1017/S143192761400498X.

Acknowledgements

An dieser Stelle möchte ich mich bei den vielen Menschen bedanken, die mich während meiner Promotion unterstützt und begleitet haben.

Mein besonderer Dank gilt Tim Salditt, der mir die Chance gegeben hat diese Dissertation zu diesem spannenden Thema zu verfassen. Ich möchte mich insbesondere dafür bedanken, dass er mich zur Entwicklung neuer Ideen und eigener Methoden ermutigt hat und mir stets mit seinem Vertrauen und seiner Expertise beiseite stand. Ohne seine Begeisterung und Anregung wäre diese Arbeit in dieser Form nicht möglich gewesen.

Für die gute Co-Betreuung möchte ich mich herzlich bei Christian Jooß bedanken. Insbesondere gilt mein Dank dem interessanten fachlichen Austausch zu Beginn der Arbeit, sowie seiner Bereitschaft zum Erstellen des Zweitgutachtens.

Natürlich gilt mein Dank auch Markus Osterhoff, ohne dessen Hilfe nicht eine *Multilagen Zonen Platte* justiert und nicht ein Detektorbild aufgenommen worden wäre. Besonders die vielen Diskussionen auch bei Nacht an der Beamline oder bei Tag spontan im Büro, hat mir beim Meistern vieler Herausforderungen sehr geholfen.

Dann darf natürlich auch nicht Christian Eberl fehlen, der diese außergewöhnlichen Multilagen Zonen Platten hergestellt hat. Vielen Dank dafür. Auch möchte ich mich bei Mike Kanbach für die Montierung der Multilagen Zonen Platten und die Herstellung der Wellenleiter Optiken bedanken.

Mein Dank gilt auch Mikhail Lyubomirskiy, der es mir auf unkomplizierte Weise ermöglichte (endlich!) eine ptychographische Charakterisierung der Multilagen Zonen Platten durchführen zu können.

Zudem möchte ich mich bei all meinen Kollegen für die zahlreichen Diskussionen, Unterstützungen, Konferenzen und die tolle Zeit bedanken. Im Besonderen sind hier Malte Vassholz, Jasper Frohn, Leon Lohse, Mareike Töpperwien, Johannes Hagemann, Simon Maretzke, Anna-Lena Robisch und Karlo Komorowski zu nennen.

Ich möchte mich bei Jan Goeman für die tolle IT Infrastruktur bedanken. Ohne die hätte keine Auswertung durchgeführt werden können. Aufgrund des reibungslosen

Datenstroms fiel es gar nicht auf, wie viele Terabytes an Daten man eigentlich im Laufe seiner Dissertation gesammelt hat. Für die Unterstützung bei allen fein- und teilweise auch grobmechanischen Angelegenheiten möchte ich mich herzlich bei Bastian Hartmann, Peter Nieschalk und Peter Luley bedanken. Außerdem möchte ich mich bei Jochen Herbst und Susanne Hengst für ihre große Hilfsbereitschaft und ihre offene Art bedanken. Mein Dank gilt auch Kerstin Pluschke, Michaela Ständer und Eva Hetzel, die stets den Überblick bewahrt und für Ordnung in den Abläufen gesorgt haben.

Ich möchte mich auch bei Michael Sprung und Fabian Westermeier bedanken, mit deren Hilfe die *GINIX* so ein fantastisches Instrument wurde.

Für das schnelle und zuverlässige Korrekturlesen meiner Dissertation möchte ich mich bei Malte Vassholz, Jasmin Pape, Leon Lohse, Jasper Frohn, Lothar Strüder, Heike Soltau und Sonia Ferkel bedanken.

Abschließend möchte ich mich bei dem gesamten Institut für Röntgenphysik für die ausgezeichnete Arbeitsatmosphäre und die freundschaftliche Stimmung bedanken. Ich hoffe sehr, dass die vielen Traditionen wie das D-Café noch lange erhalten bleiben.

Mein ganz besonderer Dank gilt Sonia Ferkel, die mich bei dieser Arbeit unglaublich unterstützt hat. Nicht zuletzt gilt mein Dank meiner Familie Lea, Heike und Lothar, auf die ich mich immer verlassen konnte.

Curriculum vitae

Jakob Alexander Soltau

Education:

since 01/2017	Doctoral student, Institute for X-ray Physics, University of Göttingen
04/2014 – 11/2016	Master studies Physics, University of Göttingen
10/2009 – 06/2013	Bachelor studies Physics, Ludwig Maximilian University of Munich
06/2009	Abitur, Michaeli-Gymnasium, München
09/1996 – 06/2009	Rudolf-Steiner-Schule Schwabing, München

X-ray microscopy is used to study the structure, dynamics and bulk properties of matter with high spatial resolutions. It is widely applied, from physics and chemistry to material and life sciences. In the past two decades, progress in X-ray microscopy was driven either by improvements in X-ray optics or by improvements in the image reconstruction by using algorithms as computational lenses. In this work both approaches are combined to exploit the advantages of X-ray imaging with a large numerical aperture and the advantages of coherent image reconstruction. It is shown that a combined X-ray microscope using both, advanced optics and algorithms, is neither limited by flawed optics nor by constraints imposed by reconstruction algorithms, which enables to go beyond current limits in resolution and applications.
The thesis is structured in four parts. In the first part hard X-ray lenses, so called multilayer zone plates, are simulated to investigate volume diffraction effects within the multilayer structure, and to study the potential for smaller focus sizes and higher efficiencies. In the second part, the multilayer zone plates are characterized and implemented in an X-ray microscope. In the third part, a new imaging scheme is presented, which combines in-line holography and coherent diffractive imaging. This method overcomes the current resolution limit of in-line holography and can achieve super-resolution with respect to the numerical aperture of the illuminating beam. Finally, in the fourth part a multilayer zone plate is used as an objective lens with a known transfer function in a novel coherent full-field imaging experiment based on iterative phase retrieval, for high resolution and quantitative contrast.

GEORG-AUGUST-UNIVERSITÄT
GÖTTINGEN

ISBN 978-3-86395-553-3
ISSN 2191-9860
eISSN 2512-6326

Universitätsverlag Göttingen